M. O'Mullane
Sept. 1993

Department of Physics and Applied Physics
University of Strathclyde

# METASTABLE RESOLVED COLLISIONAL-RADIATIVE MODELLING OF SPECTRAL EMISSION FROM THERMAL PLASMAS

William J. Dickson
8th April 1993

A thesis submitted in fulfillment of the requirements for the degree of Doctor of Philosophy.

**ABSTRACT**

The thesis addresses the prediction and simulation of population distribution and spectral emission of light impurity ions in fusion plasmas. This is of special relevance to edge and divertor zones of tokamak devices, such as the Joint European Torus (JET).

There are three major developments. Firstly, the problem of highly populated metastable states of impurity ions in dynamic plasma is examined and integrated in full collisional radiative modelling for the first time. This includes a full density dependent picture encompassing both low finely resolved populations relevant to high resolution spectroscopy as well as those of all higher excited states.

Secondly, review and development of fundamental reaction cross section data are described. These include new methods for incorporating such data in metastable resolved pictures as well as generation of original results on the dielectronic process. Also extensive critical discussion is given of basic electron impact excitation data.

The last sections of the thesis explore the implications of these developments in ionisation, radiated power and dynamic population evolution of beryllium, carbon and oxygen in representative tokamak environments.

## TABLE OF CONTENTS


**Abstract** . . . . . i
**Table of Contents** . . . . . ii
**Preface** . . . . . iv

**Chapter 1:** Introduction . . . . . 1
**1.1:** Introduction . . . . . 2
**1.2:** Laboratory Fusion Plasmas . . . . . 7
**1.3:** Plasma Diagnostics and the Role of Spectroscopy . . 18
**1.4:** Physical Conditions . . . . . 27

**Chapter 2:** Relevant Physics . . . . . 34
**2.1:** Atomic Processes . . . . . 35
**2.2** Population Structure and Spectral Emission Theory . 48
**2.3** Literature Review and Scope of Present Work . . . 58

**Chapter 3:** Atomic Data . . . . . 74
**3.1:** Introduction . . . . . 75
**3.2:** Transitions Between Bound States . . . . . 77
**3.3:** Ionisation and Autoionisation Processes . . . . 86
**3.4:** Electron-Ion Recombination Processes . . . . 107
**3.5:** Charge Transfer Recombination . . . . . 116
**3.6:** Summary . . . . . 118

**Chapter 4:** Theoretical Population Modelling . . . 120
**4.1:** The Bundle-n S model . . . . . 121
**4.2:** The Low Level Resolved Model. . . . . 145
**4.3:** The Projection/Expansion Model . . . . . 163

**Chapter 5:** Integration of Models . . . . . 184
**5.1:** Introduction . . . . . 185
**5.2:** Equilibrium Ionisation Balance and Radiated Power . 195
**5.3:** Time Dependent Ionisation Studies . . . . . 212
**5.4:** Concluding Remarks . . . . . 221

**Chapter 6:** Concluding Remarks . . . . . 223
**6.1:** Review of Present Work . . . . . 224
**6.2:** Applications . . . . . 226
**6.3:** Development and Future Work . . . . . 228

**Acknowledgements** . . . . . 230

**References** . . . . . 231

**Appendices**
**A1:** Units and Symbols
**A2:** Extended Collisional-Radiative Theory
**A3:** Included Low Levels
**A4:** Calculation of Radiated Power Coefficients

## Preface

This thesis was completed in the period October 1989 - April 1993 in association with the Dept. of Physics and Applied Physics, University of Strathclyde, Glasgow and JET Joint Undertaking, Abingdon, Oxon. The work was performed under the supervision of Prof. H.P. Summers. The author is grateful for the financial support of a Science and Engineering Research Council post-graduate studentship and additional CASE funding from Experimental Division II, JET.

The following publications and conference presentations are associated with the work of this thesis and contain substantial contributions from the author of this thesis.

*On Spectral Emission from Beryllium in Plasmas*
Summers, H.P., Dickson, W.J., Boileau, A. et al, 1991, Plasma Physics and Controlled Fusion, **34**, pp325-352.

*An Investigation of the Power Balance Associated With Recycling in JET Limiter Discharges*
Loarte, A., Harbour, P.J., Summers, H.P., Tagle, J.A. and Dickson, W.J., 1991, Proceedings of 18th Annual I.O.P. National Conference on Plasma Physics, University of Essex, U.K., 3-5th July. Also available as JET Laboratory preprint **JET-P(91)22.**

*Spectral Emission Characteristics of Beryllium Near Tokamak Plasma-Wall Boundaries*
Dickson, W.J., Breger, P, Loarte, A. et al, 1991, Proceedings of Workshop on 'Diagnostics for Contemporary Fusion Experiments', held at Villa Monastero, Varenna, Italy. Editors Stott, P.E., Akulina, D.K., Gorini, G. and Sindoni, E.. Also available as JET Laboratory preprint **JET-P(91)55.**

*Applications of Recombination*
Summers, H.P. and Dickson, W.J., 1992, Proceedings of Nato Advanced Workshop on 'Recombination of Atomic Ions', Edited by Graham, W.G. et al, Plenum Press, New York. Also available as JET Laboratory preprint **JET-P(91)57.**

*Effective Ionisation, Recombination and Emission Coefficients of Impurity Ions in Thermal Plasmas*

Dickson, W.J., Summers, H.P., Badnell, N.R. and Lang, J., 1992, Proceedings of VIth International Conference on the 'Physics of Highly Charged Ions', Kansas, USA, 28th September - 2nd October. Published as *AIP Conference Proceedings* **274**.

*Electric Field Effects on Dielectronic Recombination in a Collisional -Radiative Model*

Badnell, N.R., Pindzola, M.S., Dickson, W.J. et al, 1993, Astrophysics J. Letters, **407**, L91.

# CHAPTER 1

# INTRODUCTION

# 1.1: INTRODUCTION

There is a great deal of interest in the modelling of spectral emission from thermal plasmas. Much of this stems from the controlled thermonuclear fusion programme and from investigations into the nature of astrophysical bodies such as the sun.

In fusion plasmas, spectral emission is predominantly from impurities which are unavoidably released when the plasma is in contact with limiting surfaces. Beryllium, carbon and oxygen are the most important light impurities in fusion plasmas. The impurities are harmful because they dilute the plasma fuel and radiate a substantial part of the plasma energy. This radiation loss can disturb the stability of the plasma and plays an important role in the physics and design of present experiments and future reactors. The largest fusion experiment in the world is the Joint European Torus (JET) which utilises magnetic fields to confine a high temperature hydrogen plasma in a toroidal device of 'tokamak' type. A new phase in JET commences in 1993 with the operation of a pumped divertor configuration designed to control the influx of impurities. Compared to the bulk plasma in which electron temperatures and densities are typically several KeV and ~ $2\text{-}5\times10^{13}\text{cm}^{-3}$ respectively, the divertor will be a low temperature (10-20eV), high density ($10^{14}$ $\text{cm}^{-3}$) region of plasma which is intended to retain impurities away from the main plasma. The key to understanding and optimising divertor performance lies in knowledge of impurity transport in the region of the divertor. Spectroscopic techniques offer a unique method for investigating impurity production and transport.

Carbon and oxygen are also two of the most important elements in astrophysical plasmas. In 1995, the SOHO (Solar and Heliospheric Observatory) Satellite will be launched to study the atmosphere of the sun and solar wind. Amongst the instruments on board will be two spectrometers - CDS and SUMER. These are intended to exploit spectral emission to provide temperature and density diagnostics through the solar chromosphere, transition region and corona.

Fundamental to interpretation of spectral emission from both fusion and astrophysical plasmas is theoretical modelling of the ionisation state and emission of the radiating ions. This thesis addresses the calculation of ionisation, recombination and emission coefficients for the ions of beryllium, carbon and oxygen and pays special attention to three physical

features, namely, the presence of highly populated metastable states, the influence of finite plasma density on excited state populations and ionisation in dynamic plasmas.

It is well known that metastable states of certain ions can have populations comparable with ground state ions. For example, consider the energy level diagram of a $C^{+1}$ which is illustrated in Fig. 1.1.1 and is typical of boron-like ions. The ground state is the $1s^22s^22p\ ^2P$ term. On the left hand side of the diagram are excited terms within the doublet spin system. These converge to an ionisation threshold which leaves the beryllium-like ion in the $1s^22s^2\ ^1S$ state. This is known as a parent ion. On the right hand side of the diagram are doubly excited states within the quartet spin system. The lowest energy state in the quartet system is the $2s2p^2\ ^4P$ state. The direct ionisation threshold for these states is the $1s^22s2p\ ^3P$ parent but note that bound states converging to this parent have an energy greater than the lowest (singlet) ionisation threshold.

The $2s2p^2\ ^4P$ state is metastable because in LS coupling, the spin selection rule is $\Delta S=0$ which forbids radiative transitions between spin systems. As a result, this state evolves in a dynamic plasma on a much longer timescale than the excited states and can accumulate large populations. Similarly, the $2s2p\ ^3P$ state in beryllium-like ions is also metastable. These highly populated metastable states can have several influences. A simple 'ground to ground' ionisation model involves direct ionisation and recombination between ground state configurations only. However, the $2s2p^2\ ^4P$ and $2s2p\ ^3P$ metastables can have populations large enough to act as a significant initial state for ionisation and recombination processes.

Electrons recombining with $1s^22s2p\ ^3P$ will form doublet and quartet states in the boron like ion, populating the $1s^22s^22p\ ^2P$ and $1s^22s2p^2\ ^4P$ states respectively. Those electrons recombining into the quartet spin system thus do not contribute to the growth of the $1s^22s^22p\ ^2P$ ground state immediately. Similarly, the ionisation of inner shell 2s electrons from $1s^22s^22p\ ^2P$ will form $1s^22s2p\ ^1P$ and $1s^22s2p\ ^3P$ states, which contribute to the growth of the ground and metastable states respectively.

The fundamental rate coefficients between metastable states can differ substantially from that between the respective ground states. In ionisation, changes in threshold can be quite important. For example, the $1s2s\ ^3S$ state in helium like ions is metastable with an ionisation potential ~ 1/4 of that of the ground. The ionisation rate from this level

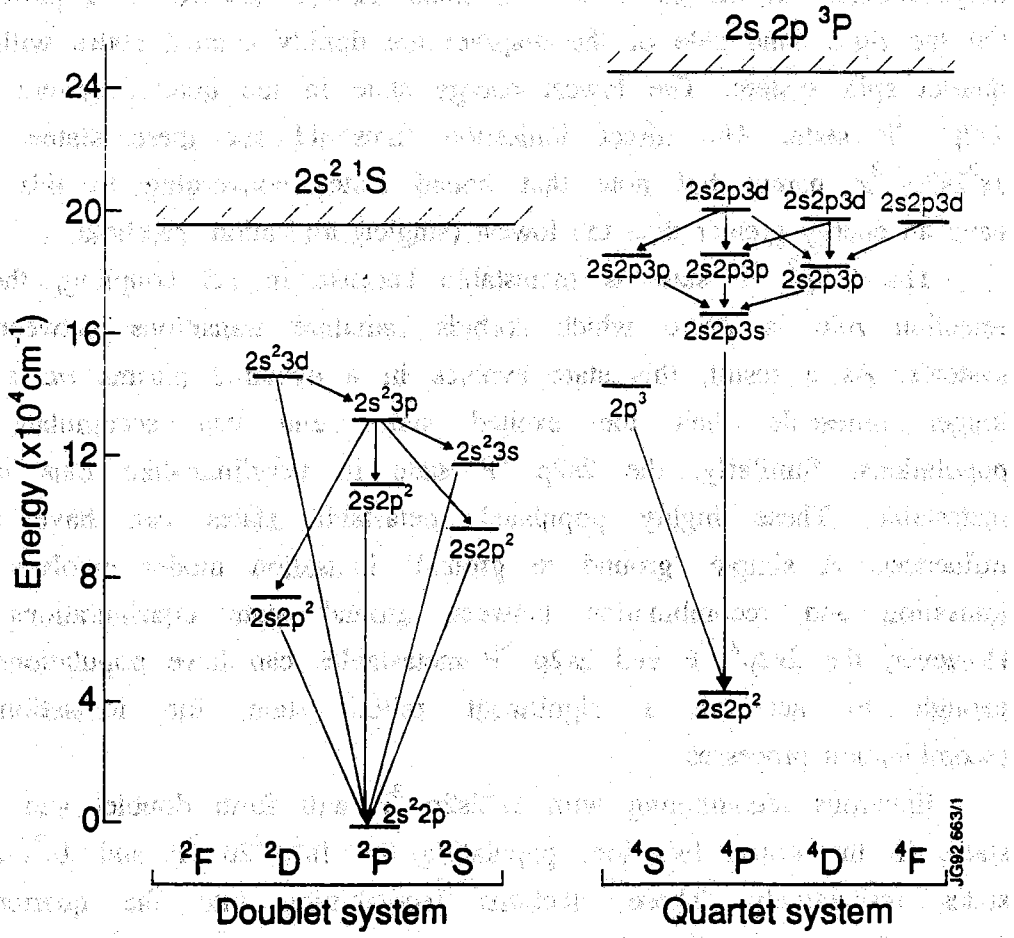


**Figure 1.1.1:** Term diagram for $C^{+1}$.

is thus much greater than that of the $1s^2\ ^1S$ ground state. An additional feature is autoionisation of excited states in the metastable system which lie above the lowest ionisation threshold. This can be a major alternative path to direct ionisation. Similarly, contributions to net recombination from an excited parent are dramatically reduced following secondary autoionisation of electrons captured into such states.

Also, with a single ground state model, it is normally assumed that the dominant contributions to line radiation will come from levels directly excited from the ground state. In a 'metastable resolved' model (i.e in which the metastable populations are distinguished and modelled), a significant proportion of radiated power and spectral emission can arise following excitation from metastable levels.

Thus in a metastable resolved model, ionisation and recombination occur through a more complex variety of pathways, linking parents and metastables. The result is that the composite rates of ionisation and recombination for a given ionisation stage depend on the initial populations of the ground and metastable states of that stage. Calculations of ionisation balance should be extended to include the influence of metastable states. In a tokamak plasma matters are complicated further because local temperatures are higher than the ionisation potentials of light ions so that metastable populations do not have time to relax to their equilibrium values before ionisation. It is thus necessary to seek a solution which maintains distinction between metastable and ground state ions in a dynamic plasma model. These issues have not been consistently explored before and are the subject of this thesis.

For the light ions of beryllium, carbon and oxygen, which at present are the principal impurities in laboratory fusion plasmas, a complete solution of the equations of statistical balance is developed. Derived quantities include metastable resolved collisional radiative recombination, ionisation and cross coupling coefficients, recombination/bremsstrahlung power, total low level line power and emission coefficients for arbitrary spectral lines. Transient and equilibrium ionisation balance calculations are then undertaken in which metastable populations are fully distinguished. The generality of the treatment is supported by detailed methods to allow the calculations to include the best available fundamental atomic data from the general literature. Metastable populations are fully distinguished and generalised

collisional-radiative theory is used throughout.

This thesis is structured as follows. Chapter 1 describes the tokamak and fusion plasma environment. Chapter 2 reviews the fundamental physics. It describes the relevant atomic processes, the population structure equations and the scope of the present work. The new work contained in this thesis is presented in Chapters 3, 4, and 5. Chapter 3 examines the sources of fundamental atomic data for the primary reaction processes. Chapter 4, presents the population model development. In Chapter 5 the integrated ionisation balance and spectral emission models are constructed and the influence of metastable populations in time dependent and equilibrium ionisation balance situations is examined. Finally, in Chapter 6 a review of the whole work is given along with suggestions for future development.

# 1.2: LABORATORY FUSION PLASMAS


1.2.1: Thermonuclear Fusion
1.2.2: The Joint European Torus
1.2.3: Impurity Behaviour


## 1.2.1: Thermonuclear Fusion

Nuclear fusion is the primary energy producing process of the sun and most stars. At temperatures of 10 - 15 million degrees Celsius, hydrogen isotopes can fuse together via a series of nuclear reactions, releasing energy in the form of radiation and in the kinetic energy of the reaction products. For such a process to supply energy on earth, via a controllable thermonuclear fusion reactor, the most relevant reaction is between the nuclei of the hydrogen isotopes deuterium and tritium :

$$D + T \rightarrow {}^{4}He + n + 17.6\ MeV \qquad E(1.2.1)$$

This is preferred to other reactions because of its low energy threshold and high cross section. Some related fusion reactions of relevance to laboratory fusion are :

$$D + D \rightarrow \begin{cases} {}^{3}He + n + 3.3\ MeV \\ T + p + 4.0\ MeV \end{cases} \qquad E(1.2.2)$$

$$D + {}^{3}He \rightarrow {}^{4}He + p + 18.3\ MeV \qquad E(1.2.3)$$

At temperatures sufficient for the particle energies to exceed nuclear reaction thresholds, the fuel gas and most impurities are fully ionised forming a hot plasma. There will be a continuous loss of power from a thermonuclear reactor via radiation and particles losses. It is a requirement that the thermonuclear power of the reactor be sufficiently large to replace these losses (Lawson 1957). In the case of D-T fusion, this must be achieved by confining the charged alpha particles within the

plasma.

If the temperature of a D-T plasma were continually increased by external heating, a point would be reached where the alpha particle heating of the plasma balanced the power losses. The plasma would then 'ignite' and the external heating could be discontinued. The minimum requirements of temperature, density and energy confinement time for ignition are

| | | | |
|---|---|---|---|
| 1. Fuel temperature | $T_i$ | is in the range | 10 - 20 keV |
| 2. Fuel density | $N_i$ | is in the range | $2 - 3 \times 10^{20} m^{-3}$ |
| 3. Energy Confinement Time | $\tau_E$ | is in the range | 1-2 s |

These conditions are usually expressed in terms of the triple fusion product:

$$N_i \tau_E T_i \geq 6 \times 10^{22} \ m^{-3} s \ keV \qquad E(1.2.4)$$

The most promising rector design is one in which the plasma is heated in a toroidal vacuum system and magnetic fields are used to confine the charged particles within the plasma, and to isolate the plasma from the vessel walls. Of the many different confinement arrangements, the most successful is the tokamak ( see Wesson 1985 and referencies therein).

A schematic of a tokamak is shown in Fig. 1.2.1. A large current is passed through the fuel gas in the toroidal vacuum vessel. This creates and heats the plasma. The two basic components of a tokamak's magnetic field system are (i) the toroidal field which is produced by coils surrounding the vacuum vessel and (ii) the poloidal field which is produced by the plasma current itself. The resultant helical magnetic field configuration forms a set of closed toroidal surfaces on which the magnetic flux is constant. Charged particles spiral along field lines but diffuse only very slowly across them.

The JET Joint Undertaking was set up in 1978, as part of the European Community Fusion Research Program, to construct and operate a large tokamak device to investigate the viability of thermonuclear fusion as a power source. A stepwise approach to a commercial reactor is foreseen including, after JET, a next step device (NEXTSTEP) and a demonstration reactor (DEMO).

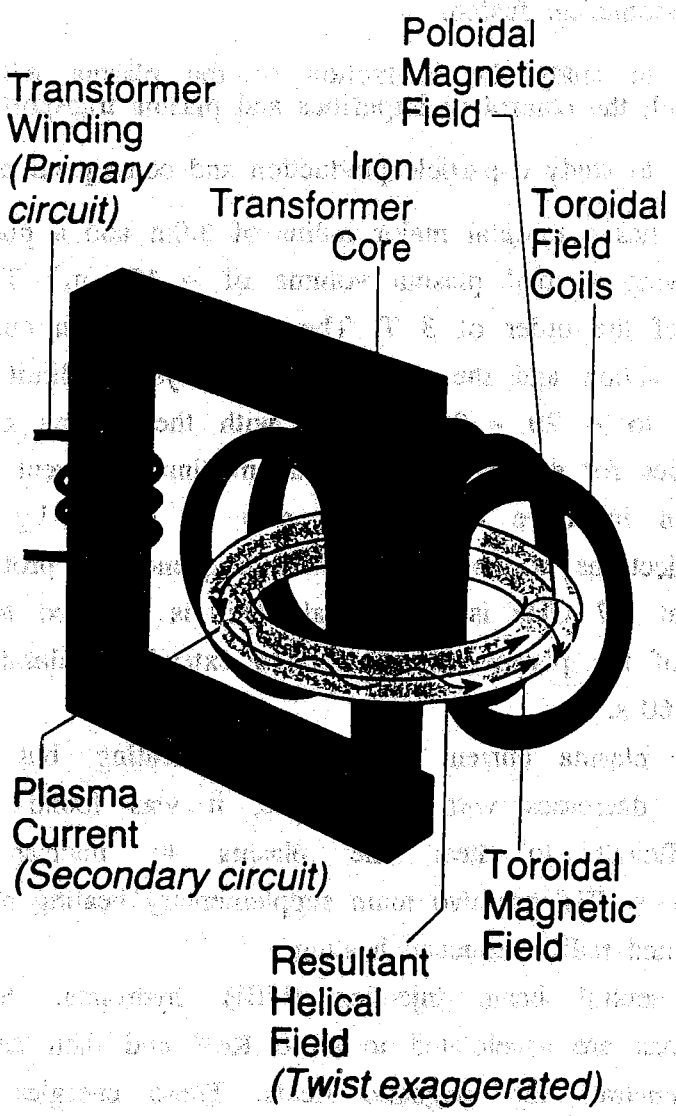


**Figure 1.2.1:** Schematic of a Tokamak.

### 1.2.2: The Joint European Torus

The Joint European Torus (JET) remains the largest tokamak in the world (Wesson 1985). Operations began in 1983 and are scheduled to continue until 1996. The objectives of the project are:

(1) to study and maintain a plasma at conditions approaching that of thermonuclear fusion.

(2) to study the interaction of the plasma with the walls of the vessel, the control of impurities and plasma transport.

(3) to study $\alpha$-particle production and consequent plasma heating

JET has a toroidal major radius of 3.0m and a plasma minor radius of 1.2m, giving a total plasma volume of ~ 120 $m^3$. The toroidal magnetic field is of the order of 3 T. The principal plasma current is produced by inductive action and the available power systems limit the duration of the discharge to ~ 20 - 30 seconds, with the plasma current sustainable at peak values for several seconds. The maximum current achieved has been 7 MA. Non inductive current can also be driven by directly accelerating plasma electrons at the lower hybrid frequency. A prototype system feeding 4 MW at 3.7 GHz is operational. This is intended to drive a significant fraction of the plasma current and to extend the duration of the discharge to up to 60 s.

The plasma current creates ohmic heating, but because the plasma resistivity decreases with temperature, it was found that this alone was not sufficient to heat the plasma to nuclear reaction threshold temperatures. JET has two main supplementary heating methods: neutral beam injection and radio frequency heating.

In neutral beam injection (NBI), hydrogen, deuterium, tritium or helium ions are accelerated to $\leq$140 KeV and then neutralised so that the atoms penetrate the magnetic fields. These energies are chosen so the atoms are subsequently ionised primarily within the plasma core where they redistribute their translational energy through collisions. Two neutral beam injector assemblies are available which can deliver a maximum of 22 MW.

In radio frequency heating, 8 antennas couple a maximum of 24 MW of radio frequency waves into the plasma. The operating frequency (27-57 MHz) is chosen to resonate with the cyclotron frequency at which minority ions

(e.g. $^3$He, H) orbit the magnetic field lines.

These methods have resulted in the three conditions for fusion being achieved individually in separate experiments, but not simultaneously during one discharge. The highest value of the fusion product so far attained is ~ $10^{21}$ $m^{-3}$skeV, which is a factor of 5 - 8 less than that required in a reactor.

One of the main problems is the control of impurities, which are released into the plasma where it is in contact with physical limiting surfaces. The impurities cause core plasma parameter degradation by radiation loss and fuel dilution. These effects are seriously limiting progress in plasma performance and the control of impurities is a major aim of future JET experimental campaigns. In particular, it is noted that magnetic geometry is a major influence in impurity control. Until the operational period ending February 1992, JET had two normal modes of operation, which are illustrated in Fig. 1.2.2.

In *limiter* operation, the magnetic surfaces are nested inside each other and the edge of the plasma is defined by the Last Closed Flux Surface (LCFS) which just touches a material limiter or the inner wall. In JET there are two belt limiters. The area outwith the LCFS is known as the *scrape-off-layer (SOL)*. The SOL mediates the interaction between the plasma and the vessel walls.

In *X-point* or *magnetic limiter* operation the magnetic field configuration is altered so that one or both nulls of the poloidal magnetic field are within the torus so defining an internal magnetic separatrix. This configuration enables the particles in the SOL to be diverted along a channel towards target plates. In this configuration, and with additional heating, the plasma can enter the so called H-mode of operation which produces better plasma confinement. It is this regime that has produced some of the best performance at JET.

In future operations, beginning late 1993, there will be a major alteration to the machine with the construction of a pumped divertor configuration (Keen et al 1992). This is illustrated in Fig. 1.2.3. Key concepts of the pumped divertor are the minimising of sputtering of impurities at the target plate of a divertor and the retention of impurities in the vicinity of the target plate. The latter it is believed can be achieved by creating a directed flow of particles along the divertor channel so that frictional forces retain impurities in the region of the target plate.

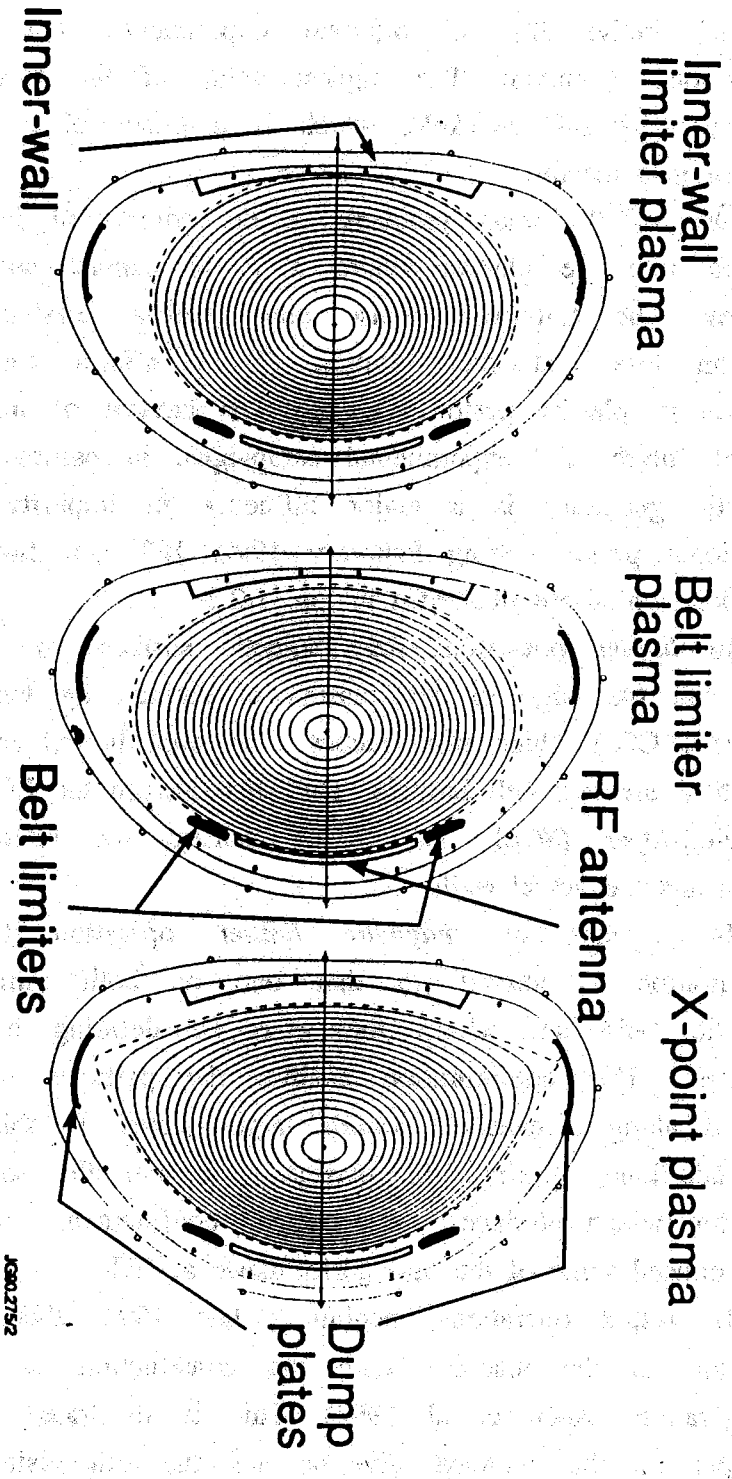


**Figure 1.2.2:** Schematic showing plasma configurations used in JET. (pre pumped divertor).

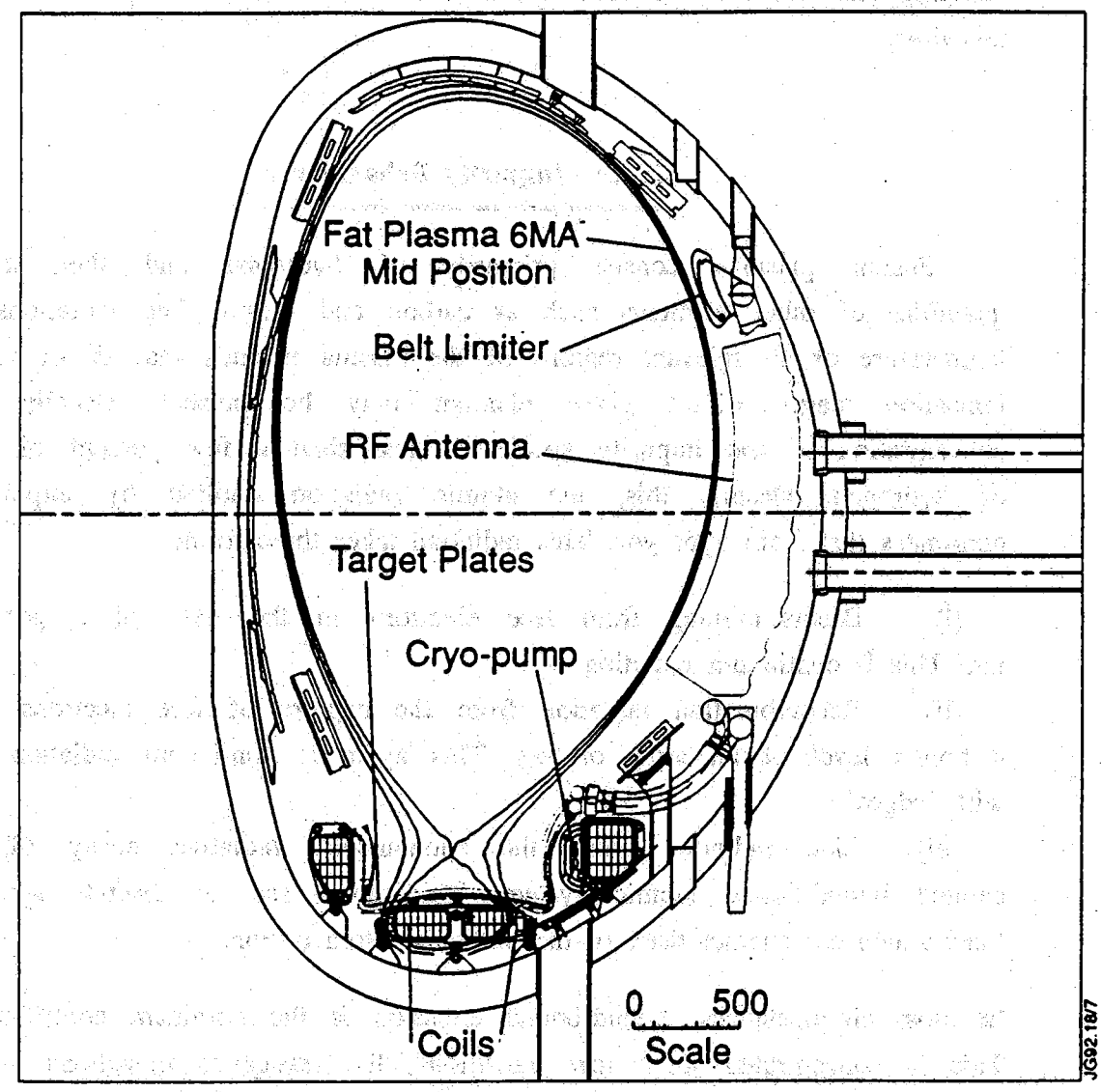


**Figure 1.2.3:** Schematic of proposed JET divertor configuration.

To reduce sputtering and induce the flow it is necessary to form a radiatively cooled, cold, dense target plasma in front of the target plates. This will radiate a significant fraction of the target plasma power, reducing the heat load on the target plates and so impurity production levels. In the vicinity of the outer target plate, a cryogenic pumping chamber may be used. Detailed divertor design is under review at this time.

### 1.2.3: Impurity Behaviour

Fusion plasmas consist primarily of hydrogen and then small quantities of other elements such as carbon and nickel. The variations in temperature of all relevant regions of the plasma is such that all or many ionisation stages of a given element may be present. Usually the concentration of the impurity species is less than a few percent of that of hydrogen. Despite this, the atomic radiation emitted by impurities dominates that from hydrogen. This radiation takes three forms.

(i) Bremsstrahlung from free electrons in the field of a positive ion. This is continuum radiation.

(ii) Recombination radiation from the capture of free electrons into a bound level of an atom or ion. This again is continuum radiation but with 'edges'.

(iii) Line radiation from the spontaneous radiative decay of an excited bound-bound atomic system. This gives rise to discrete spectral lines which are characteristic of the particular atom or ion.

In most circumstances, bound-bound emission is the dominant contribution. This is concentrated in a few transitions, the resonance transitions which are directly excited from ground states. However, for fully stripped ions bremsstrahlung only is important and for an intermediate range recombination radiation is dominant. Heavier ions are more effective radiators than low charged ions because they retain more optically active electrons at the high plasma temperatures and their radiation is at shorter wavelengths. For example, a 10% concentration of carbon is sufficient to quench a thermonuclear reactor, but only 0.01% of iron.

A useful measure of the overall impurity content of the plasma is given by the quantity $Z_{eff}$ which is defined as the average charge carried

by nuclei in the plasma

$$Z_{eff} = \Sigma_i z_i^2.( N^{+Zi}/n_e ) \qquad E(1.2.5)$$

where $N^{+zi}$ is the density of $X^{+zi}$, the summation i is over all ionisation stages of all impurity species and $n_e$ is the electron density. In a pure hydrogen plasma $Z_{eff}$ = 1.0. In JET, $Z_{eff}$ is typically in the range 1.2 - 3.0.

The main impurities of interest to JET are summarised in Table 1.2.1. These are subdivided into the classes of 'intrinsic' and 'extrinsic'.

| Impurity | Nuclear Charge | Class | Source |
|---|---|---|---|
| beryllium | 4 | intrinsic | plasma facing material |
| carbon | 6 | intrinsic | plasma facing material |
| oxygen | 8 | intrinsic | vacuum leaks, water vapour |
| chlorine | 17 | intrinsic | unknown |
| nickel,chromium, iron | 28,24, 26 | intrinsic | inconel vacuum vessel Ni(72%):Cr(15.5%):Fe(8%) |
| eg nickel,neon, argon | 28,10, 18 | extrinsic | laser ablation, gas puff |

**Table 1.2.1:** Main impurities in JET.

Intrinsic impurities are those which come from the vessel interior. To limit the metallic influxes from the inconel vacuum vessel, the interior of the vessel is tiled with light material such as beryllium or carbon. There is much debate as to which of these species is more desirable as a first wall material (Thomas 1991). Both materials have similar physical sputtering yields but beryllium radiates less energy than carbon. With carbon tiles, the dominant plasma impurities are carbon and oxygen. Beryllium acts as a getter of oxygen. Consequently, beryllium limited discharges are characterised by less oxygen content, lower $Z_{eff}$ and radiated powers. However, beryllium has a lower melting point than carbon and is prone to a melting instability. At the higher heating powers the beryllium plates were vulnerable to melting, which resulted in rapid deterioration of the discharge due to large beryllium influxes. Carbon

tiles also suffer from this effect but they can operate at higher heating powers.

Some smaller tokamaks have successfully experimented with boron films as a plasma facing material (Winter 1991). Boron has superior resistance to physical sputtering and also appears to getter oxygen.

During pre-divertor operations, JET had beryllium upper belt limiter and lower X-point target tiles and, carbon lower limiter and upper X-point target tiles. Glow discharges coated the entire interior with a layer of beryllium. For pumped divertor operations, it is planned that JET will experiment with both beryllium and carbon target plates, and possibly also use boronisation.

Extrinsic impurities are those which are added to the plasma for diagnostic purposes. Solid species can be injected by laser ablation, and gaseous species can be injected by gas puffs.

Typically, JET has a peaked electron temperature profile with central values of a few keV and values at the LCFS of the order of a few tens of eV. The distribution of ionisation stages of an impurity is determined by the interconnection of atomic reactions and plasma transport processes. Light impurities (e.g. Be, C) are fully stripped in the edge plasma whereas nickel ionisation stages are distributed over the entire plasma. The major links in the chain of impurity processes are (a) production (b) edge transport and (c) central transport.

Impurities are produced by plasma surface interactions at localised sources such as limiters or X-point target strike zones. Physical sputtering, chemical release, sublimation and evaporation are all relevant mechanisms (Stangeby and McCracken 1990). Once in the plasma, electron collisions are the dominant exciting and ionising mechanisms and, as edge plasma electron temperatures (10-50 eV) are comparable with or greater than ionisation potentials, ions are rapidly ionised. The diffusion of charged impurities is mediated by the magnetic fields. Particle transport parallel to the magnetic field lines is much faster than cross-field diffusion and this tends to distribute impurities homogeneously over magnetic surfaces.

The edge transport region can be defined as the zone from the solid surface to where the impurity density is poloidally symmetric. Typically this occurs within a few cm of the LCFS. While this zone is relatively small it is profoundly important because the impurity sources and sinks are in close proximity. Ions within the SOL flow along open field lines to

connection points with the limiter, where they are deposited. Impurities released from limiters and walls which are ionised in the SOL are therefore prevented from entering the main plasma. This is known as screening. To model trace impurity behaviour in the inherently 3-D complexity of this region, Monte Carlo techniques are employed (Stangeby 1991). Typically in such a code, a description of the the plasma background is assembled from experimental measurements, or from large hydrodynamic predictive codes. The precise limiter and magnetic geometry is specified. The impurity production distribution is calculated. Trace impurities are released into the plasma and movement between collisions in the random walk motion is followed by the Monte Carlo method.

In the central region, within the LCFS, the transport is essentially radial and the flux is represented by cross field diffusive and convective velocity terms as:

$$\Gamma(N^{+z}) = - D \frac{\partial N^{+z}}{\partial r} + N^{+z} v_c \qquad \text{E(1.2.6)}$$

In practice, the values of D and $v_c$ are anomalously large when compared with the predictions of neoclassical theory (Pasini et al 1992). The continuity equation in cylindrical coordinates yields:

$$\frac{\partial N^{+z}}{\partial t} + \frac{1}{r}\frac{\partial}{\partial r}(r\Gamma_z) = - N^{+z} n_e S_z + N^{+(z-1)} n_e S_{z-1} - N^{+z} n_e \alpha_z + N^{+(z+1)} n_e \alpha_{z+1} \qquad \text{E(1.2.7)}$$

where $N^{+z}$ is the number density of $X^{+z}$ , $S_z$ is the ionisation coefficient from $X^{+z}$ to $X^{+(z+1)}$ and $\alpha_z$ is the recombination coefficient from $X^{+z}$ to $X^{+(z-1)}$. Transport codes have been developed to solve these equations and calculate the distribution of ionisation stages throughout the central region. The code in use at JET is known as *SANCO* - Stand Alone Non-Coronal transport code (Pasini 1992). Transport coefficients *D* and $v_c$ are found empirically from experimental comparisons. The *SANCO* code requires as input many diagnostic measurements including electron density and temperature profiles and magnetic geometry details. Note that if the fluxes, $\Gamma$, are very small then E(1.2.7) reduces to equilibrium ionisation balance. Conversely, particle diffusion tends to broaden ionisation shells and convection moves their maxima to higher temperatures.

# 1.3: PLASMA DIAGNOSTICS AND THE ROLE OF SPECTROSCOPY

1.3.1: Diagnostic Overview
1.3.2: The Role of Spectroscopy
(a) Passive Spectroscopy
(b) Active Beam Related Methods

## 1.3.1: Diagnostic Overview

Fusion research requires that plasma parameters be experimentally measured as completely and accurately as possible. On JET, there are approximately 50 diagnostic systems which exploit a wide variety of physical processes. A prerequisite was that the most important plasma parameters, such as temperature and density, be measured by several independent techniques. General information on plasma diagnostics can be obtained in Hutchinson (1987) and Stott et al (1991), with more detailed information on the specific techniques and instrumentation exploited at JET being found in Orlinskij and Magyar (1988) and Stott (1992).

To interpret spectral emission it is essential to have knowledge of electron temperature and density. In the following a brief summary of the diagnostics which measure these parameters is given. Further information can be found in the above references.

In the bulk plasma, which is the hottest and densest part, the techniques in use are LIDAR Thomson scattering, electron cyclotron emission and infra-red interferometry.

LIDAR (LIght Detection And Ranging) is the optical analogue of RADAR, and is used to measure electron temperature and density profiles. A high power ruby laser (5J) of wavelength 694.3 nm emits a very short pulse of light (300ps) into the plasma. The backscattered light is collected and is analysed to give electron temperature from doppler widths and electron density from absolute intensities. The time of arrival of the backscattered light gives the radial position and profiles can be computed. The spatial and temporal resolutions are ~ 5 cm and 1 ms respectively. The repetition rate of the measurement is very poor at > 1 s and is limited by laser technology.

The electron cyclotron emission (ECE) from the free electrons in the plasma is used to measure electron temperature profiles. The electrons radiate at the characteristic cyclotron frequency at which they gyrate around the field lines. Typically this is in the range 50Ghz - 500Ghz. The radiation is from an optically thick plasma and is detected by microwave amplifiers. The electron temperature is derived from the absolute intensity and, as knowledge of the magnetic field profile is available, the position of the measurement is inferred from the frequency. These measurements have a spatial resolution of typically a few centimeters and a temporal resolution of typically 10ms.

Electron density profiles can also be measured by far infra-red interferometry. A Deuterium-cyanide laser beam (0.195 mm) is passed through the plasma and then compared with a laser beam which has traversed an identical path length. The plasma refractive index is measured by the phase change between the beams. This is related to the line averaged electron density, $\int n_e dl$. Six lines of sight are used and the electron density profile in inferred by Abel inversion, with a temporal resolution of 10μs.

The edge plasma is much more difficult to diagnose. Spatial resolution of the order of a few mm is required to resolve the steep temperature and density gradients, and strong toroidal and poloidal asymmetries are present. Several specialist systems, of for example ECE and LIDAR, have been developed to work closer to the plasma edge but none as yet give information on the region of the LCFS or the SOL. There is thus a large gap in information about this important area. The two methods which are most frequently applied to edge measurements on JET are Langmuir probes and Infra-red cameras.

Langmuir probes are mechanical devices which are bolted onto the vessel face. When the probe positively bias with respect to the plasma, it collects electrons. The saturation current is proportional to the electron density. As the bias potential is reduced below the plasma potential, the probe current has an exponential behaviour on electron temperature. From these two characteristics, electron temperature and density can be measured with good spatial and temporal resolution.

CCD (Charge Coupled Device) cameras with infra-red filters give a two dimensional heat image of the surfaces on which power is loaded. This gives data on the tile surface temperatures and power loading. Additionally, impurity influxes can be measured by using narrow band

filters which are sensitive to spectral emission from the particular impurity.

### 1.3.2: The Role of Spectroscopy

Spectroscopy is a valuable diagnostic which can give diverse information on the physical nature of the plasma and primary information on the radiating species. It is most readily applied to the study of impurities and their relation to plasma performance. Indeed, it is the only diagnostic which can give comprehensive information on impurity behaviour. Additionally, it can also supply information on general plasma parameters such as ion temperatures, rotation velocities and magnetic fields. A range of spectroscopic instruments are available on JET, which cover X-ray to visible wavelengths. These are summarised in Table 1.3.1. Note that they are divided into two types; (a) passive survey spectrometers and (b) active beam related spectrometers. Suitable reviews on spectroscopic techniques are Peacock (1984) and Engelhardt (1985).

**(a) Passive Spectroscopy**

Traditional passive plasma spectroscopy of fusion plasmas is concerned with the study of impurity ions in transport equilibrium. The radiation shells of the impurity charge states are considered to be a set of concentric shells with the higher charge states residing in the hotter central plasma. The local spectral intensity of a transition between two bound atomic states is given by

$$I(i\rightarrow j,\lambda) = A^{r}(i\rightarrow j)\, N_i^{+z} \qquad \text{E(1.3.1)}$$

where $N_i^{+z}$ is the number density of the upper state, $A^{r}(i\rightarrow j)$ is the spontaneous transition probability and $\lambda$ is the wavelength of the radiation. Spectrometers have a line of sight through the plasma and observe line integrated intensities

$$I(i\rightarrow j;\lambda) = \int A^{r}(i\rightarrow j)\, N_i^{+z}\, dl \qquad \text{E(1.3.2)}$$

The basic quantities to be derived from this measurement are the identification of plasma impurities, localisation of sources, source rates

| Impurity Survey Spectrometers | | | |
|---|---|---|---|
| Spectrometer | Type | Line of Sight | Application |
| KS1 | Xray spectroscopy | horizontal | To observe Balmer series of impurities |
| KS2 | scanning X-ray monochrometer | vertical channel | to determine shape of radiation shells of high Z impurites in bulk plasma |
| KS3 | Optical miultichannel analyser and narrow band filters | arbitrary directed at surface recieving popwer loading | To observe near neutral impurity fluxes from plasma facing materials. |
| KT1 | VUV scanning monochrometer | upper x-piont region and inner wall | To monitor impurity production and transport in target area |
| KT2 | Broad band VUV spectroscopy | horizontal | To monitor impurity behaviour in bulk plasma |
| KT4/1/2 | High resolution XUV spectroscopy | horizontal | To monitor impurity behaviour in bulk plasma |
| KX1 | high resolution X-ray spectroscopy | horizontal | To measure He-like nickel spectra from main plasma , Ni, Ti |
| Active CX Spectrometers | | | |
| Spectrometer | Type | Line of Sight | Application |
| KS4 (a) vertical | Visible spectroscopy (Czerny-Turner with CCD detectors) | vertical at 3.1m. intersecting with beams | To observe active cx lines. Ni, Ti profiles |
| KS4 (b) horizontal | Visible spectroscopy (Czerny-Turner with CCD detectors) | array of 12 horizontal channels | To observe active cx lines. Ni, Ti profiles. |
| KS5 | Visible spectroscopy (Czerny-Turner with CCD detectors) | array of 12 horizontal channels | To observe active balmer alpha spectra |

**Table 1.3.1:** List of some spectroscopic instruments on JET (pre divertor operation).

and concentrations.

Source rates can be determined by observing spectral emission from neutral and few times ionised atoms. The latter remain close to their sources and observed emission is characteristic of the flux of impurities being released by plasma surface interactions. A spectrometer directed at a limiter or X-point tile is thus able to measure impurity influxes (Behringer et al 1989). These measurements are normally in the visible or VUV. For example, Fig. 1.3.1 illustrates spectra from the O.M.A. (Optical Multichannel Analyser) survey spectrometer. Three operational phases are compared; namely the all carbon phase, Be evaporation with carbon limiter, and Be belt limiters. The reduction of carbon and oxygen in the Be limiter phase is clearly seen.

Impurity concentrations are obtained by comparing measured absolute intensities from one or two charge states with the results of a transport code simulation for all ionisation stages of the given element. The code derives the total impurity concentration by relating the measurements to the fraction of impurities which are present in those charge states. This method requires prior knowledge of transport coefficients and plasma parameters. Due to the necessity of using ions which are located in the bulk plasma, the XUV and X-ray instruments are most suited to this type of measurement.

$Z_{eff}$ is experimentally determined by measuring the enhancement of the continuum radiation over what would be expected in a pure hydrogen plasma (Morgan et al 1984). It is important to use a wavelength region in which the continuum is composed of purely bremsstrahlung with no contribution from recombination or line radiation. At JET the measurement is performed in visible regions.

At present, there is a great deal of interest in the mechanisms of impurity transport and screening in the edge plasma. One method of investigation, is to compare experimentally measured spectral intensities with the results of Monte-Carlo transport models. For example, consider Figures 1.3.2a and b which illustrate a Monte-Carlo simulation of carbon transport and measured emission profiles of C II (90.4nm) in the vicinity of the upper target plates during an X-point discharge (reproduced from Matthew et al 1992). To model this emission, the authors considered carbon being produced by sputtering at the target plates and also by neutral bombardment of the vessel walls. It can be seen that the best fit is obtained when such a latter wall source is included. The wall source was

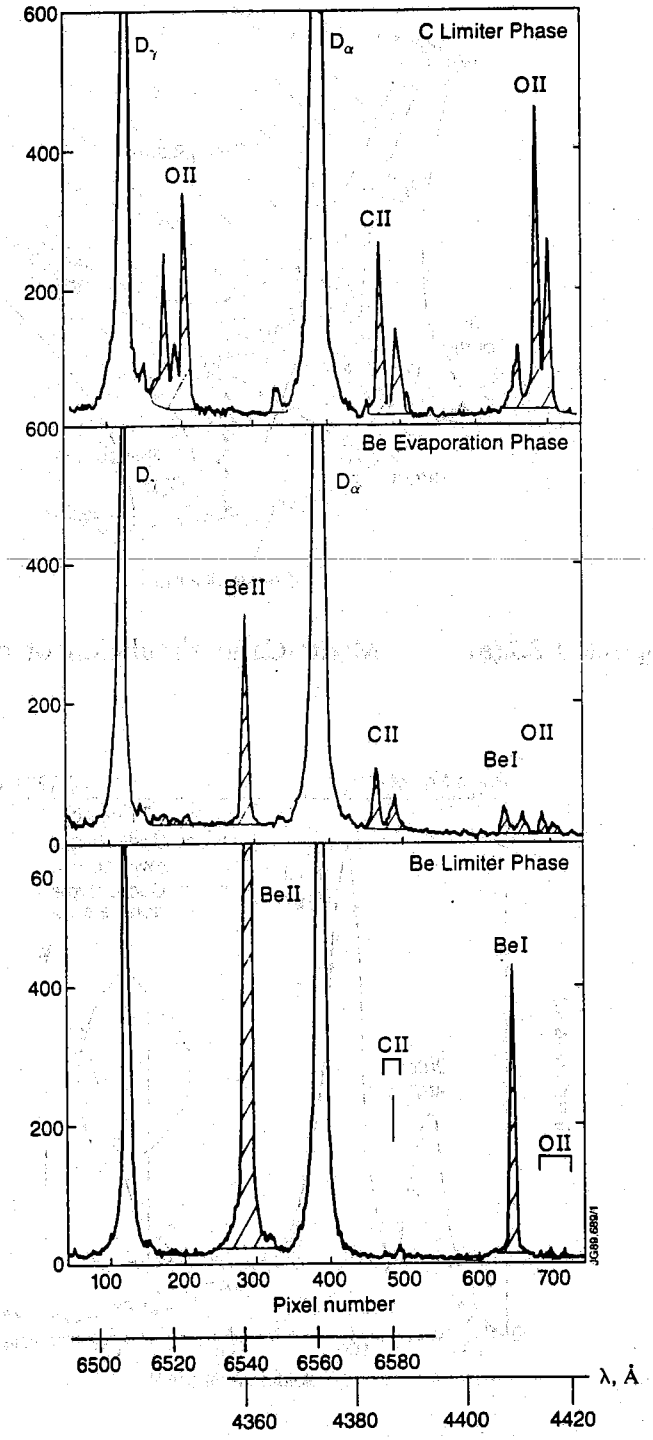


**Figure 1.3.1:** Spectroscopic survey of spectral lines in the visible region in JET for three operating phases.

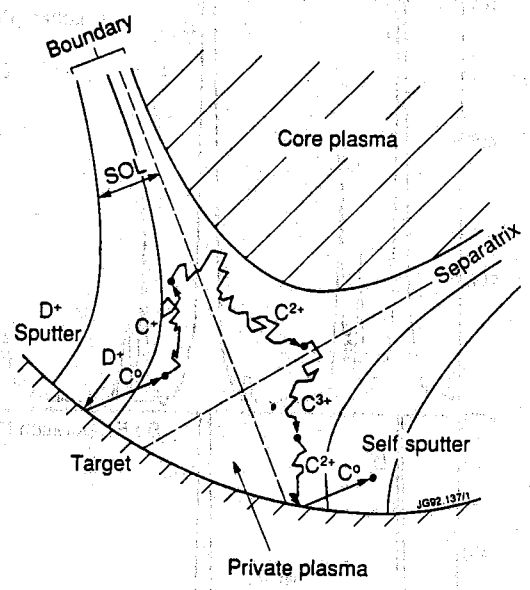


**Figure 1.3.2(a)** Monte-Carlo simulation of divertor impurities.

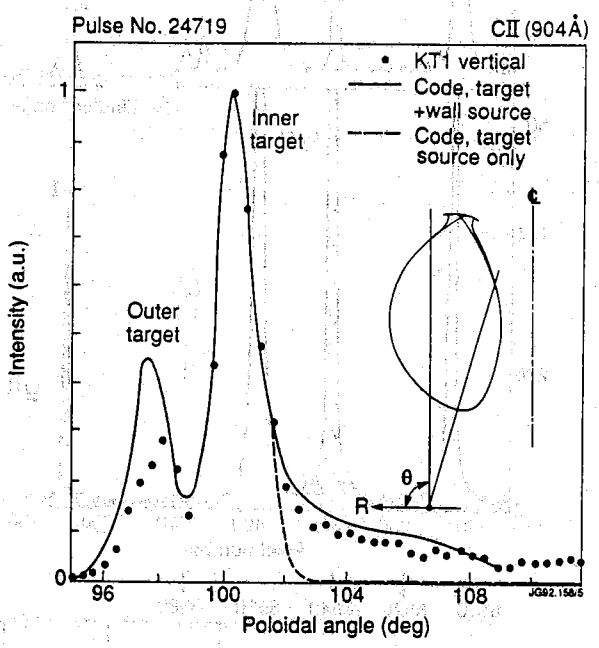


**Figure 1.3.2(b):** VUV poloidal profiles of C II obtained with the KT1 vertical system.

calculated to be ~ 25% of the target source. However, the target source is better screened than the wall source so that 40% of the impurities crossing the LCFS and entering the main plasma originate at the wall.

Bulk plasma transport is most easily investigated using transient events. A laser blow-off system is operational which can release small quantities of trace impurities into the plasma at a precise time. The time and spatial evolution of both spectral emission and soft X-ray radiation can be used to derive confinement times and transport coefficients (Pasini et al 1992).

A further application of spectral observations, although it does not rely on quantitative intensity analysis, is the utilisation of spectral line widths and shifts to measure ion temperatures and rotation velocities. Central ion temperatures are often inferred from the X-ray spectra of H-like and He-like ions (Danielsson et al 1991). A valuable insight into impurity production processes is obtained by measuring the temperature of the neutrals and ions entering the plasma (Stamp and Summers 1990).

**(b) Active Beam Related Methods**

In recent years, a number of novel diagnostics have emerged which utilise the neutral heating beams. In the core plasma, fully stripped light impurities which do not normally radiate are populated by charge transfer reaction with the neutral heating beams:

$$X^{+z} + D^0 \rightarrow X^{+(z-1)}(n) + D^+ \qquad E(1.3.3)$$

and promptly radiate by spontaneously emitting a photon

$$X^{+(z-1)}(n) \rightarrow X^{+(z-1)}(n') + h\nu \qquad E(1.3.4)$$

Observation and analysis of this radiation is known as *Charge Exchange Recombination Spectroscopy* (CXRS). The measurement is localised because of the small intersection volume between the line of sight and the heating beam. Impurity concentrations are derived from the spectral intensities. Ion temperatures and rotation velocities are derived from line widths and shifts. At JET, visible transitions between high n-shells are exploited (e.g. Be IV n=8→6 at 485.6nm) and multiple Gaussian fit techniques have been developed to distinguish the active signals from the background

plasma emission. An array of twelve spectrometers provides measurements of ion temperature, ion density and rotation velocity profiles (von Hellerman et al 1990).

Furthermore, the deuterium atoms in the Neutral Beams have an energy of 140 KeV and are crossing a magnetic field. The atoms 'see' a Lorentz induced electric field of the order of $10^5$ $Vcm^{-1}$, which causes Stark splitting of atomic levels. Observation of the Balmer $\alpha$ Stark multiplet gives information on the magnetic field strength (from the amount of splitting) and orientation (from the polarisation of the light). The absolute intensity of the beam emission is an important measure of beam attenuation. This technique is known as *Beam Emission Spectroscopy* (Mandl et al 1993).

In conclusion, spectroscopy has shown itself to be a valuable diagnostic technique which can be applied to a variety of measurements. Note that the traditional spectroscopic method of deriving electron temperature and density from measurements of spectral line ratios has been largely superseded in tokamaks by powerful non-spectroscopic techniques. Such measurements by spectroscopy are normally limited to consistency tests or in specific studies to verify atomic data and modelling procedures. There is however, potential for spectral line ratios to provide data on areas of geometric difficulty such as the plasma edge and divertor regions.

## 1.4: PHYSICAL CONDITIONS

Hot plasmas contain electrons, ions and atoms which interact via particle collisions and radiative transitions which redistribute energy, momentum and radiation. If the plasma is confined in a closed system from which no particles or radiation can escape then the electrons, ions and atoms would take up equilibrium energy distributions which define a value of temperature and the system would be in *Complete Thermodynamic Equilibrium* (CTE). In such circumstances, the distribution of energy amongst free particles, photons and internal energy states of atoms and ions can be found by statistical mechanics.

The free particle speed distribution is given by the Maxwell equation

$$f(v) = 4\pi \left(\frac{m}{2\pi kT_k}\right)^{3/2} v^2 \exp\left(-\frac{mv^2}{2kT_k}\right) \qquad \text{E(1.4.1)}$$

where m is the mass of an individual particle, v is its speed, k is Boltzmann's constant and $T_k$ is the plasma kinetic temperature.

The distribution of radiation is given by Planck's function. For the photon energy distribution U(ν) at frequency ν this takes the form

$$U(\nu) = \frac{8\pi h\nu^3/c^3}{\exp(h\nu/kT_r) - 1} \qquad \text{E(1.4.2)}$$

where h is Planck's constant and c is the speed of light. $T_r$ is the radiation temperature which in CTE with particles and radiation enclosed is equal to $T_k$.

The distribution of populations amongst discrete internal energy levels of ions and atoms is given by the Saha-Boltzmann equation

$$\frac{N_i^{+z}}{N_\gamma^{+z1}\, n_e} = \frac{\omega(z,i)}{\omega(z1,\gamma)} \frac{h^3}{2(2\pi m_e kT)^{3/2}} \exp(I/kT) \qquad \text{E(1.4.3)}$$

where $N_i^{+z}$ and ω(z,i) represent the number density and statistical weight of state $X_i^{+z}$, $N_\gamma^{+z1}$ and ω(z1,γ) represent the number density and statistical weight of the parent state $X_\gamma^{+z1}$, with z1 = z+1, $m_e$ is the mass

of an electron, and I is the ionisation potential energy of state $X_i^{+z}$ with respect to $X_\gamma^{+z1}$. Comparing two excited state populations within one charge state gives the Boltzmann equation:

$$\frac{N_i^{+z}}{N_j^{+z}} = \frac{\omega(z,i)}{\omega(z,j)} \exp(-E_{ij}/kT) \qquad E(1.4.4)$$

where $E_{ij}$ is the energy difference between states i and j.

Furthermore, in complete thermodynamic equilibrium the rate at which particles make transitions from one state to another is exactly balanced by the inverse rate. This is known as the principle of detailed balance.

Fusion plasmas are far from CTE in general. This is mainly due to two physical reasons. Firstly, the plasma parameters (especially temperature and density) are changing faster than the equilibration time for atomic processes which establish ionisation balance, and secondly, radiation emitted from the ions and electrons escapes from the plasma before it can be reabsorbed. A main point is that the plasma density is low (typically $10^{12}$ - $10^{14}$ $cm^{-3}$). The rate of reaction for collisional processes is directly proportional to the plasma density and so in higher density plasmas, the atomic system reaches collisional equilibrium more quickly, and radiative processes are suppressed by more frequent collisional processes.

However, some of the concepts of CTE are still valid and may be applied in certain circumstances. The time taken for free charged particles to reach thermal equilibrium has been considered by Spitzer (1956). Collisions between particles of the same mass are most effective at redistributing momentum and energy. Therefore, the kinetic energy redistribution time scale for a particular species is primarily determined by collisions between particles of that species. Expressions are given by Spitzer (1956). It is shown that the self collision thermalisation time for electrons is given by

$$\tau(e\text{-}e) = \frac{1.67^{+7}}{n_e \ln(\Lambda)} \left(\frac{kT}{I_H}\right)^{3/2} \quad (s) \qquad E(1.4.5)$$

where $n_e$ is the electron density in $cm^{-3}$ and $\ln(\Lambda)$ is the Coulomb logarithm which typically has values between 5 and 20. Furthermore, because of mass factors, the redistribution time for protons, $\tau(p\text{-}p)$ and the equipartition time for electrons and protons $\tau(e\text{-}p)$ are given by the expressions

$$\tau(p\text{-}p) = (m_p/m_e)^{1/2}\,\tau(e\text{-}e) \approx 43\,\tau(e\text{-}e) \qquad E(1.4.6)$$

$$\tau(e\text{-}p) = (m_p/m_e)\,\tau(e\text{-}e) \approx 1836\,\tau(e\text{-}e) \qquad E(1.4.7)$$

In a plasma with an electron temperature of 1 keV and an electron density of $10^{13}$ $cm^{-3}$, $\tau(e\text{-}e) \approx 10^{-4}$s. The particle confinement time in JET is of the order of 1 s and so it can be considered that the electron and proton distributions are Maxwell-Boltzmann. However, the timescales indicate that the equipartition of energy may occur separately for electrons and protons, but without equipartition between them. In these circumstances, electron and proton temperatures are not necessarily equal.

Now consider the populations of discrete energy states of ions and atoms. For these to be in CTE, it is necessary that the plasma is optically thick to photons emitted by transitions between atomic levels. In fusion plasmas, the impurity density is too low for this condition to be satisfied. A lesser condition is *Local Thermodynamic Equilibrium* (LTE) in which collisional processes balance. For an ion or atom to be excited to a state of higher energy a collision with a sufficiently energetic particle is required. In contrast, an excited state can either de-excite collisionally or by spontaneously emitting a photon. When the collisional de-excitation rate exceeds the radiative transition probability, the system will be in LTE. This condition is most easily satisfied for high levels of atoms or ions. Such levels are nearly degenerate and collisional transitions between them have very large cross sections. Above a limit termed the collision limit, the populations are in LTE and can be described by the Saha-Boltzmann and Boltzmann equations. This limit depends on ion charge and the electron and proton densities. As the density is increased, collisions become more frequent and more levels tend to LTE. An approximate scaling is given by Griem (1963,1964)

$$n_{cl} = \frac{z^{14/17}}{2^{2/17}\,\pi^{1/17}} \left(\frac{\alpha}{a_0}\right)^{6/17} n_e^{-2/17} \left(\frac{kT}{z1^2\ I_H}\right) \exp\left(\frac{4z^2 I_H}{17 n_{cl}^3\ kT}\right) \qquad E(1.4.7)$$

where $n_{cl}$ denotes the principal quantum shell of the lowest level which is in LTE. Griem comments that the exponential term is not usually important.

Otherwise $n_{cl}$ can be found by iteration.

For low lying levels, LTE is not approached except at the very highest densities. The populations of these levels, $N_i^{+z}$, are given by a statistical balance of all the individual atomic processes which populate and depopulate that level

$$d/dt(N_i^{+z}) = \text{(sum of all populating processes)} - \text{(sum of all depopulating processes)} \quad \text{E(1.4.8)}$$

In fusion plasmas, the atomic processes of relevance are those of spontaneous radiative decay, non-radiative Auger decay (autoionisation), collisional excitation and de-excitation, electron impact ionisation, charge exchange recombination, and radiative, dielectronic and three-body electron recombination. These are described more fully in Chapter 2.

The relaxation times of the various state populations of an atom or ion can vary enormously.

Doubly excited states which lie above the normal ionisation threshold can autoionise. The lifetimes are very short and are approximately given by $\tau_{au} \approx 10^{-12}$ s.

For excited states, the relaxation lifetime is determined by the sum of radiative and collisional transition probabilities from that state. This sum is normally dominated by large radiative terms, and with considerable approximation, the lifetime scales as $\tau_{ex} \approx 10^{-7}/z1^4$ seconds.

For ground state ions, the lifetimes are entirely determined by the collisional processes of ionisation, excitation and recombination. The time constants associated with these processes are typically many orders of magnitude longer than the radiative lifetimes of excited levels. The lifetimes of ground states can be approximately expressed as $\tau_{gs} \approx 10^8 z1^3/n_e$ seconds, where $n_e$ is the electron density in $cm^{-3}$.

Metastables are an intermediate class of states between ground and excited states. These states do not de-excite rapidly by spontaneous radiative emission processes because the only available radiative decay paths are via quantum mechanically forbidden transitions (a detailed description of the various types of transition and selection rules is given in Section 2.1). For example, returning to Figure 1.1.1, the $2s2p^2\ ^4P$ state is forbidden to decay because in LS coupling, the spin selection rule is $\Delta S = 0$. Transition probabilities for several radiative transitions in boron like ions are given in Table 1.4.1.

| | $2s2p^2\ {}^4P \rightarrow 2s^22p\ {}^2P$ | $2s2p^2\ {}^2P \rightarrow 2s^22p\ {}^2P$ | $2p^3\ {}^4S \rightarrow 2s2p^2\ {}^4P$ |
|---|---|---|---|
| $C^{+1}$ | $4.41^1$ | $4.12^9$ | $3.42^9$ |
| $O^{+3}$ | $5.36^2$ | $7.44^9$ | $6.55^9$ |

**Table 1.4.1:** Radiative transition probabilities ($s^{-1}$) for some excited states in Boron-like ions. Data from the sources listed in Chapter 3.

Excited states in the doublet spin system readily decay to the $2s^22p\ {}^2P$ ground state and those in the quartet system readily decay to $2s2p^2\ {}^4P$. Because this state is metastable, it tends to accumulate a relatively high population and to evolve on timescales similar to that of the ground.

The relaxation times thus satisfy the relationship

$$\tau_{au} << \tau_{ex} << \tau_{gs}\ ,\ \tau_m \qquad \text{E(1.4.9)}$$

where no distinction has been made between ground and metastable states.

In any plasma, atomic states can be naturally classified by comparing atomic relaxation timescales with timescales for changes in plasma conditions (especially temperature and density). Quasi-static populations are those which relax almost instantaneously compared to plasma timescales and dynamic populations are those which relax on comparable or slower timescales. For low density laboratory fusion plasmas and many astrophysical plasmas, excited state populations are in a quasi-static situation, whereas ground and metastable state populations are in a dynamic situation. It is justifiable then to separate the establishment of excited state populations from that of ionisation charge state populations.

Ground and metastable populations are dynamic populations which evolve with plasma conditions. These populations are coupled by a set of effective ionisation and recombination coefficients which are evaluated at local conditions. These coefficients can be used as the source terms to describe the time and spatial development of charge states in plasma models (c.f. E(1.2.7)).

Excited state populations relax rapidly with changes in the plasma environment and so they are in equilibrium with the ground and metastable state populations at local conditions of temperature and density.

Statistical balance population models can provide solutions for these populations as functions of instantaneous ground and metastable populations at local plasma conditions. Spectral intensities can then be synthesised from the excited state populations.

In the limit of low electron density, the excited state populations are very small due to low excitation rates. Atomic populations accumulate in ground and metastable states. Excited states are populated directly by electron impact excitation from ground or metastable states and then promptly decay by spontaneously emitting a photon before further ionising or exciting collisions occur. This is often known as the *coronal approximation* because this approximates the situation found in the solar corona. In these circumstances, ionisation only takes place from the ground and metastable states, while electrons can recombine with the parent ion to form the ion in any excited state. Indeed, very many principal quantum shells (~n=500) may need to be considered in recombination. All those captured into high principal quantum shells cascade down and eventually reach the ground or metastable states. The effective ionisation and recombination coefficients are essentially those of fundamental rate coefficients for the individual atomic processes, or simple sums over them.

As the electron density increases, collisions become more frequent and this situation changes. Excited state populations may be disturbed by further exciting or redistributing collisions before they radiatively decay. Recombination coefficients are reduced through ionisation of captured electrons before they can cascade to ground or metastable states. Also, ionisation takes place directly from ground states and indirectly via stepwise excitation and ionisation.

The basic theory which accounts for these effects was first fully established by Bates et al (1962), and later expanded by, amongst others, Burgess and Summers (1969, 1976), Summers (1977), Jacobs and Davis (1978) and Kastner (1981). Level populations are derived from a set of collisional-radiative couplings between the bound states and the ground and parent states. Effective ionisation and recombination coefficients in a plasma of finite electron density are derived from the level populations of the given ion. When metastable states are identified, these coefficients are referred to as *generalised collisional-dielectronic coefficients*. These coefficients are denoted by $S^{eff}$ and $\alpha^{eff}$, and are dependent on both temperature and density. In the limiting case of low

electron density,

$$\mathrm{Lim}(n_e \rightarrow 0)\ S^{eff}(X_\rho^{+z} \rightarrow X_\gamma^{+z1}) = S(X_\rho^{+z} \rightarrow X_\gamma^{+z1}) \qquad \text{E(1.4.10a)}$$

$$\mathrm{Lim}(n_e \rightarrow 0)\ \alpha^{eff}(X_\gamma^{+z1} \rightarrow X_\rho^{+z}) = \alpha(X_\gamma^{+z1} \rightarrow X_\rho^{+z}) \qquad \text{E(1.4.10b)}$$

where S and $\alpha$ are the fundamental rate coefficients which are only a function of temperature, $X_\gamma^{+z1}$ denotes the relevant parent configuration and $X_\rho^{+z}$ denotes the relevant ground configuration. More completely, collisional-radiative theory can be used to define effective contributions to excited state populations, effective emission coefficients for arbitrary spectral lines, and effective radiated power coefficients. As the electron density is continually increased, collisional processes will dominate over radiative decay and the equations will correspond to those of LTE. Collisional-radiative theory thus encompasses both the low density coronal approximation and the high density limit when the populations approach those of LTE.

# CHAPTER 2

# RELEVANT PHYSICS

## 2.1: ATOMIC PROCESSES IN PLASMAS

In theory, all possible atomic processes which can populate and depopulate atomic levels of an impurity ion $X^{+z}$ should be considered when attempting to describe level populations. In practice, many can be neglected due to the particular plasma environment.

Fusion plasmas are optically thin to radiation emitted by impurities (see Peacock 1984). It is then correct to neglect radiation induced processes such as photo-ionisation and -excitation and stimulated emission.

It is also possible to make a distinction between majority and minority species. The majority constituents are protons, electrons and neutral hydrogen. Typical impurity densities are $\leq 10^{-3}n_e$ for metals (e.g. nickel) and $\leq 10^{-2}n_e$ for light impurities. Collisions between impurities, which are a minority species can be neglected without loss of accuracy. The collisional processes of importance to impurity atomic populations are those between impurity ions and electrons, protons and atomic hydrogen. In fusion plasmas, hydrogen can be present in either of its isotopic forms. There is no distinction between protons, deuterons and tritons except in their speed. From this point on, without loss of generality, each are simply referred to as protons.

The subset of atomic processes which are considered relevant are listed in Table 2.1.1 and are now discussed individually. Ground and excited states of the recombined ion, $X^{+z}$ are represented by $X^{+z}(\gamma,n\mathit{l})$ or by $X^{+z}(i)$ where i denotes the configuration $\gamma,n\mathit{l}$.

*Spontaneous Radiative Decay*

$$X^{+z}(i) \rightarrow X^{+z}(j) + h\nu$$

*Radiationless Auger Decay (or autoionisation)*

$$X^{+z}(i) \rightarrow X^{+(z+1)}(j) + e^-$$

*De-excitation and excitation by electron and proton collision*

$$X^{+z}(i) + e^- \rightleftharpoons X^{+z}(j) + e^-$$

$$X^{+z}(i) + p^+ \rightleftharpoons X^{+z}(j) + p^+$$

*Electron Impact Ionisation*

$$X^{+z}(i) + e^- \rightarrow X^{+(z+1)}(\gamma) + e^- + e^-$$

*Radiative (or free electron) Recombination*

$$X^{+(z+1)}(\gamma) + e^- \rightarrow X^{+z}(i) + h\nu$$

*Dielectronic Recombination*

$$X^{+(z+1)}(\gamma) + e^- \rightleftharpoons X^{+(z+1)}(\gamma',j) \quad \text{Resonance Capture}$$

$$\rightarrow X^{+(z+1)}(\gamma'',j) + h\nu \quad \text{Radiative Stabilisation}$$

*Three-body Recombination*

$$X^{+(z+1)}(\gamma) + e^- + e^- \rightarrow X^{+z}(i) + e^-$$

*Charge Transfer with Neutral Hydrogen*

$$X^{+(z+1)}(\gamma) + H^0 \rightarrow X^{+z}(i) + H^+$$

**Table 2.1.1:** Relevant Atomic Processes

Spontaneous radiative decay occurs between two bound atomic states

$$X^{+z}(i) \rightarrow X^{+z}(j) + h\nu \qquad \text{E(2.1.1)}$$

and gives rise to a discrete spectral line of wavelength $\lambda = c/\nu$, where $\nu$ is the frequency and c is the speed of light. The coefficient describing the rate of this reaction is the spontaneous transition probability or Einstein coefficient which is denoted by $A^r(i \rightarrow j)$ or $A^r_{ji}$ and has units of $s^{-1}$. The values of these coefficients depend on details of atomic structure and on the particular type of transition. The three main types of transition are electric dipole, non-dipole and spin change (Cowan 1981).

The strongest transitions are the electric dipole (or E1) transitions, which are termed 'allowed'. These give rise to the most intense spectral lines. The quantum mechanical selection rules for these transitions in Russell-Saunders notation are

$$\begin{aligned} \Delta L &= \pm 1 \\ \Delta S &= 0 \\ \Delta J &= 0, \pm 1 \text{ with } J=0 \rightarrow J=0 \text{ forbidden} \end{aligned} \qquad \text{E(2.1.2)}$$

In addition, E1 transitions only occur between states of opposite parity. This forbids transitions within a configuration.

Excited levels in neutral atoms which can decay by emission of E1 radiation have lifetimes of the order of $10^{-7}$-$10^{-9}$ s, whereas much shorter values are found in highly stripped ions. The probabilities for E1 transitions scale approximately as z+1 for $\Delta n=0$ and $(z+1)^4$ for $\Delta n=1$ transitions.

Non-dipole or *forbidden transitions* have very low probabilities in neutral and few times ionised atoms, but the transition rates increase strongly with z1 (scaling as $\sim (z+1)^6$-$(z+1)^{10}$). The various types of transition follow specific selection rules :

Magnetic dipole transitions

$$\begin{aligned} \Delta L &= 0 \\ \Delta J &= 0, \pm 1 \end{aligned} \qquad \text{E(2.1.3)}$$

Electric quadrupole transitions

$$\Delta L = 0, \pm 2 \quad \text{with } L=0 \rightarrow L=0 \text{ forbidden} \qquad \text{E(2.1.4)}$$

In particular, these interactions give rise to transitions within configurations.

In pure LS coupling, the spin selection rule is $\Delta S = 0$, which forbids transitions between different spin systems. However, this selection rule is not rigid in relativistic theory. Intersystem or intercombination transitions take place via spin-orbit interactions which mix levels in different spin systems. Again these transitions are very weak in neutral atoms but scale very strongly with ionic charge, being approximately proportional to $(z+1)^7$ or $(z+1)^{10}$ for $\Delta n = 0$ or $\Delta n = \pm 1$ transitions respectively.

Spectral lines from non-dipole and spin changing transitions are normally very weak for neutral atoms but can become more prominent for highly charged ions, and may even dominate the allowed transitions.

Bound-bound transitions can also be induced by collisions with free particles. The collisions of relevance are electron and proton collisional excitation and de-excitation

$$X^{+z}(i) + e^- \leftrightharpoons X^{+z}(j) + e^- \qquad \text{E(2.1.5a)}$$

$$X^{+z}(i) + p^+ \leftrightharpoons X^{+z}(j) + p^+ \qquad \text{E(2.1.5b)}$$

The cross sections for electron and proton impact excitation are approximately equal when their velocities are equal. Electrons are much lighter than protons ($m_e/m_p = 1/1826$), and in conditions of equipartition will be travelling much faster. The cross sections are a maximum when the electron energy is around 10 times the transition energy (i.e. when the proton energy is around 20,000 times) Proton collisions are thus only important for transitions with a very small energy difference. For low levels of ions and atoms, where the states are well separated in energy, electron collisions are the dominant collisional mechanism.

Collisional cross sections and rate coefficients are represented in various forms. The dimensionless collision strength $\Omega(i,j)$ is related to the excitation cross section $\sigma(i \rightarrow j)$ (measured in units of $\pi a_o^2$) by

$$\Omega(i,j) = w_i \cdot (k_i/I_H)^2 \cdot \sigma(i \rightarrow j)/\pi a_o^2 \qquad \text{E(2.1.6)}$$

where $k_i^2$ is the energy (in Rydbergs) of the incident electron relative to the lower state i, and $w_i$ is the statistical weight of the lower state. The energy averaged collision strength over a Maxwellian electron distribution is referred to as gamma ($\gamma$) or upsilon (Y). The relationships between the collision strength, de-excitation rate coefficient, $q(j \rightarrow i)$,

and gamma parameter are

$$q(j\rightarrow i;T_e) = 8.63\times10^{-6}\ \gamma(j\rightarrow i;T_e) / (\omega_i\ T_e^{1/2}) \qquad cm^3s^{-1} \qquad \text{E(2.1.7)}$$

$$\gamma(j\rightarrow i;T_e) = \int_0^{\infty} \Omega(i,j)\ \exp(-\Delta E\ U / kT_e)\ d(\Delta E\ U / kT_e) \qquad \text{E(2.1.8)}$$

where $\Delta E = (E_j - E_i)$ is the transition energy, $kT_e$ is the equivalent electron temperature and $U = k_j^2/\Delta E$. Excitation and de-excitation rate coefficients satisfy the detailed balance relationship

$$q(i\rightarrow j)/q(j\rightarrow i) = \omega_j/\omega_i\ \exp(-\Delta E/kT_e) \qquad \text{E(2.1.9)}$$

The collision strength and gamma parameters are useful because their definitions exclude the exponential transition energy dependence of the excitation cross sections and rate coefficients respectively. This makes these quantities much more suited to interpolation.

Collisional transitions can again be classified as dipole (d), non-dipole (n-d) and spin changing (s-c). Each has a characteristic behaviour which is identified in Gordon et al (1984). In particular spin changing cross sections fall away with energy much more quickly than dipole transitions. At high energy, the collision strengths have the asymptotic behaviour (see Gordon et al 1984, Henry 1981):

$$\Omega_d(i\rightarrow j) \sim d\ \ln(4U) \qquad \text{E(2.1.10a)}$$

$$\Omega_{n\text{-}d}(i\rightarrow j) \sim \text{constant} \qquad \text{E(2.1.10b)}$$

$$\Omega_{s\text{-}c}(i\rightarrow j) \sim U^{-2} \qquad \text{E(2.1.10c)}$$

where d is related to the optical oscillator strength. Spin changing transitions are possible by either (i) the breakdown of LS coupling so that apparent spin change transitions have a dipole contribution, or (ii) by exchange of incident and bound electrons. Contributions from type (ii) are generally larger for ions of low charge.

The largest collision cross sections are those between levels within a principal quantum shell i.e. $\Delta n = 0$, $\Delta l = \pm 1$. For high n-shells where the separate $l$-subshells are nearly degenerate, such collisions have the effect of statistically populating the $l$-subshells. Because of the small

energy differences, proton collisions are more effective than electrons at causing such transitions. Proton collisions are also more effective than electrons at inducing electric quadrupole transitions between close fine structure levels belonging to the same LS term e.g. $2s^2 2p$ ($^2P_{0.5} \rightarrow {}^2P_{1.5}$). This process can be particularly important in influencing the relative populations of fine structure split ground configurations.

In subscript notation, the rate coefficients for electron and proton impact excitation from $X_i^{+z}$ to $X_j^{+z}$ are denoted by $q_{ji}^e$ and $q_{ji}^p$ respectively. The rates of reaction are then $n_e q_{ji}^e N_i^{+z}$ and $n_p q_{ji}^p N_i^{+z}$.

The corresponding bound-free collisional process is collisional ionisation by electron impact, and its inverse reaction three body (two electron and ion) recombination

$$X^{+z}(\gamma,nl) + e^- \leftrightharpoons X^{+z1}(\gamma) + e^- + e^- \qquad \text{E(2.1.11)}$$

The forward reaction is that of ionisation. This occurs when the incident particle transfers enough energy to excite the bound electron to the

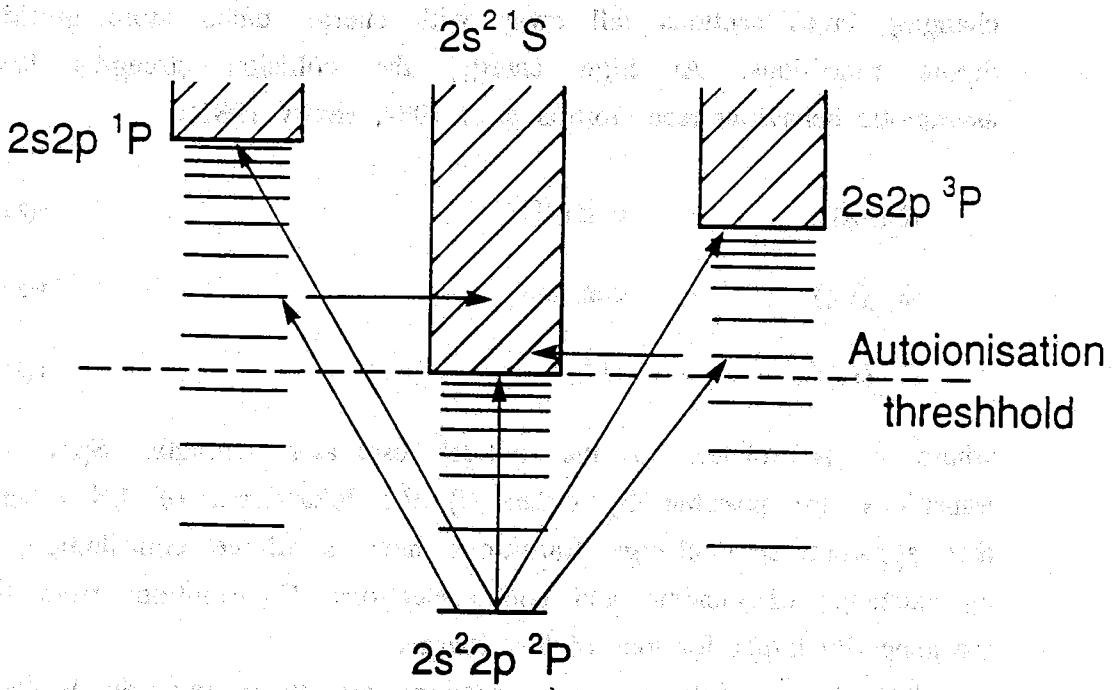


**Figure 2.1.1:** Ionisation channels from $2s^2 2p\ ^2P$.

continuum. The total direct ionisation cross section, σ, from a given configuration is usually given as the sum over all sub-shells from which an electron can be removed, that is

$$\sigma(E) = \Sigma_j \zeta_j \sigma(j,E) \qquad \text{E(2.1.12)}$$

where $\zeta_j$ is the number of equivalent electrons in subshell j, and E is the energy of the incident electron. For example, consider the ionisation of a Boron-like ion with $2s^2 2p$ configuration. This is illustrated in Figure 2.1.1. The outer 2p electron ionises directly to the $2s^2\ ^1S$ configuration in the Be-like ion. The inner 2s electrons ionise to leave either $2s2p\ ^1P$ or $2s2p\ ^3P$ fragments.

The inner shell 2s electrons which are excited in the series $(2s2p\ ^1P)\ nl$ or $(2s2p\ ^3P)\ nl$ may also contribute to the overall ionisation rate by the process of Auger breakup (or autoionisation). This process is also illustrated in Fig. 2.1.1. Bound states with energy greater than the normal ionisation threshold may interact with the continuum and a radiationless Auger transition takes place in which one of the electrons relaxes to a lower energy level and the other is released into the continuum. In this example, the reactions are

$$X^{+z}(\ 2s2p\ ^1P)\ nl\ ^2L \rightarrow X^{+z1}(\ 2s^2\ ^1S) + e^- \qquad \text{E(2.1.13)}$$

$$X^{+z}(\ 2s2p\ ^3P)\ nl\ ^2L \rightarrow X^{+z1}(\ 2s^2\ ^1S) + e^- \qquad \text{E(2.1.14)}$$

This reaction can be written generally as a transition between core configurations

$$X^{+z}(\gamma\ S_p L_p, nl\ SL) \rightarrow X^{+z1}(\gamma'\ S'_p\ L'_p) + e^- \qquad \text{E(2.1.15)}$$

The transition probability for autoionisation is denoted as $A^a$ $(s^{-1})$. If autoionisation takes place via an allowed Coulomb interaction the spin selection rule (in LS coupling) is

$$|\ (2S+1) - (2S'_p+1)\ | = 1 \qquad \text{E(2.1.16)}$$

For example, both reactions E(2.1.13) and E(2.1.14) are allowed. However, the reaction

$$X^{+z}(\ 2s2p\ ^3P)\ nl\ ^4L \rightarrow X^{+z1}(\ 2s^2\ ^1S) + e^- \qquad \text{E(2.1.17)}$$

is forbidden under LS coupling selection rules and can proceed only through relativistic interactions.

As for radiative transitions, the values of autoionisation transition probabilities depend strongly on atomic structure. Transition probabilities for allowed transitions are very large, ~ $10^{13}$ - $10^{15}$ $s^{-1}$, and are thus much faster than radiative decay. The transition probabilities for forbidden transitions are typically a factor of $10^{-3}$ of allowed transitions. Scaling laws reported by Hahn (1985) for allowed transitions show that $A^a$ varies as $n^{-3}$ for high n states and that the $l$ dependence is approximately Gaussian in form for low $l$ and then drops exponentially. This reflects the fact that electrons in high n-shells and in non penetrating high $l$ orbitals have less interaction with the core configuration and have the smallest probability of making an autoionising transition. Hahn (1985) suggests that subshells with $l \leq 6$ contribute for for low Z ions and up to $l \leq 15$ for high z ions. Griffin et al (1985) present Auger transition probabilities for $C^{+2} \rightarrow C^{+3}$. These values suggest that $A^a$ is only significant for $l \leq 6$.

The total ionisation cross section from a given configuration is thus composed of direct outer shell ionisation, direct inner shell ionisation and inner-shell excitation autoionisation. Ionisation rate coefficients are denoted by $S(\gamma,nl \rightarrow \gamma)$ or in subscript notation as $S_{\gamma_i}$ where i represents $\gamma,nl$. The corresponding rate of reaction is $n_e S_{\gamma_i} N_i^{+z}$.

Three body recombination, with rate coefficient $\alpha^t$, is the inverse process to collisional ionisation, and the reverse reaction in E(2.1.11). The rate coefficients for collisional ionisation and three body recombination will thus satisfy a detailed balance relationship. Due the small cross sections for three body interactions, the rate coefficients for this process are generally very small. But note, the rate of reaction is $n_e^2 N_\gamma^{+z1} \alpha^t(\gamma \rightarrow \gamma,nl)$ which is directly proportional to the square of the electron density. This process is usually the dominant recombination mechanism in high density plasmas.

A general feature of recombination is that the free electron and parent configuration couple together so that the spin quantum numbers of the parent configuration, $S_p$ and the recombined system, S, satisfy the relationship

$$S = S_p \pm 1/2 \qquad \text{E(2.1.18)}$$

With the exception of singlet parents which can only recombine to form doublets, each parent state can thus recombine into two spin systems.

The two other electron-ion recombination processes of relevance are radiative and dielectronic recombination.

Radiative (or free electron) recombination is a bound-free radiative transition

$$X^{+z1}(\gamma\ L_p S_p) + e^- \rightarrow X^{+z}(\gamma\ L_p S_p, nl\ LS) + h\nu \qquad \text{E(2.1.19)}$$

This involves a free electron being captured to a bound state with the excess energy being emitted as a photon. This is the inverse process to photoionisation. The rate of this reaction is proportional to the product of the electron and parent ion densities and the radiative recombination rate coefficient $\alpha^r(\gamma \rightarrow \gamma,nl)$. The rate coefficient is expressed in subscript notation as $\alpha^r_{\gamma i}$, where i represents $\gamma,nl$. Radiative recombination rate coefficients are required for all levels $nl$ of the recombined ion.

Dielectronic recombination (Burgess 1964; see Hahn 1985 for an overview) can be the dominant recombination process in low density plasmas. This is a two stage process. Firstly, in resonance capture, a free electron excites a core electron in the parent ion and simultaneously loses enough energy so that it enters a bound orbit

$$X^{+z1}(\gamma) + e^- \rightleftharpoons X^{+z}(\gamma',nl) \qquad \text{Resonance Capture} \qquad \text{E(2.1.20)}$$

This stage is known as resonance capture and is the inverse to Auger breakup (or autoionisation). The doubly excited state lies above the normal ionisation threshold for the initial parent configuration, and can either break up by autoionisation or stabilise by radiatively relaxing to a lower configuration. Because the core excitation involves low lying levels, the most likely stabilisation involves spontaneous radiative decay of the core excited electron. This completes the recombination process

$$X^{+z}(\gamma',nl) \rightarrow X^{+z}(\gamma'',nl) + h\nu \quad \text{Radiative Stabilisation} \qquad \text{E(2.1.21)}$$

where $\gamma$ and $\gamma''$ are not necessarily the same configuration. The dielectronic recombination rate coefficient, $\alpha^d$, for a particular core excited transition $\gamma \rightarrow \gamma'$ can thus be expressed in terms of a branching ratio between Auger breakup and radiative stabilisation

$$\alpha^d(\gamma \rightarrow \gamma'',nl) = \frac{A^r(\gamma',nl \rightarrow \gamma'',nl)}{A^r(\gamma',nl \rightarrow \gamma'',nl) + \Sigma_{\gamma,,} A^a(\gamma',nl \rightarrow \gamma'')} \cdot A^{cap}(\gamma \rightarrow \gamma',nl) \qquad \text{E(2.1.22)}$$

where $A^r$ and $A^a$ are the transition probabilities for core electron radiative stabilisation and Auger breakup and $A^{cap}$ is the probability of dielectronic capture into n,l. This is the formulation developed by Burgess (1964,1965). The probability of capture, $A^{cap}$, is directly related to the Auger transition probability for the reverse process by a detailed balance relationship. E(2.1.22) can thus be written entirely in terms of radiative and Auger transition probabilities.

The captured electron binding energy

$$I(nl) = \Delta E - E_{free} \qquad \text{E(2.1.23)}$$

where $\Delta E$ is the core transition energy and $E_{free}$ is the energy of the initial free electron. The lowest level available to the captured electron thus corresponds to $I(nl) \leq \Delta E$. Conversely, a particular feature of dielectronic recombination is that very high levels can be populated by electrons with energy approaching $E_{free} = \Delta E$. In practice, it may be necessary to include levels up to $n \sim 500$.

Schematics of dielectronic recombination for ground and metastable states of beryllium-like ions are illustrated in Figures 2.1.2a and b respectively. $n_0$ indicates the lowest level available for capture. Dielectronic recombination based on the metastable 2s2p $^3$P parent leads to stabilisation to levels which may be above the $2s^2$ $^1$S autoionisation threshold. These states in turn can autoionise again, a process known as

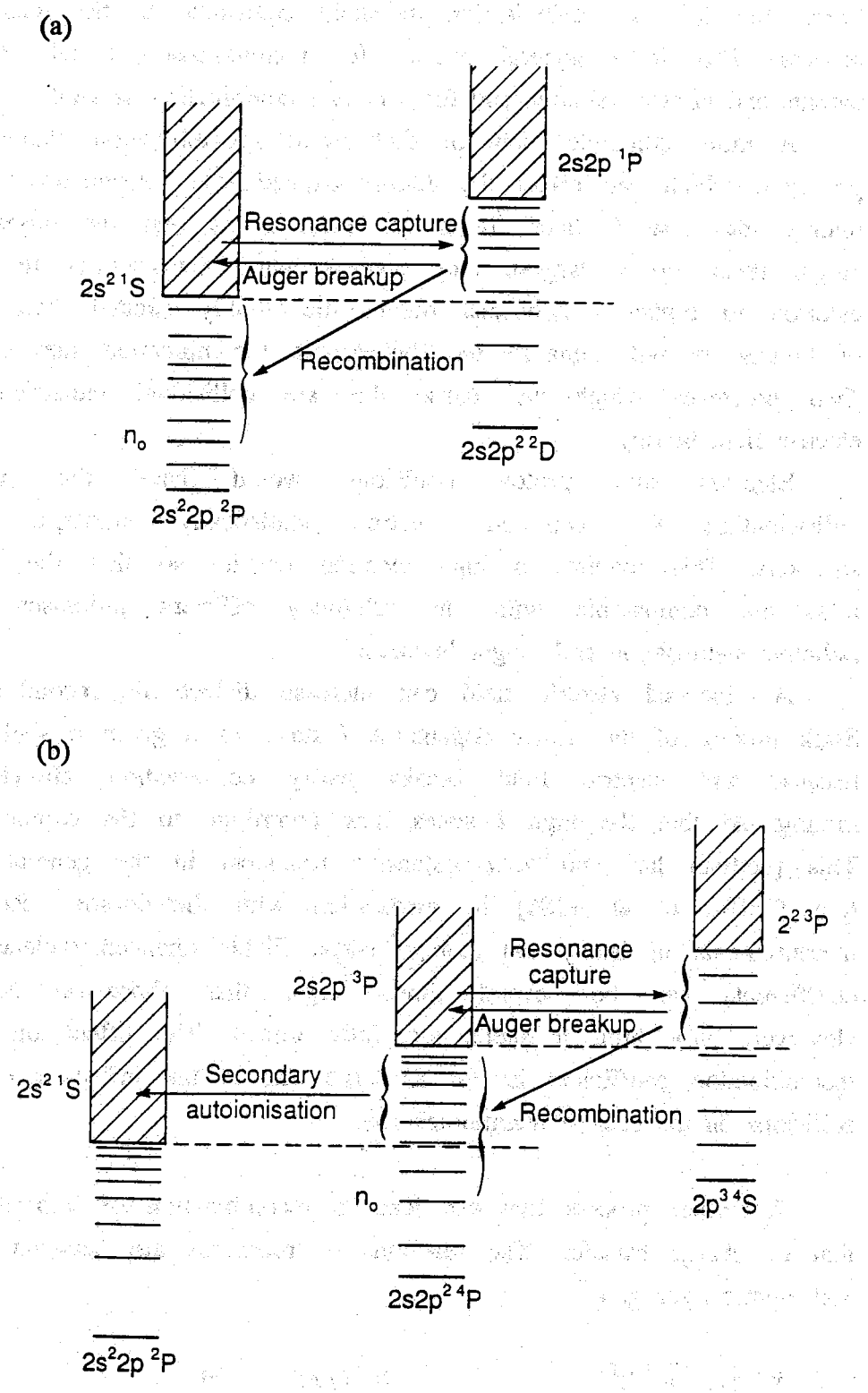


**Figure 2.1.2:** Schematics of dielectronic recombination
(a) $2s^2\ ^1S$ parent
(b) $2s2p\ ^3P$ parent

secondary autoionisation, so that effectively only electrons captured below the $2s^2\ ^1S$ autoionisation threshold contribute to the recombination process. This is a general feature for recombination based on excited parents and affects radiative and three body recombination as well.

A more complete view of dielectronic recombination should include processes which can affect the doubly excited state. Resonance capture is mainly into low $l$ states. It is for these states that the probability of Auger break up is largest. Any process which redistributes the captured electron to higher $l$ subshells before the doubly excited state stabilises or breaks up will enhance the dielectronic recombination rate coefficient. Two processes which can cause this are collisional redistribution and electric field mixing.

Electron and proton collisions would have the effect of redistributing the captured electron statistically amongst the $l$ subshells. This requires a high electron density so that the collisional rates are comparable with the relatively efficient processes of core radiative stabilisation and Auger breakup.

An induced electric field can increase dielectronic recombination by Stark mixing of the nearly degenerate $l$ states of a given n shell. This is because the electric field breaks parity conservation allowing $l \rightarrow l \pm 1$ mixing, so that the high $l$ states now contribute to the capture process. This problem has undergone extensive treatment in the general literature (e.g Griffin et al 1986) in association with dielectronic recombination measurements in heavy ion storage rings. Field enhanced dielectronic rate coefficients can be several times larger than those at zero field. However, only high n shells are fully mixed. The effect on the total recombination coefficient is not as large due to the influence of electron collisions on the excited recombined ion.

A further process that can lead to recombination of impurity ions is that of charge transfer. The reactions of relevance are between impurities and atomic hydrogen

$$X^{+z1}(\gamma) + H^0 \rightarrow X^{+z}(\gamma, nl) + H^+ \qquad \text{(E2.1.24)}$$

The charge exchange rate coefficients, $\alpha^{cx}$, can be comparable with or exceed those of electron-ion recombination. The rate of reaction is $n_H N_\gamma^{+z1} \alpha^{cx}$. When neutral atoms are present, the addition of charge transfer processes leads to a revised ionisation balance. The effect is to decrease

the average charge of the ions in the plasma, which leads to increased radiated power. These effects have been studied by Hulse et al (1980). For small tokamaks, neutral hydrogen can penetrate to central regions and have considerable influence. However, for large high temperature tokamaks like JET, neutral hydrogen is only present in appreciable quantities at the plasma edge and in the vicinity of the X-point. Also, in the pumped divertor phase, neutral hydrogen will be actively pumped into the divertor region to enhance recombination and radiative cooling.

When neutral heating beams are present, charge exchange between the neutral beams and impurity ions is an important process determining the beam penetration. The exploitation of this process as a plasma diagnostic has already been discussed in Section 1.3.

The magnitude of charge transfer cross sections is sensitive to the relative velocity, $v_r$, of the donor and receiver species in comparison to the hydrogen ground state electron orbital velocity ($v_0$ = 2.188 x $10^8$ $cms^{-1}$, which is equivalent to a relative collision energy of ~ 25 keV/amu). The dynamics in the three-body interaction involves different physical processes as the velocity changes. At low velocities, there is a quasi-molecular intermediate state requiring a full molecular quantal picture. On the other hand, classical trajectory models are applicable when $v_r > v_0$. At sufficiently high impacting velocities ion impact ionisation always becomes the dominant process. A survey of the various theoretical models is given by Janev and Presnyakov (1981).

A particular feature of charge transfer is the resonant nature of the capture at low and moderate energies. Ryufuku and Watanabe (1978) estimate that capture into separate quantum levels maximises at a principal quantum shell of

$$n_{max} = (z+1)^{0.774} \qquad \text{E(2.1.25)}$$

For example, the preferential shell for capture is n=5 for $O^{+8}$ and n=2 for $Be^{+2}$. Above this level the cross sections to separate shells fall rapidly as

$$\sigma^{cx}(n) = (n/n_{max})^{-\beta(v_r)}\, \sigma^{cx}(n_{max}) \qquad \text{E(2.1.26)}$$

Experimental evidence suggests that $\beta$ is ~ 3 at high $v_r$ and increases at low $v_r$ (Hoekstra 1990). Thus at low energy, almost all of the electron capture is into the dominant n-shell.

# 2.2: POPULATION STRUCTURE AND SPECTRAL EMISSION THEORY


2.2.1: Discussion
2.2.2: Model of Statistical Balance
(a) Basic equations
(b) Level populations and Effective Contributions
(c) Metastable Populations
(d) Spectral Emissivity Coefficients
(e) Effective Collisional-Radiative Coefficients
2.2.3: A Generalised View of Projection and Condensation
2.2.4: Radiative Power Loss Coefficients


## 2.2.1: Discussion

The following sections construct the population structure equations of statistical balance used to determine level populations, collisional-radiative coefficients, spectral emission coefficients and radiated power coefficients. The initial algebraic description follows closely that developed by Burgess and Summers (1976), Summers (1977) and Spence and Summers (1985). However, the theory is extended to maintain resolution between parent and metastable states.

It is necessary to clarify the notation that will be used for the metastable resolved model. The z times ionised state of element X is denoted by $X^{+z}$. No distinction is made between the *m* ground and metastable configurations. These are denoted by the subscripts $\rho$ and $\epsilon$. The parent ion $X^{+z1}$, with charge $z1 = z + 1$, has *m1* parent metastable levels denoted by the subscripts $\gamma$ and $\sigma$. At this stage, in a strictly formal sense, no identification of which particular levels are metastable is required.

## 2.2.2: Model of Statistical Balance

### (a) Basic Equations

Consider a complete set of levels of $X^{+z}$ indexed by 1, 2, 3, ..... $i_{max}$ irrespective of whether metastables, normal excited states or doubly excited states. When all the relevant processes are considered, the rate

of change of an arbitrary level, i, is given by

$$d/dt\ N_i^{+z} = -\left( \Sigma_j A_{ji}^r + \Sigma_j n_e q_{ji}^e + \Sigma_j n_p q_{ji}^p + \Sigma_\gamma n_e S_{\gamma i} + \Sigma_\gamma A_{\gamma i}^a \right) N_i^{+z}$$
$$+ \Sigma_j \left( A_{ij}^r + n_e q_{ij}^e + n_p q_{ij}^p \right) N_j^{+z}$$
$$+ \Sigma_\gamma \left( \alpha_{i\gamma}^d + \alpha_{i\gamma}^r + n_e \alpha_{i\gamma}^t + \frac{n_H}{n_e} \alpha_{i\gamma}^{cx} \right) n_e N_\gamma^{+z1}$$
$$1 \le i,j \le i_{max} \qquad \text{E(2.2.1)}$$

Keeping with the notation of Summers and co-workers, collisional-radiative matrix elements are defined

$$C_{ij} = -\left( A_{ij}^r + n_e q_{ij}^e + n_p q_{ij}^p \right) \quad \text{for } i \neq j \qquad \text{E(2.2.2)}$$

with the element $C_{ii}$ representing the total losses from level i

$$C_{ii} = -\left( \Sigma_j A_{ji}^r + \Sigma_j n_e q_{ji}^e + \Sigma_j n_p q_{ji}^p + \Sigma_\gamma n_e S_{\gamma i} + \Sigma_\gamma A_{\gamma i}^a \right) \qquad \text{E(2.2.3)}$$

In addition, a composite recombination coefficient is defined as

$$r_{i\gamma} = \alpha_{i\gamma}^d + \alpha_{i\gamma}^r + n_e \alpha_{i\gamma}^t + \frac{n_H}{n_e} \alpha_{i\gamma}^{cx} \qquad \text{E(2.2.4)}$$

This enables E(2.2.1) to be rewritten more conveniently as

$$d/dt\ N_i^{+z} = -\Sigma_j C_{ij} N_j^{+z} + \Sigma_\gamma r_{i\gamma} n_e N_\gamma^{+z1} \qquad \text{E(2.2.5)}$$

which is the standard representation.

**(b) Level Populations and Effective Contributions**

The complete set of levels is partitioned, without loss of generality, into the subsets of metastable and excited states. Suppose that the first m levels are metastable. From the quasi-static approximation, only the excited states are assumed to be in steady state equilibrium. i.e.

$$d/dt\ N_\rho^{+z} \neq 0 \quad \text{for } 1 \le \rho \le m \qquad \text{E(2.2.6)}$$

$$d/dt\ N_i^{+z} = 0 \quad \text{for } i > m \qquad \text{E(2.2.7)}$$

If the subset of metastable populations is exclusively partitioned out of E(2.2.5) this reduces to

$$d/dt\ N_i^{+z} = -\Sigma_j C_{ij} N_j^{+z} - \Sigma_\rho C_{i\rho} N_\rho^{+z} + \Sigma_\gamma r_{i\gamma} N_\gamma^{+z1} n_e$$

$$= 0 \qquad \text{E(2.2.8)}$$

where from now on, the subscripts i and j just index normal excited states:

$$m+1 \le i,j \le i_{max} \qquad \text{E(2.2.9)}$$

The equilibrium populations of the excited states are obtained by rearranging E(2.2.8)

$$\Sigma_j C_{ij} N_j^{+z} = -\Sigma_\rho C_{i\rho} N_\rho^{+z} + \Sigma_\gamma r_{i\gamma} N_\gamma^{+z1} n_e \qquad \text{E(2.2.10)}$$

and then multiplying by the inverse matrix, $C_{ji}^{-1}$

$$N_j^{+z} = -\Sigma_\rho \Sigma_i C_{ji}^{-1} C_{i\rho} N_\rho^{+z} + \Sigma_\gamma \Sigma_i C_{ji}^{-1} r_{i\gamma} N_\gamma^{+z1} n_e$$

$$= \Sigma_\rho F_{j\rho} N_\rho^{+z} n_e + \Sigma_\gamma R_{j\gamma} N_\gamma^{+z1} n_e \qquad \text{E(2.2.11)}$$

where

$$F_{j\rho} = -\Sigma_i C_{ji}^{-1} C_{i\rho} / n_e \qquad \text{E(2..2.12)}$$

$$R_{j\gamma} = \Sigma_i C_{ji}^{-1} r_{i\gamma} \qquad \text{E(2.2.13)}$$

are the effective contributions to the population of $N_j^{+z}$ from excitation and recombination from metastables $\rho$ and parents $\gamma$ respectively. This expresses the excited state populations in terms of the dynamic populations and identifies the primary populating mechanisms. More detailed information of the separate contributions from the different recombination processes can be obtained by substituting E(2.2.13) for $r_{i\gamma}$. In particular, the charge exchange contribution is often expressed independently.

**(c) Metastable Populations**

If it is assumed that metastable populations have reached steady state equilibrium, then their populations can be derived by setting their time derivatives, $d/dt(N_\rho^{+z})$, equal to zero and obtaining the equilibrium populations of the entire level set. This is equivalent to considering that the metastables are in quasi-static equilibrium with the ground state populations.

**(d) Spectral Emissivity Coefficients**

The intensity of spectral emission due to spontaneous radiative decay between bound atomic states is given by

$$I(i \rightarrow j, \lambda) = A_{ji}^{r} N_i^{+z} \qquad \text{E(2.2.14)}$$

From the expression for excited state populations given above it is possible to express spectral intensities in terms of effective emission coefficients,

$$I(i \rightarrow j, \lambda) = \Sigma_\rho \, \varepsilon_{ex}^{eff}(\lambda,\rho) \, N_\rho^{+z} \, n_e + \Sigma_\gamma \, \varepsilon_{rec}^{eff}(\lambda,\rho) \, N_\gamma^{+z1} \, n_e \qquad \text{E(2.2.15)}$$

where $\varepsilon_{ex}^{eff}(\lambda,\rho) = A_{ji}^{r} \, F_{i,\rho}$ and so on E(2.2.16)

These emission coefficients provide the theoretical link between experimentally observed spectral intensities and dominant (i.e metastable) impurity densities in the plasma. Note again that this formulation enables the intensities to be expressed in terms of the dynamic populations and enables the individual contributions from excitation and recombination processes to be derived.

**(e) Effective Collisional-Radiative Coefficients**

Several different methods for calculating effective collisional radiative coefficients have appeared in the general literature (see Kastner (1981) and references therein). The present work follows the procedures of Summers and co-workers. This method is based on the explicit solution of the statistical balance equations and is entirely equivalent to other random-walk solutions.

For simplicity, it is more convenient to consider first the case of an ion with single ground ($\rho$) and parent ($\gamma$) levels. The rate of change of the ground state population is given by

$$d/dt\ N_\rho^{+z} = -\Sigma_j\ C_{\rho j}\ N_j^{+z} - C_{\rho\rho}\ N_\rho^{+z} + r_{\rho\gamma}\ n_e\ N_\gamma^{+z1} \qquad \text{E(2.2.17)}$$

Substituting for $N_j^{+z}$ from E(2.2.11) gives

$$d/dt\ N_\rho^{+z} = -\Sigma_j\ C_{\rho j}\ (\ R_{j\gamma}\ n_e\ N_\gamma^{+z1} + F_{j\rho}\ n_e\ N_\rho^{+z}) - C_{\rho\rho}\ N_\rho^{+z} + r_{\rho\gamma}\ n_e\ N_\gamma^{+z1} \qquad \text{E(2.2.18)}$$

$$d/dt\ N_\rho^{+z} = -\ (\ C_{\rho\rho} + \Sigma_j\ C_{\rho j}\ F_{j\rho}\ n_e\ )\ N_\rho^{+z} + (\ r_{\rho\gamma} - \Sigma_j\ C_{\rho j}\ R_{j\gamma}\ )\ n_e\ N_\gamma^{+z1} \qquad \text{E(2.2.19)}$$

From which the effective collisional-radiative recombination and ionisation coefficients are defined as

$$S_{\gamma\rho}^{eff} = (\ C_{\rho\rho} + \Sigma_j\ C_{\rho j}\ F_{j\rho}\ n_e\ )\ /\ n_e \qquad \text{E(2.2.20)}$$

$$\alpha_{\rho\gamma}^{eff} = r_{\rho\gamma} - \Sigma_j\ C_{\rho j}\ R_{j\gamma} \qquad \text{E(2.2.21)}$$

Physically, the effective ionisation rate coefficient $S_{\gamma\rho}^{eff}$ is the growth rate coefficient of $X^{+z1}$ due to ionisation from metastable $\rho$ together with multiple steps through excited states of $X^{+z}$, and the effective recombination rate $\alpha_{\rho\gamma}^{eff}$, describes the rate at which electrons are captured from $X_\gamma^{+z1}$ but including only those which cascade to the state $\rho$ of $X^{+z}$. In the case of multiple parents and metastables, the method is readily generalised. Consider the rate of change of an arbitrary metastable denoted by $\varepsilon$ :

$$d/dt\ N_\varepsilon^{+z} = -\Sigma_j\ C_{\varepsilon j}\ N_j^{+z} - \Sigma_\rho\ C_{\varepsilon\rho}\ N_\rho^{+z} + \Sigma_\gamma r_{\varepsilon\gamma}\ n_e\ N_\gamma^{+z1} \qquad \text{E(2.2.22)}$$

Again eliminate the excited state populations by back substituting from E(2.2.11)

$$d/dt\ N_{\varepsilon}^{+z} = -\Sigma_j C_{\varepsilon j}\left(\Sigma_\gamma R_{j\gamma}\, n_e\, N_\gamma^{+z1} + \Sigma_\rho F_{j\rho}\, n_e\, N_\rho^{+z}\right) - \Sigma_\rho C_{\varepsilon\rho} N_\rho^{+z} + \Sigma_\gamma r_{\varepsilon\gamma}\, n_e\, N_\gamma^{+z1} \quad \text{E(2.2.23)}$$

$$= \Sigma_\rho \left( C_{\varepsilon\rho} + \Sigma_j C_{\varepsilon j} F_{j\rho}\, n_e \right) N_\rho^{+z} + \Sigma_\gamma \left( r_{\varepsilon\gamma} - \Sigma_j C_{\varepsilon j} R_{j\gamma} \right) n_e\, N_\gamma^{+z1} \quad \text{E(2.2.24)}$$

which gives the collisional radiative coefficients as

$$\alpha_{\varepsilon\gamma}^{eff} = r_{\varepsilon\gamma} - \Sigma_j C_{\varepsilon j} R_{j\gamma} \quad \text{E(2.2.25)}$$

$$S_{\varepsilon\varepsilon}^{eff} = \left( C_{\varepsilon\varepsilon} - \Sigma_j C_{\varepsilon j} F_{j\varepsilon}\, n_e \right) / n_e \quad \text{E(2.2.26)}$$

$$q_{\varepsilon\rho}^{eff} = \left( C_{\varepsilon\rho} - \Sigma_j C_{\varepsilon j} F_{j\rho} \right) / n_e \quad \text{E(2.2.27)}$$

where $\alpha_{\varepsilon\gamma}^{eff}$ is the effective recombination coefficient from parent $\gamma$ to metastable $\varepsilon$, $S_{\varepsilon\varepsilon}^{eff}$ is the effective total loss coefficient from metastable $\varepsilon$ and includes effective excitation to other metastables $\rho$ as well as the effective ionisation coefficients to all parents $\gamma$. The coefficient $q_{\varepsilon\rho}^{eff}$ is a measure of coupling of metastable populations via collisions and radiative transitions within the excited states. This coefficient is defined as the *effective metastable cross coupling coefficient*, from metastable $\rho$ to metastable $\varepsilon$.

Note that the loss coefficient gives the total loss rate from the particular ground or metastable state. For a single metastable this is the effective ionisation coefficient summed over several parents. No resolution is obtained on the final configuration of the parent ion. This is because the algebraic description of Summers and co-workers only considered the rate of change of the dynamic populations in $X^{+z}$. To obtain detailed information on the final states following ionisation it is necessary to consider the rates of change of the dynamic populations of the parent ion, $X^{+z1}$.

The various parents can be populated either by direct ionisation from ground and excited states or by autoionisation of doubly excited states which lie above the direct ionisation threshold to that particular parent. If a loss vector, L, is constructed

$$L_{\gamma i} = n_e S_{\gamma i} + A^a_{\gamma i} \qquad \text{E(2.2.28)}$$

then the rate of change of an arbitrary parent configuration, $\sigma$, is given by

$$d/dt\ N^{+z1}_{\sigma} = - \left( \Sigma_j r_{j\sigma} + \Sigma_\rho r_{\rho\sigma} \right) n_e N^{+z1}_{\sigma} + \Sigma_j L_{\sigma j} N^{+z}_{j} + \Sigma_\rho L_{\sigma\rho} N^{+z}_{\rho} \qquad \text{E(2.2.29)}$$

Again back substitute for the excited state populations

$$d/dt\ N^{+z1}_{\sigma} = - \left( \Sigma_j r_{j\sigma} + \Sigma_\rho r_{\rho\sigma} \right) n_e N^{+z1}_{\sigma} + \Sigma_j L_{\sigma j} \left( \Sigma_\rho n_e F_{j\rho} N^{+z}_{\rho} + \Sigma_\gamma n_e R_{j\gamma} N^{+z1}_{\gamma} \right) + \Sigma_\rho L_{\sigma\rho} N^{+z}_{\rho} \qquad \text{E(2.2.30)}$$

which after rearranging gives

$$d/dt\ N^{+z1}_{\sigma} = - \left( \Sigma_j r_{j\sigma} + \Sigma_\rho r_{\rho\sigma} - \Sigma_j L_{\sigma j} R_{j\sigma} \right) n_e N^{+z1}_{\sigma} + \Sigma_{\gamma\neq\sigma} \Sigma_j L_{\sigma j} R_{j\gamma} n_e N^{+z1}_{\gamma} + \Sigma_\rho \left( L_{\sigma\rho} + \Sigma_j L_{\sigma j} F_{j\rho} n_e \right) N^{+z}_{\rho} \qquad \text{E(2.2.31)}$$

$$= - \alpha^{eff}_{\sigma\sigma} n_e N^{+z1}_{\gamma} + \Sigma_{\gamma\neq\sigma} \beta^{eff}_{\sigma\gamma} n_e N^{+z1}_{\gamma} + \Sigma_\rho S^{eff}_{\sigma\rho} n_e N^{+z}_{\rho} \qquad \text{E(2.2.32)}$$

where

$$\alpha^{eff}_{\sigma\sigma} = \Sigma_j r_{j\sigma} + \Sigma_\rho r_{\rho\sigma} - \Sigma_j L_{\sigma j} R_{j\sigma} \qquad \text{E(2.2.33)}$$

$$S^{eff}_{\sigma\rho} = \left( L_{\sigma\rho} + \Sigma_j L_{\sigma j} F_{j\rho} n_e \right) / n_e \qquad \text{E(2.3.34)}$$

$$\beta^{eff}_{\sigma\gamma} = \Sigma_j L_{\sigma j} R_{j\gamma} \qquad \text{E(2.3.35)}$$

are the parent resolved collisional-radiative coefficients. Physically, $S^{eff}_{\sigma\rho}$ is the parent resolved ionisation coefficient due to direct and auto-ionisation processes, and $\alpha^{eff}_{\sigma\sigma}$ is the total recombination rate coefficient from parent $X^{+zl}_{\sigma}$. The relationships between these coefficients and those derived by considering the rates of change of the metastable populations of $X^{+z}$ are clear. The sum of the parent resolved ionisation coefficients (E(2.2.33)) will be equal to the total loss rate from a given metastable, as given by E(2.2.26) excluding the effective excitations to other metastables of $X^{+z}$, and the total recombination rate from a given parent, E(2.2.34), will be equal to the sum of the metastable resolved recombination rate coefficients (E2.2.25). A formal proof of these relationships is given in Appendix A2.1.

The nature of the coefficient $\beta^{eff}_{\sigma\gamma}$ needs further discussion. This coefficient is driven by recombination processes and couples together parent populations of $X^{+zl}$. It is a measure of the rate at which electrons recombine into levels above the autoionisation threshold and subsequently Auger to an alternative parent. $\beta^{eff}_{\sigma\gamma}$ is thus a form of cross coupling coefficient. No reference to this type of coefficient has previously been made in the general literature. For the present work, it shall be defined as the *parent cross coupling coefficient*, as distinct from the *metastable cross coupling coefficient* defined by E(2.2.27).

In conclusion, to maintain resolution between parent and metastable populations of $X^{+z}$ and $X^{+zl}$, four types of generalised collisional-radiative coefficients are required - ionisation, recombination, metastable cross coupling and parent cross coupling. These coefficients can all be calculated by considering the recombined population structure of $X^{+z}$. The collisional-radiative coefficients contain not only direct processes between metastable and parent populations but all indirect processes via excited states, and provide the source terms for determining the time and spatial evolution of dynamic populations in plasma models.

### 2.2.3: A General View of Projection and Condensation

The collisional-radiative coefficients derived in Section 2.2.2 contain the direct processes between the dynamic populations and also all the indirect processes via the excited states. This is equivalent to

projecting the influence of the excited state populations onto the dynamic populations. This technique is also known as a condensation of the whole set of equations onto the set describing the dynamic populations (Summers and Hooper 1983). However, the techniques of projection and condensation are entirely general and can be applied to any population groups. The particular application of this technique envisaged for the work of this thesis is the projection of a calculation of bundled high level populations onto a low level calculation of resolved populations.

To illustrate this, again consider equation E(2.2.5), which describes the rates of change of the entire population set before being partitioned into dynamic and quasi-static groups. The levels can be partitioned instead into a low level set indexed by I,J, ... and a high level set indexed by i,j, ... , so that

$$d/dt\ N_J^{+z} = - \Sigma_I C_{JI}\ N_I^{+z} + \Sigma_i C_{Ji}\ N_i^{+z} + \Sigma_\gamma r_{J\gamma}\ N_\gamma^{+z1} \qquad \text{E(2.2.36)}$$

The high level population set can then be eliminated from the equations by expressing them in terms of the low level set, leaving a set of equations which are expressed entirely in terms of the low level set

$$d/dt\ N_J^{+z} = - \Sigma_J \left( C_{JI}^{dir} + C_{JI}^{ind} \right) N_I^{+z} + \Sigma_\gamma \left( r_{J\gamma}^{dir} + r_{J\gamma}^{ind} \right) N_\gamma^{+z1} \qquad \text{E(2.2.37)}$$

where $C^{dir}$, $r^{dir}$ are the direct couplings between the low level set and $C^{ind}$, $r^{ind}$ are the indirect couplings involving pathways through the high level group. In this way, the equations for the low level set contain all excitation and ionisation pathways via the high level group and all cascade contributions. General algebraic expressions for projection and indirect couplings are derived in Appendix A2.2. It will be shown that these are important procedures for refined calculations of low level emission.

The process may be continued by condensing the low level set onto the metastable group. The level populations, effective contributions and collisional-radiative coefficients can then be derived as before.

### 2.2.4: Radiative Power Loss Coefficients

The radiative loss rate is the rate at which radiant energy is lost per unit volume. For the present work, metastable resolved radiated power coefficients are sought which have contributions from various atomic processes. The description of radiated power considered here is of the net loss summed over all emitting frequencies, and is therefore not concerned with the frequency distribution of the radiated energy. Consider the configuration $X_{\gamma}^{+z1}$. The individual components of the radiated power are given by the coefficients

| | |
|---|---|
| $P_L(\gamma,z1)$ | spontaneous radiative decay of $X^{+z1}$ arising from excitation from metastable $\gamma$ |
| $P_{RR}(\gamma\rightarrow\rho,z1)$ | continuum radiation arising from radiative recombination of $X_{\gamma}^{+z1}$ towards $X_{\rho}^{+z}$. |
| $P_{RS}(\gamma\rightarrow\rho,z1)$ | radiation from dielectronic stabilisation arising from recombination of $X_{\gamma}^{+z1}$ towards $X_{\rho}^{+z}$. |
| $P_{RC}(\gamma\rightarrow\rho,z1)$ | radiation from cascade of captured electrons |
| $P_B(\gamma,z1)$ | Bremsstrahlung |

$P_L$, $P_{RC}$ and $P_{RS}$ are all forms of line radiation, whereas $P_{RR}$ and $P_B$ are continuum radiation. Note that radiation from $P_{RC}$ and $P_{RS}$ appears as part of the spectrum of $X^{+z}$ but arises from the recombination of $X^{+z1}$. The total radiated power density arising from $X_{\gamma}^{+z1}$ is given by

$$n_e N_{\gamma}^{+z1} P_{rad}(\gamma,z1) = n_e N_{\gamma}^{+z1} \left( P_L(\gamma,z1) + P_B(\gamma,z1) + \Sigma_{\rho} \left( P_{RR}(\gamma\rightarrow\rho,z1) + P_{RS}(\gamma\rightarrow\rho,z1) + P_{RC}(\gamma\rightarrow\rho,z1) \right) \right) \quad \text{E(2.2.38)}$$

It is convenient to define a composite recombination/bremsstrahlung coefficient so that the radiated power density is expressed as

$$n_e N_{\gamma}^{+z1} P_{rad}(\gamma,z1) = n_e N_{\gamma}^{+z1} \left( P_L(\gamma,z1) + P_{RB}(\gamma,z1) \right) \quad \text{E(2.2.39)}$$

These definitions are as in Summers and Hooper (1983) but with the addition of metastable resolution. The electron and ion densities are usually expressed in units of $cm^{-3}$ and the total radiated power, $P_{rad}$, is expressed in units of $Wcm^{-3}$ so that the radiated power coefficients - $P_L$, $P_B$, $P_{RR}$, $P_{RS}$ and $P_{RC}$ are in units of $Wcm^3$.

# 2.3: LITERATURE REVIEW AND SCOPE OF PRESENT WORK


2.3.1: Literature Review
(a) Solutions to the Population Structure Equations
(b) Ionisation Balance Calculations and Metastable Effects
2.3.2: Scope of Present Work
(a) Discussion
(b) Level Bundling and Choice of Metastable States
(c) Population Models


## 2.3.1: Literature Review

### (a) Solutions to the Population Structure Equations

The solution of the sets of equations for level populations, effective contributions and effective collisional radiative coefficients, represents a considerable computational difficulty because of the number of states which need to be included in the population calculation. Examination of metastable states requires a resolved level classification (such as LS or LSJ). Also, important line radiation tends to come from transitions between a highly populated group of low levels, which only span a few quantum shells. Thus a resolved level classification and population subdivision is essential for spectral modelling. The resolution required for these states can be described as

$$(\gamma, L_p, S_p)\ n\ l\ ^{2(S+1)}L_J$$

where $\gamma$ is the parent configuration with quantum numbers $L_p$ and $S_p$. This assumes an LS or intermediate coupling scheme.

Conversely, to address the problem of collisional-radiative coefficients, very many principal quantum shells need to be considered, particularly when dielectronic recombination is active. Fortunately, highly excited state populations do not need to be treated with the same degree of precision as low lying state populations as the separate $l$ levels of the same n become nearly degenerate. It is possible then to

introduce a grosser level of resolution for high levels in which levels are combined or bundled into groups. Various degrees of bundling are possible:

($\gamma$, $L_p$,$S_p$) bundle-n *l* S
($\gamma$, $L_p$,$S_p$) bundle-n S
($\gamma$, $L_p$,$S_p$) bundle-n

The successive approximations involve summing and averaging over resolved rate coefficients, and assuming that the resolved levels within the bundled group are populated according to their statistical weights. Whether the chosen bundling approximation is reasonable depends on the physical conditions and the objectives of the calculation. For example, in the bundle-n model, levels are bundled into principal quantum shell and it is assumed that the populations of the separate l orbitals are given by

$$N(n,l) = N(n)\ 2(2l+1)/2n^2 \qquad \text{E(2.3.1)}$$

This condition will only be satisfied if the plasma density is sufficiently high to ensure collisional redistribution.

The complete set of level populations for a given ion can thus be partitioned into four sets

(i) Dynamic (or ground and metastable) populations, described in a resolved coupling scheme such as LSJ or LS
(ii) Low level excited state populations in a resolved coupling scheme
(iii) High level excited state populations in a grosser bundling approximation
(iv) Doubly excited populations formed by dielectronic capture.

Due to the complexity of this problem, simplifications are generally made of which four types of solution have been widely explored in the general literature.

Firstly, for low level populations, the standard practice (e.g. Dufton 1977, Kato et al 1989, and many others ) is to consider a closed set of resolved levels which span the lowest few quantum shells. The justification in this approximation is that the excitation rates from ground and metastable states to higher levels decreases rapidly with n and so the higher levels will have very small populations. This approach will

not allow accurate evaluation of collisional-radiative coefficients.

Secondly, if interest is directed at highly excited states and the evaluation of collisional-radiative coefficients, a grosser bundling approximation can be used for all levels. The work of Burgess and Summers (1976) and Summers (1974) adopted the bundle-n approach. This work will be expanded as part of the present work and so will be described in some detail. A computer code was written to solve the equations of statistical balance and calculate excited state populations. The system considered was that of a series of n shells built upon a single parent, which was the ground state of the recombining ion. The single ground state of the recombined system was the lowest occupied n-shell of the recombined ion. The energy of excited states was defined by

$$E_n = Z1^2/(n-\delta)^2 \cdot I_H \qquad \text{E(2.3.2)}$$

where $\delta$ is a quantum defect chosen to correctly reproduce the actual shell averaged term energies. This was only non zero for the first few shells.

The collisional radiative coefficients calculated were the expressions E(2.2.20) and E(2.2.21), relevant to a single ground/ single parent model and based on the rates of change of the dynamic populations of $X^{+z}$. These coefficients were most conveniently obtained by defining a complete collisional radiative matrix as

$$[\mathbb{C}_{ij}] = \begin{bmatrix} C_{\rho\rho} & C_{\rho j} \\ C_{j\rho} & C_{ij} \end{bmatrix} \qquad \text{E(2.3.3)}$$

so that

$$S^{eff}_{\rho\rho} = 1/n_e\,[\mathbb{C}^{-1}]_{11} \qquad \text{E(2.3.4)}$$

$$\alpha^{eff}_{\rho\gamma} = S^{eff}_{\rho\rho} \cdot N^{+z}_{\rho} / N^{+z1}_{\gamma} \qquad \text{E(2.3.5)}$$

At a later stage, these coefficients were corrected by normalising the internally generated zero density ionisation and recombination coefficients with an external source of preferred data.

Up to 500 n-shells needed to be considered to account fully for the collisional-radiative influence on recombination. To reduce the calculation to a tractable size, matrix condensation techniques were developed. The calculation was performed for a series of representative

n-shells, typically

$n_{(i)}$ = 1, 2, 3, 4, 5, 6, 7, 8, 9, 10, 12, 15, 20, 30,
40, 50, 70, 100, 150, 200, 250, 300, 400, 500

The above set of 24 representative levels was found to produce satisfactory precision. The populations of the complete set of levels are related to that of the representative set by 3 point Lagrangian interpolation. The equations of statistical balance written in terms of the representative level set are identical in form with those obtained from the full set of equations (see Appendix A2.2). The solution of the population equations could now be obtained by inverting matrices of order 24x24, instead of 500x500. These procedures were used in the ionisation balance calculations of Summers (1974a,b).

Thirdly, several calculations have been performed which link population sets of different resolutions. Some of the most precise calculations have been done for hydrogen atoms and hydrogen-like ions. Ljepojevic et al (1985) took account of the separate $nl\ ^{(2S+1)}L_J$ sublevels up to and including n = 4, with levels above that, up to a maximum value of n = 100, being represented by a bundle-n resolution. The two population sets were coupled by statistical weight factors. This type of approach allows the calculation of both spectral intensities and collisional-radiative coefficients with a high degree of accuracy.

Summers (1977) developed a bundle-n *l* model in which low n-shells were characterised by $nl\ ^{(2S+1)}L$ up to a set value (typically n = 30), with levels above represented by bundle-n resolution. This work was originally applied to the population structures of hydrogen and helium like ions. This was later exploited as part of a study of charge transfer processes in fusion plasmas (Spence and Summers 1986). It would be very difficult to apply this model to more complex many electron ions which may have several parent configurations.

Fourthly, a few authors (Jacobs and Davis 1978, Summers et al 1987) have investigated the effects of collisional redistribution of the resonant state formed by dielectronic capture. This is known as a doubly excited population structure calculation. The zero density dielectronic recombination rate for capture into level $X^{+z}(\gamma,nl)$ following the resonant capture process

$$X^{+z1}(\gamma) + e^- \rightarrow X^{+z}(\gamma',nl) \qquad E(2.3.6)$$

is obtained by considering the branching ratio between Auger breakup and radiative stabilisation of the doubly excited state $X^{+z}(\gamma',nl)$. The recombination coefficient at finite electron density is given by including the effects of redistributing collisions of the form

$$X^{+z}(\gamma',nl) + e^-,p^+ \rightarrow X^{+z}(\gamma',nl') + e^-,p^+ \qquad E(2.3.7)$$

before Auger breakup. Summers et al (1987) examined this effect for the Na-, Ne- and F- like ions of iron, nickel and chromium. It was found that at typical tokamak electron densities ($2x10^{13}$ $cm^{-3}$), that the rate coefficients $\alpha(\gamma \rightarrow \gamma,n)$ for capture into a particular n-shell were increased by a factor of up to ~ 5 for $n > 20$. However, the effective recombination coefficient was not affected because at those high densities electrons captured into $n \geq 20$ were reionised before cascading to the ground state. Similar results were found by Jacobs and Davis (1978) who examined this effect for the ions of $Fe^{+8}$-$Fe^{+13}$.

As a general point, it is often numerically advantageous to express populations of atomic levels in the so called Saha-Boltzmann b or c factor representations (Menzel and Peckeris 1934, Burgess and Summers 1976). These are the ratios of the actual populations to those at LTE

$$b_i = N_i^{+z} / N_i^{+z}(S\text{-}B) \qquad E(2.3.8)$$

$$= \frac{N_i^{+z}}{N_\gamma^{+z1}\, n_e} \left(\frac{2\pi\, m_e\, kT_e}{h^2}\right)^{3/2} \frac{2\omega(z1,\gamma)}{\omega(z,i)} \exp\left(\frac{-I_i}{kT_e}\right) \qquad E(2.3.9)$$

$$c_i = b_i - 1 \qquad E(2.3.10)$$

For very high levels, the c representation is more accurate since detailed balance relations can be imposed exactly. At low temperatures and for low n-shell populations, the $\exp(I/kT_e).b$ representation is numerically

convenient since overflows and underflows can be avoided. The equations of statistical balance can be easily transformed between these representations and the exact population representation, without loss of form. A further advantage of the b or c representation is that the deviation of populations from LTE is an important point for study.

**(b) Modelling of Ionisation Balance and Metastable Effects**

Whilst the problem of metastable effects has received much attention from a variety of authors, there has still not been a complete treatment. The broad theoretical basis of the subject was discussed by Summers and Hooper (1983), but no complete practical calculations were performed. Specialist calculations of fundamental ionisation and recombination cross sections normally only consider the situation of the initial ion in the ground state only.

In ionisation balance calculations, the standard practice is to consider coupling between ground state ions only. The earliest works were by Jordan (1969, 1970) and Summers (1974a,b). That of Summers is particularly notable because a full collisional-radiative model was used to evaluate effective ionisation and recombination coefficients as a function of electron density and temperature. These works have been superseded as the fundamental atomic data has been gradually updated and modified. More recent calculations include those of Jacobs et al (1977), Shull and Van Steenberg (1981) and Arnaud and Rothenflug (1985). The latter present data for the ions of H, He, C, N, O, Ne, Na, Mg, Al, Si, S, Ar, Ca, Fe and Ni, and is the current benchmark for astrophysical studies. All these later works, however, determine ionisation balance including only the fundamental direct rate coefficients involving ground states and neglect collisional-radiative effects. Their justification is that they are directed at solar coronal studies where electron densities are low ($10^8$ $cm^{-3}$) and so collisional radiative effects are negligible. This is not correct, especially for recombination.

Some partial calculations have been done which include the influence of metastable states. Most of these involve the formation of a composite coefficient, in which metastable resolved rate coefficients are weighted by the fractional population of the metastable. Such a coefficient does not correct metastable populations for changes due to ionisation and recombination processes and does not follow all ionisation/recombination pathways.

For example, Roszman (1989) considered both collisional-radiative and metastable effects on the recombination coefficient of oxygen-like $Fe^{+18}$. The treatment was restricted in several ways. In calculating the recombination rate coefficient from metastable states, the so-called frozen core approximation was used. This excludes the parent changing Auger transitions which can considerably reduce the recombination coefficient. Collisional-radiative effects were accounted for by an approximate density correction factor, based on scaled hydrogenic results.

Nussbaumer and Storey (1975) presented an ionisation balance for carbon ions which attempted to account for the influence of metastable states. This work was continued by Vernazza and Raymond (1979). They found that the relative abundance of the Li-, Be- and B- like stages was density dependant. This was jointly attributed to the density sensitivity of the recombination coefficient, and to the density dependence of metastable state populations in the lower charge states. These authors went on to discuss the consequences of this on spectral line emissivities, coronal abundances and spectral line ratio diagnostics. This work was restricted by its use of atomic data and by its formation of a composite coefficient.

Similarly, Kato et al (1990) considered the influence of varying metastable populations on the spectral line emissivities and diagnostic line ratios of O V. At electron densities of greater than $10^{10}$ $cm^{-3}$ it was calculated that the relative populations of the $2s2p\ ^3P$ metastable and $2s^2\ ^1S$ ground state were ~0.8. Ionisation reduced the population of the metastable state and changed line ratios by 10 - 60 %. However, no account was taken of the influence of recombination processes on the metastable population.

Behringer et al (1989) considered the stepwise ionisation from stage to stage of neutral carbon and oxygen atoms released into the 10 - 150 eV temperature environment of a tokamak plasma edge. The motivation for this work was in the study of impurity fluxes from plasma limiting material surfaces. Metastable populations were resolved but the model was used in association with observations to infer experimentally the metastable fluxes. The model was not developed to calculate explicit metastable populations or to include electron recombination and charge exchange processes. Similarly, Welton et al (1991) considered the stepwise ionisation of carbon, nitrogen and oxygen ions to determine relative metastable fractions in atomic beams used in collision experiments. This work is limited by its use of fundamental data and by its neglect of coupling between metastable populations.

Over the years, radiated power coefficients have been evaluated with varying degrees of complexity. Post et al (1977) used an average ion model with semi empirical rate coefficients. More refined calculations have used detailed atomic physics models and recommended atomic data (Summers and McWhirter 1979, Keane and Skinner 1986, Lee 1987). None of these calculations considered metastable resolution. Summers and Hooper (1983) reviewed the theoretical calculation of these coefficients and proposed a generalisation to accommodate metastable levels consistently. The most recent calculations have been by Bonnin et al (1992) who calculated radiative power loss coefficients for carbon and oxygen ions in a modified coronal approximation. This assumed that metastable populations were in quasi-static equilibrium with the ground state populations and that excitation from metastables could contribute to the radiated power.

### 2.3.2: Scope of Present Work

**(a) Discussion**

It is necessary that the atomic models developed for the present work allow calculation both of low level populations and collisional radiative coefficients with high accuracy. To overcome the practical difficulties associated with the number of states which must be included in the calculations, and merging population groups of different resolutions, a two stage strategy is adopted.

Firstly, a separation is made between the calculation of (1) collisional radiative coefficients using a many principal quantum shell approach and (2) low level populations in a resolved coupling scheme. Degrees of resolution and bundling are chosen for each calculation separately which achieve the necessary degree of accuracy while maintaining resolution between parents and metastables and allowing tractable calculations.

Secondly, the two calculations are merged by projecting the influence of the high level bundled populations onto the resolved low level group. This step greatly improves the accuracy of the level populations and collisional radiative coefficients and is the final objective of the theoretical population modelling.

The remainder of this section discusses the levels of resolution and bundling which are appropriate to a metastable resolved calculation, and identifies the relevant metastables and parents. This leads onto a more

detailed discussion on the various population models.

**(b) Level Bundling and Choice of Metastable States**

To model metastable states and low level excited state populations for spectroscopic studies it is necessary to address the actual energy level structure and coupling scheme of the ion. Either LS or LSJ resolution is required. For the light ions of Be, C and O, the separate J levels are nearly degenerate and atomic processes maintain statistical relative populations of these levels to a good approximation. It is therefore acceptable to limit the low level population modelling to LS terms only. This term resolution can be described as bundle-n*l* SL, and does not imply neglect of transitions forbidden by LS coupling.

Examination of the term structure of the H-like to O-like isoelectronic sequences, identifies terms tabulated in Table 2.3.1 as metastable. States indexed by 1 denote the lowest energy, or ground state. The criterion for selection of a metastable is that the state be unable to decay to the ground state or lower lying metastable by an allowed transition, and that the state can act as a significantly populated recombining parent.

| Sequence | Nmet | Parent/Metastable Index 1 | 2 | 3 | 4 |
|---|---|---|---|---|---|
| H-like | 1 | $1s\ ^2S$ | | | |
| He-like | 2 | $1s^2\ ^1S$ | $1s2s\ ^3S$ | | |
| Li-like | 1 | $1s^22s^1\ ^2S$ | | | |
| Be-like | 2 | $1s^22s^2\ ^1S$ | $1s^22s2p\ ^3P$ | | |
| B-like | 2 | $1s^22s^22p\ ^2P$ | $1s^22s2p^2\ ^4P$ | | |
| C-like | 4 | $1s^22s^22p^2\ ^3P$ | $1s^22s^22p^2\ ^1D$ | $1s^22s^22p^2\ ^1S$ | $1s^22s2p^3\ ^5S$ |
| N-like | 3 | $1s^22s^22p^3\ ^4S$ | $1s^22s^22p^3\ ^2D$ | $1s^22s^22p^3\ ^2P$ | |
| O-like | 4 | $1s^22s^22p^4\ ^3P$ | $1s^22s^22p^4\ ^1D$ | $1s^22s^22p^4\ ^1S$ | $1s^22s^22p^33s\ ^5S$ |

**Table 2.4.1:** *Relevant Parents and Metastables*

Note that the main criteria for selection of metastable states is the spin selection rule (e.g. $1s^22s2p\ ^3P$ is forbidden to decay to the $1s^22s^2\ ^1S$ ground state because of the spin selection rule). However, due to the parity selection rule, states which are in the same spin system as an

energetically lower lying level but in the same configuration are also classed as metastable. Namely the $2s^22p^2\ ^1S$ state in the C-like system, the $2s^22p^3\ ^2S$ state in the N-like system and the $2s^22p^4\ ^1S$ state in the O-like system. The inclusion of these states is preliminary. Although it is clear that the direct coupling between say $2s^22p^2\ ^1D$ and $^1S$ is very small ($A(^1S \rightarrow {}^1D = 1.2x10^{-1}\ s^{-1}$ for $O^{+2}$), there may be considerable indirect mixing of these metastables via collisional excitation to normally excited states in the singlet spin system followed by radiative cascade. This would be a relatively fast process and would provide a mechanism to de-excite the $2s^22p^2\ ^1S$ state. The magnitude of this effect is assumed unknown at this point and will be obtained as part of the calculations of this thesis.

A similar situation occurs in the hydrogen and helium sequences with the $2s\ ^2S$ and $1s2s\ ^1S$ terms respectively. These are also forbidden to decay to the ground terms by the parity selection rule. Hydrogen like ions have been considered by Ljepojevic et al (1984). It was shown that there is sufficient collisional transfer between the $2s\ ^2S$ term and the $2p\ ^2P$ term (which can freely decay) to ensure a rapid relaxation of the $2s\ ^2S$ term. This is because these states are energetically very close together. A similar situation is expected between the $1s2s\ ^1S$ and $1s2p\ ^1P$ terms in helium-like ions. Because of this, it was decided not to include these levels in the list of metastable states. Furthermore, these states are separated from the respective ground states by a complete principal quantum shell. They will not act as significant initial parents for recombination because all of the captured electrons will autoionise.

For more highly charged ions, LS coupling breaks down and fine structure splitting becomes large. An LSJ energy level resolution is required. This gives fine structure split ground configurations. For example, Boron like ions have $2s^22p\ ^2P$ with J = 0.5 and J=1.5.

In contrast, the calculation of collisional-radiative coefficients involves many principal quantum shells. A grosser bundling scheme is required to make this calculation tractable. A useful bundling approximation for a parent/metastable resolved model is one which still distinguishes between the spin of the recombined ion states. This arises from the coupling of the recombining free electron and parent configuration. For example, consider the case of a recombining beryllium-like ion. The states in the Be-like ion which can act as significant recombining parents have been identified as $1s^22s^2\ ^1S$ and

$1s^2 2s2p\ ^3P$. The recombination pathways are

| Recombining pathway | | | Parent Index | Spin System |
|---|---|---|---|---|
| $X^{+z1}\ 2s^2\ ^1S$ | → | $X^{+z}\ (2s^2\ ^1S)\ nl\ ^2L$ | 1 | 2 |
| $X^{+z1}\ 2s2p\ ^3P$ | → | $X^{+z}\ (2s2p\ ^3P)\ nl\ ^2L$ | 2 | 2 |
| $X^{+z1}\ 2s2p\ ^3P$ | → | $X^{+z}\ (2s2p\ ^3P)\ nl\ ^4L$ | 2 | 4 |

It can be seen that the lowest levels of the recombined spin systems are the $2s^2 2p\ ^2P$ and $2s2p^2\ ^4P$ states in the boron-like ion. These states are metastable because of the spin selection rule. A separation of levels into parent and spin thus allows connection to be retained between recombining parents and recombined metastables.

This is known as the bundle-n S approximation i.e. excited states are grouped into principal quantum shells and distinguished by parent and spin. The breakdown of parentage as an effective quantum number is accounted for by including autoionisation transition probabilities in the equations of statistical balance. Because of this, lifetimes of levels with the same n but different parent can vary strongly.

In conclusion, the present work treats three sets of population groups for the recombined ion :

(i) Metastable levels, indexed by $\rho$ and representing LS terms.

(ii) Low levels, indexed by i,j,... representing LS terms. This population group includes relevant metastables and spans transitions which substantially contribute to radiated power. This includes all terms within the lowest few quantum shells. For example, in $Be^{+0}$, the 20 LS resolved terms within $2 \leq n \leq 4$ constitute the low level set. A complete list of all the low levels included for the ions of Be, C and O is given in Appendix A.3.

(iii) Bundle-n S levels, classified according to the parent metastable upon which they are built and also by spin system. These levels are denoted by the notation $X^{+z}(\ (\gamma)\ ^{(2S+1)}n)$.

High precision energies and atomic data matters only for the populations of groups (i) and (ii), and in the quasi-static approximation, time dependence matters only for the populations of (i).

**(c) Types of calculation**

The above classification allows three separate types of calculation to be developed in which the levels of bundling are varied or merged:

(1) Parent resolved bundle-n S → lowest spin system n shell.

This is a calculation of bundle n populations which are built upon a particular parent, and distinguished by spin system. The ground state of this calculation is assigned an effective quantum number which is consistent with the appropriate metastable. This calculation spans up to 500 n-shells and will enable derivation of metastable resolved collisional-radiative ionisation and recombination coefficients. This work involved a significant development of the single parent/ground state bundle-n model of Burgess and Summers (1976).

(2) Low LS resolved → metastable states.

This is a conventional population calculation for resolved low levels within a fixed range of n-shells (typically 2 or 3). This will enable derivation of low level populations (including effective contributions) and collisional cross coupling coefficients between each metastable.

(3) Projection of influence of high n-shells onto low level set.

The high level bundle-n S calculation is merged with the low-level resolved calculation.

The initial work of this thesis was concerned with developing models (1) and (2) independently. Both models function separately as self-contained calculations. The development of the projection model was a main objective of this work. This procedure improves the accuracy of both the bundle-n S and low level calculations. Low level populations are corrected for excitation to high levels and stepwise ionisation, and for recombination and cascade from high n-shells. The collisional radiative coefficients from the bundle-n S calculation are improved by inclusion of accurate energies and collisional data for resolved levels within the lowest n-shells.

It is appropriate at this stage to mention a few features and limitations of the present work.

A distinction is made between doubly excited states formed by excitation from an excited parent and doubly excited states formed by resonance capture. For example, the configuration $2s2p^2\ ^4P$ is metastable to decay but it is singly excited with respect to the $2s^22p\ ^2P$ ground term. States of the form $(2s2p\ ^3P)$ nl $^4L$ are doubly excited with respect to the ground state but singly excited with respect to the metastable. These states are thus considered as singly excited.

The population models do not consider any collisional redistribution of doubly excited states formed by resonance capture. Following Jacobs and Davis (1978) and Summers et al (1987), it is considered that at electron densities sufficient for collisional redistribution of the doubly excited state to be efficient, that any enhancement of dielectronic recombination will be offset by collisional ionisation of the excited state.

An investigation is undertaken however of the influence of field enhanced dielectronic recombination in a collisional radiative model. This was motivated by the recent study of Reisenfeld (1992). The results of this work indicated that field enhanced dielectronic recombination rate coefficients for $C^{+1}$, $C^{+2}$ and $C^{+3}$ are up to a factor of 10 greater than those at zero field. When these were used as input to a collisional-radiative model, only $C^{+3}$ was found to exhibit an increase in the effective recombination coefficient, with an enhancement of ~ 3 at a plasma density of $n_H = 10^9$ cm$^{-3}$. However, Reisenfeld calculated the field enhanced dielectronic recombination rate coefficients using very approximate procedures. Badnell et al (1993) argue that this leads to an overestimation of the rate coefficients, based upon the results of their more refined calculations. To investigate this process, the quantal calculations of field enhanced dielectronic recombination rate coefficients for $C^{+3}$ of Badnell et al (1993) were made available for inclusion in the collisional radiative studies of the present work.

The calculation of radiated power coefficients naturally falls into two parts, reflecting the origins of the radiation. Normally the dominant contribution is from line radiation from within the low level group. This is calculated from the low level populations in either the low level calculation or the projection calculation. Radiation from radiative recombination, dielectronic stabilisation and cascade arises from recombination to a large number of n-shells. The contributions from these processes are derived from the bundle-n S model. It is also convenient to calculate the bremsstrahlung radiation at this point. The radiation from these processes is most important for hydrogen- and helium-like ions for

which the bundle-n S model should be an adequate representation.

The bundle-n S model explicitly includes autoionisation transition probabilities in the equations of statistical balance. This model considers population structures of the form $X^{+z}(\gamma,^{(2S+1)}n)$ where $X^{+z1}(\gamma)$ is a significant recombining parent. This enables autoionisation reactions to be followed. This is relevant to:

(i) Secondary autoionisation following recombination from excited parents. For example,

$$X^{+z1}\ 2s2p\ ^3P + e^- \rightarrow X^{+z}(2s2p\ ^3P)\ ^4n \rightarrow X^{+z1}\ 2s^2\ ^1S + e^- + e^-$$

Effectively only electrons captured below the secondary autoionisation threshold contribute to the recombination process. This process is responsible for the parent cross coupling coefficient.

(ii) Inner-shell excitation/autoionisation (E-A). For example,

$$X^{+z}\ 1s^22p\ ^2S + e^- \rightarrow X^{+z}(1s2s\ ^3S)\ ^2n + e^- \rightarrow X^{+z1}\ 1s^2\ ^1S + e^- + e^-$$

$$X^{+z}\ 2s^22p\ ^2P + e^- \rightarrow X^{+z}(2s2p\ ^3P)\ ^2n + e^- \rightarrow X^{+z1}\ 2s^2\ ^1S + e^-$$

This can be a substantial alternative path to direct ionisation.

(iii) Autoionisation of outer electrons singly excited from excited metastables. For example,

$$X^{+z}(2s2p^2\ ^4P) + e^- \rightarrow X^{+z}(2s2p\ ^3P)\ ^4n + e^- \rightarrow X^{+z1}\ 2s^2\ ^1S + e^- + e^-$$

The consequences of (i) are easily evaluated and present no difficulty. To evaluate the parent cross coupling coefficients accurately it is necessary to include the recombination rate coefficients into levels above the autoionisation threshold in the equations of statistical balance.

The evaluation of the ionisation contributions is more complicated. The bundle-n S model only considers population structures built upon significant recombining parents. For example in the B-Be like calculation, recombination from $2s^2\ ^1S$ and $2s2p\ ^3P$ only are considered. The excitation pathways to $2s2p\ ^1P$ are thus not evaluated. Also, the bundle n-S model is not a very good representation of the term structures and energies of the

low lying autoionising levels. Moores and Reid (1989) and Reid et al (1991) have considered the E-A processes for Ne- and Na- like ions. It was shown that E-A enhancement results largely from excitation to a few intermediate states which have large excitation cross sections and also large probabilities for Auger decay. It was also shown that it is necessary to carry out detailed calculations of excitation cross sections and branching ratios for each intermediate state since the contributions of these few levels could be missed if averaging techniques are used.

For these reasons the bundle-n S model is not used to calculate rate coefficients for inner shell E-A processes. For H-like, He-like and Be-like ions there are no significant E-A channels. For Li-like ions, several authors have provided accurate estimates of the E-A cross sections for 1s inner shell electrons. These are treated as a correction to the direct ionisation cross section. The justification for this is that the autoionisation process is so fast that it is not disturbed by electron collisions for plasmas with typical tokamak densities. For the more complex B-, C-, N- and O-like sequences the strategy adopted was to adjust the direct ionisation cross sections to account for EA. This is done by adopting the method of Burgess et al (1977) and Burgess and Chidichimo (1983).

A systematic and complete study of the influence of charge transfer reactions is not presented. This is mainly due to the lack of comprehensive data for low energy state selective charge transfer cross sections to partially ionised species. Although it would have been feasible to study some specific cases, it is not yet possible to treat this process in sufficient detail to match the completeness of the metastable resolved treatment of free electron recombination. However, most of the models have been developed so that charge transfer can be included in a fully consistent way and a future study of this process will proceed when data becomes available. A limited study is presented of the influence of charge transfer on the transient and equilibrium ionisation balance of beryllium. The data sources for this study are described in Section 3.2.

There is also a lack of high quality collision cross sections for electron impact excitation of some neutral atoms. For neutral beryllium comprehensive 12 and 20 state R matrix calculations were recently completed (Fon et al 1992). For neutral carbon however, there appears to be no satisfactory data available and for neutral oxygen there is only a

limited amount (Laher and Gilmore 1990, Itikawa and Ichimura 1990). To obtain complete data sets for these atoms, cross sections were calculated in the Born approximation. This data is only of intermediate quality and will provide at least a tentative estimation of radiated power and resonance line intensities. However, spin changing transitions due to exchange are not considered and this seriously limits the study of metastable effects in neutral carbon and oxygen. Again, high quality data can easily be incorporated into the models when available and work is in progress on filling this gap.

# CHAPTER 3

# FUNDAMENTAL ATOMIC DATA

# 3.1: INTRODUCTION

This chapter examines the fundamental atomic data which was required as input to the population models. A principle of this thesis was to make use of and be guided by the best available fundamental data from the general literature. Such data exists for zero density dielectronic recombination rate coefficients, direct ionisation cross sections, autoionisation transition probabilities and excitation cross sections and radiative transition probabilities for transitions between resolved low levels. However, for many ions there is no precise data, yet completeness is necessary for the models. In these cases data was generated from either our own ab initio calculations or from semi-empirical formulae. The former 'data fill-in' operation was possible at JET because of the availability of several major atomic physics computational packages. These include the atomic structure code *Superstructure*, developed by Eissner et al (1974) at University College, London, its extension *Autostructure* (Badnell 1986) and the suite of codes developed by Cowan (1981).

*Superstructure* is a general purpose multi configuration atomic structure code which can be used for calculation of term energies, intermediate coupling energy levels, term-coupling coefficients and allowed and forbidden radiative transition probabilities. The one electron radial functions are calculated in scaled Thomas-Fermi-Dirac potential. Wave functions are generated from multi-configuration type expansions. Relativistic corrections are in the Breit-Pauli approximation. The scaling factors of the potentials are l-dependent and can be optimised so that chosen sums of the energies of terms included in the calculation are mimimised.

The *Autostructure* code (Badnell 1986) is an extension of *Superstructure* which includes continuum orbitals. Autoionisation transition probabilities are calculated in first order perturbation theory. This allows derivation of dielectronic recombination rate coefficients. Also, there is an option to use a model potential based on Slater-type orbitals.

The Cowan codes are based upon a multi-configuration Hartree-Fock atomic structure code with a statistical exchange term. The radial Slater integrals can be adjusted to account empirically for omitted

electron-correlation effects with outer shells. The wave functions can be used to calculate cross sections and collision strengths for electron collisions but only in plane-wave Born approximation.

*Superstructure* and *Autostructure* were used to supplement the available specialist calculations of radiative and autoionisation transition probabilities. The Cowan code was used to generate Born collision strengths to supplement the available collision data.

# 3.2: TRANSITIONS BETWEEN BOUND STATES

3.2.1: The Low Level Resolved Model
3.2.2: The Bundle-n S Model

## 3.2.1: The Low-Level Resolved Model

A complete list of all the relevant low levels is given in Appendix A3. Radiative transition probabilities and collisional rate coefficients for transitions between these levels were taken from critically assessed data sets which form part of the *Atomic Data and Analysis Structure* implemented at JET (Summers 1993) This data has been compiled and processed by a variety of workers for use in many atomic physics studies. The primary source of data was results from fundamental calculations available in the general literature. For electron collision cross sections, there are many computational methods, as reviewed by Henry (1981). The methods used in the present work are briefly summarised in increasing order of accuracy below:

*Impact Parameter:* This is a semi-classical approximation which treats the motion of the incident electron classically and the electron-ion interaction quantum mechanically (Burgess 1964, Burgess and Summers 1975). It allows calculation of dipole transitions only but makes allowance for strong coupling. Impact parameter cross sections have correct high energy behaviour and give properly finite cross section at threshold for positive ions.

*Born-approximation:* The influence of the atomic field on the incident electron is neglected in evaluating its approximate wave function. The incident electron wave function is therefore simply a plane wave. This assumes that the incident electron does not penetrate the target and is only valid for distant encounters and high energies. Errors are typically a factor of two or more at low energy, but smaller at high energy. It treats non-dipole transitions but excludes spin change transitions.

*Coulomb-Born:* The incident electron wave function is evaluated in the Coulomb potential of the target ion. This approximation has been widely used by many authors. Errors are still large, ≤50%, but are smaller at high energy. Electron exchange can be incorporated.

*Distorted Wave:* This is a comprehensive method for complex ions. A substantial data base of collision strengths has been established. This takes into account distortion of the Coulomb field experienced by the incident electron. Electron exchange can be incorporated.

*Close Coupling Approximations:* With the exception of the impact parameter approximation, all of the above approximations assume that the coupling between the initial and final states is weak and that coupling to other states is weak. These approximations effectively reduce to the solution of a single integro-differential equation. In a close coupling approximation, it is assumed that there is strong coupling between a closed group of low levels. The N+1 electron wave function is expanded in terms of N-electron target wave functions. Several computer codes have been developed to solve the resultant set of coupled integro-differential equations (see Henry 1981). The IMPACT code developed by Seaton and colleagues (Eissner and Seaton 1972) at University College London uses a linear algebraic method. A non-iterative integral equation method (NIEM) has been developed by Henry and colleagues (Smith and Henry 1973). The R-Matrix code of Burke and coworkers (1973) has been developed at Queen's University Belfast and is based upon the R-matrix method of nuclear physics. All of these codes incorporate a proper treatment of resonances and are good for non-dipole and spin changing transitions.

It is important to consider two points when compiling data. Firstly, to determine the coupling between metastable states it is essential to include spin changing transitions. The most important transitions are those directly excited from the ground or metastable states. The effective cross coupling coefficients will have contributions from direct transitions between the ground and metastables and then indirect contributions arising from spin changing excitation to normal excited states followed by radiative decay. Spin changing collisional transitions directly between excited states is not normally a very important process. Secondly, visible spectroscopy of near neutrals is important in edge

plasma interpretation. It is thus necessary to include data for excitations to n=3 or 4 and $\Delta n=0$, $\Delta n=\pm 1$ redistributing collisions within the excited states. Dipole transitions are not necessarily dominant for $\Delta n \geq 1$ excitations and so non-dipole excitations must also be included. Spin changing redistributing collisions can be neglected without loss of accuracy.

In almost all cases, high quality data was available for the most important transitions (e.g. spin changing transitions and resonance excitations within the ground complex, and for $\Delta n=1$ excitations) but not for a complete set of transitions ( e.g. excitations to higher quantum shells and for redistributing collisions within the excited states). In these instances, intermediate quality data was generated. The adopted method was to use the atomic structure code and plane-wave Born collision strengths of Cowan (1981). This procedure is set up for semi-automatic execution at JET so that collision strengths can be calculated for arbitrary ions. Cowan considers that the collision strengths will be most accurate for neutral or weakly ionised atoms and for large values of incident energy and claims that they typically agree with distorted wave and close-coupling values to within 25 or 50% even for threshold parameter values as small as 3 or 4. Exchange effects are not included so that spin changing transitions are not calculable. The collision strengths for the redistributing, $\Delta n=0$, collisions calculated in this way should be reasonably accurate because of the low transition energies. Collision strengths for $\Delta n \geq 1$ excitations will be less reliable at typical incident electron energies.

The collision cross sections are used to prepare Maxwell averaged rate coefficients. This was done by mapping the the ratio of the source cross section to an approximate form as a function of energy. A scaled energy variable is used so that the entire energy range is mapped onto the interval [0,1]. The various types of transition - dipole, non-dipole and spin change - each have well defined behaviour at threshold and at high energy. The approximate forms for each transition are as described by Gordon et al (1982). The advantages of this method are that (i) the ratio remains close to unity and is easier to interpolate or extrapolate than the cross section data itself so that rate coefficients can be formed for extended temperature regimes, and (ii) it is easy to spot errors in the original data and to assess the behaviour of cross sections.

A brief review of the various data sources is now given. Due

acknowledgement is given to the workers who compiled and processed this data by listing their initials after each ion. Namely

| | |
|---|---|
| HPS | Prof. H.P. Summers |
| JL | Dr. J. Lang, Rutherford Appleton Laboratory |
| PMcW | Dr. R.W.P. McWhirter, formerly Rutherford Appleton Laboratory |
| MoM | Martin o' Mullane, Cork University/Culham Laboratory |
| WJD | Self |

**(a) H-like ions**

Radiative transition probabilities were taken from Wiese et al (1966). The collision data is taken from Z-scaled hydrogenic collision strengths of Clark et al (1982). These were calculated using the Coulomb-Born-Oppenheimer approximation in the limit of infinite Z. This data is for all transitions of the type nl $\rightarrow$ n'l' with n,n' $\leq$ 5 and $\Delta n \geq 1$. The authors consider the data to be suitable for $Z \geq 3$. (HPS,WJD,MOM)

**(b) He-like ions**

$Be^{+2}$: Energy levels are taken from Bashkin and Stoner (1978). Transition probabilities for levels within the n=1,2 complex are from Lin et al (1982). All other transition probabilities were calculated by Superstructure calculations. Electron impact excitation rate coefficients for levels within n=1,2 and for transitions between n=1,2 and n=3,4,5 are taken from Sampson et al (1983). Rate coefficients for dipole allowed transitions within n=3,4,5 were calculated in the Impact Parameter approximation. (HPS)

$C^{+4}$: Energy levels are taken from Kelly (1985). Transition probabilities and excitation rate coefficients are taken from the 11-state R-matrix calculations of Tayal (1986). Transition probabilities for the forbidden transitions (2-1,3-1,4-1) are taken from Gabriel and Jordan (1972). (JL,HPS).

$O^{+6}$: Energy levels are taken from Kelly (1985). Transition probabilities are taken from Kingston and Tayal (1983) and Gabriel and Jordan (1972). The collision data for transitions from levels 1,2 to levels 1-11 are taken from the 11 state R-matrix calculation of Tayal and Kingston (1984). The data for other transitions is taken from the calculations of distorted wave calculations of Pradhan et al (1981) and the Coulomb Born Exchange calculations of Sampson et al (1983) and

Sampson and Parks (1974). (JL, HPS)

**(c) Li-like ions**

$Be^{+1}$: Energy levels are taken from Bashkin and Stoner (1978) and transition probabilities from Wiese et al (1966). The collision data was calculated in the distorted wave approximation by Summers et al (1992) using the codes developed at University College London (Eissner and Seaton 1972). In Figure 3.2.1 a comparison is made between gamma parameters derived from the distorted wave collision strengths and those derived from plane wave Born collision strengths calculated with Cowan's code. It can be seen that the Born results are unreliable at low temperature (differing from between 10% - 100%) but are in reasonable agreement for all transitions at high temperature. For the $\Delta n=0$ 4f-4d transition the Born and distorted wave results are in good agreement over the entire temperatures range. The small systematic difference (~10 - 20%) is attributed to differences in atomic structure between *Superstructure* and Cowan's code. (HPS, WJD)

$C^{+3}$: The data for n=2,3 is taken from the review of Cochrane and McWhirter (1983). This presented a critical compilation of close coupling and distorted wave calculations. Data for transitions involving n=4 were calculated in the plane wave Born approximation using Cowan's codes. (HPS, WJD, MOM)

$O^{+3}$: The collision data and radiative transition probabilities for transitions within n=2 and from n=2 - n=3,4,5 were taken from the relativistic distorted wave calculations of Zhang et al (1990). Transitions within n=3,4,5 were calculated in the plane wave Born approximation using Cowan's codes. (HPS,WJD,MOM)

**(d) Be-like ions**

$Be^{+0}$: Energy levels are taken from Bashkin and Stoner (1978) and transition probabilities from a number of sources including Wiese et al (1966), Weiss (1972), Fawcett (1984) and Cohen and McEachran (1979). The collision data for transitions within n=2 and from n=2 to n=3,4 is taken from the 12 and 20 state R-matrix calculations of Fon et al (1991). Data for transitions within n=3,4 is taken from effective potential Born calculations of Summers et al (1992). (HPS, WJD)

$C^{+2}$: Energy levels are taken from Kelly (1985). Transition probabilities for allowed transitions are from Fawcett (1984), and

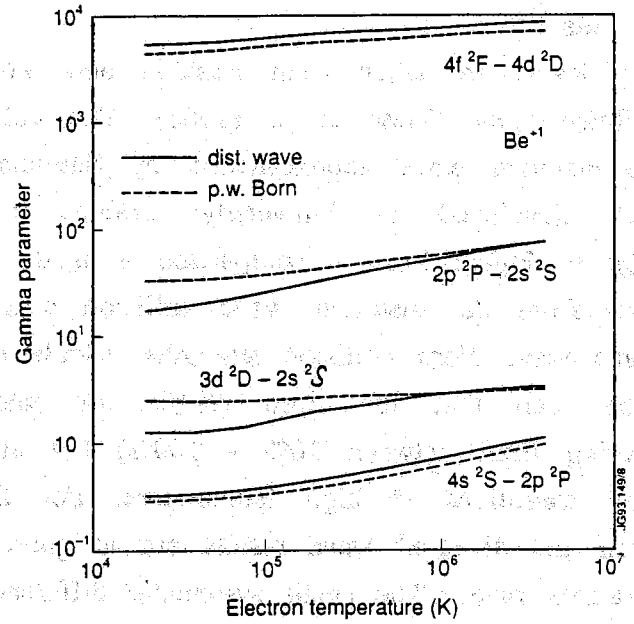


**Figure 3.2.1:** Gamma parameters for electron impact excitation of $Be^{+1}$. The distorted wave data is from calculations of Summers et al (1992) using the University College, London codes. The plane wave Born data was calculated using Cowan's code.

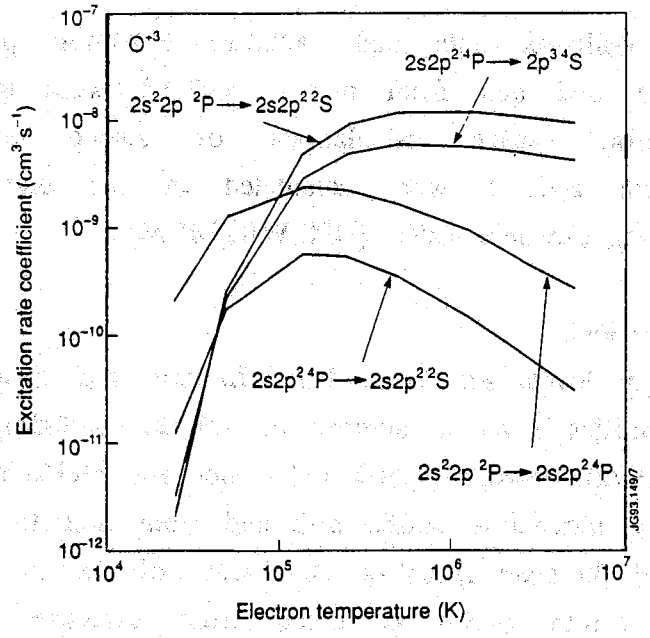


**Figure 3.2.2:** Electron impact excitation rate coefficients for $O^{+3}$. These are taken from the close coupling calculations of Hayes (1983).

forbidden transitions are from Nussbaumer and Storey (1978). The electron impact excitation rate coefficients are from the 12 state R-matrix calculations of Berrington (1985) and Berrington et al (1989). (JL,HPS)

$O^{+4}$: Energy levels are taken from Kelly (1985). Transition probabilities were taken from Hibbert (1980) and Nussbaumer and Storey (1979). The collision data for collisions within n=2 is from the R-matrix calculations of Berrington et al (1979, 1985). For n=2-3 transitions the close coupling data of Widing et al (1982) and Tayal et al (1982) are used. For collisions within n=3, collision strengths were calculated in the impact parameter approximation. (JL,HPS,WJD)

**(e) B-like ions**

$C^{+1}$: Energy levels are taken from Moore (1970). Transition probabilities are from Nussbaumer and Storey (1981), Lennon et al (1985) and Weise et al (1966). These were supplemented by Superstructure calculations. The collisional data for transitions within n=2 are from close coupling calculations of Hayes and Nussbaumer (1984) and Robb (Magee et al 1977). Data for n=2-3 and n=3-3 transitions are calculated in an effective potential Born approximation (Behringer et al 1989). (JL,HPS)

$O^{+3}$: Energy levels are taken from Edlen (1983). Transition probabilities are from Saraph (1980). Data for collisions from terms $2s^2 2p\ ^2P$ and $2s2p^2\ ^4P$ to all other terms in the configurations $2s2p^2$ and $2p^3$ are from the close coupling calculations of Hayes (1983). Figure 3.2.2 illustrates some excitation rate coefficients for this ion. The spin changing transitions decrease with energy more strongly than allowed transitions (see Section 2.1, *Atomic Processes*). Data for transitions within $2s2p^2\ ^2P$, $^2D$ and $^2S$ are from Merts et al (1980). Collision strengths for all transition involving the configurations $2s^2 3l$ and 2s2p3l were calculated in the plane wave Born approximation using Cowan's codes. (JL, HPS, WJD, MOM)

**(f) C-like ions**

$C^{+0}$: Energy levels were taken from Moore (1970) and transition probabilities from Wiese et al (1966). There have been no specific high quality calculations of collision data for this ion. Data was taken from the plane wave Born collision strengths generated by the Cowan code. WJD, MOM).

$O^{+2}$: Energy levels are taken from Edlen (1985). Transition

probabilities are taken from Fischer and Saha (1985) and Bhatia et al (1979). The collision data for transitions between the configurations $2s^22p^2$, $2s2p^2$ and $2p^4$ is taken from the 12 state close coupling R-matrix calculations of Aggarwal (1983, 1985, 1986) and the calculations of Bhatia et al (1979). Collision data for all transitions involving the $2s^22p3l$ configurations were calculated in the plane wave Born approximation using Cowan's codes. (JL, HPS, WJD, MOM)

**(g) N-like ions**

$O^{+1}$: Energy levels are taken from Moore (1970). Transition probabilities are from Ho and Henry (1983), Westhaus and Sinanoglu (1969), Luken and Sinanoglu (1976) and Weise et al (1966). These were supplemented by some Superstructure calculations. Collision data for transitions 1-4 and 1-8 are from the close coupling calculations of Ho and Henry (as above). For transitions within the $2s^22p^3$ configuration, the collision data is from the close coupling calculations of Phadhan (1976). All other allowed transitions are calculated in the Born approximation (Behringer et al 1989). (JL,HPS)

**(h) O-like ions**

$O^{+0}$: Energy levels and transition probabilities were taken from Wiese et al (1966). There is a limited amount of collision data available for this ion. This was reviewed by Laher and Gilmore (1990) and Itikawa and Ichimura (1990). The recommendations of Laher and Gilmore are preferred, which are based upon compilations of experimentally measured cross sections. This consists of data for excitations from the $2s^22p^4\ ^3P$ ground state, including excitations to the $2s^22p^4\ ^1D$, $2s^22p^4\ ^1S$ and $2s2p^33s\ ^5S$ metastables. Collision data for other transitions were were calculated in the plane wave Born approximation using the Cowan's codes. (WJD, MOM)

### 3.2.2: The Bundle-n S model

Radiative transition probabilities for spontaneous emission and rate coefficients for electron impact excitation and de-excitation were calculated by the procedures described by Burgess and Summers (1976) and Spence and Summers (1986). For completeness, the methods are summarised here.

**(a) Radiative Transition Probabilities**

Radiative transition probabilities between principal quantum shells are due to dipole transitions and are evaluated from

$$A_{ij} = \frac{16\alpha^4 c}{3\sqrt{3}\,\pi a_0} \frac{z1^4}{\omega(z,j)} \frac{g^I(i,j)}{\nu(j)\nu(i)[\nu^2(j) - \nu^2(i)]} \qquad \text{E(3.2.1)}$$

where $A_{ij}$ is the transition probability for a transition j→i
$\nu(i)$ is the effective quantum number of level i
$g^I$ is the bound-bound Gaunt factor

and the other symbols have their usual meaning. An expression for the hydrogenic bound-bound Gaunt factor can be found in Burgess and Summers (1976).

**(b) Electron Impact Excitation and De-excitation**

Following Spence and Summers (1986), bundled cross sections and rate coefficients are taken from the combined treatment of Percival and Richards (1978). This is based upon the classical and semi-classical theories of Percival and Richards (1975) and Percival (1973). The rate coefficients are provided as an explicit functional fit in terms of initial shell n, final shell n', (z+1) and energy E. Note that the Percival-Richards formulae break down for n<5, displaying incorrect functional form if n' is large. Spence and Summers traced this to an approximation made for the first Bethe coefficient, and proposed adjustments which yield the correct functional form for all n,n'. This formulation is adopted.

# 3.3: IONISATION AND AUTOIONISATION PROCESSES


3.3.1: Direct Ionisation and Excitation-Autoionisation from ground and Metastable Configurations
3.3.2: Direct Ionisation from Excited States
3.3.3: Autoionisation From Excited States


## 3.3.1: Direct ionisation and Excitation-Autoionisation From Ground and Metastable Configurations

In recent years, electron impact ionisation has received considerable attention in the general literature. Burgess et al (1977) reviewed various theoretical techniques for the calculation of ionisation cross sections by comparison with available experimental measurements. It was clear that there is much better agreement between experiment and theory when autoionisation contributions are included. Bell et al (1983) published a recommended list of cross sections for all ions of the elements hydrogen through oxygen. These recommendations are based upon a critical review of experimental measurements and theoretical calculations and served as an excellent source of preferred data. Similarly, in their evaluation of ionisation balance, Arnaud and Rothenflug (1985) also reviewed the ionisation cross sections of these ions. The recommendations of Bell et al and Arnaud and Rothenflug were compared by Kato et al (1991) and were found to be very similar. Unfortunately these works only considered composite ionisation cross sections for ground state ions with no resolution of final state. The present work requires resolution of the normal stage to stage ionisation cross section into initial metastable and final parent states. Account must be taken of both direct ionisation and excitation-autoionisation processes.

The total cross section for a given configuration, $\rho$, is written as a sum over subshells as

$$\sigma(\rho) = \Sigma_j \zeta_j \sigma_j^{eff}(I_j) \qquad E(3.3.1)$$

where $I_j$ is the ionisation potential of shell j, $\sigma^{eff}$ is the effective ionisation cross section (comprising direct and excitation- autoionisation

contributions) and $\zeta_j$ is the number of electrons in subshell j. E(3.3.1) assumes that the autoionisation contribution can be added onto the direct ionisation cross sections as a zero density correction. This is reasonable because the autoionisation transition probabilities are large ($\sim 10^{13}$ $s^{-1}$) so that autoionisation processes will not be disturbed by electron collisions at tokamak densities. This assumption will be tested by the bundle-n S population model which has the capability to resolve excitation- autoionisation contributions.

Two types of inner-shell excitation- autoionisation were identified by Burgess et al (1977): (i) the lowest autoionising configuration accessible by inner shell excitation lies well above the outer shell ionisation threshold (e.g. $C^{+3}$ $1s^22s \rightarrow 1s2s^2$); and (ii) those in which it is well below (e.g. $C^+$ $2s^22p \rightarrow 2s2p^2$). Case (i) leads to a series of large distinct jumps in the total cross section well above threshold. In case (ii) ions there are many autoionising states near the outer electron ionisation threshold. These quasi-bound states effectively form a continuum.

It was suggested by Burgess et al (1977) that direct ionisation cross sections could be adjusted to account for excitation- autoionisation by lowering the ionisation potential of the inner shell electron to that of the first autoionising level. For case (i) ions this gives a reduced ionisation threshold. For case (ii) ions, the effective ionisation threshold is that of the outer electron. Chidichimo (1982) confirmed this procedure by performing explicit calculations for $N^{+2}$ using the Coulomb-Born and distorted wave approximations. This method gives an effective total cross section which accounts for direct and autoionisation processes. The magnitude of the autoionisation process alone can be obtained from the difference between the effective total cross section and the direct ionisation cross sections.

For the present work, information on the partial contributions from outer and inner shell direct ionisation from ground and metastable configurations were inferred from theoretical calculations of direct ionisation cross sections which were in good agreement with experimental measurements. The effects of inner shell excitation autoionisation could then be deduced as above. If no precise calculations were available, data was inferred from trends in scaled cross sections or from semi-empirical formulae. An improvement was sought in our semi-empirical formula by systematically correcting it to achieve as good a match as possible with

the available experimental data.

The scaled ionisation cross section is often referred to in the general literature. This is defined as

$$\sigma^{scale} = \sigma U I^2 \qquad E(3.3.2)$$

where U is the threshold parameter, U = E/I. This definition removes much of the energy and charge state dependence of the cross section. Classically, the scaled cross section for a given threshold parameter is constant along isoelectronic sequences. This assumption is also supported by the distorted wave calculations of Younger (1981a,b 1982). For lithium like ions, the 1s scaled cross section is constant for many ion charges. For beryllium like ions, the 2s scaled cross section for the channels

$$1s^2 2s^2\ {}^1S + e^- \rightarrow 1s^2 2s\ {}^2S + e^- + e^-$$
$$1s^2 2s2p\ {}^3P + e^- \rightarrow 1s^2 2p\ {}^2P + e^- + e^-$$

are approximately equal for a given threshold parameter and are both slowly varying along the isoelectronic sequence. This calculation considered ions from $C^{+2}$ - $Ar^{+14}$. Also for ionisation from the configurations $1s^2 2s^2 2p^n$, $0 \le n \le 6$ for the ions $Fe^{+22}$ - $Fe^{+16}$ the scaled 2s cross sections are constant and the total scaled 2p cross sections varied linearly with the number of 2p electrons. Such scaling laws are not expected to be as precise for ions of low charge state.

Several general ionisation formulae are available. These include the semi-empirical formula (SEF) of Seaton (1964), the Exchange Classical Impact Parameter approximation (Burgess 1964), the Lotz formula (1967) and that of Burgess and Chidichimo (1983). The last named is preferred in this work because it is more readily optimised. This represents ionisation cross sections by the semi-empirical formula:

$$\frac{\sigma_{em}(j,E)}{\pi a_o^2} = C \cdot \zeta_j (I_H/I_j)^2 \cdot (I_j/E) \cdot \ln(E/I_j) \cdot W(E/I_j) \qquad E(3.3.3)$$

where $I_j$ is the effective ionisation potential of subshell j and $I_H$ is the ionisation potential of hydrogen. The parameter C is an optimisation parameter which is chosen to get best agreement with experimental data. After detailed comparison with a wide range of cross beam experimental data for ions of charge $z \ge 2$, Burgess and Chidichimo recommended two values of C, depending on whether on not adjustment is made for autoionisation. Firstly, with no adjustment, the recommended value is C = 2.7. Secondly, if autoionisation is accounted for by reducing the

ionisation threshold of the inner shell electrons to that of the first autoionising level, the value of C = 2.3 was recommended. In the latter case, a much better fit was obtained between experimental data and empirical formula. The function $W(E/I_j)$ is designed to correct behaviour near threshold and is given as

$$W(E/I_j) = \begin{cases} 0 & E \le I_j \\ \ln(E/I_j)\,\beta I_j/E & E > I_j \end{cases} \qquad \text{E(3.3.4)}$$

with

$$\beta = 1/4 \left\{ \left[ (100z + 91)/(4z + 3) \right]^{1/2} - 5 \right\} \qquad \text{E(3.3.5)}$$

For specific cases, the accuracy of this formula can be improved by specifying more accurate values for the optimisation parameter C. In particular, some allowance for energy dependence of C would be an improvement.

The empirical formula was used in the following manner to obtain partial metastable to metastable ionisation cross sections.

The final state proportions following the ionisation process can be determined by assigning statistical weights to the fragments. The parameter $\zeta^{eff}$ is defined as the effective number of electrons in subshell j which will ionise and leave the parent ion in configuration $\gamma$. This is given by

$$\zeta^{eff} = \zeta\, \omega_j(\rho \to \gamma) \qquad \text{E(3.3.6)}$$

where $\omega$ is an estimate of fractional parentage. For example, consider the direct ionisation of a C-like ground state ion, $1s^2 2s^2 2p^2\ ^3P$, as illustrated in Figure 3.3.1.

The outer 2p electrons ionise to $2s^2 2p\ ^2P$ with an ionisation potential of $I_1^d$. The inner-shell 2s electrons are excited in the series $(2s2p^2\ ^2D)$ nl $^3L$ and $(2s2p^2\ ^4P)$ nl $^3L$. The lowest autoionising states have excitation potentials of $I_1^a$ and $I_2^a$ respectively. The direct ionisation potentials of the $2s2p^2\ ^2D$ and $2s2p^2\ ^4P$ parents are denoted by $I_2^d$ and $I_3^d$ respectively. There is no ambiguity concerning the final state following 2p ionisation. The $2s^2 2p\ ^2P$ parent is formed with a weight of 1.00. For 2s ionisation, it is assumed that the $2s2p^2\ ^2D$ and $2s2p^2\ ^4P$ parents are formed in relative fractions of 0.33 and 0.67. This is based on parent

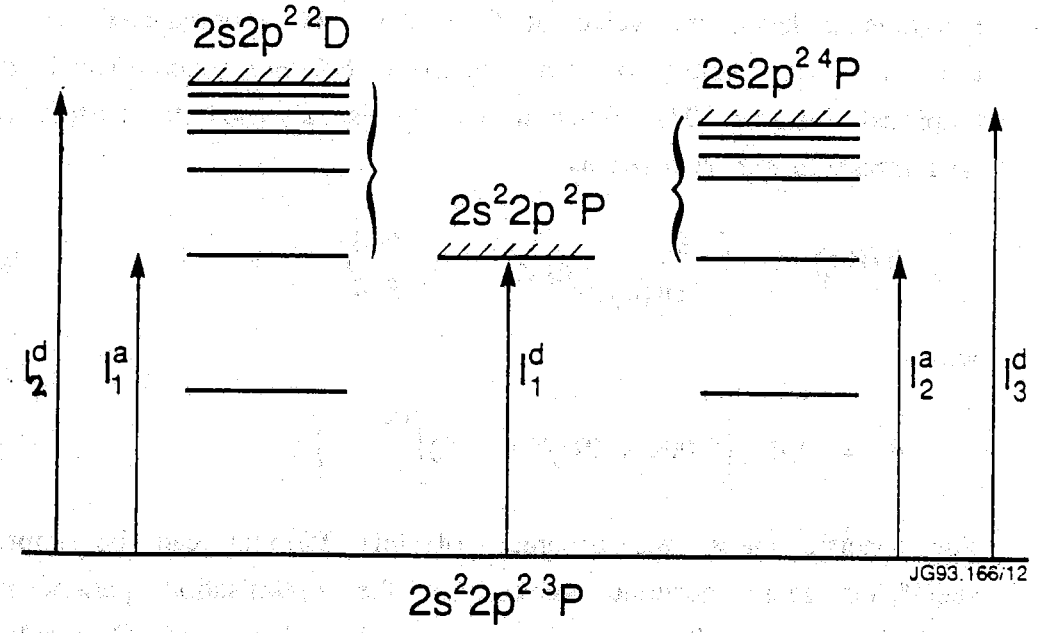


**Figure 3.3.1:** Ionisation channels from $2s^2 2p^2\ ^3P$ showing ionisation thresholds and open Auger Pathways.

spin system weights.

Following the prescription of Burgess et al (1977), the total ionisation cross sections from the ground state is then

$$\begin{aligned} \sigma(2s^2 2p^2\ ^3P) \quad = \quad & 2 \times 1.0 \times \sigma(I_1^d) \\ & + \quad 2 \times 0.33 \times \sigma(I_1^a) \\ & + \quad 2 \times 0.67 \times \sigma(I_2^a) \end{aligned}$$

The first term represents 2p direct ionisation, the second term represents 2s ionisation and excitation autoionisation towards $2s2p^2\ ^2D$, and the third term represents ionisation and excitation autoionisation towards $2s2p^2\ ^4P$.

The cross section to the $2s2p^2\ ^4P$ parent is

$$\sigma(2s^2 2p^2\ ^3P \rightarrow 2s2p^2\ ^4P) \quad = \quad 2 \times 0.67 \times \sigma(I_3^d)$$

which only has a direct ionisation contribution.

The cross section to the $2s^2 2p\ ^2P$ parent is

$$\sigma(2s^2 2p^2\ ^3P \rightarrow 2s^2 2p\ ^2P) = 2 \times 1.0 \times \sigma(I_1^d) + 2 \times 0.25 \times \sigma(I_1^a) + 2 \times 0.75 \times ( \sigma(I_2^a) - \sigma(I_3^d) )$$

The first term is the direct 2p loss. The second terms is the 2s loss to the doublet spin system. All bound states excited above $I_1^a$ autoionise to form $2s^2 2p\ ^2P$ and the $2s2p^2\ ^2D$ state is assumed to radiate to form $2s^2 2p\ ^2P$. The third term represents the autoionisation contribution following excitation towards the triplet parent.

For all ground and metastable ions of Be, C and O, a list of all relevant direct and auto- ionisation channels (indexed as (d) and (a) respectively), along with the parameters $\zeta$, $\omega$ and the ionisation potentials are given in Table 3.3.1(a)-(d). Autoionisation channels are indexed as type (i) or (ii), as described above.

The rules for determining the value of $\omega$ were as follows:

1. The relative fractions ionising into each parent spin system was entirely determined by spin system weights

$$\omega(S_i) = (2S_i+1)/\Sigma_i(2S_1+1) \qquad \text{E(3.3.7)}$$

2. When there is further resolution within a spin system, $\omega$ is determined by the statistical weight of the angular momentum quantum number

$$\omega(L_k,S_i) = (2L_k+1)/\Sigma_k(2L_k+1) \cdot \omega(S_i) \qquad \text{E(3.3.8)}$$

For ions with a partially filled 2p shell, inner shell ionisation of 2s electrons only is accounted for. The contribution from ionisation of 1s electrons was found to be small due to their high ionisation potential.

Ionisation potentials between the ground state ions were obtained from Kelly (1987). Ionisation potentials for inner-shell and metastable states were calculated by adding and subtracting term energies from the ground state ionisation potential. For example,

$$I_p(2s2p^2\ ^4P \rightarrow 2s2p\ ^3P) = I_p(2s^2 2p\ ^2P \rightarrow 2s^2\ ^1S) + \Delta E(2s^2\ ^1S \rightarrow 2s2p\ ^3P) - \Delta E(2s^2 2p\ ^2P - 2s2p^2\ ^4P) \qquad \text{E(3.3.9)}$$

Term energies were again taken from Kelly (1987). The energies were

| Sequence | Met. Index | Configuration | Channel | Type | Final Parent | Fract. Prtage | Izeta | Ionisation Potentials (eV) Be | C | O |
|---|---|---|---|---|---|---|---|---|---|---|
| H-like | 1 | $1s\ ^2S$ | | d | 1 | 1.000 | 1 | 217.720 | 489.987 | 871.417 |
| He-like | 1 | $1s^2\ ^1S$ | $1s\ ^2S$ | d | 1 | 1.000 | 2 | 153.896 | 392.090 | 739.338 |
| | 2 | $1s2s\ ^3S$ | $1s\ ^2S$ | d | 1 | 1.000 | 1 | 35.303 | 92.863 | 177.865 |
| | | | $2s\ ^2S$ | d | 1 | 1.000 | 1 | 198.660 | 460.198 | 830.905 |
| Li-like | 1 | $1s^22s\ ^2S$ | $1s^2\ ^2S$ | d | 1 | 1.000 | 1 | 18.211 | 64.494 | 138.12 |
| | | | $1s2s\ ^1S$ | d | 1 | 0.250 | 2 | 139.86 | 368.88 | 707.01 |
| | | | | a | 1 | | | 117.3(i) | 295.5(i) | 555.4(i) |
| | | | $1s2s\ ^3S$ | d | 2 | 0.750 | 2 | 136.80 | 363.45 | 699.10 |
| | | | | a | 1 | | | 117.3(i) | 295.5(i) | 555.4(i) |
| Be-like | 1 | $1s^22s^2\ ^1S$ | $1s^22s\ ^2S$ | d | 1 | 1.000 | 2 | 9.323 | 47.888 | 113.90 |
| | 2 | $1s^22s2p\ ^3P$ | $1s^22s\ ^2S$ | d | 1 | 1.000 | 1 | 6.597 | 41.389 | 103.70 |
| | | | $1s^22p\ ^2P$ | d | 1 | 1.000 | 1 | 10.556 | 49.393 | 115.70 |
| | | | | a | 1 | | | 7.88(i) | 41.39(ii) | 103.70(ii) |
| B-like | 1 | $1s^22s^22p\ ^2P$ | $1s^22s^2\ ^1S$ | d | 1 | 1.000 | 1 | - | 24.384 | 77.414 |
| | | | $1s^22s2p\ ^1P$ | d | 1 | 0.250 | 2 | - | 37.071 | 97.103 |
| | | | | a | 1 | | | - | 24.384(ii) | 77.414(ii) |
| | | | $1s^22s2p\ ^3P$ | d | 2 | 0.750 | 2 | - | 30.880 | 87.609 |
| | | | | a | 1 | | | - | 24.384(ii) | 77.414(ii) |
| | 2 | $1s^22s2p^2\ ^4P$ | $1s^22s2p\ ^3P$ | d | 2 | 1.000 | 2 | - | 25.544 | 78.727 |
| | | | | a | 1 | | | - | 19.05(ii) | 68.53(ii) |
| | | | $1s^22p^2\ ^3P$ | d | 2 | 1.000 | 1 | - | 36.090 | 95.033 |
| | | | | a | 1 | | | - | 30.00(i) | 68.53(ii) |

**Table 3.3.1(a):** Ionisation channels from ground and metastable states. 'd' denotes direct ionisation and 'a' denotes excitation-autoionisation according to Burgess and Chidichimo Type (i) or (ii).

| Sequence | Met. Index | Configuration | Channel | Type | Final Parent | Fract. Prtage | Izcta | Ionisation Potentials (eV) C | O |
|---|---|---|---|---|---|---|---|---|---|
| C-like | 1 | $1s^22s^22p^2\ ^3P$ | $1s^22s^22p\ ^2P$ | d | 1 | 1.000 | 2 | 11.260 | 54.936 |
| | | | $1s^22s2p^2\ ^2D$ | d | 1 | 0.333 | 2 | 20.551 | 70.675 |
| | | | | a | 1 | | | 13.12(i) | 55.00(ii) |
| | | $1s^22s2p^2\ ^4P$ | | d | 2 | 0.667 | 2 | 16.596 | 63.818 |
| | | | | a | 1 | | | 13.12(i) | 55.00(ii) |
| | 2 | $1s^22s^22p^2\ ^1D$ | $1s^22s^22p\ ^2P$ | d | 1 | 1.000 | 2 | 9.997 | 52.448 |
| | | | $1s^22s2p^2\ ^2D$ | d | 1 | 1.000 | 2 | 19.287 | 68.187 |
| | | | | a | 1 | | | 10.83(i) | 52.500(ii) |
| | 3 | $1s^22s^22p^2\ ^1S$ | $1s^22s^22p\ ^2P$ | d | 1 | 1.000 | | 8.576 | 49.608 |
| | | | $1s^22s2p^2\ ^2D$ | d | 1 | 1.000 | 2 | 17.867 | 65.346 |
| | | | | a | 1 | | | 9.54(i) | 49.70(ii) |
| | 4 | $1s^22s2p^3\ ^5S$ | $1s^22s2p^2\ ^4P$ | d | 2 | 1.000 | 3 | 12.414 | 56.365 |
| | | | | a | 1 | | | 8.66(i) | 46.00(i) |
| | | | $1s^22p^3\ ^4S$ | d | 2 | 1.000 | 1 | 24.687 | 76.189 |
| | | | | a | 1 | | | 21.00(i) | 56.90(i) |

**Table 3.3.1(b):** Ionisation channels from ground and metastable states.

| Sequence | Met. Index | Configuration | Channel | Type | Final Parent | Fract. Prtage | Izeta | Ionisation Potentials (eV) O |
|---|---|---|---|---|---|---|---|---|
| N-like | 1 | $1s^2 2s^2 2p^3\ ^4S$ | $1s^2 2s^2 2p^2\ ^3P$ | d | 1 | 1.000 | 3 | 35.118 |
| | | | $1s^2 2s 2p^3\ ^3D$ | d | 1 | 0.375 | 2 | 50.021 |
| | | | | a | 1 | | | 44.00(i) |
| | | | $1s^2 2s 2p^3\ ^5S$ | d | 4 | 0.625 | 2 | 42.571 |
| | | | | a | 1 | | | 36.60(i) |
| | 2 | $1s^2 2s^2 2p^3\ ^2D$ | $1s^2 2s^2 2p^2\ ^3P$ | d | 1 | 0.750 | 3 | 31.793 |
| | | | $1s^2 2s^2 2p^2\ ^1D$ | d | 2 | 0.208 | 3 | 34.280 |
| | | | | a | 1 | | | 31.79(ii) |
| | | | $1s^2 2s^2 2p^2\ ^1S$ | d | 3 | 0.042 | 3 | 37.121 |
| | | | | a | 1 | | | 31.79(ii) |
| | | | $1s^2 2s 2p^3\ ^1D$ | d | 2 | 0.156 | 2 | 54.966 |
| | | | | a | 1 | | | 49.00(i) |
| | | | $1s^2 2s 2p^3\ ^1P$ | d | 2 | 0.082 | 2 | 57.886 |
| | | | | a | 1 | | | 51.90(i) |
| | | | $1s^2 2s 2p^3\ ^1P$ | d | 3 | 0.012 | 2 | 57.886 |
| | | | | a | 1 | | | 51.90(i) |
| | | | $1s^2 2s 2p^3\ ^3D$ | d | 1 | 0.750 | 2 | 46.696 |
| | | | | a | 1 | | | 40.79(i) |
| | 3 | $1s^2 2s^2 2p^3\ ^2P$ | $1s^2 2s^2 2p^2\ ^3P$ | d | 1 | 0.750 | 3 | 31.100 |
| | | | $1s^2 2s^2 2p^2\ ^1D$ | d | 2 | 0.208 | 3 | 32.587 |
| | | | | a | 1 | | | 31.10(ii) |
| | | | $1s^2 2s^2 2p^2\ ^1S$ | d | 3 | 0.042 | 3 | 35.428 |
| | | | | a | 1 | | | 31.10(ii) |
| | | | $1s^2 2s 2p^3\ ^1D$ | d | 2 | 0.156 | 2 | 53.273 |
| | | | | a | 1 | | | 47.30(i) |
| | | | $1s^2 2s 2p^3\ ^1P$ | d | 2 | 0.082 | 2 | 56.194 |
| | | | | a | 1 | | | 50.20(i) |
| | | | $1s^2 2s 2p^3\ ^1P$ | d | 3 | 0.012 | 2 | 56.194 |
| | | | | a | 1 | | | 50.20(i) |
| | | | $1s^2 2s 2p^3\ ^3D$ | d | 1 | 0.750 | 2 | 45.003 |
| | | | | a | 1 | | | 39.00(i) |

**Table 3.3.1(c):** Ionisation channels from ground and metastable states.

| Sequence | Met. Index | Configuration | Channel | Type | Final Parent | Fract. Ptage | Izcta | Ionisation Potentials (eV) O |
|---|---|---|---|---|---|---|---|---|
| O-like | 1 | $1s^22s^22p^4\ ^3P$ | $1s^22s^22p^3\ ^4S$ | d | 1 | 0.667 | 4 | 13.618 |
| | | | $1s^22s^22p^3\ ^2D$ | d | 2 | 0.208 | 4 | 16.943 |
| | | | | a | 1 | | | 14.06(i) |
| | | | $1s^22s^22p^3\ ^2P$ | d | 3 | 0.125 | 4 | 18.635 |
| | | | | a | 1 | | | 14.11(i) |
| | | | $1s^22s2p^4\ ^4P$ | d | 1 | 0.667 | 2 | 28.488 |
| | | | | a | 1 | | | 15.65(i) |
| | | | $1s^22s2p^4\ ^2D$ | d | 2 | 0.300 | 2 | 34.198 |
| | | | | a | 1 | | | 23.00(i) |
| | | | $1s^22s2p^4\ ^2D$ | d | 3 | 0.030 | 2 | 34.198 |
| | | | | a | 1 | | | 23.00(i) |
| | 2 | $1s^22s^22p^4\ ^1D$ | $1s^22s^22p^3\ ^2D$ | d | 2 | 0.625 | 4 | 14.966 |
| | | | | a | 1 | | | 12.10(i) |
| | | | $1s^22s^22p^3\ ^2P$ | d | 3 | 0.375 | 4 | 16.658 |
| | | | | a | 1 | | | 12.15(i) |
| | | | $1s^22s2p^4\ ^2D$ | d | 2 | 0.910 | 2 | 32.211 |
| | | | | a | 1 | | | 21.00(i) |
| | | | $1s^22s2p^4\ ^2D$ | d | 3 | 0.090 | 2 | 32.211 |
| | | | | a | 1 | | | 21.00(i) |
| | 3 | $1s^22s^22p^4\ ^1S$ | $1s^22s^22p^3\ ^2D$ | d | 2 | 0.625 | 4 | 12.743 |
| | | | | a | 1 | | | 9.88(i) |
| | | | $1s^22s^22p^3\ ^2P$ | d | 3 | 0.375 | 4 | 14.436 |
| | | | | a | 1 | | | 9.93(i) |
| | | | $1s^22s2p^4\ ^2D$ | d | 2 | 0.910 | 2 | 29.999 |
| | | | | a | 1 | | | 19.00(i) |
| | | | $1s^22s2p^4\ ^2D$ | d | 3 | 0.090 | 2 | 29.999 |
| | | | | a | 1 | | | 19.00(i) |
| | 4 | $1s^22s^22p^33s\ ^5S$ | $1s^22s^22p^3\ ^4S$ | d | 1 | 1.000 | 1 | 4.472 |
| | | | $1s^22s^22p^23s\ ^4S$ | d | 1 | 1.000 | 4 | 27.451 |
| | | | $1s^22s2p^33s\ ^4S$ | d | 1 | 1.000 | 1 | 36.086 |

**Table 3.3.1(d):** Ionisation channels from ground and metastable states.

weighted over sublevels belonging to the same term,

$$E_{LS} = (\Sigma_J(2J+1))^{-1} . \Sigma_J(2J+1)E_{LSJ} \qquad E(3.3.10)$$

Energies of the lowest autoionising levels were obtained from external sources (e.g. Moore 1971, or Kelly 1987), or calculated by the atomic structure code *Superstructure.*

The ionisation cross section data for ions of Be, C and O are now considered by isoelectronic sequence.

**(a) hydrogen-like - bare nucleus**

Cross sections were taken from Bell et al (1983). These values are based on theoretical calculations.

**(b) helium-like - Hydrogen-Like**

Cross sections from both ground and metastable states of $C^{+4}$ and $O^{+6}$ have been recently explicitly calculated by Attaourti et al (1991), and so this data is adopted. The ground state cross sections differ by at most 10% from the recommended data of Bell et al (1983), which are based on experiment. Cross sections for the ground state of $Be^{+2}$ were taken from Bell et al (1983). Cross sections for metastable ionisation of $Be^{+2}$ were estimated from Fig. 3.3.2. This plots scaled cross sections for $C^{+4}$ and $O^{+6}$ calculated from the data of Attaourti et al (1991). It can be seen that there is very little variation.

**(c) Lithium-like - Helium-Like**

The distorted wave exchange calculations of Younger (1981a) are used. This paper tabulates scaled cross sections for 1s and 2s ionisation. It is assumed that the scaled cross section for 1s ionisation is independent of pathway. This assumption is suggested by Younger's data, which indicates that the 1s scaled cross section is constant for many ion charges. The cross sections for the direct and autoionisation pathways were obtained from the scaled ionisation cross sections using the ionisation potentials from Table 3.3.1. The total ionisation cross section from the ground state is in good agreement with the recommended data of Bell et al (1983), differing by 10% at most.

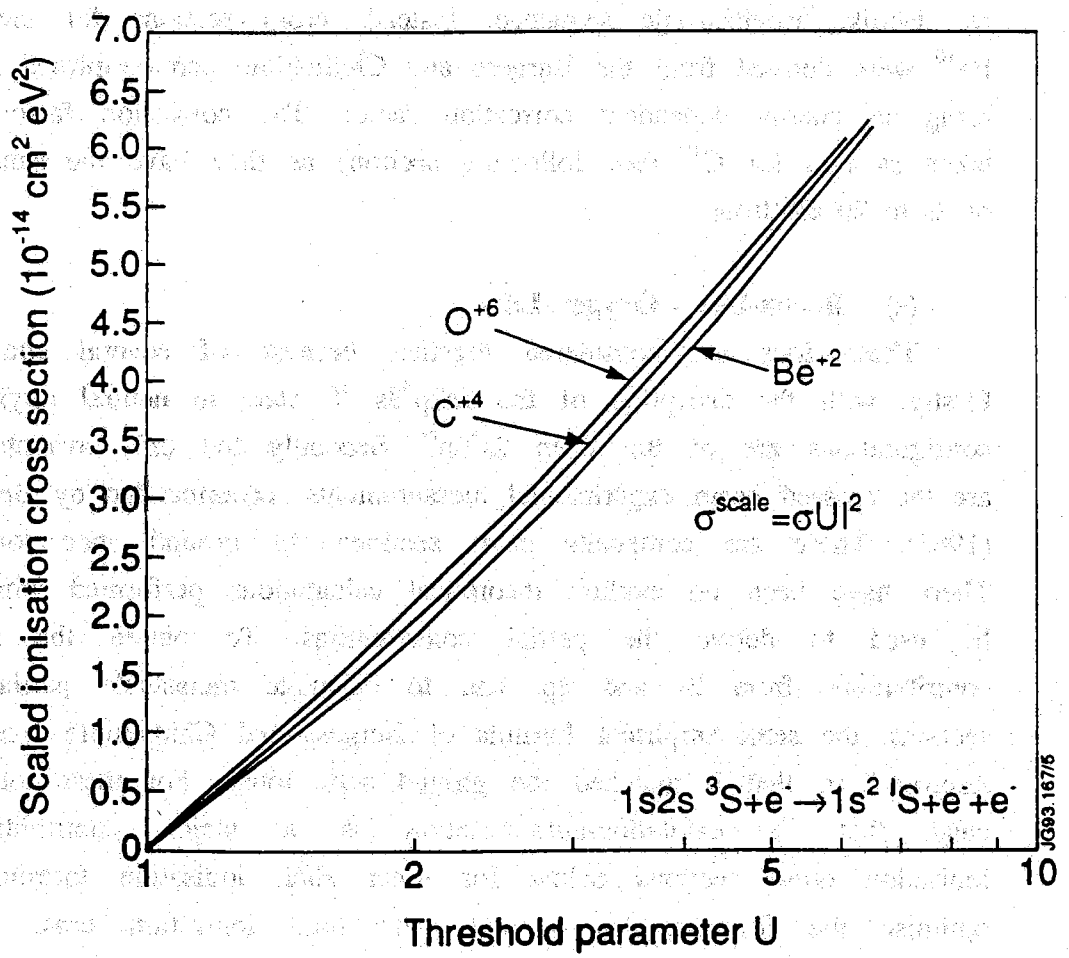


**Figure 3.3.2:** Scaled cross sections for 1s2s $^3$S ionisation in He-like ions. The values for $Be^{+2}$ were determined by extrapolating from the values of Attaourti et al (1992) for $C^{+4}$ and $O^{+6}$.

(d) **Beryllium-like - Lithium-Like**

For the ions of $C^{+4}$ and $O^{+2}$, the recommended data of Bell et al (1983) is again in very good agreement with the theoretical calculations of Younger (1981b). For $1.25 \leq U \leq 5.00$ the maximum difference is less than 10%. Younger tabulated cross sections for both 2s and 2p losses from ground and metastable states. This data was adopted.

For neutral beryllium, only ground state cross sections are available. These are given by Bell et al (1983), and are based on trends in cross sections. Due to the particular behaviour of neutrals, the cross sections for metastable ionisation cannot be derived from other ions in the Be-like isoelectronic sequence. Instead, cross sections for metastable $Be^{+0}$ were derived from the Burgess and Chidichimo semi-empirical formula using an energy dependent correction factor. The correction factor was taken as that for $C^{+0}$ (see following section) as they have the same ratio of 2s to 2p electrons.

(e) **Boron-like - Oxygen-Like**

These ions are considered together because of several similarities. Firstly, with the exception of the $2s2p^3 3s\ ^5S$ state in neutral oxygen, all configurations are of the form $2s^n 2p^m$. Secondly the only available data are the crossed beam experimental measurements recommended by Bell et al (1983). These are composite cross sections for ground state ionisation. There have been no explicit theoretical calculations performed which can be used to derive the partial contributions. To obtain the separate contributions from 2s and 2p, and to calculate metastable partial cross sections, the semi empirical formula of Burgess and Chidichimo was firstly improved so that it matched the ground state totals. For these ions it is clear that 2s excitation-autoionisation is a major contribution to ionisation cross sections below for inner shell ionisation threshold. To optimise the formula, the ground state total ionisation cross sections were compared with the recommended cross sections of Bell et al (1983). This served to define a value for the optimisation parameter C for each ion. This is illustrated in Figure 3.3.3. Two comparisons are given - (a) neglecting autoionisation channels, and (b) accounting for autoionisation channels. The behaviour of the neutrals is markedly different from that of the ions. An average value of C was defined for the ions, and is summarised in Table 3.3.2.

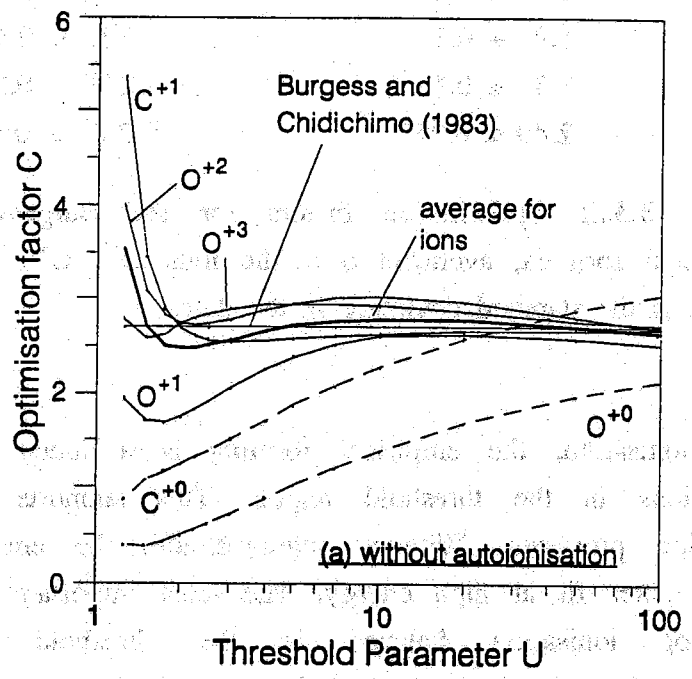


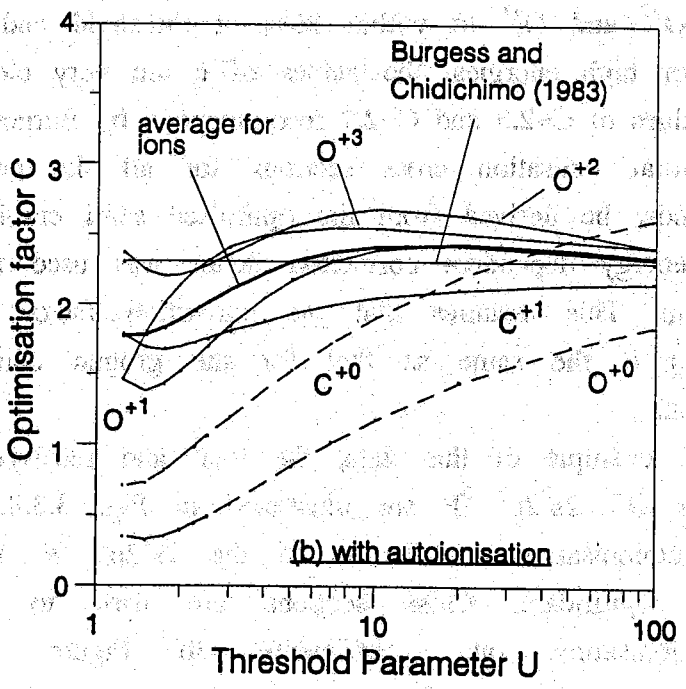


**Figure 3.3.3:** Optimisation factor C for Burgess and Chidichimo semi-empirical formula. (a) without autoionisation, (b) with autoionisation. Threshold parameter U is the ratio of incident electron energy to transition energy.

| | C | |
|---|---|---|
| U | With Autoionisation | Without Autoionisation |
| 1.25 | 1.8 ± 0.4 | 3.5 ± 1.3 |
| 2.0 | 1.9 ± 0.3 | 2.5 ± 0.4 |
| 5.0 | 2.3 ± 0.3 | 2.70 ± 0.25 |
| 10.0 | 2.40 ± 0.25 | 2.8 ± 0.2 |

**Table 3.3.2:** Optimisation factors for the Burgess and Chidichimo semi-empirical formula, averaged over the ions $C^{+1}$, $O^{+3}$, $O^{+2}$ and $O^{+1}$. The error given is the standard deviation in the data.

With autoionisation, the empirical formula is a much better fit to the cross sections in the threshold region. This supports the inclusion of autoionisation processes. Without autoionisation, the empirical formula is a slightly better fit at high energy. The most important part of the cross section for ionisation balance is the threshold region, so the optimisation factors obtained including autoionisation contributions were used. The average value of C for ions represents the cross sections for $C^{+1}$, $O^{+3}$, $O^{+2}$ and $O^{+1}$ to within 20% at threshold and ~10% at higher energies. For high energies, the values of c are very close to the energy averaged values of C=2.3 and C=2.7 recommended by Burgess and Chidichimo.

The total ionisation cross sections for all the pathways in Table 3.3.1 can now be derived from the optimised semi empirical formula. An individual energy dependent correction factor was used for each ion and neutral atom. This assumes that the correction factor for a metastable configuration is the same as that for the ground configuration of the particular ion.

As an example of this data, the total and resolved ionisation cross sections for $O^{+2}$ $2s^2 2p^2$ $^3P$ are illustrated in Fig. 3.3.4. It can be seen that the autoionisation contribution to the $2s^2 2p^2$ $^3P \rightarrow 2s^2 2p$ $^2P$ cross section is significant. Cross sections are used to prepare Maxwell averaged ionisation rate coefficients. In Figure 3.3.5 the total ionisation rate coefficients for ground and metastable states of $C^{+1}$, $C^{+2}$ and $C^{+4}$ are illustrated. These are summed over final states. The rate coefficients from metastable states are greater than those for ground states reflecting changes in threshold. In particular, there is an very large difference for the helium like ion, $C^{+4}$. This is due to the active

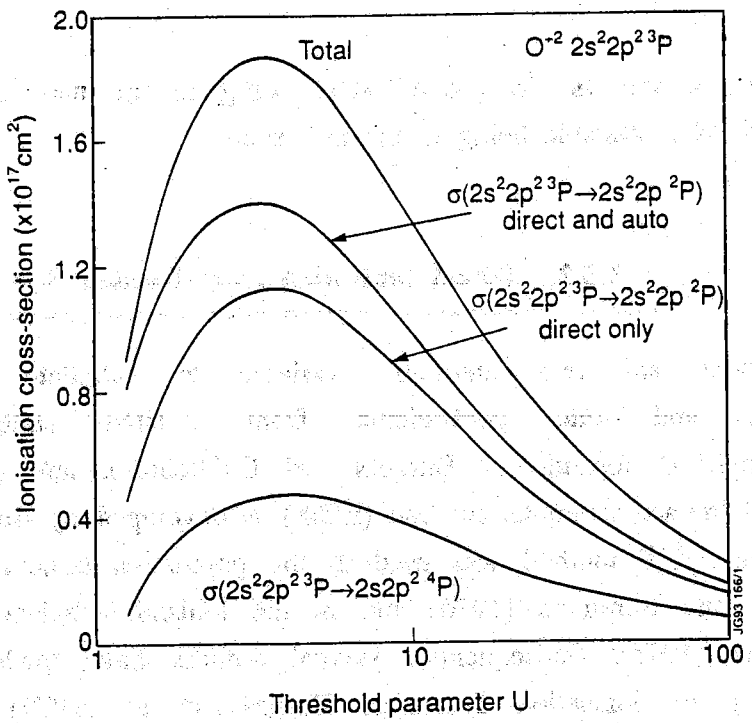


**Figure 3.3.4:** Total (i.e. summed over final state) and resolved ionisation cross sections for $O^{+2}$ $2s^2 2p^2$ $^3P$.

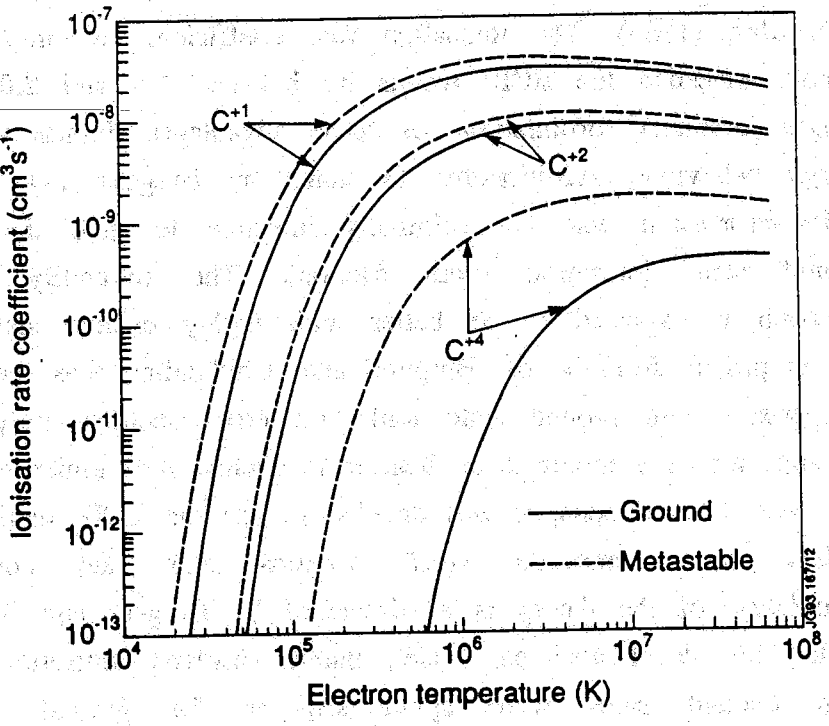


**Figure 3.4.5:** Ionisation rate coefficients from ground and metastable states of $C^{+1}$, $C^{+2}$ and $C^{+4}$. Summed over final states. The ground state terms are $2s^2 2p$ $^2P$, $2s^2$ $^1S$ and $1s^2$ $^1S$. The metastable terms are $2s 2p^2$ $^4P$, $2s 2p$ $^3P$ and $1s 2s$ $^3S$.

electron for the $1s^2\ ^1S$ ground state being in the n=1 shell and that for the 1s2s $^3S$ metastable being in the n=2 shell.

### 3.3.2: Direct Ionisation from Excited States

There are two methods available to calculate ionisation cross sections and rate coefficients from excited states - (i) the semi-empirical formula of Burgess and Chidichimo, and (ii) the exchange classical impact parameter method (ECIP) as developed by Burgess (1964).

The ECIP method was used in the population structure calculations of Burgess and Summers (1976) and in the ionisation balance calculations of Summers (1974). Subsequently, several authors have made studies of the reliability of ionisation formulae. Burgess et al (1977) stated that the ECIP tends to be in quite good agreement with experimental data for ground state ionisation of ions of low charge state. For other ions, ECIP/experiment ~ 0.6. A similar conclusion was made by Arnaud and Rothenflug (1985). The ionisation rate coefficients recommended by these authors exceeded the ECIP results by between 1.5 and 2.0. However, the impact parameter formulation has some advantages. It has the correct high energy behaviour. Additionally, as noted by Burgess and Chidichimo, the ECIP expression was not originally intended to give the most accurate ground state ionisation cross sections. The reliability of the ECIP approach is expected to be better with highly excited states. Conversely, the empirical formula of Burgess and Chidichimo has been derived by comparison with ground state ionisation cross sections only. There is no evidence for its accuracy in application to excited state ionisation.

For these reasons, it was decided to use the ECIP method to calculate excited state ionisation cross sections and rate coefficients. The formulation of the theory is as described by Burgess and Summers (1976). In the low level resolved model, parent resolved ionisation cross sections from excited sates were synthesised as for ground and metastable configurations by assigning values of $\zeta$, fractional parentage and ionisation potentials. In the bundle-n S model, effective principal quantum numbers were used to prescribe the energies of the lowest few quantum shells.

### 3.3.3: Autoionisation From Excited States

The bundle-n S calculation explicitly follows autoionisation processes of the form

$$X^{+z}(\gamma_i)\ ^{2S+1}n \quad \rightarrow \quad X^{+(z+1)}(\gamma_j) + (kl)\ e^- \qquad \text{E(3.3.11)}$$

where the initial parent $X^{+(z+1)}(\gamma_i)$ is sufficiently populated to act as a significant recombining parent. Autoionisation is relevant for electrons excited from inner shell configurations and electrons recombining onto excited parents. The threshold value of n is denoted by $n_{th}$ such that electrons with $n \geq n_{th}$ can autoionise. All relevant Auger pathways are listed in Table 3.3.3 along with the values of $n_{th}$. Those indexed by 'a' and 'f' are allowed and forbidden by LS coupling.

Auger transition probabilities for allowed transitions were explicitly calculated in LS coupling as part of the main dielectronic recombination calculations (see Section 3.4, *Electron Ion Recombination Processes*). There is a simplification. It is assumed that resolved transitions

$$X^{+z}(\gamma,nl) \quad \rightarrow \quad X^{+(z+1)}(\gamma) + kl\pm1 \qquad \text{E(3.3.12)}$$

with $l$=0,1,2 only contribute. A $(2l+1)/n^2$ average over the n-shell is taken. This data was for a representative range of n-shells from $n_{th}$ up to $n \sim 1000$. These could be interpolated and drawn directly into the population calculation. It was found that the LS resolved Auger transition probabilities obeyed the expected $n^{-3}$ scaling. When the n-shell average was taken the scaling changed to $n^{-5}$ so that

$$A^a(\gamma_i,n \rightarrow \gamma_j) \quad = \quad A^a(\gamma_i,(n_{th}) \rightarrow \gamma_j) \cdot (n_{th}/n)^5 \qquad \text{E(3.3.13)}$$

To obtain data for forbidden transitions, configuration interaction intermediate coupling calculations were undertaken with the *Autostructure* code, which is available on the JET IBM mainframe computer. This multi- configuration, multi- electron code is described by Badnell (1986,1988). The following configurations were used in the structure calculations (the $1s^2$ core is implicit):

| Recombining Ion Sequence | Initial Parent | Reaction | Final Parent | Type | Threshold Value of n (Be , C , O) |
|---|---|---|---|---|---|
| He-like | 2 | $(1s2s\ ^3S)\ ^2n \rightarrow 1s^2\ ^1S + e^-$ | 1 | a | 2, 2, 2 |
| Be-like | 2 | $(1s^22s2p\ ^3P)\ ^2n \rightarrow 1s^22s^2\ ^1S + e^-$ | 1 | a | -, 4*, 5 |
| | | $(1s^22s2p\ ^3P)\ ^4n \rightarrow 1s^22s^2\ ^1S + e^-$ | 1 | f | -, 5, 6 |
| B-like | 2 | $(1s^22s2p^2\ ^4P)\ ^3n \rightarrow 1s^22s^22p\ ^2P + e^-$ | 1 | a | -, 3*, 4 |
| | | $(1s^22s2p^2\ ^4P)\ ^5n \rightarrow 1s^22s^22p\ ^2P + e^-$ | 1 | f | -, 5*, 5 |
| C-like | 2 | $(1s^22s^22p^2\ ^1D)\ ^3n \rightarrow 1s^22s^22p^2\ ^3P + e^-$ | 1 | a | -, -, 6* |
| | 3 | $(1s^22s^22p^2\ ^1S)\ ^2n \rightarrow 1s^22s^22p^2\ ^3P + e^-$ | 1 | a | -, -, 4 |
| | | $(1s^22s^22p^2\ ^1S)\ ^2n \rightarrow 1s^22s^22p^2\ ^1D + e^-$ | 2 | a | -, -, 5 |
| | 4 | $(1s^22s2p^3\ ^5S)\ ^4n \rightarrow 1s^22s^22p^2\ ^3P + e^-$ | 1 | a | -, -, 4* |
| | | $(1s^22s2p^3\ ^5S)\ ^4n \rightarrow 1s^22s^22p^2\ ^1D + e^-$ | 2 | f | -, -, 4 |
| | | $(1s^22s2p^3\ ^5S)\ ^4n \rightarrow 1s^22s^22p^2\ ^1S + e^-$ | 3 | f | -, -, 4 |
| N-like | 2 | $(1s^22s^22p^3\ ^2D)\ ^3n \rightarrow 1s^22s^22p^3\ ^4S + e^-$ | 1 | a | -, -, 4* |
| | | $(1s^22s^22p^3\ ^2D)\ ^1n \rightarrow 1s^22s^22p^3\ ^4S + e^-$ | 1 | f | -, -, 4* |
| | 3 | $(1s^22s^22p^3\ ^2P)\ ^3n \rightarrow 1s^22s^22p^3\ ^4S + e^-$ | 1 | a | -, -, 4 |
| | | $(1s^22s^22p^3\ ^2P)\ ^1n \rightarrow 1s^22s^22p^3\ ^4S + e^-$ | 1 | f | -, -, 3 |
| | | $(1s^22s^22p^3\ ^2P)\ ^3n \rightarrow 1s^22s^22p^3\ ^2D + e^-$ | 2 | a | -, -, 4 |
| | | $(1s^22s^22p^3\ ^2P)\ ^1n \rightarrow 1s^22s^22p^3\ ^2D + e^-$ | 2 | a | -, -, 3 |

* a few levels in the shell lower than this autoionise but these are omitted because they are not representative in the bundle n-S model

**Table 3.3.3:** Autoionisation channels, a - allowed, f - forbidden.

| | | |
|---|---|---|
| B-like | $2s^22p$ , $2s2p^2$, $2s2p\ nl$, $2s^2\ kl'$ | $l\leq3$, $l'\leq5$, |
| C-like | $2s^22p^2$, $2s2p^3$, $2s2p^2\ nl$, $2s^22p\ kl'$ | $l\leq3$, $l'\leq5$ |
| N-like | $2s^22p^3$, $2s2p^4$, $2s2p^3\ nl$, $2s^22p^2\ kl'$ | $l\leq3$, $l'\leq5$ |
| O-like | $2s^22p^4$, $2s2p^3$, $2s2p^2\ nl$, $2s^22p^3\ kl'$ | $l\leq3$, $l'\leq5$ |

where k$l$ denotes a continuum orbital. The spectroscopic orbitals for the structure calculations were determined in an optimised central potential based on Slater type screening. Allowed and forbidden Auger transition probabilities were calculated in first order perturbation theory using the multi- electron intermediate coupling eigenfunctions from the structure calculation. The required Auger transition probabilities were isolated from the very large complete set of Auger data in a post processing step on the output files where constraints were placed on the spin of the bound configuration and on the energy range of the free states. The average over levels, terms and l-shells for each n was then formed as

$$A^a(\gamma_i,n \rightarrow \gamma_j) = 1/(\omega(\gamma_i)n^2) \sum_{l=0}^{3} \Sigma_{L,J} (2J+1)\ A^a(\gamma_i,nl\ SLJ \rightarrow \gamma_j)$$

E(3.3.14)

It was found that the behaviour of the forbidden Auger transition probabilities was not as regular as that of the allowed transition probabilities. For example, the allowed and forbidden transition probabilities for $O^{+3}$ are illustrated in Fig. 3.3.6. It can be seen that at the threshold n, the allowed transition probabilities are ~ $10^4$ greater than the forbidden transition probabilities. As n is increased, the allowed transition probabilities follow closely the expected $n^{-5}$ behaviour but the forbidden transition probabilities change irregularly at first before the asymptotic scaling becomes established. This is principally due to an increase in spin orbit mixing as n is increased and related to the quantum defects of the series. The irregularities can occur at n-shells significantly above $n_{th}$ and can be substantial. This is a new phenomenon which has not previously been reported.

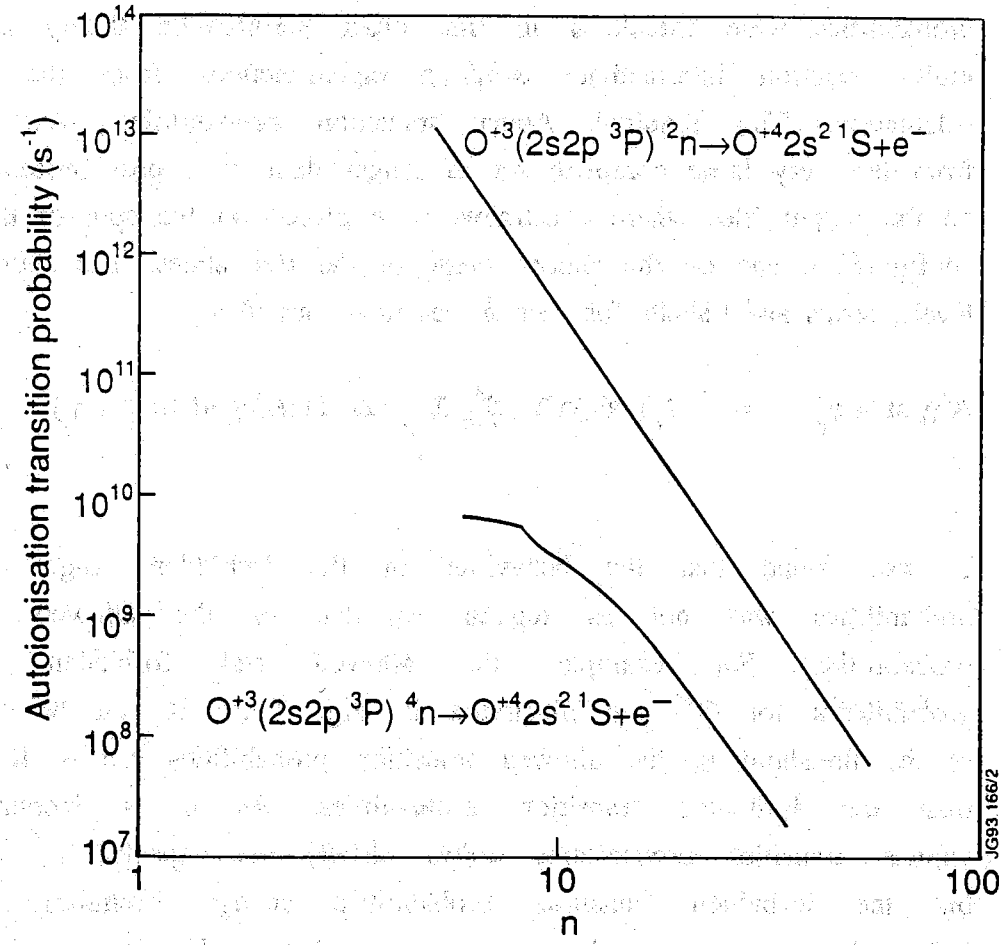


**Figure 3.3.6:** Forbidden and allowed n-shell averaged Auger transition probabilities for $O^{+3}$ $(2s2p\ ^3P)\ ^{2,4}n \rightarrow O^{+4}\ 2s^2\ ^1S\ +\ e^-$

# 3.4: ELECTRON-ION RECOMBINATION PROCESSES


3.4.1: Three Body Recombination
3.4.2: Radiative Recombination
3.4.3: Dielectronic Recombination


For the bundle-n S calculation, parent and spin system resolved recombination rate coefficients are required into all principal quantum shells of the recombined system. For the low level resolved model, parent resolved rate coefficients are required for each LS term.

## 3.4.1: Three Body Recombination

Three body recombination is the inverse process from ionisation and so the rate coefficients for these two processes satisfy a detailed balance relationship. In complete thermodynamic equilibrium

$$\alpha^t(\gamma \rightarrow \gamma, n\ell)\ n_e^2\ N^{+(z+1)}(\gamma) \quad = \quad S(\gamma, n\ell \rightarrow \gamma)\ n_e\ N^{+z}(\gamma, n\ell) \qquad \text{E(3.4.1)}$$

where $N^{+(z+1)}(\gamma)$ and $N^{+z}(\gamma,n)$ are related by the Saha-Boltzmann equation. This gives

$$\frac{S(\gamma, n\ell \rightarrow \gamma)}{\alpha^t(\gamma \rightarrow \gamma, n\ell)} = \frac{\omega(\gamma)}{\omega(\gamma, n\ell)} 2 \frac{(2\pi m_e kT)^{3/2}}{h^3} \exp\left(\frac{-I}{kT}\right) \qquad \text{E(3.4.2)}$$

from which three-body recombination rate coefficients can be calculated.

## 3.4.2: Radiative Recombination

Radiative recombination rate coefficients are generally expressed in terms of bound-free Gaunt factors. This gives the radiative recombination rate coefficient from parent configuration $X^{+(z+1)}(\gamma)$ to recombined state $X^{+z}(\gamma,n\ell)$ as

$$\alpha^r = 8\left(\frac{\pi a_0^2 I_H}{kT_e}\right)^{\frac{3}{2}} \frac{4\,\alpha^4 c}{3\sqrt{3}\,\pi a_0} z1^4 \left(\frac{2}{\nu^3}\right) \exp\left(\frac{z1^2\, I_H}{\nu^2\, kT_e}\right) \zeta^{eff} \int_{X_{min}}^{\infty} g^{II} \frac{\exp(-X)}{X}\, dX \qquad E(3.4.3)$$

where

| | | |
|---|---|---|
| $a_0$ | = | Bohr radius |
| $z1$ | = | z+1 |
| $\alpha$ | = | fine structure constant |
| $X_{min}$ | = | $(z1^2\, I_H)/(\nu^2 kT_e)$ |
| $\nu$ | = | effective quantum number of final bound state |
| $\zeta^{eff}$ | = | statistical weight factor |
| $g^{II}$ | = | bound free Gaunt factor |

For the bundle-n S calculation, the present work follows almost exactly the procedures of Burgess and Summers (1976). The Gaunt factors are calculated in the hydrogenic approximation. The parameter $\zeta^{eff}$ was taken to be the relative spin system weight of the recombining parent.

$$\zeta^{eff} = (2S_\rho+1)/2(2S_\gamma+1) \qquad E(3.4.4)$$

For example, a doublet parent can recombine into singlet and triplet spin systems with $\zeta^{eff}$ = 0.25 and 0.75 respectively.

For capture into the lowest n-shell two refinements are made. The effective quantum number is obtained by a statistically weighted average of all recombined term energies (in LS coupling) belonging to configurations associated with the recombining parent and spin system. Following Griem (1964) and Van Goeler et al (1976), a phase factor, *PHFRAC*, is introduced to account for partial occupancy of the ground state shell. This is a ratio of available states to the whole shell weight such that $0.0 \leq PHFRAC \leq 1.0$. This parameter is calculated from analysis of the recombined structure. The modified rate coefficient for lowest level capture is thus given by

$$\alpha^r(\gamma \rightarrow \gamma, n_0) = PHFRAC \times \alpha^r(\gamma \rightarrow \gamma, n_0) \qquad E(3.4.5)$$

For the resolved low level model a more complete calculation of the Gaunt factor was undertaken. This was based on the algorithms and

numerical methods for radiative Gaunt factors developed by Burgess and Summers (1986). These algorithms are available on the JET IBM mainframe. The Gaunt factors are expressed in terms of bound-free radial integrals, which are in turn evaluated using one electron wave functions in a Slater Potential adjusted to match the binding energy of the recombined electron.

For levels within the low level group, the parameter $\zeta^{eff}$ was determined for each relevant parent by multiplying the number of electrons in the subshell, $\zeta$, by the fractional parentage of the recombining ion. As an example, the parameters used to calculate $\zeta^{eff}$ for recombined states in boron-like ions are given in Table 3.4.1.

| Term | Parent | Subshell | $\zeta$ | Fract. Prtage | $\zeta^{eff}$ |
|---|---|---|---|---|---|
| $2s^2 2p\ ^2P$ | 1 | 2p | 1 | 1.00 | 1.00 |
| $2s^2 2p\ ^2P$ | 2 | 2s | 2 | 0.75 | 1.50 |
| $2s2p^2\ ^2D$ | 1 | - | - | - | - |
| $2s2p^2\ ^2D$ | 2 | 2p | 2 | 0.75 | 1.50 |
| $2s2p^2\ ^4P$ | 2 | 2p | 2 | 1.00 | 2.00 |
| $2p^3\ ^4S$ | - | - | - | - | - |

**Table 3.4.1:** Parameters used to calculate $\zeta^{eff}$ for some recombined states in Boron-like ions. The relevant parents in the Be-like ion are $2s^2\ ^1S$ and $2s2p\ ^3P$.

Some states within the low level group (e.g. $2p^3$) do not connect with a parent in a one electron transition and are excluded for recombination. Term energies were taken from standard sources, principally Kelly (1985) and Moore (1970).

Radiative recombination rate coefficients from the $O^{+4}$ $2s2p\ ^3P$ parent are illustrated in Fig. 3.4.1. Recombination into low $l$ states is more important at high temperature (c.f. Spence and Summers 1987). The bundle-n S coefficient for recombination into $(2s2p\ ^3P)\ ^2n$ with n=2 is in reasonable agreement with the sum of the LS resolved coefficients at low temperature but fails to match the temperature dependence of the rate coefficient at higher temperature mainly due to the special behaviour of the capture into 2s.

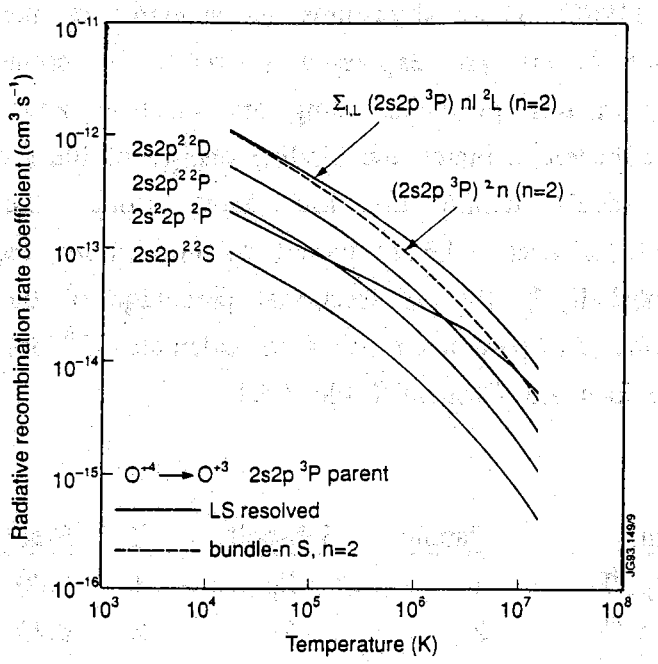


**Figure 3.4.1:** Radiative recombination rate coefficients for the reaction $O^{+4} + e^- \rightarrow O^{+3} + h\nu$. All curves are for 2s2p $^3$P parent.

### 3.4.3: Dielectronic Recombination

For all ions of Be, C and O detailed calculations of high temperature dielectronic recombination rate coefficients were undertaken by Badnell (1992) (using the methods described in earlier papers 1989a,b, 1990) in conjunction with the work of this thesis. The data were calculated by the *Autostructure* code in configuration interaction LS coupling. The rate coefficients for capture into LS resolved low levels and for a representative set of spin resolved n-shells were stored in formatted data sets and drawn directly into the population calculations. Several factors need to be considered in assessing this data :

(i) Any difference between LS coupled and Intermediate coupling (IC) calculations

(ii) Relevant core transitions

(iii) The importance of low temperature dielectronic recombination

(iv) Recombination from excited parents

(v) The influence of field enhanced dielectronic recombination

The LS coupling results for oxygen ions agree very well with more complete calculations which have been performed in intermediate coupling (Badnell 1989a). For $O^{+2}$, $O^{+3}$ and $O^{+4}$ the IC total rate coefficients (summed over all n) are no more than 5% larger than the LS coupled results, whereas for $O^{+1}$ and $O^{+5}$ the increase is about 25% in the worst case. This is due to the neglect of Auger transitions which are forbidden in LS coupling. Unfortunately, the results of the IC calculations are not available at present in a parent/spin system resolved organisation but are expected to be incorporated at a future date.

The data spans the core principal quantum shell transitions listed in Table 3.4.2. For $O^{+2}$ - $O^{+4}$ and $C^{+1}$ - $C^{+2}$ the $\Delta n=1$ transitions could be neglected without loss of accuracy. For recombining lithium like ions, $Be^{+1}$, $C^{+3}$ and $O^{+5}$, the $1s \rightarrow 2p$ inner shell core transitions become important at high temperature.

| Recombining Ion Sequence | Parent Index | Core Transition Types |
|---|---|---|
| H-like | 1 | $\Delta n=1$ |
| He-like | 1 | $\Delta n=1$ |
| | 2 | $\Delta n=1$ |
| Li-like | 1 | $\Delta n=0$, $\Delta n=1$, $\Delta n=1$(I) |
| Be-like | 1,2 | $\Delta n=0$, $\Delta n=1$ |
| B-like | 1,2 | $\Delta n=0$, $\Delta n=1$ |
| C-like | 1,2,3,4 | $\Delta n=0$, $\Delta n=1$ |
| N-like | 1,2,3 | $\Delta n=0$ |

**Table 3.4.2:** Dielectronic core excited transitions. (I) denotes the inner shell transition $1s^2 2s + e^- \rightarrow (1s2s2p)\ nl$.

At low temperatures, dielectronic recombination via a few low lying autoionising states becomes important (Storey 1981). Such data is very sensitive to precise energy levels of the autoionising states which require more elaborate calculations or experimental values. Detailed LS coupling calculations for the ions of $C^{+3}$ - $C^{+1}$ and $O^{+5}$ - $O^{+1}$ have been

carried out by Nussbaumer and Storey (1983) for the temperature range $10^3$ - $6x10^4$ K and in intermediate coupling for $C^{+2}$ and $O^{+4}$ by Badnell (1988). In general, although low temperature dielectronic recombination can considerably influence equilibrium ionisation balance, it occurs at temperatures too low to be of importance in fusion plasmas. It is thus neglected in the present work.

Figure 3.4.2 illustrates the total dielectronic and radiative recombination rate coefficients from $C^{+2}$ $1s^2 2s^2$ $^1S$. This compares the high and low temperature IC results of Badnell (1989, 1988) with the high temperature LS coupling results of Badnell (1989), which are the basis of the present work, and the low temperature LS coupling results of Nussbaumer and Storey (1983). In both cases there is good agreement between the IC and LS coupled results.

In all cases dielectronic recombination from metastable parents was found to be considerably smaller than that from ground state parents. This reflects the high n-shell nature of dielectronic recombination. Effectively, only electrons captured below the secondary autoionisation threshold contribute to the recombination process. The peak DR rate coefficient from metastable parents is no more than a few percent of the rate coefficient from ground terms, although the peak may be at a lower temperature. For $O^{+2}$ parents, the data is illustrated in Fig. 3.4.3. For comparison the radiative recombination rate coefficients for a few reactions are also plotted. Because radiative recombination is mainly into low quantum shells, secondary autoionisation has less influence on this process. Other radiative recombination rate coefficients not shown in this figure are of similar magnitude. The dielectronic recombination rate coefficients from excited parents are comparable with or less than those for radiative recombination.

As discussed in Chapter 2.1, electric fields can considerably increase dielectronic recombination because of Stark mixing of high $nl$ states. A recent study by Reisenfeld (1992) in which field enhanced dielectronic recombination rate coefficients were used in conjunction with a collisional radiative model has indicated that $C^{+3}$ (a lithium- like ion) is particularly sensitive to this effect. At a particle density of $n_H$ = $10^9$ $cm^{-3}$, Reisenfeld's calculations suggest that the plasma microfield increases the effective dielectronic recombination rate by nearly a factor of three. In order to investigate this problem further, Badnell et al (1993) calculated zero field and field enhanced dielectronic recombination

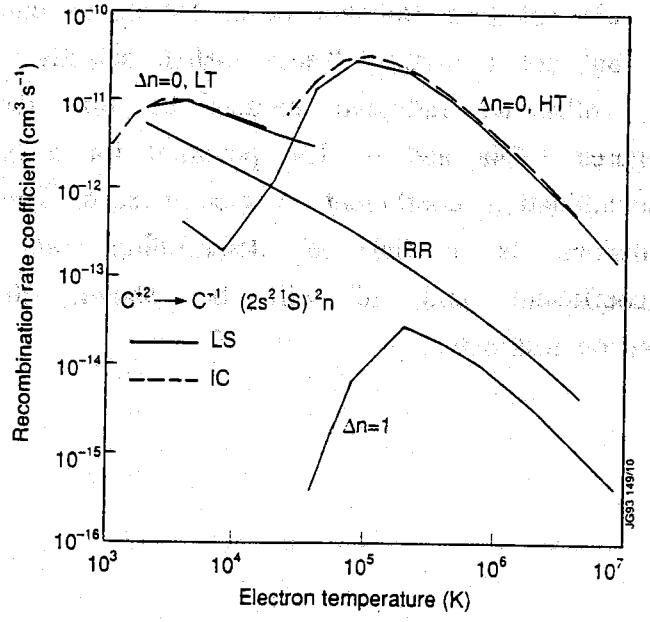


**Figure 3.4.2:** Total (summed over all n) dielectronic and radiative (RR) recombination rate coefficients for $C^{+2} \rightarrow C^{+1}$. $(1s^2 2s^2\ ^1S)\ ^2n$. LT - low temperature, HT - high temperature.

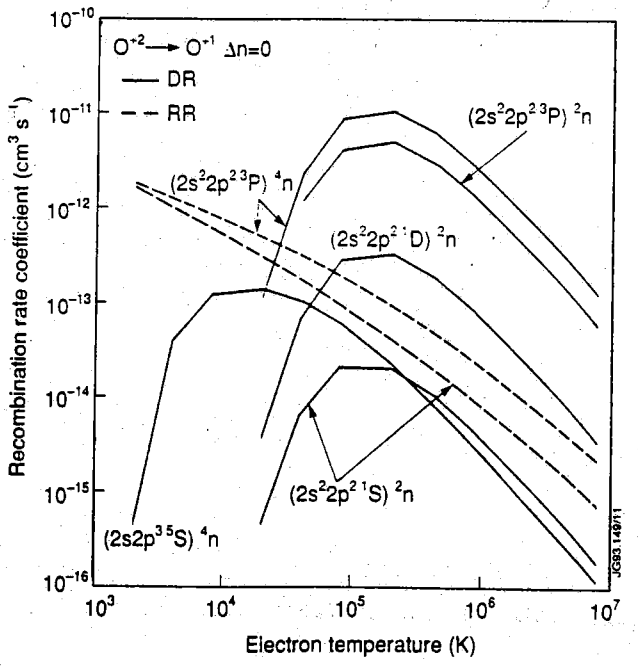


**Figure 3.4.3:** Total (summed over all n) parent and spin system resolved dielectronic (DR) and radiative (RR) recombination rate coefficients for various parent and spin systems of $O^{+2}$.

rate coefficients for $C^{+3}$. The calculations were fully quantal and involved, for each n, the diagonalisation of a Hamiltonian that included the Stark matrix element (see Bottcher et al 1986). In this way *l* mixing is accounted for but not n mixing. These n-shell selective data have been merged in the collisional radiative models of this thesis. They are illustrated in Figures 3.4.4a and b. The potential for a large increase in the effective recombination coefficient is clearly seen. However, the role of further collisions is crucial in determining the final effective recombination coefficient and it will be shown that Reisenfeld's calculations are an overestimate.

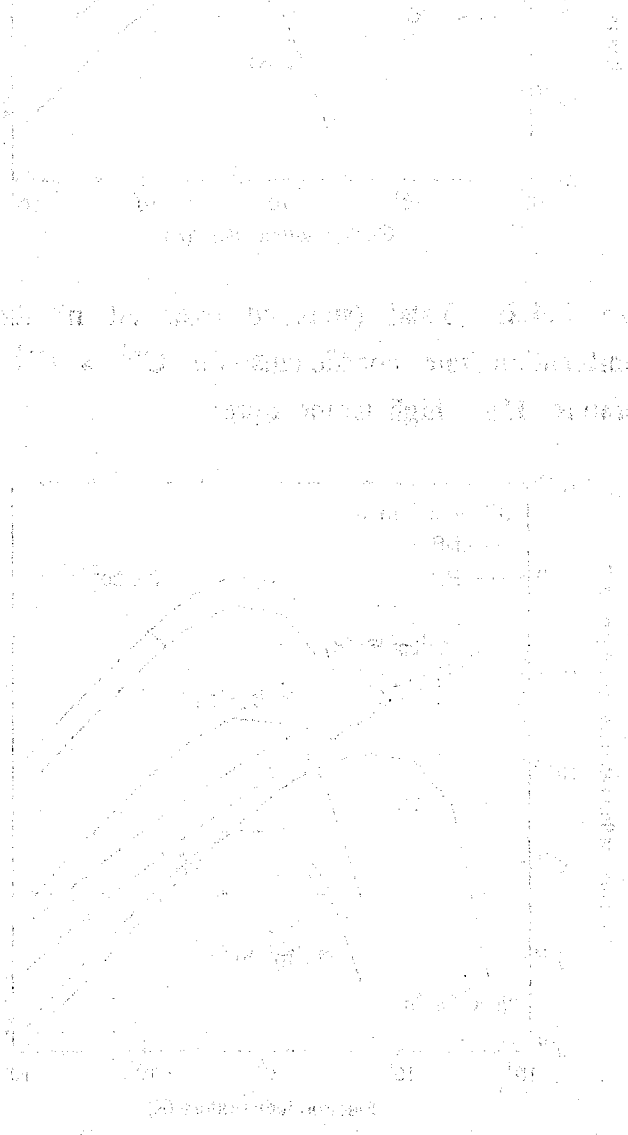

(a)

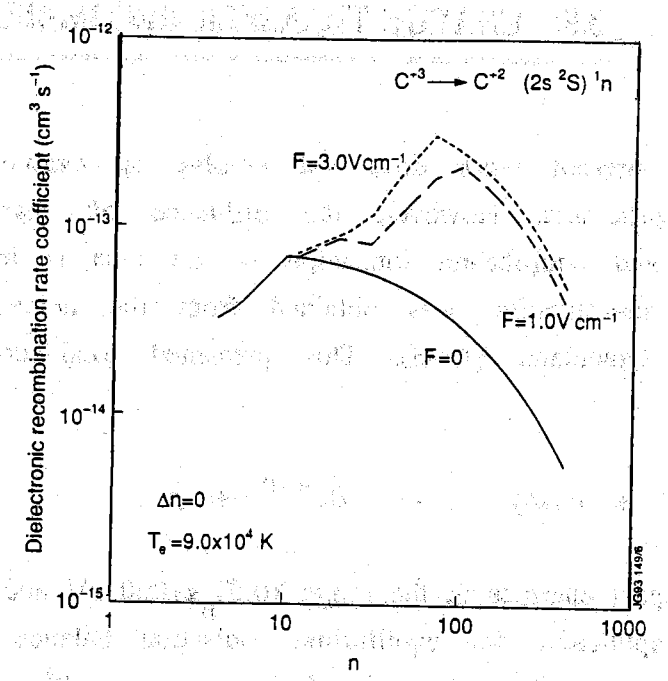


(b)

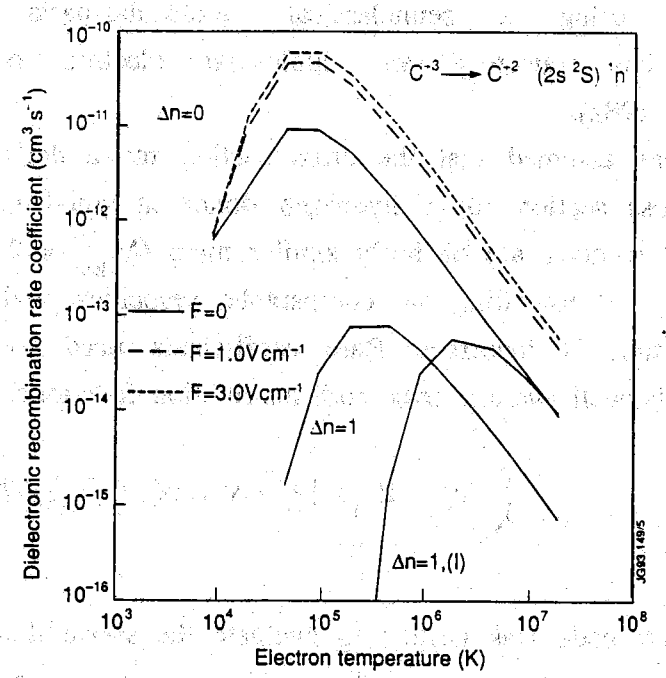


**Figure 3.4:** Zero field and field enhanced dielectronic recombination rate coefficients for $C^{+3} \rightarrow C^{+2}$. $(1s^2 2s\ ^2S)\ ^1n$.

**(a)** The Δn=0 'core' (parent) transition recombination rate coefficients plotted as a function of n.

**(b)** Total (summed over all n) recombination rate coefficients at zero electron density for the various core transitions.

## 3.5: CHARGE TRANSFER RECOMBINATION

The present work does not involve an extended study of charge transfer processes. However, the influence of charge transfer on the transient and equilibrium ionisation of Be ions is investigated. The data for this investigation was obtained from the unresolved state to stage data of Greenland (1988). This presented total cross section for the reactions

$$Be^{+z} + H(1s) \rightarrow Be^{+(z-1)} + p$$

for H impact energies in the range $10 \leq E_H \leq 1000$ eV and for $1 \leq z \leq 4$. This data is thus applicable for equilibrium ionisation balance calculations and for the study of influx ions in fusion plasmas. The cross sections were calculated using a semiclassical -molecular-basis method (that is, classical ion trajectory and molecular electron orbital basis - see Greenland 1982).

It was assumed that the cross section for a deuterium donor is equal to the cross section for a hydrogen donor at equal velocity. Because both donor and receiver are of fairly similar mass ($M_{deut}$ = 2 amu, $M_{Be}$ = 9 amu) they may be travelling at comparable velocities and a stationary target approximation is incorrect. Rate coefficients need to be calculated from the full Maxwell average over both distribution functions:

$$\langle \sigma v \rangle = \int_{V_a} \int_{V_b} f(v_a)\, f(v_b)\, |v_a - v_b|\, \sigma(|v_a - v_b|)\, dv_b dv_a \qquad \text{E(3.5.1)}$$

A computer code was written to evaluate the above double integral from the cross section data and then tabulate rate coefficients. The rate coefficients for $Be^{+2}$ are illustrated in Fig. 3.5.1. It can be seen that the rate coefficients for charge transfer are considerably larger than those for ionisation of $Be^{+2}$.

In the absence of precise data on the n-shell distribution of the captured electron, these coefficients were used without entering them into full collisional radiative population models. The justification for this is that preferred n-shells for capture for ions of low charge are n=2 and

3. Populations of these levels will be only slightly affected by stepwise ionisation at tokamak densities. Thus the effective (collisional radiative) charge transfer recombination rate coefficient is just the sum of the captures into separate n-shells.

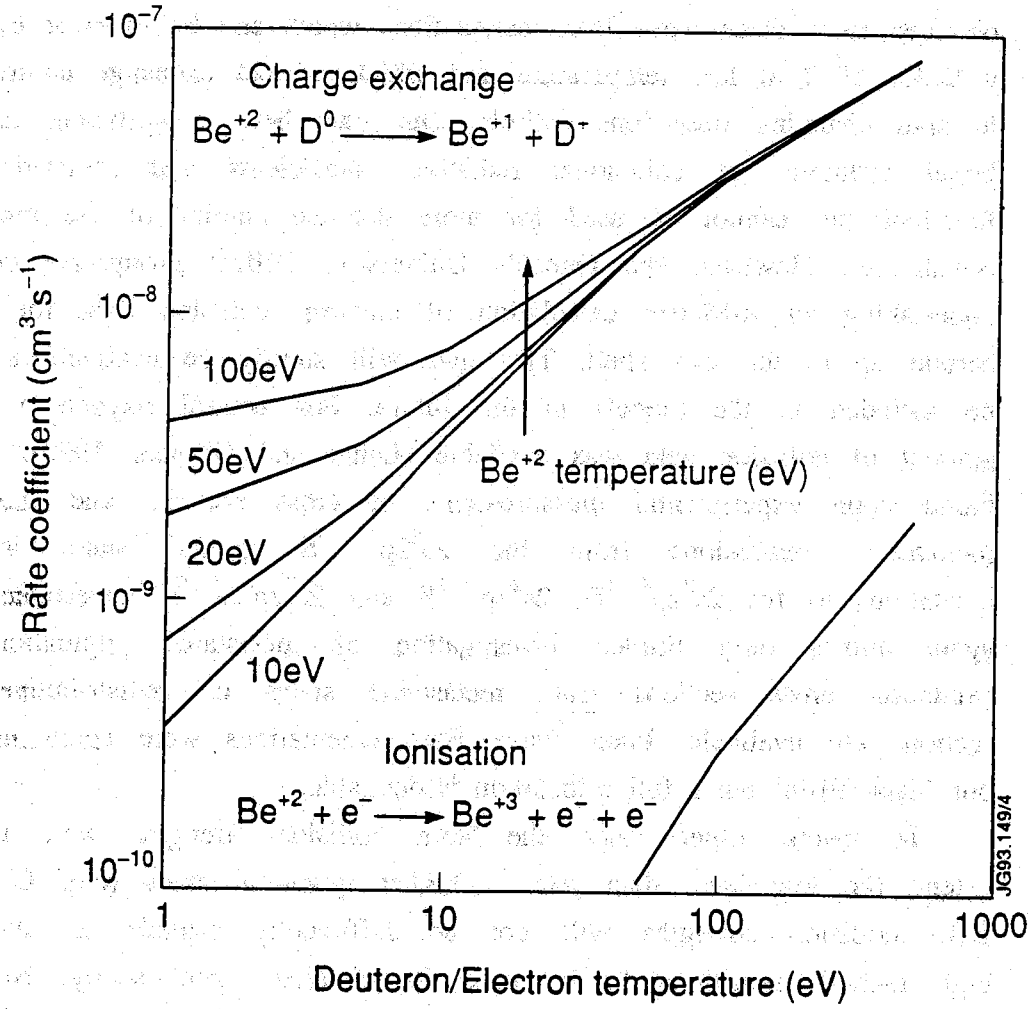


**Fig. 3.5.1:** Thermal charge transfer rate coefficients for the reaction

$$Be^{+2} + D^0 \rightarrow Be^{+1} + D^+$$

as a function of donor and receiver temperature. The ionisation rate coefficient for

$$Be^{+2} + e^- \rightarrow Be^{+3} + e^- + e^-$$

as a function of electron temperature is also illustrated.

## 3.6: SUMMARY

In general, our low level data base is comprehensive and accurate except for a few cases where no high quality data is available. It is poorest for the neutral atoms of carbon and oxygen. For neutral carbon there is no high quality collision data available at present. Data were obtained from plane wave Born calculations which can be in error by about a factor of 2 at low temperature and which neglect exchange contributions to spin changing transitions entirely. Our data here is sufficient to make broad estimates of collisional radiative coefficients and radiated power functions but cannot be used for more detailed studies of the metastable populations. However, the Queen's University, Belfast group are currently undertaking an R-Matrix calculation of electron collision data for neutral carbon up to the n=4 shell. This data will shortly be available and will be included in the models in the future. For neutral oxygen a limited amount of collision data was available (Laher and Gilmore 1990). This is based upon experimental measurements of cross sections and thus only includes excitations from the $2s^2 2p^4\ ^3S$ ground state, including excitations to the $2s^2 2p^4\ ^1D$, $2s^2 2p^4\ ^1S$ and $2s^2 2p^3 3s\ ^5S$ metastables. This again allows only limited investigation of metastable populations. No excitation cross sections from metastable states or redistributive cross sections are available. Plane wave Born calculations were again used for our 'data fill-in' but a full calculation is desirable.

In several other cases, the Born collision strengths were used to extend the low level data sets to higher quantum shells (e.g. $C^{+3}$). The Born collision strengths will not be sufficiently reliable to allow the high n-shell transitions to be used for detailed spectroscopy. None the less, the main objective in including the higher terms is to ensure a smooth merging of the low level data sets with the high bundle-n S shells during the projection calculation. The bundled principal quantum shells are not a good representation of the low levels and so it is advantageous to extend the low level data sets as far as possible.

For the ions of the H-, He-, Li- and Be- sequences high quality ionisation cross sections were used which are in excellent agreement with the recommendations of Bell et al (1983). For configurations in the B-, C-, N- and O-like sequences no resolved ionisation cross sections were available in the general literature. These were derived in the present

work by using the semi-empirical formula of Burgess and Chidichimo (1983) to derive partial cross sections for the various channels and then by applying a systematic correction to match the total cross sections onto experimental data. This appears to result in total cross sections which are accurate to within 20%. For excited state ionisation the ECIP method was used in preference to the empirical formula of Burgess and Chidichimo (1983)

The rate coefficients used for dielectronic and radiative recombination are comprehensive and comparable with any other data in the general literature. To extend modelling to low temperatures (< 5 eV) it will be necessary to improve the low temperature dielectronic recombination rate coefficients.

# CHAPTER 4

# THEORETICAL POPULATION MODELLING

# 4.1: THE BUNDLE-N S MODEL


4.1.1: The Multiple Parent/Metastable Model
4.1.2: Numerical Evaluation of Ionisation Coefficient
4.1.3: Calculation Methodology
4.1.4: Illustration of Results
4.1.5: Resolution Within Spin Systems
4.1.6: Concluding Remarks


## 4.1.1: The multiple parent/metastable model

The model is an extension of the bundle-n model of Burgess and Summers (1976) which treated a single parent/ground system, and was described in Section 2.3, *Literature Review and Scope of Present Work.* To obtain resolution between parents and metastables, the n-shells are now distinguished by recombined parent and by recombined spin system. The assumption is that the populations of principal quantum shells of the same value of n but with different spins are separable. A separate calculation is performed for each excited state system formed by such a recombination pathway. A complete list of all the calculation of relevance is given in Table 4.1.1. These were decided upon by first defining the important parents (from Table 2.3.1) and then by identifying which spin systems are active in recombination. The metastables in the recombined ion which correspond to these spin systems can then be identified.

The metastable and parent indices in Table 4.1.1 are as Table 2.3.1. The parameter *Nsys* specifies how many spin systems in the recombined ion that are accessible by recombination of the particular parent. The spin system weight of a spin system is the fractional statistical weight of the spin resolved n-shells relative to the whole n shell for the parent. In the bundle-n model, the statistical weight of an n-shell is given by

$$\omega( X^{+z} (\gamma) \, n ) \quad = \quad 2n^2 \, \omega( X^{+(z+1)} \, \gamma ) \qquad \text{E(4.1.1)}$$

where $\omega(X^{+(z+1)} \, \gamma)$ is the statistical weight of the parent. For the present case, when the n-shells are distinguished by spin the statistical weight is given by

| Recombining Ion Sequence | Prt. Index | Excited State Structure | Nsys | Recombined Spin System | Spin Sys. Weight | Met. Index | $N_{min}$ | $N_0$ |
|---|---|---|---|---|---|---|---|---|
| H-like | 1 | $(1s\ ^2S)\ n$ | 2 | 1 | 0.250 | 1 | 1 | 1 |
| | | | | 3 | 0.750 | 2 | 2 | 2 |
| He-like | 1 | $(1s^2\ ^1S)\ n$ | 1 | 2 | 1.000 | 1 | 2 | 2 |
| | 2 | $(1s2s\ ^3S)n$ | 1 | 2 | 1.000 | 1 | 1 | 2 |
| Li-like | 1 | $(1s^22s^1\ ^2S)\ n$ | 2 | 1 | 0.250 | 1 | 2 | 2 |
| | | | | 3 | 0.750 | 2 | 2 | 2 |
| Be-like | 1 | $(1s^22s^2\ ^1S)\ n$ | 1 | 2 | 1.000 | 1 | 2 | 2 |
| | 2 | $(1s^22s2p\ ^3P)\ n$ | 2 | 2 | 0.333 | 1 | 2 | 2 |
| | | | | 4 | 0.667 | 2 | 2 | 2 |
| B-like | 1 | $(1s^22s^22p\ ^2P)\ n$ | 2 | 3 | 0.750 | 1 | 2 | 2 |
| | | | | 1 | 0.250 | 2,(3) | 2 | 2 |
| | 2 | $(1s^22s2p^2\ ^4P)\ n$ | 2 | 3 | 0.375 | 1 | 2 | 2 |
| | | | | 5 | 0.625 | 4 | 2 | 2 |
| C-like | 1 | $(1s^22s^22p^2\ ^3P)\ n$ | 2 | 4 | 0.667 | 1 | 2 | 2 |
| | | | | 2 | 0.333 | 2,(3) | 2 | 2 |
| | 2 | $(1s^22s^22p^2\ ^1D)\ n$ | 1 | 2 | 1.000 | 2,(3) | 2 | 2 |
| | 3 | $(1s^22s^22p^2\ ^1S)\ n$ | 1 | 2 | 1.000 | 2,(3) | 2 | 2 |
| | 4 | $(1s^22s2p^3\ ^5S)\ n$ | 1 | 4 | 1.000 | 1 | 2 | 2 |
| N-like | 1 | $(1s^22s^22p^3\ ^4S)\ n$ | 2 | 3 | 0.375 | 1 | 2 | 2 |
| | | | | 5 | 0.625 | 4 | 2 | 2 |
| | 2 | $(1s^22s^22p^3\ ^2D)\ n$ | 2 | 3 | 0.750 | 1 | 2 | 2 |
| | | | | 1 | 0.250 | 2,(3) | 2 | 2 |
| | 3 | $(1s^22s^22p^3\ ^2P)\ n$ | 2 | 3 | 0.750 | 1 | 2 | 2 |
| | | | | 1 | 0.250 | 2,(3) | 2 | 2 |

**Table 4.1.1:** Bundle-n S calculation pathways. The parameters Nsys, $N_{min}$ and $N_0$ are as described in the text. Parent and metastable indices as given in Table 2.3.1.

$$\omega( X^{+z} (\gamma)\, ^{(2S+1)}n ) = SSYSWT \cdot 2n^2\, \omega( X^{+(z+1)}\, \gamma ) \quad E(4.1.2)$$

where SSYSWT is the fractional spin system weight of the recombined spin system. For example, the 2s2p $^3$P parent can recombine into the doublet and quartet spin systems, with SSYSWT = 0.333 and 0.667 respectively. It is essential to include this factor when converting between populations in the $b_n$ and population representation and when calculating detailed balance relationships.

The parameters $n_{min}$ and $n_0$ in Table 4.1.1 refer to the lowest n-shell of the calculation and the lowest n-shell accessible by recombination respectively. Except for the case of the inner-shell excitation of lithium like ions, these parameters are equal. Care was taken to represent the energies of the lowest few quantum shells by effective quantum numbers. This was done by taking statistically weighted averages of the energies of LS terms associated with each parent and spin system group. The term energies were taken from the reliable sources given in Chapter 3. In general, the quantum defect corrections were only necessary for the ground and first excited quantum shells. There is some uncertainty as to the best representation of the ground quantum shell as there is often a substantial difference between the quantum defect of the ground state itself and the mean quantum defect arising from a weighted average of the ground shell terms. For example, in $Be^{+1}$, the 2s $^2$S ground term has a quantum defect of $\delta$=0.271 whereas the averaged quantum defect of 2s $^2$S and 2p $^2$P is $\delta$=0.102. The n=3 and n=4 shells have averaged quantum defects of 0.05 and 0.03 respectively. The problem concerns which ground state energy will best represent excitation between n=2 and n=3 in general calculation. At low electron densities, the ground state is the only significant population so that the ground state energy is more appropriate. However at high electron densities, the 2p state will be significantly populated and will contribute to the excitation to n=3. In these circumstances the averaged energy will be more appropriate. The choice of this parameter is important as it influences the stepwise part of the collisional-radiative ionisation coefficient. It is one of the limitations of a bundle-n population structure (a situation corrected by the projection model of section 4.3). In this Section, the quantum defect of the ground state n-shell was chosen to be that of the ground state configuration. The influence of $\Delta$n=0 ground shell excitations on the collisional-radiative ionisation coefficient will be re-examined in detail in Section 4.3 when

the projection calculation is discussed and the low level structure is explicitly included in the model.

A second limitation of the parent/spin system model is that it does not distinguish recombined metastables within the same spin system. For example, the $2s^22p\ ^2P$ parent in the B-like system is considered as recombining into the singlet system of the C-like ion. This system has two metastables - $2s^22p^2\ ^1D$ and $2s^22p^2\ ^1S$. In this calculation, the effective ground state is taken as the lowest energy metastable (the $2s^22p^2\ ^1D$ state in this example). In Table 4.1.1, these states are unbracketed. As a prescription for completeness, statistically weighted populations are used to obtain coefficients which tentatively resolve between recombined metastables. This is described in Section 4.1.5. However, the true solution is given by the projection model which distinguishes explicitly between the LS terms in the lowest few quantum shells from the beginning. This will accurately determine cascade and excitation channels.

The calculation for a given pathway involves the excited state population structure connecting the recombining parent $\gamma$ and ground $\rho$. However, alternative parents, which do not act as a recombination starting point, are also considered. These can be populated by Auger transitions from excited states above the autoionisation threshold. For example, consider Figure 4.1.1. The parent and ground states of the pathway are indexed by $\gamma$ and $\rho$ respectively and the alternative parent is indexed by $\sigma$.

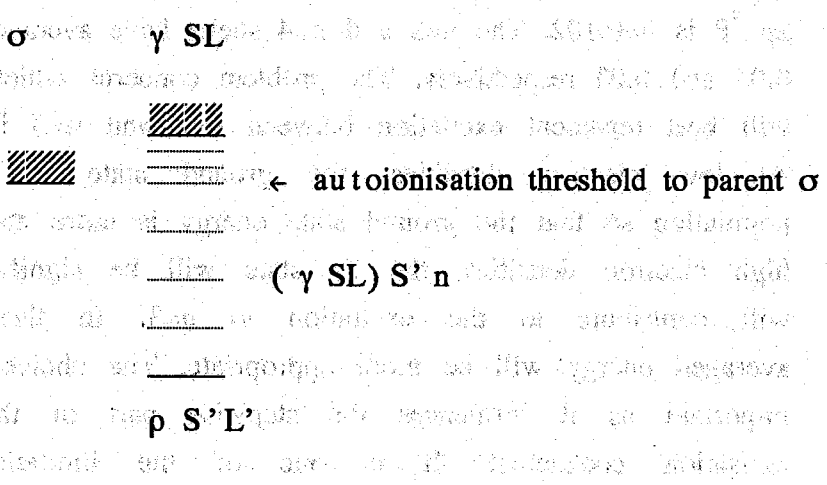


**Figure. 4.1.1:** schematic of model for calculation.

The excited state populations are calculated by first establishing the complete collisional-radiative matrix as done by Burgess and Summers (1976), but with the inclusion of autoionisation processes. Initially, the

maximum n-shell of the calculation was set at $n_{max}$ = 520. This upper limit is necessary for an accurate calculation of the collisional-radiative recombination coefficient. The matrix condensation techniques were exploited with the main inversion for the calculation finally performed for a set of 24 representative levels (as given in Section 2.3, *Literature Review and Scope of Present Work*). The populations were evaluated in the $b_n$ and $c_n$ representations and then converted to the population representation.

The original collisional-radiative ionisation and recombination coefficients of Burgess and Summers (1976), E(2.3.20) and E(2.3.21), are still relevant and give the recombination rate from $\gamma$ to $\rho$ and the total loss rate from $\rho$ (i.e. with no resolution of final parent after ionisation). The recombination coefficient is already correctly parent/metastable resolved and needs no further adjustment. The parent resolved ionisation coefficients and parent cross coupling coefficients are derived by constructing the loss vector from each level. Because the model considers the excited state populations $X^{+z}(\gamma)\ ^{(2S+1)}n$, direct ionisation only populates $X^{+(z+1)}(\gamma)$. The alternative parents are populated by autoionisation. The parent resolved loss vectors are thus given by

$$L_{\gamma i} = n_e S_{\gamma i} \qquad \text{E(4.1.3)}$$

$$L_{\sigma i} = L^{a}_{\sigma i} \qquad \text{E(4.1.4)}$$

Parent resolved ionisation coefficients and parent cross coupling coefficients are obtained from expressions E(2.2.34) and E(2.2.35).

For example, Figure 4.1.2 illustrates the loss vector for excited states $O^{+3}(2s2p\ ^3P)\ ^2n$. This excited state structure is built upon an excited parent so that the excited states can decay by either direct or auto- ionisation. Above the autoionisation threshold, and at low electron densities, autoionisation is the dominant loss mechanism. However, the autoionisation transition probabilities scale as $n^{-5}$ and are independent of electron density, whereas direct ionisation loss rates scale as $n^4$ and vary directly with electron density. For high n-shells, direct ionisation is the dominant loss process. As the electron density increases, direct ionisation becomes the dominant loss process for all n-shells and autoionisation is quenched.

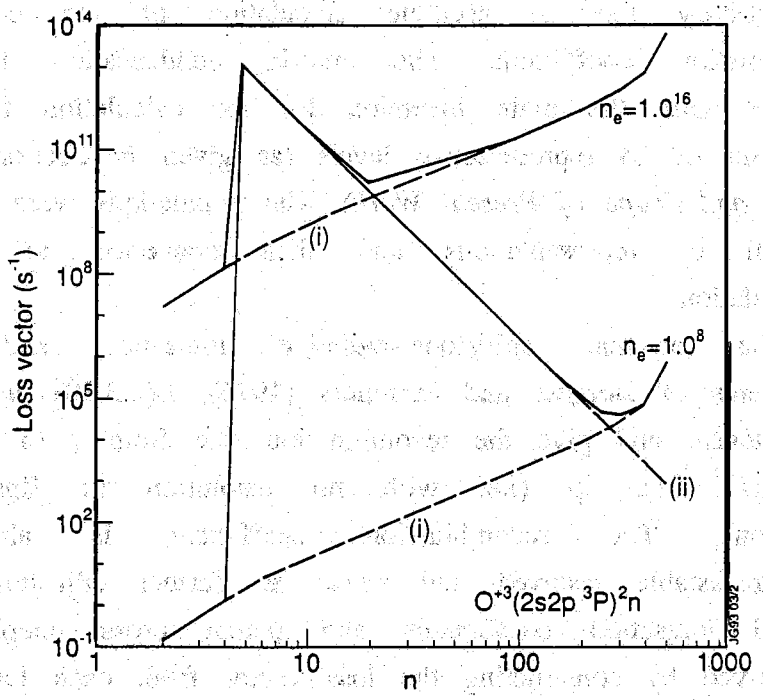


**Figure 4.1.2:** Loss vector for the excited state structure $O^{+3}(2s2p\ ^3P)\ ^2n$. $n_e = 1.0^8$ represents an electron density of $1.0x10^8$ $cm^{-3}$. The solid line is the total. The dotted lines represent (i) direct ionisation to $O^{+4}$ $2s2p\ ^3P$ and (ii) autoionisation to $O^{+4}$ $2s^2\ ^1S$. $T_e = 4x10^4$ K.

The inclusion of autoionisation transition probabilities in the statistical balance equations leads to dramatic changes in the population structure. For example, Figure 4.1.3 illustrates the populations of $C^{+1}$ $(2s^2\ ^1S)\ ^2n$, which are built upon a ground state parent so that no autoionisation pathways are accessible from the excited states. The populations are expressed in terms of the Saha-Boltzmann b factors. The overpopulation of the high n-shells at low electron density is due to dielectronic recombination. As the electron density is increased, the dielectronic recombination influence becomes less due to ionisation of the high n-shell populations. Note that as the electron density increases all the b factors tend to 1 correctly as the system tends to LTE. This illustration is typical for ground state parent configurations.

In contrast, Figure 4.1.4 illustrates the populations of $C^{+1}(2s2p\ ^3P)\ ^2n$. These are built upon an excited parent so that there is a powerful depopulation above the autoionisation threshold. However, as the electron density is increased the collisions start to compete more strongly and the

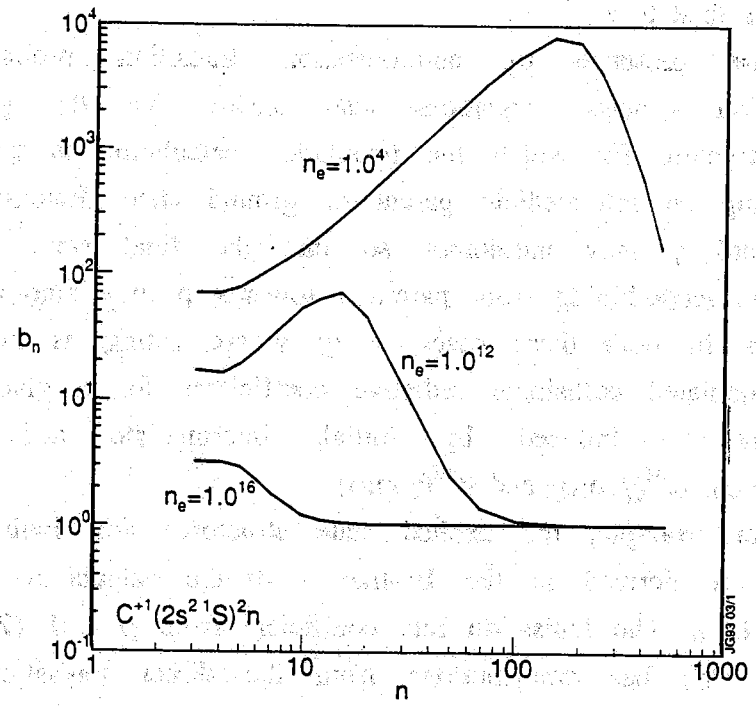


**Figure 4.1.3:** b factors for the excited state populations $C^{+1}$ $(2s^2\ {}^1S)\ {}^2n$. $T_e$ = 4.0x10$^4$K. 1.0$^4$ represents $n_e$ = 1.0x10$^4$ cm$^{-3}$.

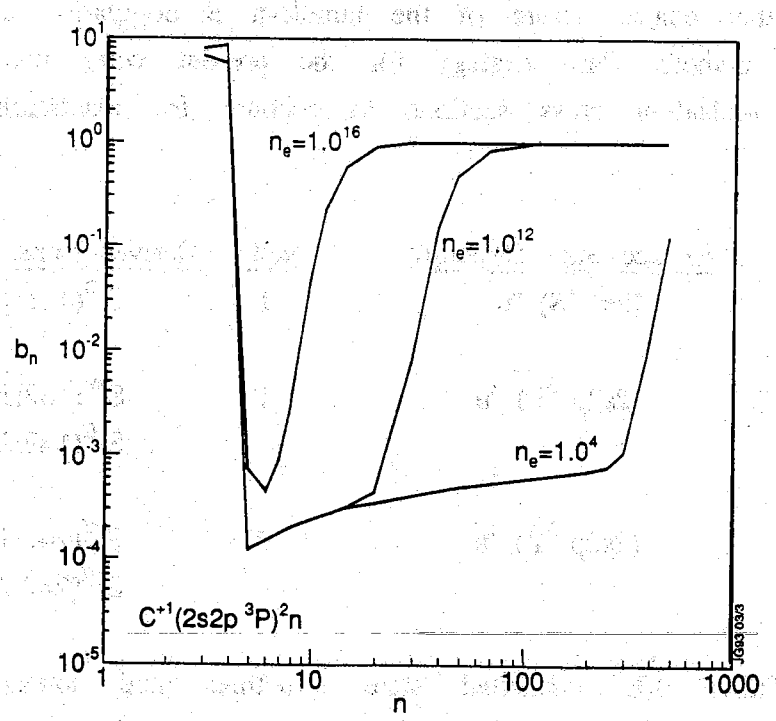


**Figure 4.1.4:** b factors for the excited state populations $C^{+1}$ $(2s2p\ {}^3P)\ {}^2n$. $T_e$ = 4.0x10$^4$K. 1.0$^4$ represents $n_e$ = 1.0x10$^4$ cm$^{-3}$.

b-factors tend to 1.

The presence of autoionisation transition probabilities in the population structure equations also means that the particular excited state structure for which the population calculation is performed is only specifying an intermediate parent or ground state. Electrons excited from $\rho$ toward $\gamma$ may autoionise so that the final state is $\sigma$. Similarly, electrons recombining from parent $\gamma$ towards $\rho$ may autoionise to the final state $\sigma$. In both these cases, $\rho$ or $\gamma$ are acting as intermediate states. The calculated collisional radiative coefficients for a given pathway must therefore be indexed by initial, intermediate and final state - $S^{eff}(\rho\rightarrow\gamma;\sigma)$, $\alpha^{eff}(\gamma\rightarrow\rho;\sigma)$ and $\beta^{eff}(\gamma\rightarrow\rho;\sigma)$.

For example, the excited state structures and ionisation coefficients which are derived in the Be-like - -B-like calculation are recorded in Table 4.1.2. The ionisation rate coefficient from $\rho$ = 1 ($2s^2 2p\ ^2P$) to $\sigma$ = 1 ($2s^2\ ^1S$) has contributions from the direct ionisation of the outer electron excited towards $\gamma$ = 1 and from the excitation autoionisation of 2s electrons excited towards $\gamma$ = 2 ($2s2p\ ^3P$). As discussed in Section 2.3, *Literature Review and Scope of Present Work*, the excitation-autoionisation contributions calculated in this way are not very accurate. This is due to the rather coarse nature of the bundle-n S population structure for the lowest n-shells. The strategy for the present work was to adjust the direct ionisation cross sections to account for excitation- autoionisation

| Parent | Excited State Structure | Met. | Derived Ionis. Coef. | Type |
|---|---|---|---|---|
| 1 | $(2s^2\ ^1S)\ ^2n$ | 1 | $S^{eff}(1\rightarrow1;1)$ | d |
| 2 | $(2s2p\ ^3P)\ ^2n$ | 1 | $S^{eff}(1\rightarrow2;1)$ | e-a |
| | | | $S^{eff}(1\rightarrow2;2)$ | d |
| | $(2s2p\ ^3P)\ ^4n$ | 2 | $S^{eff}(2\rightarrow2;1)$ | e-a |
| | | | $S^{eff}(2\rightarrow2;2)$ | d |

**Table 4.1.2:** Excited state structures and ionisation coefficients calculated for the Be-B series. Ionisation coefficients are indexed by $S(\rho\rightarrow\gamma;\sigma)$ where $\rho$ and $\gamma$ index the metastable and parent states of the calculation and $\sigma$ indexes the final parent. 'd' denotes direct ionisation and 'e-a' denotes inner shell excitation-ionisation contributions.

effects (see Section 3.3.1, *Direct Ionisation and Excitation-Autoionisation from Ground and Metastable Configurations*). The zero density ionisation coefficients which are used as preferred data thus contain autoionisation corrections. Because of this, the excitation-autoionisation contributions explicitly derived by the bundle-n S population structure calculation are not used as adjustments to the ionisation rate coefficient. However, these coefficients are of interest because they allow the collisional- radiative behaviour of the excitation-autoionisation contributions to be investigated.

After the calculations for all relevant pathways for a given ion, it is necessary to obtain the final composite parent cross coupling coefficient by summing over intermediate states

$$\beta^{eff}_{\sigma\gamma} = \Sigma_{\rho}\, \beta^{eff}(\gamma\rightarrow\rho;\sigma) \qquad \text{E(4.1.5)}$$

For example, the parent cross coupling coefficient from $2s2p\ ^3P \rightarrow 2s^2\ ^1S$ includes contributions from recombination from $2s2p\ ^3P$ towards $2s^22p\ ^2P$ and $2s2p^2\ ^4P$. There is no ambiguity over the final state of the ionisation and recombination coefficient. These are simply

$$S^{eff}_{\sigma\rho} = S^{eff}(\rho\rightarrow\gamma;\gamma) \qquad \text{E(4.1.6)}$$

$$\alpha^{eff}_{\rho\gamma} = \alpha^{eff}(\gamma\rightarrow\rho;\rho) \qquad \text{E(4.1.7)}$$

If the autoionisation contributions derived by the bundle-n S population structure calculation coefficient were being used as adjustments to the composite ionisation coefficient, it would have been necessary to sum over intermediate states so that

$$S^{eff}_{\sigma\rho} = \Sigma_{\gamma}\, S^{eff}(\rho\rightarrow\gamma;\sigma) \qquad \text{E(4.1.8)}$$

The model is also used to calculate parent and spin system resolved recombination power coefficients. These were again derived for each parent and spin system excited state structure. The separate components arising from dielectronic stabilisation, cascade and recombination radiation (see Section 2.4, *Radiative Power Loss Coefficients*) were calculated as described in Appendix A4. For convenience an effective spin system

resolved Bremsstrahlung coefficient was defined so that the parent/spin system resolved composite radiated power coefficient is given as

$$P_{RB}(\gamma\rightarrow\rho;z1) = SSYSWT(\gamma\rightarrow\rho).P_B(\gamma,z1) + P_{RC}(\gamma\rightarrow\rho,z1) + P_{RS}(\gamma\rightarrow\rho,z1) + P_{RR}(\gamma\rightarrow\rho,z1) \quad W\ cm^3 \qquad E(4.1.9)$$

where SSYSWT is the spin system weight of the recombined spin system. As for the effective recombination coefficients, the radiated power coefficients do not need to be summed over intermediate states.

### 4.1.2: Numerical Evaluation of Ionisation Coefficients

Consider again the definitions of the collisional-radiative ionisation coefficient as given by Summers and co-workers. This gives the total effective ionisation loss coefficient from the metastable state $\rho$ through the excited state structure as

$$S^{eff}_{\rho\rho}|_{BS} = C_{\rho\rho} - \Sigma_j C_{\rho j} F_{j\rho}$$

$$= L_{\rho\rho} + \Sigma_j C_{j\rho} - \Sigma_j C_{\rho j} F_{j\rho} \qquad E(4.1.10)$$

where $L_{\rho\rho}$ is the total ionisation loss from the ground state, $\Sigma_j C_{j\rho}$ is the total excitation loss from the ground state and $C_{\rho j} F_{j\rho}$ represents the proportion of electrons excited to level j which make it back to the ground state. The terms $C_{j\rho}$ , $C_{\rho j}$ and $F_{j\rho}$ all decrease rapidly with n so that the above expression converges rapidly.

Summers (1969) undertook extensive tests of various interpolation schemes and concluded that the evaluation of these expressions was stable as long as $n_{max}$ was sufficiently high and a sufficient range of representative n-shells was included in the calculation. The representative set in use here was considered suitable.

However, the parent resolved coefficients derived in the present work are not so well conditioned. The coefficient can be re-written as

$$S^{eff}(\rho\rightarrow\gamma;\sigma)|_{PW} = L_{\sigma\rho} + \Sigma_j L_{\sigma j} F_{j\rho} \qquad E(4.1.11)$$

The sum in this expression is weighted to high n-shells due to the

n-scaling of ionisation coefficient. To evaluate this expression reliably, it is thus essential to evaluate the excitation contributions to the highest n-shells accurately. This proved to be a problem for the following reasons.

Consider the populations of $C^{+2}(2s^2\ ^1S)\ ^2n$, and for illustrative purposes the total level set reduced from n=520 to n=30. This enables the calculation to be performed with and without condensation interpolations. The populations, in b-factor form, and excitation contributions are tabulated in Table 4.1.3. Case (1) has no interpolation whereas (2) and (3) use a representative set of levels. The total populations are evaluated with good accuracy both with and without interpolation. However the excitation contributions decrease with n and there is considerable variation in these coefficients for high n-shells.

The influence of this variation on the ionisation coefficients is given in Table 4.1.4. This is a single parent calculation, so the expressions $S^{eff}_{\rho\rho}|_{BS}$ and $S^{eff}(\rho\rightarrow\gamma;\sigma)|_{PW}$ should be equal. With no interpolation, the level set was increased from n=10,20,30 and 40. It can be seen that the two forms of ionisation coefficient are equal and both slowly converge to a constant value as the level set is increased. However when the interpolation scheme is introduced for the $n_{max}$ = 30 calculation, the parent resolved coefficient becomes inaccurate. This is attributed to inaccuracies introduced by the interpolation scheme in the highest n-shell excitation contribution. There is little improvement when the representative level set was adjusted to include the highest 6 shells explicitly. For the calculation involving the full 520 n-shell set with condensation, the coefficient is still in error. This presents considerable difficulties. It is essential to include n shells up to ~ 500 to quantify properly collisional radiative influences on recombination. On the other hand, it is impractical to invert matrices of such size and so matrix condensation techniques are indispensable. In an attempt to solve this problem, the parent resolved C-R coefficient was rewritten so that the sum over excited states is better conditioned. After algebraic manipulation the following expression was considered

$$S^{eff}(\rho\rightarrow\gamma;\sigma)|_{PW\text{-}2} = L_{\sigma\rho} + \Sigma_j\, C_{j\rho} - \Sigma_j\,(C_{\rho j} + \Sigma_{\gamma\neq\sigma}\, L_{\gamma j})\, F_{j\rho}$$

E(4.1.12)

where the sum of loss vectors excluded the parents for which the

Excited state structure $C^{+2}$ $(2s\ ^2S)\ ^1n$

$n_e = 1.0 \times 10^{14}$ cm$^{-3}$ $T_e = 9 \times 10^5$ K

Case (1) $n_{max} = 30$, no interpolation
Case (2) $n_{max} = 30$, 14 representative levels
Case (3) $n_{max} = 30$, 18 representative levels

| | Case (1) | | Case (2) | | Case (3) | |
|---|---|---|---|---|---|---|
| n | $F_{n2}$ | $b_n$ | $F_{n2}$ | $b_n$ | $F_{n2}$ | $b_n$ |
| 2 | | $1.493^{-1}$ | | $1.492^{-1}$ | | 1.491 |
| 3 | $4.697^{-5}$ | 7.590 | $4.668^{-5}$ | 7.585 | $4.696^{-5}$ | 7.582 |
| 4 | $1.600^{-5}$ | 6.058 | $1.588^{-6}$ | 6.053 | $1.599^{-5}$ | 6.051 |
| 5 | $9.119^{-6}$ | 6.498 | $8.923^{-6}$ | 6.492 | $9.100^{-6}$ | 6.489 |
| 6 | $5.425^{-6}$ | 6.322 | $5.322^{-6}$ | 6.322 | $5.395^{-6}$ | 6.318 |
| 7 | $3.072^{-6}$ | 4.934 | $2.473^{-6}$ | 4.920 | $3.031^{-6}$ | 4.914 |
| 8 | $1.731^{-6}$ | 3.430 | $1.619^{-6}$ | 3.413 | $1.681^{-6}$ | 3.406 |
| 9 | $1.001^{-6}$ | 2.664 | $9.026^{-7}$ | 2.664 | $9.436^{-7}$ | 2.636 |
| 10 | $6.000^{-7}$ | 2.174 | $5.026^{-7}$ | 2.152 | $5.327^{-7}$ | 2.144 |
| 12 | $2.418^{-7}$ | 1.621 | $1.685^{-7}$ | 1.600 | $1.847^{-7}$ | 1.591 |
| 15 | $7.963^{-8}$ | 1.280 | $4.963^{-8}$ | 1.273 | $5.517^{-8}$ | 1.264 |
| 20 | $2.186^{-8}$ | 1.110 | $1.425^{-8}$ | 1.115 | $1.528^{-8}$ | 1.105 |
| 25 | $1.078^{-8}$ | 1.064 | $7.738^{-9}$ | 1.072 | $7.736^{-9}$ | 1.062 |
| 26 | $9.872^{-9}$ | 1.059 | | | $7.087^{-9}$ | 1.058 |
| 27 | $9.170^{-9}$ | 1.056 | | | $6.585^{-9}$ | 1.054 |
| 28 | $8.621^{-9}$ | 1.053 | | | $6.191^{-9}$ | 1.051 |
| 29 | $8.189^{-9}$ | 1.050 | | | $5.882^{-9}$ | 1.049 |
| 30 | $7.850^{-9}$ | 1.048 | $6.070^{-9}$ | 1.058 | $5.639^{-9}$ | 1.047 |

**Table 4.1.3:** Effects of interpolation on populations. $b_n$ is the Saha-Boltzmann factor for quantum shell n. $F_{n2}$ is the contribution to $b_n$ from excitation from the n=2 ground state.

Excited state structure $C^{+2}$ $(2s\ ^2S)\ ^1n$

$n_e = 1.0 \times 10^{14}$ cm$^{-3}$ $\quad T_e = 9 \times 10^5$ K

$\rho = 2s^2\ ^1S$ $\quad \gamma = 2s\ ^2S$

(1) $n_{max}$ = 10, no interpolation
(2) $n_{max}$ = 20, no interpolation
(3) $n_{max}$ = 30, no interpolation
(4) $n_{max}$ = 40, no interpolation
(5) $n_{max}$ = 520, 24 representative levels
(6) $n_{max}$ = 30, 14 representative levels
(7) $n_{max}$ = 30, 18 representative levels

| | $S^{eff}(\rho \rightarrow \gamma;\gamma)\|_{PW}$ | $S^{eff}_{\rho\rho}\|_{BS}$ |
|---|---|---|
| case (1) | $5.556^{-9}$ | $5.556^{-9}$ |
| case (2) | $5.730^{-9}$ | $5.730^{-9}$ |
| case (3) | $5.759^{-9}$ | $5.759^{-9}$ |
| case (4) | $5.770^{-9}$ | $5.770^{-9}$ |
| case (5) | $5.333^{-9}$ | **$5.789^{-9}$** |
| case (6) | $5.530^{-9}$ | $5.763^{-9}$ |
| case (7) | $5.586^{-9}$ | $5.763^{-9}$ |

**Table 4.1.4:** Influence of interpolation scheme on the effective ionisation coefficient ($cm^3s^{-1}$). The ionisation coefficient at zero electron density is $5.29^{-9}$ $cm^3s^{-1}$. The value in bold print is derived from the original expression of Burgess and Summers (1976) with $n_{max}$ = 520 and using a representative level set. In this case, is the best estimate of the effective coefficient.

coefficient is required. This coefficient is now similar in structure to that of Burgess and Summers (1976). The terms $L_{\sigma\rho}$ and $\Sigma_j C_{j\rho}$ give the loss from the ground term by ionisation and excitation. The term $(C_{\rho j} + \Sigma_{\gamma \neq \sigma} L_{\gamma j}) F_{j\rho}$ gives the fraction of electrons that are excited to level j that either return to the ground state or ionise to another parent. Indeed for a single parent calculation, this coefficient is identical to that of Burgess and Summers. This coefficient proved to be more accurate than the previous parent resolved coefficient but inaccuracies in the calculated parent resolved coefficients were still obtained. This is due to the presence of the loss vector in the summation which again weights the summation to higher n-shells.

However, it is apparent from Table 4.1.4 that a reasonable estimate of the collisional-radiative ionisation coefficient can be obtained from a calculation spanning 30 or 40 n-shells. It was thus decided to perform two separate calculations. The recombination coefficient is obtained from a calculation with $n_{max}$ = 520 and with 24 representative levels. This calculation is also used for completeness to give the total ionisation rate using the expression of Summers and co workers. The parent resolved ionisation coefficients and the parent cross coupling coefficients are therefore obtained from a smaller calculation with $n_{max}$=40 and no interpolation. This proved to be an acceptable solution. In all cases the sum of the parent resolved ionisation coefficients derived from the 40x40 calculation were within a few percent of the total ionisation coefficient from the 520x520 calculation in the worst case, and generally within 0.5%.

### 4.1.3: Calculation Methodology

The methodology of the bundle-n S calculation is summarised in the flow chart, Figure 4.1.5. After selection of a particular ion, a bundle-n S calculation is performed for each ionisation/recombination pathway. At the end of the calculation, the parent cross coupling coefficients are summed over intermediate states.

Preferred atomic data was drawn as input from external sources at the start of each calculation. This included (zero density) ionisation rate coefficients, dielectronic recombination rate coefficients and autoionisation transition probabilities. Other internally calculated data used in the procedures are described in detail in Chapter 3.

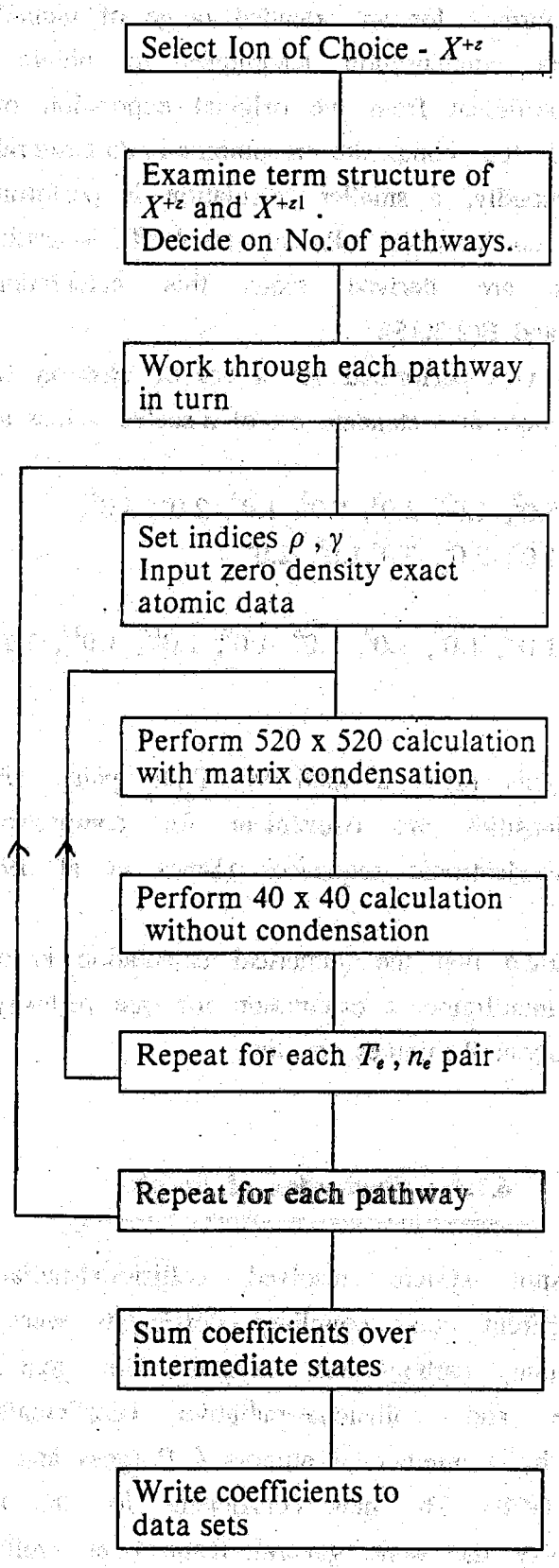


**Figure 4.1.5:** Flow chart of bundle-n S calculation

Two calculation procedures are performed for each pathway. Firstly, the calculation is performed for an extended range of n-shells ($n_{max}$ = 500) and uses the matrix condensation techniques to obtain the effective recombination rate coefficient from the original expression of Burgess and Summers (1976) and the composite recombination/bremsstrahlung radiated power coefficient. Secondly, a smaller calculation is performed with $n_{max}$ = 40 without matrix condensation. Parent resolved ionisation and cross coupling coefficients are derived from this calculation using the expressions E(2.2.34) and E(2.3.35).

Each calculation was performed for a set of electron temperature and density values. These were at a standard set of z-scaled values as follows

$$\frac{T_e/z1^2}{K} = 5.0^2,\ 1.0^3,\ 2.0^3,\ 5.0^3,\ 1.0^4,\ 2.0^4,\ 5.0^4,\ 1.0^5,\ 2.0^5,\ 5.0^5, 1.0^6,\ 2.0^6$$

$$\frac{n_e/z1^7}{cm^{-3}} = 1.0^{-3},\ 1.0^0,\ 1.0^3,\ 1.0^6,\ 1.0^9,\ 1.0^{12},\ 1.0^{15},\ 1.0^{18}$$

where z1 = z+1. This gives a total 96 $T_e/n_e$ pairs. Use of z-scaled temperatures and densities are convenient for comparison of derived coefficients along iso-electronic sequences (Bates et al 1963, McWhirter and Summers 1983).

It should be noted that the numerical calculation is quite large. On the JET IBM 3090 mainframe, a calculation for one pathway, involving 96 $T_e/n_e$ pairs, requires about 8 minutes cpu time.

### 4.1.4: Illustration of Results

Parent and spin system resolved collisional-radiative ionisation, recombination and parent cross coupling coefficients were calculated for all ions of beryllium, carbon and oxygen. The general features of population structure and collisional-radiative coefficients have been discussed previously by a number of authors ( Burgess and Summers 1976, Jacobs and Davis 1978). The new coefficients for the parent/metastable resolved model display the same general features as well as some new aspects which are unique to a resolved model.

**(a) Ionisation Coefficients**

The ionisation coefficients calculated with the excited state structures $C^{+1}(2s^2\ ^1S)\ ^2n$ and $C^{+1}(2s2p\ ^3P)\ ^2n$ are illustrated in Figure 4.1.6. The density dependent collisional- radiative increase in the ionisation coefficient is only visible for $S^{eff}(1\rightarrow1;1)$.

Figure 4.1.7 examines the variation with density of the collisional radiative ionisation coefficients derived for the $C^{+1} \rightarrow C^{+2}$ calculation. This is plotted at an electron temperature of $4.0x10^4$ K, which is the temperature of maximum abundance of $C^{+1}$ in equilibrium ionisation balance (Arnaud and Rothenflug 1985). At electron densities greater than ~ $10^{11}$ $cm^{-3}$, the 'direct' ionisation coefficients for a spin system to its natural parent start to increase due to stepwise ionisation. The coefficients continue to rise until the excited state populations reach LTE, at which point a constant value is attained. The contributions from excitation-autoionisation show a different behaviour with electron density. As the electron density is increased, the rate of collisional stabilisation becomes greater than that for autoionisation and so these coefficients decrease with electron density. Due to the magnitude of the autoionisation transition probabilities, the density onset for collisional radiative effects is much higher for excited state structure involving autoionisation from excited states. Autoionisation transition probabilities for the forbidden pathway from the quartet spin system, $S^{eff}(2\rightarrow2;1)$ are much smaller than for the allowed pathway $S^{eff}(1\rightarrow2;1)$, so that the forbidden contribution starts to decrease at a much lower density. However, the threshold for collisional-radiative effects on the 'indirect' ionisation rate coefficients involving autoionising pathways is at an electron density greater than those attained in the JET experiment (~$10^{14}$ $cm^{-3}$). Also illustrated in Figure 4.1.7 is the ionisation coefficient calculated by Summers (1974) with the bundle-n model. This should be compared with the sum of losses from $2s^22p\ ^2P$. The absolute value of the coefficient at zero density differs substantially and reflects the difference in input data. Summers (1974) used the ECIP approximation for the ground state ionisation rate whereas the present work is based upon a separation of experimental data. However, the main reason for plotting the coefficient of Summers (1974) was to compare the density dependence of the collisional- radiative coefficient. It can be seen that the bundle n-S model retains the behaviour of the original bundle-n model. The above examples serve to illustrate the main features of the ionisation coefficients calculated by the bundle n-S model.

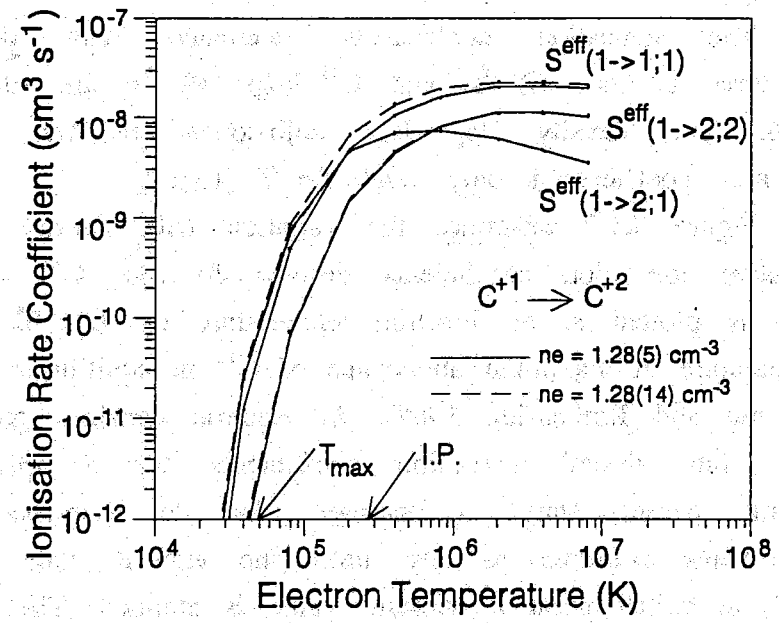


**Figure 4.1.6:** Effective ionisation coefficient calculated from the excited state structures $C^{+1}(2s^2\ ^1S)\ ^2n$ and $C^{+1}(2s2p\ ^3P)\ ^2n$. IP marks the ground state ionisation potential of $C^{+1}$ and $T_{max}$ marks the temperature of maximum abundance of $C^{+1}$ in equilibrium ionisation balance.

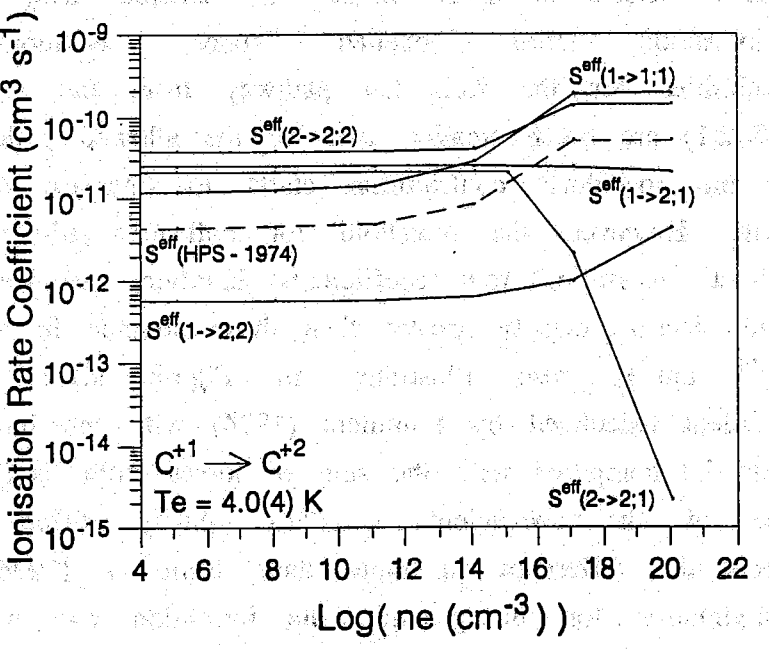


**Figure 4.1.7:** Behaviour of effective ionisation coefficients for all pathways between $C^{+1}$ and $C^{+2}$ as a function of electron density. The coefficients are indexed by $S^{eff}(\rho\rightarrow\gamma;\sigma)$, where $\rho$ and $\gamma$ are the ground and parent states of the population calculation and $\sigma$ is the final parent state.

**(b) Recombination and Parent Cross Coupling Coefficients**

These two coefficients are considered together because they are both driven by recombination processes and display similar behaviour. A typical recombination coefficient for a ground state parent is illustrated in Figure 4.1.8. This is for $O^{+3}$ $2s^2 2p\ ^2P \rightarrow O^{+2}$ $2s^2 2p^2\ ^3P$, which was calculated from the excited state structure $O^{+2}(2s^2 2p\ ^2P)\ ^3n$. The influence of electron density is much greater than for ionisation coefficients because of the high n-shell captures occurring in dielectronic recombination. The initial decrease in the coefficient as the electron density is increased is due to the ionisation of electrons captured into high n-shells. As the electron density is increased, the populations tend to LTE and three body recombination becomes the dominant recombination process. As the three body coefficient is included in the composite two body coefficient this ultimately causes a linear increase in the effective coefficient with density.

In contrast, Figure 4.1.9 illustrates the recombination coefficient from a metastable parent. This is for $O^{+3}$ $2s2p^2\ ^4P \rightarrow O^{+2}$ $2s^2 2p^2\ ^3P$. This is much smaller because of autoionisation of electrons captured above the secondary Auger threshold. Also, these coefficients do not show the usual strong collisional-radiative dependence on density until a much higher value of electron density. This is because the electron density has to be sufficiently high so that collisional redistribution of the captured electrons exceeds autoionisation.

The parent cross coupling coefficient due to autoionisation of recombining electrons is illustrated in Figure 4.1.10. This is for $O^{+3}$ $2s2p^2\ ^4P \rightarrow O^{+3}$ $2s^2 2p\ ^2P$ and arises from recombination from $O^{+3}$ $2s2p^2\ ^4P$ towards the tripet and quintet spin systems. This coefficient increases with density at the onset of three body recombination into the high n-shells. It is interesting to compare the scaling of the total loss rate from $O^{+3}$ $2s2p^2\ ^4P$ due to recombination and parent cross coupling coefficients. These are given in Table 4.1.5. It can be seen that the recombination coefficients do not vary linearly with electron density at the highest densities as expected. In some cases, the coefficient is increasing faster than the electron density, at the same time as the parent cross coupling coefficient is decreasing. These features are due to collisional de-excitation of the recombined electrons becoming more efficient than autoionisation. The total loss rate for the $O^{+3}$ $2s2p^2\ ^4P$ state follows the expected linear behaviour with electron density at the highest values of electron density.

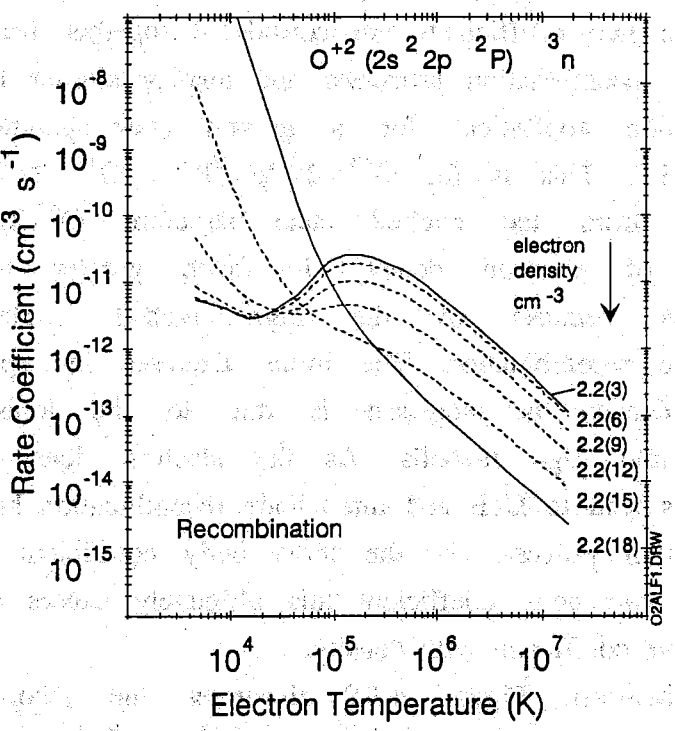


**Figure 4.1.8:** Total recombination rate coefficient calculated from the excited state structure $O^{+2}(2s^2 2p\ ^2P)\ ^3n$. Full curves are for the lowest and highest electron density values plotted, dashed curves are for intermediate values. 2.2(3) represents an electron density of $2.2 \times 10^3$ $cm^{-3}$.

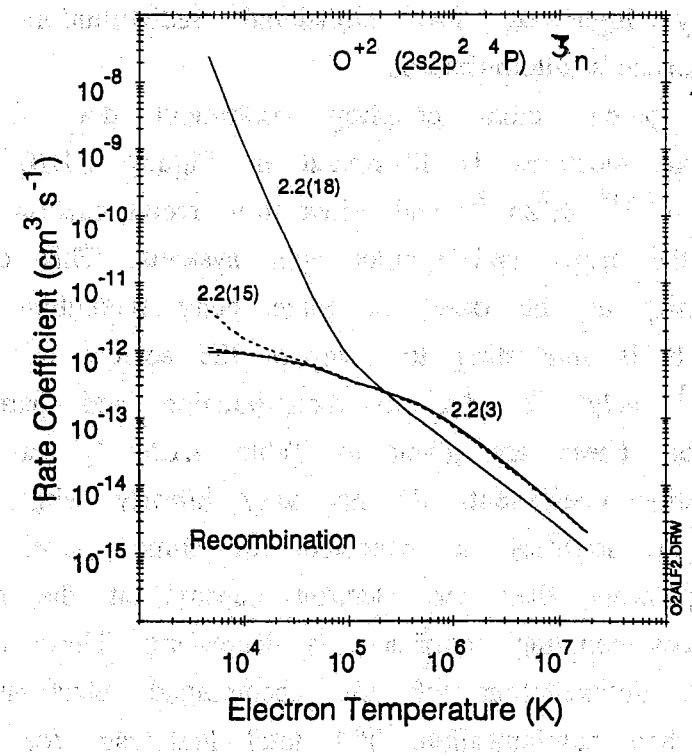


**Figure 4.1.9:** Total recombination rate coefficient calculated from the excited state structure $O^{+2}(2s2p^2\ ^4P)\ ^3n$. Annotation as Fig. 4.1.8.

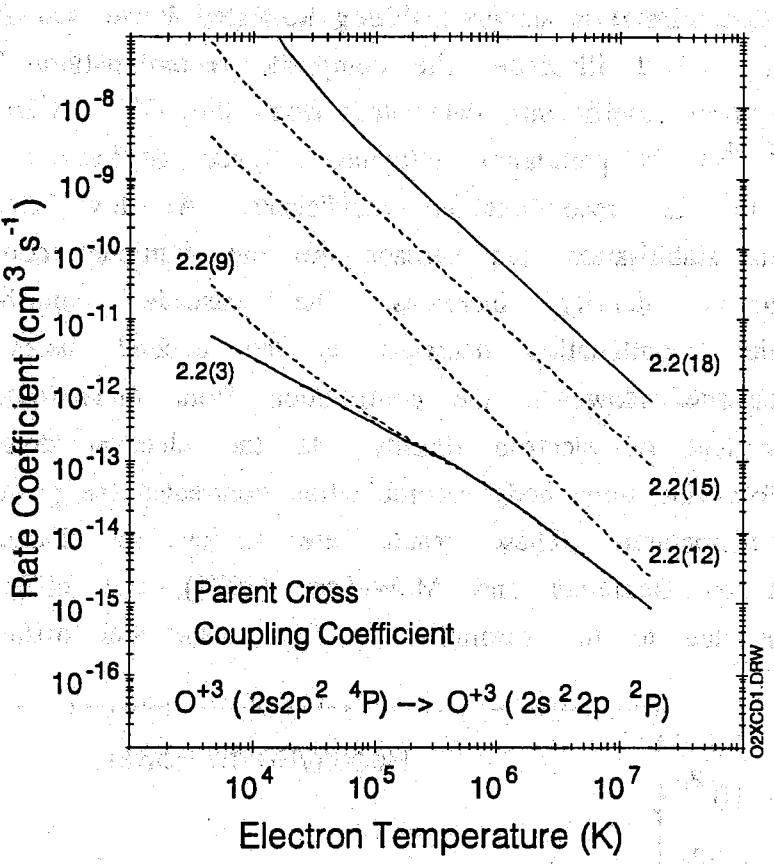


**Figure 4.1.10:** Parent cross coupling coefficient for $O^{+3}$ $2s2p^2$ $^4P \rightarrow O^{+3}$ $2s^2 2p$ $^2P$ derived from the $O^{+2}(2s2p^2$ $^4P)$ $^3n$ and $O^{+2}(2s2p^2$ $^4P)$ $^5n$ excited state structures. Annotation as Figure 4.1.7.

| Electron Density ($cm^{-3}$) | 2.19(12) | 2.19(15) | 2.19(18) | 2.19(21) |
|---|---|---|---|---|
| Coefficient ($cm^3 s^{-1}$) | | | | |
| $\alpha^{eff}(2s2p^2$ $^4P \rightarrow 2s^2 2p^2$ $^3P)$ | 1.09(-12) | 3.95(-12) | 2.34(-8) | 4.05(-3) |
| $\alpha^{eff}(2s2p^2$ $^4P \rightarrow 2s2p^3$ $^5S)$ | 3.18(-12) | 2.24(-10) | 6.90(-6) | 7.12(-3) |
| $\beta^{eff}(2s2p^2$ $^4P \rightarrow 2s^2 2p$ $^2P)$ | 3.02(-9) | 6.92(-8) | 5.33(-6) | 2.24(-4) |
| Total | 3.02(-9) | 6.94(-8) | 1.46(-5) | 1.14(-2) |

**Table 4.1.5:** recombination rate coefficients and parent cross coupling coefficients from $O^{+3}$ $2s2p^2$ $^4P$. $T_e = 4.5 \times 10^3 K$.

**(c) Recombination Bremsstrahlung Radiated Power Coefficients**

Figure 4.1.11 illustrates the composite recombination/ bremsstrahlung radiated power coefficients calculated from the $O^{+2}$ $(2s^2 2p\ ^2P)\ ^3n$ and $O^{+2}(2s2p^2\ ^4P)\ ^3n$ population structures. These coefficients have similar features to the recombination coefficients. At low electron density dielectronic stabilisation and cascade are the dominant contributions. As the electron density increases, the cascade contributions from dielectronic recombination decrease as the excited states are ionised before cascade. However, the contribution from dielectronic stabilisation is independent of electron density. As the electron density increases, cascade following three body recombination dominates the power loss at low electron temperature. These results are similar in character to those calculated by Summers and McWhirter (1979), but differ in absolute magnitude due to the resolution in final state and differences in the

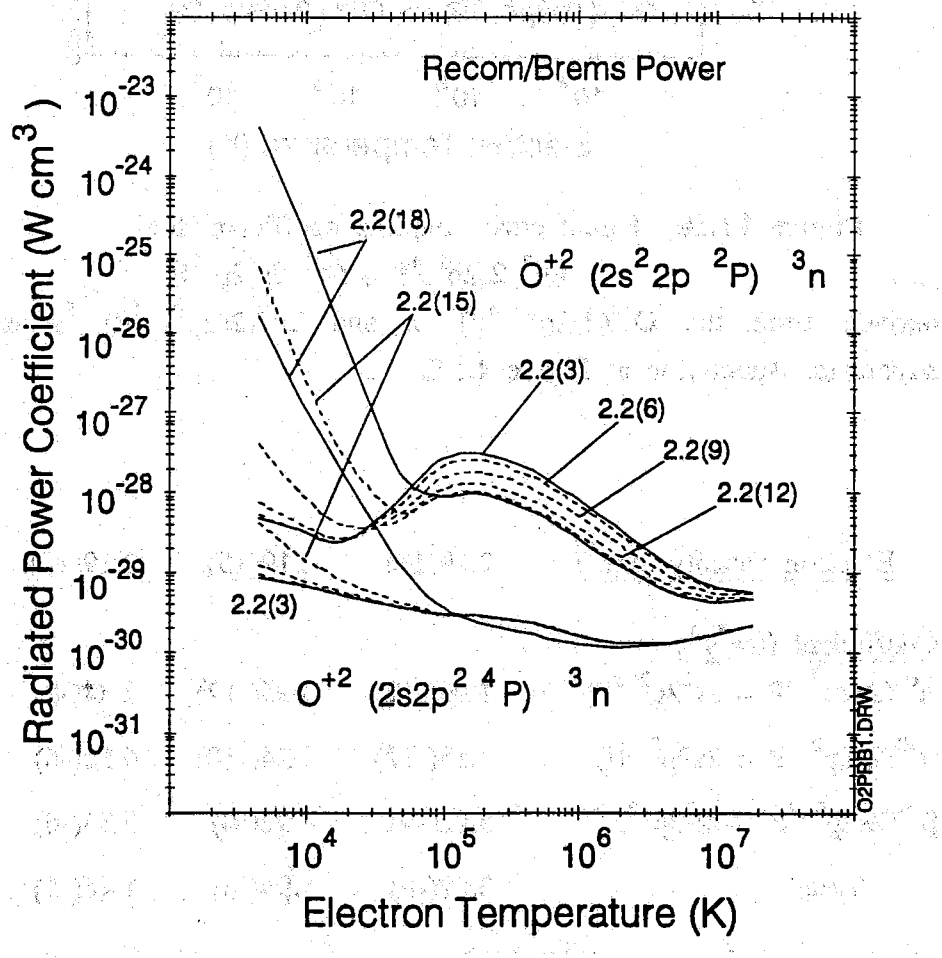


**Figure 4.1.11:** Composite recombination and bremsstrahlung radiated power coefficients derived from the $O^{+2}(2s^2 2p\ ^2P)\ ^3n$ and $O^{+2}(2s2p^2\ ^4P)\ ^3n$ excited state structures. Annotation as Figure 4.1.8.

dielectronic recombination data. The radiated power function for the metastable parent $O^{+3}$ $2s2p^2$ $^4P$ is two orders of magnitude smaller than that from the ground state parent. This is because the dielectronic stabilisation contribution and cascade contributions are reduced by autoionisation.

### 4.1.5: Resolution Within Spin Systems

A manipulation is required for completeness in the case of a parent recombining into a spin system which has more than one metastable. Namely,

| Recombining Ion Sequence | Recombined Spin System | Recombined Met. Indices |
|---|---|---|
| B-like | singlet | 2,3 |
| C-like | doublet | 2,3 |
| N-like | singlet | 2,3 |

The recombination and radiated power coefficients calculated in the previous subsections give a recombination coefficient from a particular parent to a particular spin system. Let this be denoted by $\alpha^{eff}(\gamma \rightarrow isys)$. The resolved coefficients are tentatively obtained by determining the proportions of this total which cascade to each metastable

$$\alpha^{eff}(\gamma \rightarrow isys,\rho) = \omega(\rho)\ \alpha^{eff}(\gamma \rightarrow isys) \qquad E(4.1.11)$$

$$P_{RB}^{eff}(\gamma \rightarrow isys,\rho) = \omega(\rho)\ P_{RB}^{eff}(\gamma \rightarrow isys) \qquad E(4.1.12)$$

Similarly, the ionisation coefficient calculated in the above subsections is the sum of direct losses from the effective ground state and ionisation/auger losses from excited states

$$S^{eff}(isys \rightarrow \gamma) = S_{\gamma\rho} + S^{ex}(isys \rightarrow \gamma) \qquad E(4.1.13)$$

The resolved coefficients are again obtained by assigning proportions of the excited state losses which arise from each initial metastable

$$S_{\gamma\rho}^{eff} = S_{\gamma\rho} + \omega(\rho)\ S^{ex}(isys \rightarrow \gamma) \qquad E(4.1.14)$$

To a first approximation, the factors $\omega(\rho)$ are prescribed in proportion to

the statistical weights of the initial metastables. The more complete solution is to use the results from the projection/expansion calculation (see Section 4.3) in which the metastables and lowest excited levels are LS resolved from the beginning. This will accurately determine cascade pathways and excitation contributions.

### 4.1.6: Concluding Remarks

The parent resolved bundle n-S model has enabled parent and spin system resolved effective ionisation and recombination coefficients and recombination and bremsstrahlung radiative power coefficients to be calculated. The behaviour of the collisional-radiative coefficients with temperature, density and ion charge agree with general previous work giving confidence in the consistency of the new model.

The inclusion of autoionisation transition probabilities in the equations of statistical balance leads to dramatic changes in the population structure. The model copes with these stably, with Saha-Boltzmann populations always being correctly recovered at high electron density. Autoionisation contributions to the ionisation rate coefficients can be resolved. Although these are not of high precision due to the bundle-n S population structure for the lowest few n-shells, it is very revealing of the collisional-radiative behaviour of the new more complex coefficients. The autoionisation contribution to ionisation does not exhibit any strong electron density dependence with electron density until a value which is larger than that of JET experimental conditions. This justifies the practice of 'adding on' autoionisation contributions as a zero density correction to the direct ionisation rate coefficient.

The recombination rate coefficients from metastable parents are considerably less than those from ground state parents. Indeed, the parent cross coupling coefficients are of comparable magnitude to these coefficients and both must be considered together to give the total depopulation rate of metastable parents due to recombination processes.

In a simplistic way, statistical weight factors can be used to partition recombined metastables within a spin system. This procedure is not expected to be very reliable (see however Section 4.3).

# 4.2: THE LOW LEVEL RESOLVED MODEL


4.2.1: Introduction
4.2.2: Populations and Spectral Emission
4.2.3: Cross-Coupling Coefficients and Relaxation Timescales
4.2.4: Concluding Remarks


## 4.2.1: Introduction

In contrast to the bundle-n approach for collisional-radiative modelling, high precision low level populations are derived by considering individual transitions between a closed set of resolved levels

$$n\ l\ ^{(2S+1)}L \qquad \text{with } n_{min} \leq n \leq n_{max}$$

where $n_{min}$ = 1 or 2 (depending on the particular isoelectronic- sequence) and $n_{max}$ = 3- 5 (depending on the availability of resolved data in the present work). The low level group encompasses all relevant parent and spin systems groups. For example, Figure 4.2.1 illustrates the main levels included in the $O^{+2}$ low level model, which is typical of carbon-like ions. The $2s^22p^2\ ^3P$, $2s^22p^2\ ^1D$, $2s^22p^2\ ^1S$ and $2s2p^3\ ^5S$ metastables, $2s^22p\ ^2P$ and $2s2p^2\ ^4P$ parents and 19 normal excited states within n=2 and n=3 are present. Terms belonging to the $2p^4$ configuration are included but not shown in the figure to avoid confusion.

The present work developed the low level population model originally outlined by Gordon et al (1985) and Summers and Wood (1988). The minimum data input for this model is a defined set of low levels, including a distinction between metastable and normal excited states, and then all radiative transition probabilities and collisional rate coefficients for transitions between these levels. For the present work the original model was extended by

(i) Allowing several parent states in the $X^{+z1}$ ion to be specified.

(ii) Including ionisation from metastables and excited bound levels to specific parents.

(iii) Including radiative, dielectronic and three body recombination rate coefficients from specific parents to specific metastables and excited states.

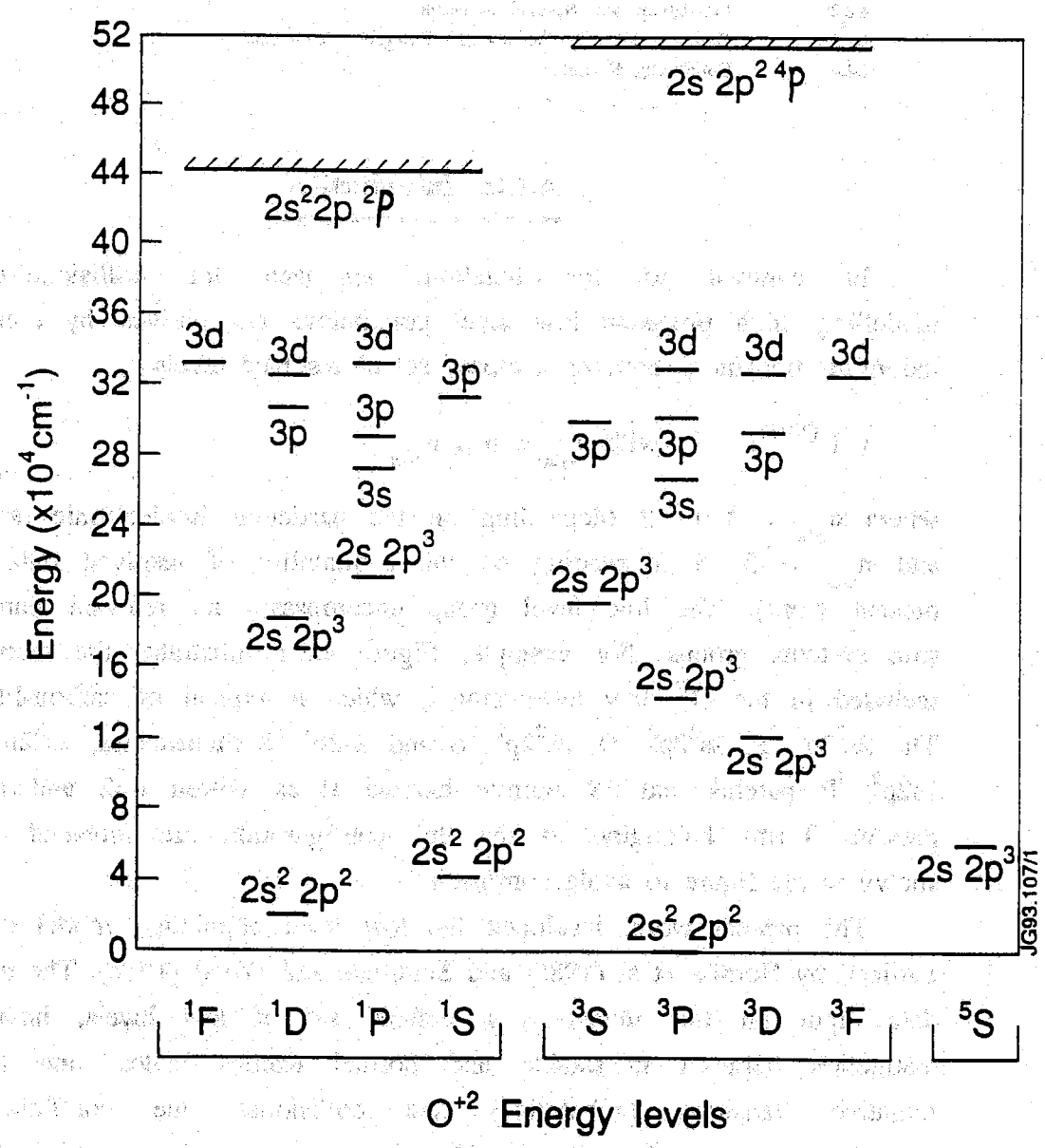


**Figure 4.2.1:** Term diagram for $O^{+2}$. 4 metastables, 2 parents and 19 normal excited states are illustrated.

(iv) Including charge exchange reactions between specific parent ions and neutral hydrogen to specific metastables and excited states.

Although the present work does not include a systematic study of charge transfer reactions, the model has been developed to deal with this process if required and for completeness the charge transfer contributions are retained in the equations presented in this section. Some preliminary work on the influence of charge transfer on the spectral emission of carbon in fusion plasmas has been undertaken by Maggi (1992) exploiting the models developed in this thesis. Another limitation of the low level model is that explicit autoionisation transition probabilities are not included. Excited states above the lowest ionisation threshold are assumed to autoionise with unit probability. This is not a simplification as these levels do not contribute to spectral emission.

The main quantities calculated by the model are low level populations, effective contributions to the populations, effective emission coefficients, total radiated line power and collisional-radiative coefficients. The collisional- radiative coefficients in this model depend only on processes directly involving the low level group. They do not include the influence of recombination or excitation to higher levels outside the low level set followed by cascade or ionisation. The ionisation and recombination coefficients are therefore, at this point intermediate and are not examined in this section but reserved for discussion in the context of results from the projection model in the following section.. However, the metastable cross coupling coefficients are discussed fully. Also, the relaxation times of metastable states are studied in this section and compared with the relaxation times of the normal excited states and ionisation timescales.

The model can address an arbitrary number of metastables for each ion. If only the ground state is specified as being metastable then an equilibrium balance of all populations is calculated. With this option, the effective contributions, emission coefficients and radiated power coefficients are derived in terms of the ground state population only. This is the actual situation for hydrogen- like and lithium- like ions, which have no additional metastables. For the other isoelectronic sequences, the excited state populations are first solved for effective contributions due to excitation and recombination from each individual metastable and parent metastable as

$$N_i^{+z} = \Sigma_\rho F(i,\rho)\, n_e\, N_\rho^{+z} + \Sigma_\gamma R(i,\gamma)\, n_e\, N_\gamma^{+z1} + \Sigma_\gamma C(i,\gamma)\, n_H\, N_\gamma^{+z1}$$

E(4.2.1)

where the symbols are as defined in Section 2.2, *Population Structure and Spectral Emission Theory.* A final equilibrium balance can then be completed to give the relative populations of the ground and metastable states as determined by excitation, ionisation and radiative processes within the low level group only. The equilibrium excited state populations are then again expressible in terms of the ground state population (which has $\rho$=1) as

$$N_i^{+z} = \left( \Sigma_\rho F(i,\rho)\, n_e\, (N_{\rho\text{-}eq}^{+z} / N_{\rho=1}^{+z}) \right) N_{\rho=1}^{+z}$$

E(4.2.2)

where $(N_{\rho\text{-}eq}^{+z} / N_{\rho=1}^{+z})$ are the equilibrium metastable fractional populations. Recombination contributions can be included in the equilibrium calculation only if the relative abundances of the $X^{+z}$ and $X^{+z1}$ stage populations are known.

### 4.2.3: Populations and Spectral Emission

The equilibrium populations of some levels of $O^{+2}$ are plotted in Figure 4.2.2. The calculation assumes an equilibrium balance of the entire level set and expresses populations in terms of their ratio to the ground state population. The behaviour of the populations can be understood by considering a simple excitation/radiative cascade model, in which it is assumed that the excited state is only populated by collisional excitation from a ground or metastable state and is depopulated by radiative cascade or by collisional de-excitation. The ratio of the excited state population (i) to that of the ground ($\rho$) is given by

$$N_i^{+z} / N_\rho^{+z} = \frac{n_e\, q_{i\rho}^e}{n_e\, \Sigma_j\, q_{ji}^e + \Sigma_j\, A_{ji}^r}$$

E(4.2.3)

where $q_{i\rho}^e$ and $q_{ji}^e$ represent the rate coefficients for collisional excitation from the ground state and collisional de-excitation from i

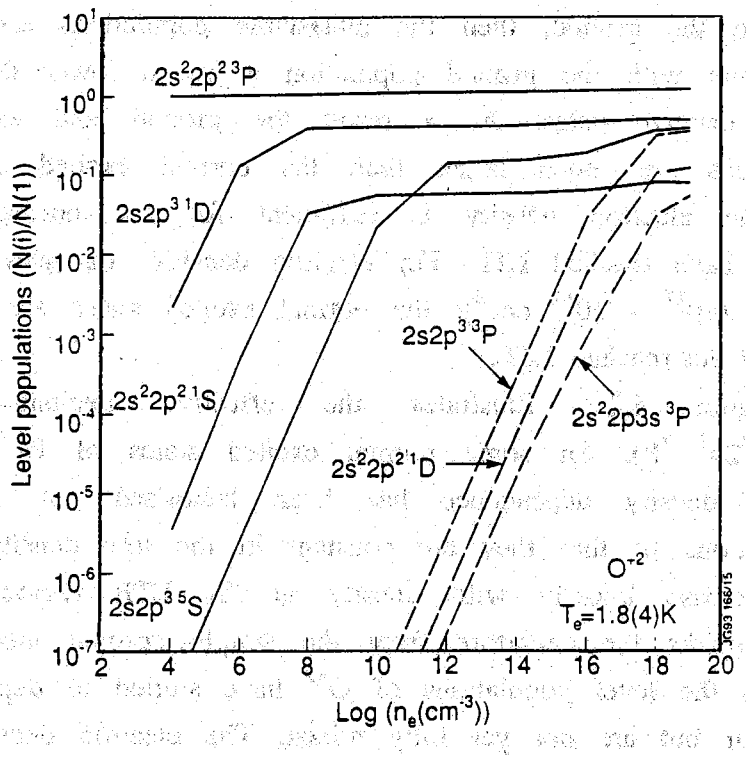


**Figure 4.2.2:** Equilibrium populations for some metastable (full lines) and normal excited states (dashed lines) of $O^{+2}$. Expressed in terms of the ground state population.

respectively, and $A^r_{ji}$ are spontaneous emission transition probabilities.

In the limit of low electron density, the collisional de-excitation rate is very small compared to the radiative decay rate and the population can be expressed as

$$N_i^{+z}/N_\rho^{+z} = n_e \left( q^e_{i\rho} / \Sigma_j A^r_{ji} \right) \qquad \text{E(4.2.4)}$$

In this situation, at a given temperature, excited state populations increase linearly with the electron density. This is the familiar 'coronal approximation'.

At higher electron densities, the rate of collisional redistribution amongst excited states may be comparable to that of radiative decay so that the populations are more complex functions of electron density and electron temperature. As the electron density is increased further, collisional processes eventually dominate and the populations tend to LTE and are constant with electron density.

The low and high density limits can be seen in Figure 4.2.2. Since the metastable levels have small transition probabilities for radiative

decay to the ground, then the metastable populations establish collisional equilibrium with the ground population at much lower densities than the normal excited states. As a result the ground and excited metastable populations are much larger than the normal excited state populations, until the electron density is sufficient for the normal excited states also to have reached LTE. For electron densities of relevance to tokamak plasmas ($10^{12}$ - $10^{14}$ $cm^{-3}$), the normal excited states are approaching but have not yet reached LTE.

Figure 4.2.3 illustrates the effective excitation contributions, F(i, $2s^2 2p^2\ ^3P$), for some normal excited states of $O^{+2}$. Note that the electron density dependence has been factorised out of the effective contributions so that they are constant in the low density coronal region and decrease linearly with density in the LTE region. The transition region marks the departure from the simple coronal model. At tokamak densities the level populations of $O^{+2}$ have started to depart from coronal behaviour but are not yet fully mixed. The electron density threshold for onset of collisional redistribution is a function of ion charge. For comparison, Figure 4.2.4 plots effective contributions to populations of some excited states of $Be^{+0}$. In this case, the effective contributions are influenced by collisional redistribution and direct ionisation of excited states at densities appropriate to fusion plasmas. From both these diagrams it can be seen that the separate LS terms are not statistically populated until collisional redistribution has occurred at high electron density.

Spectral intensities for radiative transitions within the low level group are synthesised from the effective emission coefficients

$$I(i \rightarrow j, \lambda) = A_{ji} N_i^{+z}$$

$$= \Sigma_\rho \varepsilon_{ex}^{eff}(\lambda,\rho)\, n_e\, N_\rho^{+z} + \Sigma_\gamma \varepsilon_{rec}^{eff}(\lambda,\gamma)\, n_e\, N_\gamma^{+z1} + \Sigma_\gamma \varepsilon_{cx}^{eff}(\lambda,\gamma)\, n_H\, N_\gamma^{+z1} \qquad E(4.2.5)$$

where

$$\varepsilon_{ex}^{eff}(\lambda,\rho) = A_{ji}\, F(i,\rho) \qquad E(4.2.6)$$

$$\varepsilon_{rec}^{eff}(\lambda,\gamma) = A_{ji}\, R(i,\gamma) \qquad E(4.2.7)$$

$$\varepsilon_{cx}^{eff}(\lambda,\gamma) = A_{ji}\, C(i,\gamma) \qquad E(4.2.8)$$

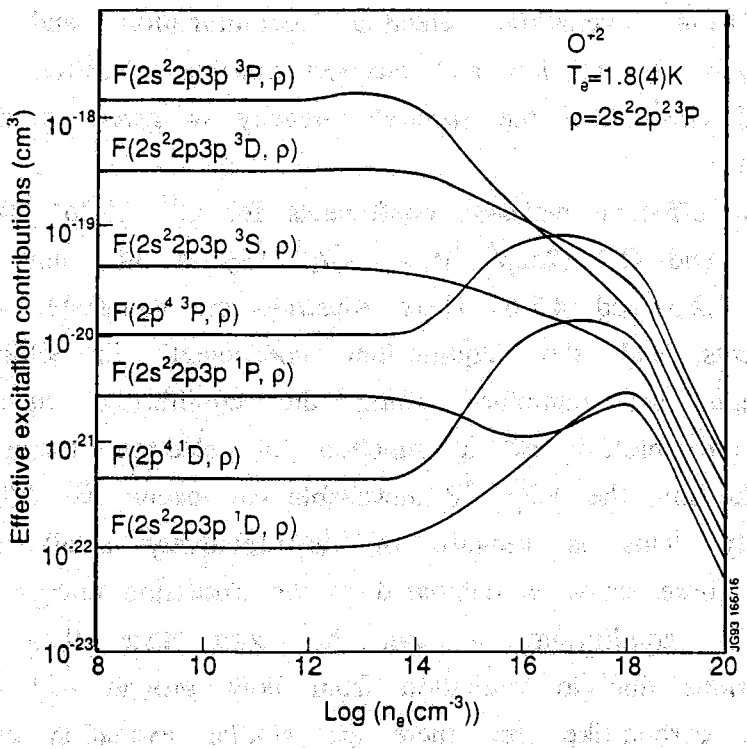


**Figure 4.2.3:** Effective excitation contributions to populations of some normal excited states of $O^{+2}$. $2s^2 2p^2\ ^3P$ metastable.

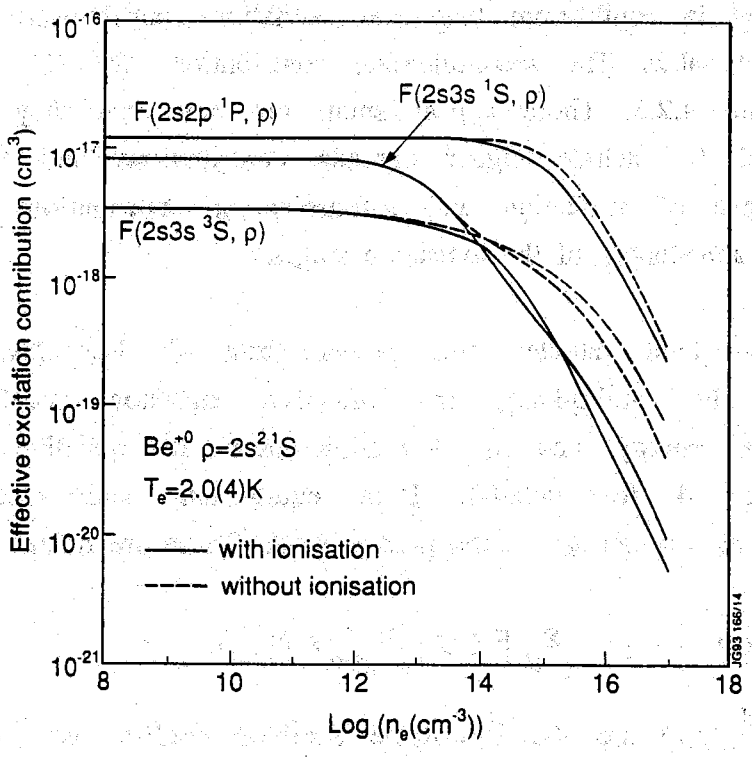


**Figure 4.2.4:** Effective excitation contributions to populations of some normal excited states of $Be^{+0}$. $2s^2\ ^1S$ metastable.

result from excitation, electron recombination and charge transfer respectively. If the ion and electron densities densities are expressed in units of $cm^{-3}$, then the spectral intensity is given in units of (photons $s^{-1}$ $cm^{-3}$).

The effective emission coefficients for $C^{+1}$ ($2s2p^2$ $^2D$ - $2s^22p$ $^2P$) at 133.5nm and $O^{+2}$ ($2s2p^3$ $^1P$ - $2s^22p^2$ $^1S$) at 59.7 nm are illustrated in Figures 4.2.5 and 4.2.6. These illustrate the metastable resolved emission coefficients and the 'equilibrium coefficient' in which the resolved coefficients are combined using the equilibrium metastable fractions. These are plotted as a function of electron temperature. For the boron-like ion, the $2s2p^2$ $^4P$ metastable can excite the $2s2p^2$ $^2D$ state very efficiently. This is because of the relatively small energy difference between these states as compared to the excitation energy from the ground state. In equilibrium it can be seen that there are substantial contributions due to excitation from both ground and metastable states. For the carbon-like ion, there are similar excitation energies from all the metastables to the $2s2p^3$ $^1P$ state. In these circumstances, the spin changing contribution is smaller so that the $2s^22p^2$ $^1S$ and $2s^22p^2$ $^1D$ states are most efficient at exciting the $2s2p^3$ $^1D$ state. Again it can be seen that in equilibrium there are excitation contributions from more than one metastable. The recombination contributions for $C^{+1}$ are also plotted in Figure 4.2.5. These appear small but note that they do need to be corrected to include higher cascade contributions and that the relative importance of excitation and recombination contributions depend on the relative abundances of the ionisation stages.

The total radiated line power from all low level transitions is derived by multiplying the effective emission coefficients by the transition energy and by summing over all radiative transitions (see Appendix 4 for details). Both equilibrium and metastable resolved coefficients are derived in the present work. These are related by

$$P_L(z) = \Sigma_\rho \, P_L(\rho,z) \, (N^{+z}_{\rho\text{-}eq} / N^{+z}_{\rho=1}) \qquad \text{E(4.2.9)}$$

where $P_L(\rho,z)$ are the metastable resolved coefficients, $(N^{+z}_{\rho\text{-}eq} / N^{+z}_{\rho=1})$ are the equilibrium metastable/ground population fractions and $P_L(z)$ is the 'equilibrium coefficient' which assumes that the metastable populations are in quasi- static equilibrium with the ground state population. Figure

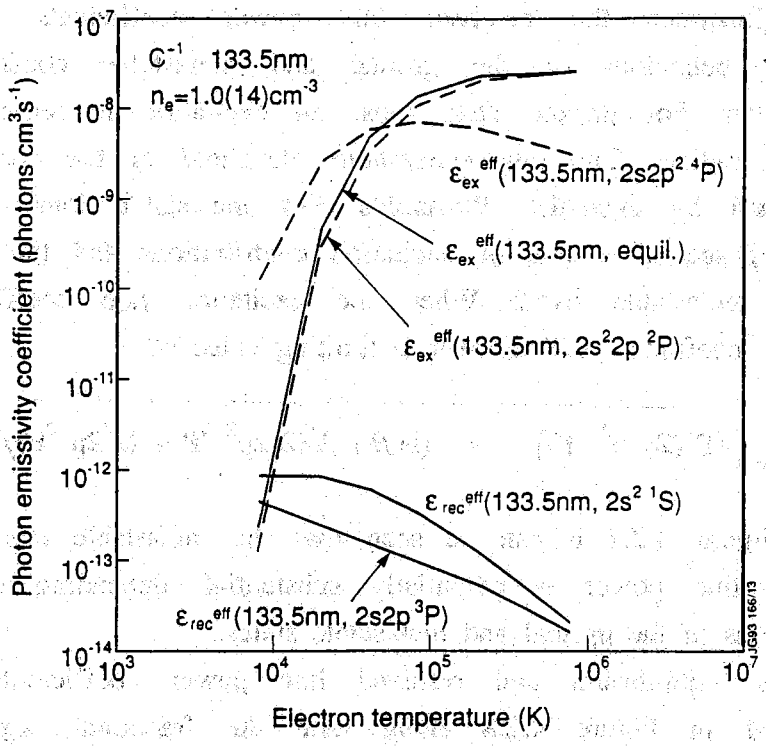


**Figure 4.2.5:** Effective emission coefficients for $C^{+1}$ ($2s2p^2$ $^2D$ - $2s^22p$ $^2P$) at 133.5nm. Excitation and recombination coefficients.

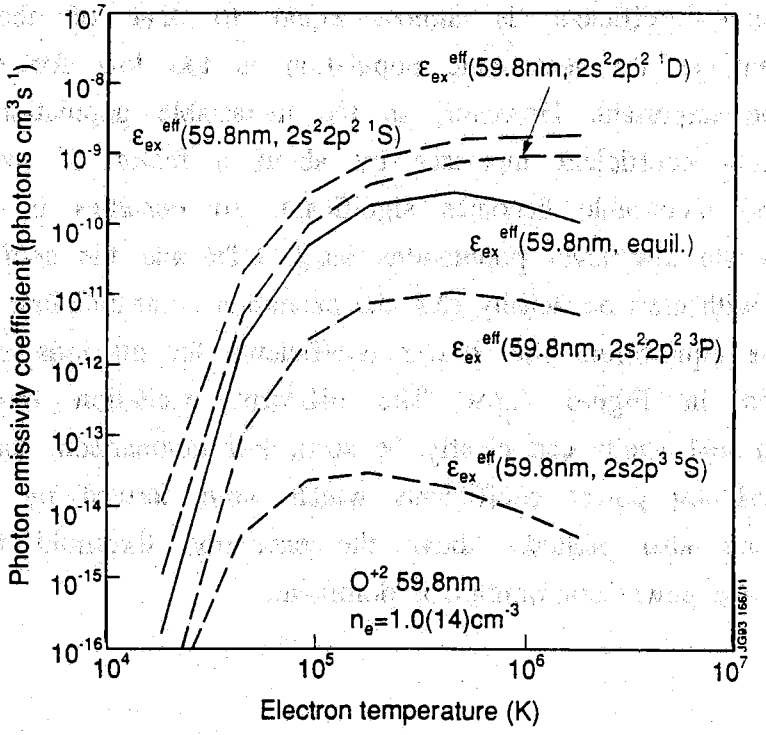


**Figure 4.2.6:** Effective emission coefficients for $O^{+2}$ ($2s2p^3$ $^1P$ - $2s^22p^2$ $^1S$) at 59.7nm. Excitation coefficients only.

4.2.7 illustrates the resolved line power coefficients for $C^{+1}$. The different behaviour of the ground and metastable coefficients requires explanation. For ground state ions, an excitation is required before the ion can radiate. The low temperature threshold of the coefficient is thus determined by excitation thresholds. For metastable ions, the coefficients are composed of a sum of excitation contributions and the radiative decay of the metastable itself. When the excitation rate coefficients tend to zero, the coefficient still tends to a limiting value of

$$\mathrm{Lim}_{Te,ne\to 0}\left(P_L(2s2p^2\ {}^4P)\right) = (hc/\lambda)\ A^r(2s2p^2\ {}^4P - 2s^2 2p\ {}^2P)/n_e \qquad E(4.2.10)$$

From Figure 4.2.7 it can be seen that the metastable contribution to the radiated line power is potentially substantial, depending on the relative populations of the ground and metastable states.

The equilibrium and resolved line power coefficients for $C^{+2}$ are illustrated in Figure 4.2.8 along with the fractional population of the 2s2p $^3P$ metastable. The metastable fraction reaches a first de-excited limit (not full LTE but due to collisional transfer to the singlet side) at an electron density of ~ $10^{10}$ $cm^{-3}$, at which the ground and metastable populations are approximately equal. At low electron densities the equilibrium coefficient is almost equal to that of the ground state coefficient, as the metastable population is too low for excitations from it to be important. However, as the metastable population increases, the equilibrium coefficient increases by about a factor of two as excitation from the metastable becomes significant. At densities in excess of $10^{16}$ $cm^{-3}$ all the low level populations reach LTE and the coefficient decreases linearly with electron density (c.f. the excitation contributions).

The equilibrium line power coefficients for all ions of beryllium are illustrated in Figure 4.2.9. The different excitation thresholds of the n=2 and n=1 shells can clearly be seen. For comparison, the recombination/ bremsstrahlung power coefficients which were derived by the bundle-n S model are also plotted. Above the excitation threshold for a particular ion the line power contribution is dominant.

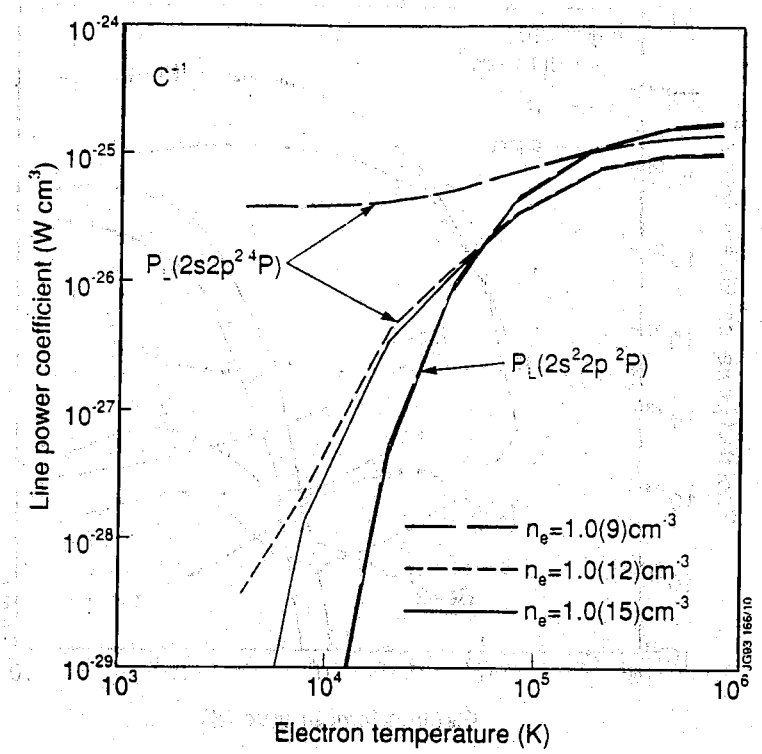


**Figure 4.2.7:** Resolved line power coefficients for $C^{+1}$ as a function of electron temperature and density.

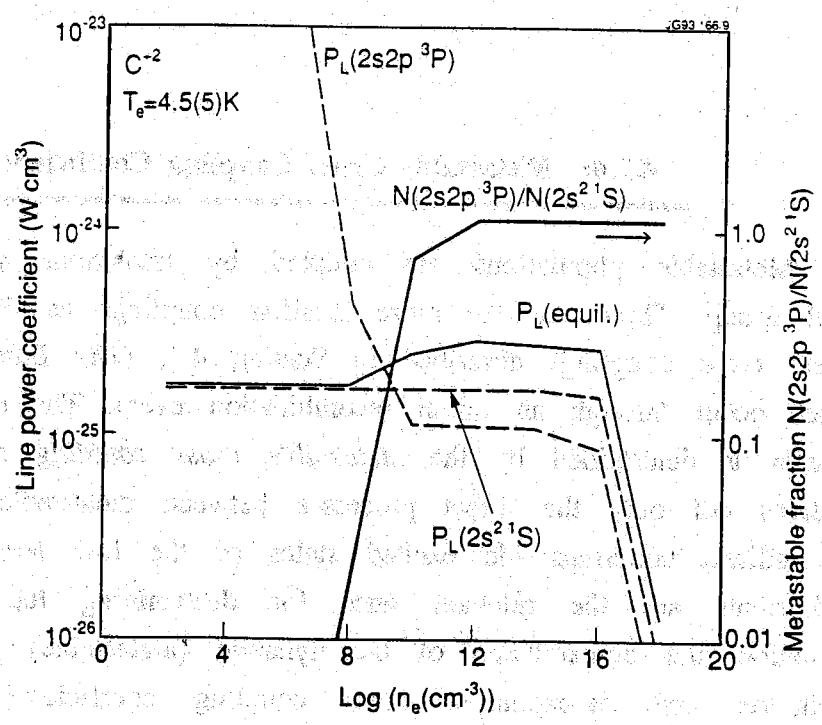


**Figure 4.2.8:** Resolved and equilibrium line power coefficients for $C^{+2}$ as a function of electron density. The metastable/ground population fraction in quasi-static equilibrium is also plotted.

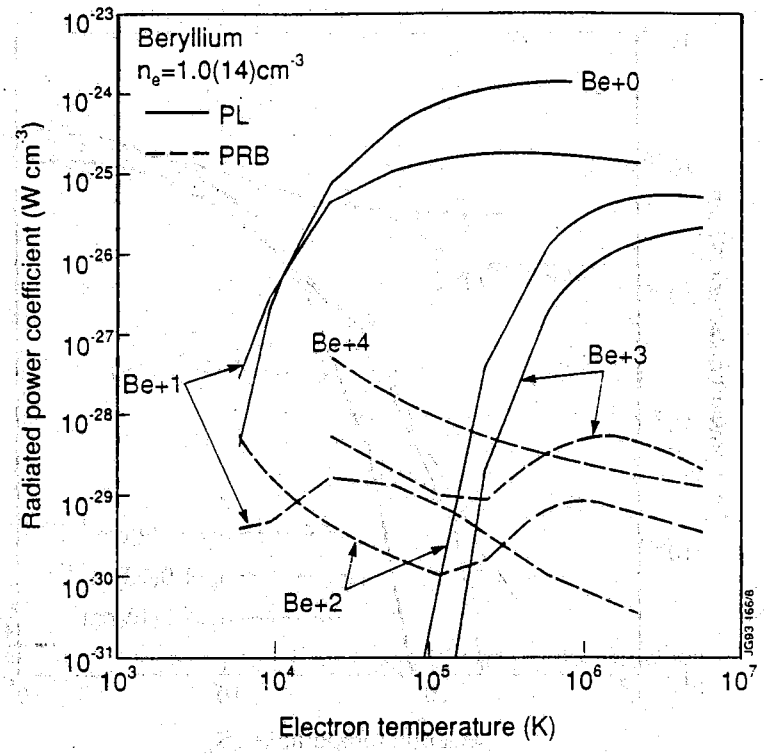


**Figure 4.2.9:** Equilibrium line power (PL) and composite recombination/ bremsstrahlung (PRB) radiated power coefficients for all ions of beryllium.

### 4.2.4: Metastable Cross Coupling Coefficients

Metastable populations are coupled by transitions within the low level group. These are the more familiar couplings as distinct from the parent cross couplings described in Section 4.1, (*The Bundle-n S Model*) which occur through an initial recombination event. The effective rate of transfer is determined by the *metastable cross coupling coefficient* which contains not only the direct processes between metastable levels but all the indirect couplings via excited states of the low level group. These coefficients are the relevant ones for determining the timescales for excitation and de-excitation of the dynamic (metastable) populations. The excitation and de-excitation cross coupling coefficients for $O^{+2}$ are illustrated in Figures 4.2.10(a) and (b) respectively. The ion has four metastables - $2s^22p^2\ ^3P$, $2s^22p^2\ ^1D$, $2s^22p^2\ ^1S$, and $2s2p^3\ ^5S$ - and was chosen for illustration because it gives the opportunity to compare the relaxation times of metastables in different spin systems with the relaxation times of metastables within a spin system. For comparative

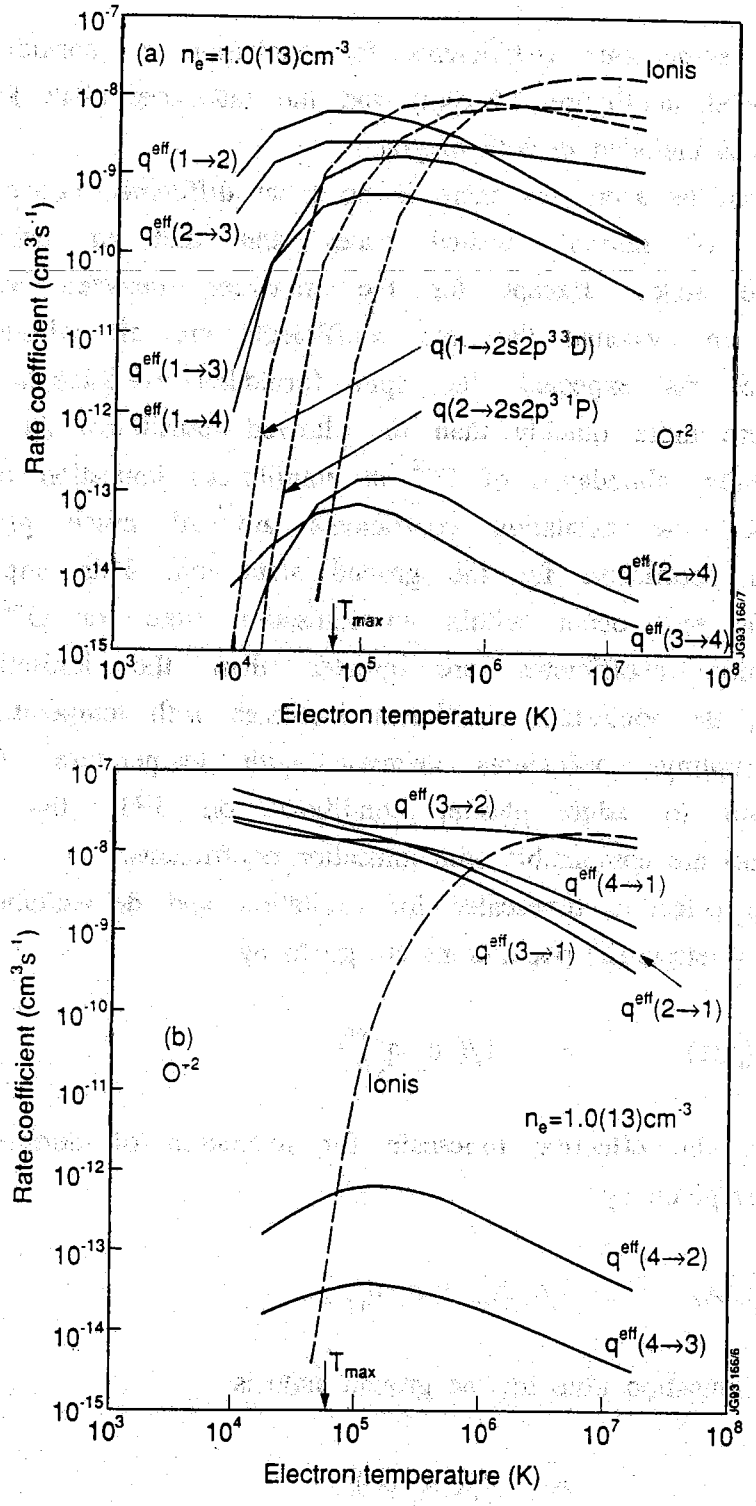


**Figure 4.2.10:** Metastable cross coupling coefficients ($q^{eff}$) for $O^{+2}$. The indices 1,2,3,4 refer to $2s^22p^2\ ^3P$, $2s^22p^2\ ^1D$, $2s^22p^2\ ^1S$ and $2s2p^3\ ^5S$ respectively. Also illustrated (dashed lines) are rate coefficients for ground state ionisation and for electron impact excitation within the triplet and singlet spin systems.

(a) excitation cross coupling coefficients

(b) de-excitation cross coupling coefficients

purposes, some rate coefficients for excitation of normal excited states are included in Figure 4.2.10(a) and the rate coefficient for ground state ionisation is included in both diagrams.

It can be seen that there is no great difference between the rates of excitation of normal excited states and that of excitation of the metastable states. Except for the transition between the singlet and quintet spin systems, the rate coefficients are all within an order of magnitude. As expected, the spin forbidden coefficients decrease with temperature more quickly than the allowed transitions. At the temperature of maximum abundance of $O^{+2}$ in equilibrium ionisation balance ($T_{max}$ = $6x10^4$ K), the excitation coefficients are all much greater than the ionisation coefficient for the ground state ion. This implies that many excitations will occur within an ionisation time for $O^{+2}$. Similarly the de-excitation coefficients are greater than the ionisation coefficient. However, the ionisation coefficient increases with temperature whereas the cross coupling coefficients decrease with temperature. At temperatures appropriate to edge plasma conditions on JET, the cross coupling coefficients are comparable with ionisation coefficients.

The effective timescales for excitation and de-excitation between the dynamic (metastable) populations are given by

$$\tau^{eff}_{rel}(\rho\rightarrow\varepsilon) \quad = \quad 1/( n_e \, q^{eff}_{\varepsilon\rho}) \qquad \text{E(4.2.11)}$$

Similarly, the effective timescale for relaxation of normal excited states directly is given by

$$\tau^{eff}_{rel}(i\rightarrow\varepsilon) \quad 1/( A^r_{\varepsilon i} + n_e \, q_{\varepsilon i} ) \qquad \text{E(4.2.12)}$$

and the ionisation time for the ground state is

$$\tau_{ion} \quad = \quad 1/( n_e \, S ) \qquad \text{E(4.2.13)}$$

In Figure 4.2.11 the de-excitation timescales between the dynamic populations are plotted in comparison with the ionisation timescale and the de-excitation timescales of a few normal excited states. The de-excitation timescales reflect the effective timescales for the populations to relax to their equilibrium values. This is plotted for an electron temperature of $2.9x10^5$ K which is relevant to conditions experienced by ions in the edge region of JET. This diagram provides clear

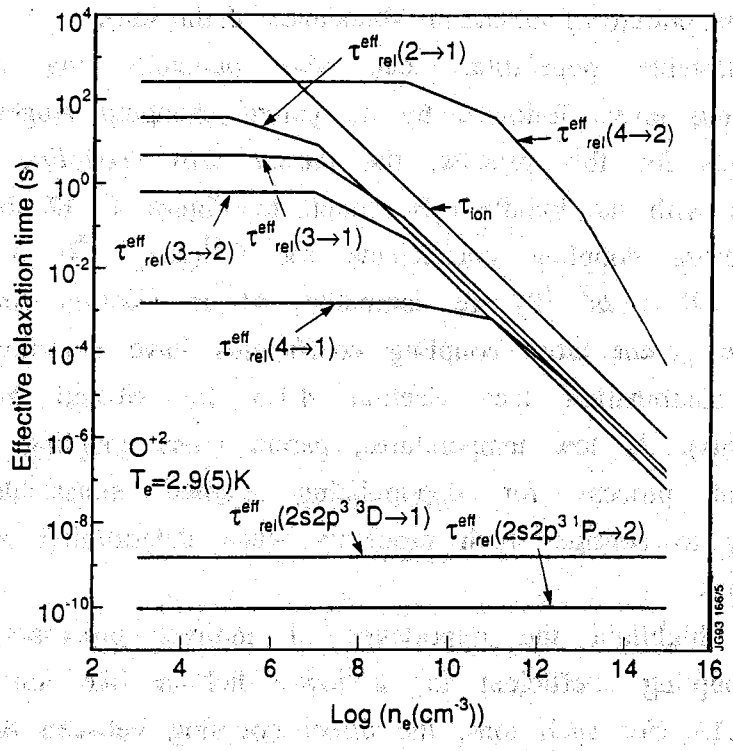


**Figure 4.2.11:** Effective relaxation timescales for dynamic (metastable) and some normally excited populations of $O^{+2}$. $\tau_{ion}$ indicates the ionisation time for ground state ions. Indices as Figure 4.2.10.

illustration of the different timescales for ground, metastable and normal excited states.

At low electron density, the relaxation timescales of both the metastables and normal excited states are constant. This is because de-excitation by radiative decay is the dominant process. The decays of the normal excited states are orders of magnitude shorter than those of the metastables. As the electron density increases, collisional de-excitation of the metastable populations becomes effective and the timescales decrease linearly with electron density. The ionisation timescale is comparable with the relaxation timescales of the metastable states, and both are much greater than the relaxation timescales of the normal excited states.

Figures 4.2.10 and 4.2.11 suggest that in relatively low temperature plasmas, metastables populations will reach equilibrium well within the ionisation time of the ion. In relatively high temperature plasmas however, metastable populations will not have reached equilibrium and will

evolve with ground state populations (temperatures are considered relative to the temperature of maximum abundance of the ion).

Metastable populations can also de-excite via recombination to autoionising levels followed by an parent changing Auger transition. Rate coefficients for this process, the *parent cross coupling coefficient*, were evaluated with the bundle-n S model. In Figure 4.1.12 the metastable and parent cross coupling coefficients for $C^{+1}(2s2p^2\ ^4P \rightarrow 2s^22p\ ^2P)$ and $C^{+2}(2s2p\ ^3P \rightarrow 2s^2\ ^2P)$ are compared. At an electron density of $1.0x10^{13}$ $cm^{-3}$, the parent cross coupling coefficients have contributions from three body recombination (see Section 4.1.5 for overall behaviour of the coefficients). At low temperatures, parent cross coupling appears to be a substantial process for depopulating excited metastables. It is thus necessary to consider both processes when determining relative metastable populations.

To highlight the importance of indirect processes, the metastable cross coupling coefficient for a low-z helium like ion is illustrated in Fig. 4.2.13. For such ions, the direct coupling between the $1s^2\ ^1S$ ground state and $1s2s\ ^3S$ metastable is very inefficient. For $C^{+4}$ it is found that the excitation cross coupling from $1s^2\ ^1S$ to $1s2s\ ^3S$ is dominated by excitation from $1s^2\ ^1S \rightarrow 1s2p\ ^3P$ and then radiative decay. This accounts for about 50% of the coefficient. Note that the $1s2p\ ^3P$ state has branching ratios of 0.97 and 0.03 for radiative decay to $1s2s\ ^3S$ and $1s^2\ ^1S$ respectively. The effective de-excitation coefficient between triplet to singlet states is almost entirely due to excitation from $1s2s\ ^3S$ - $1s2p\ ^3P$ followed by radiative decay to $1s^2\ ^1S$, which accounts for about 80% of the coefficient.

## 4.2.5: Concluding Remarks

The low level model enables detailed evaluation of low level populations and relaxation timescales. At tokamak densities, the excited state populations of the low charge states are no longer in coronal equilibrium and are influenced by collisional redistribution and direct ionisation from excited states. The coupling between spin systems can be evaluated by including spin changing transitions in the model. In general, level populations may be dependent on excitation from more than one metastable level (including spin changing excitation). Similarly, metastable resolved radiated power coefficients indicate that excitation

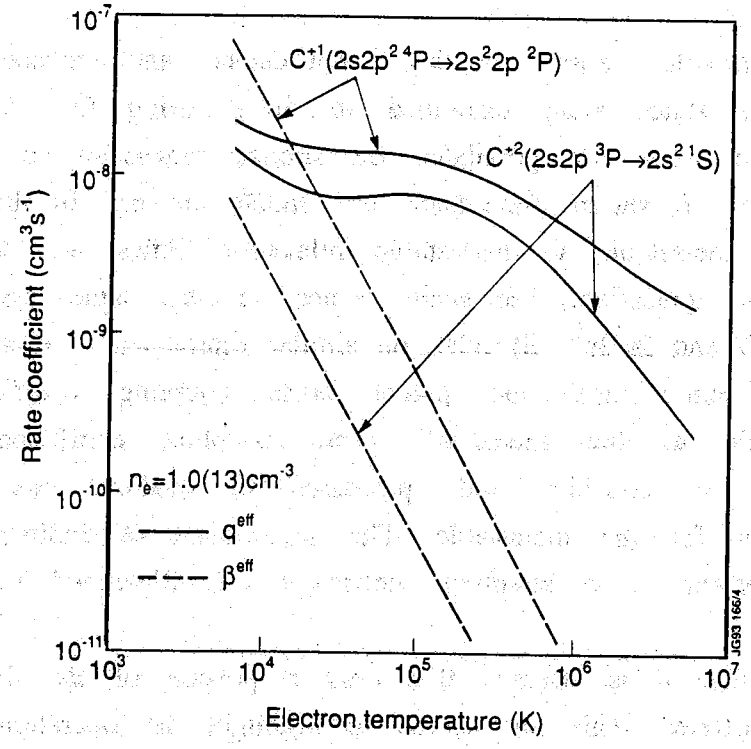


**Figure 4.2.12:** Comparison between metastable ($q^{eff}$) and parent ($\beta^{eff}$) cross coupling coefficients for $C^{+1}$ and $C^{+2}$.

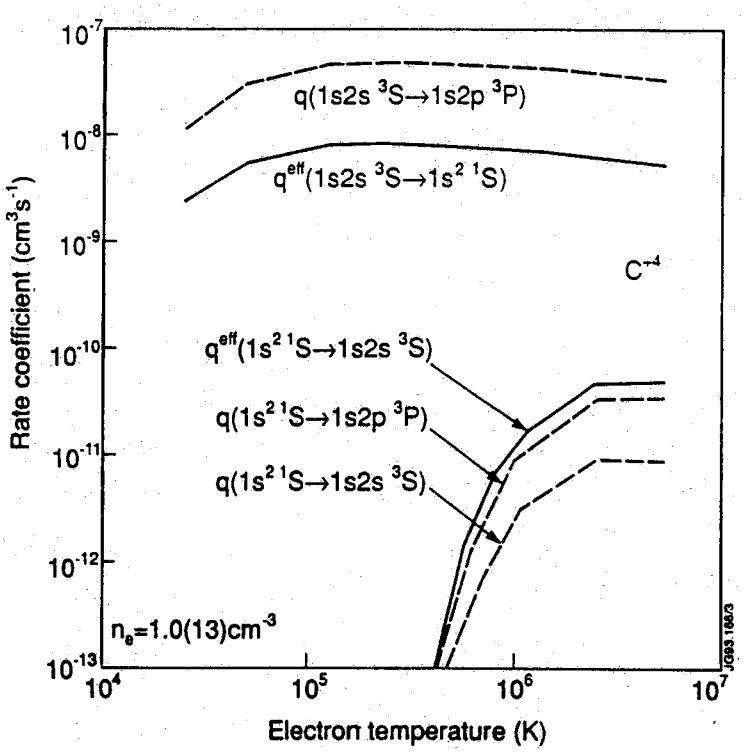


**Figure 4.2.13:** Comparison between effective cross coupling coefficients ($q^{eff}$, full lines) for $C^{+4}$ $1s^2\ ^1S$ - $1s2s\ ^3S$ and component excitation rate coefficients (q, dashed lines).

from metastable states can be a considerable contribution to radiated line power.

Metastable cross coupling coefficients and relaxation times of metastable states were examined in detail using $O^{+2}$ as an example. Metastable states are populated on similar timescales to normal excited states but relaxation timescales are much slower. In high temperature plasmas, metastable to metastable relaxation times are comparable with those for ionisation. Metastable states in the same spin system (i.e. $2s^2 2p^2\ ^1D$ and $2s^2 2p^2\ ^1S$) relax on similar timescales to each other. At low electron temperatures the parent cross coupling coefficients can be comparable to the metastable cross coupling coefficients and it is necessary to consider both processes to evaluate the effective rate coefficient for the metastable. The importance of indirect processes on the metastable cross coupling coefficient was illustrated using $C^{+4}$ as an example.

Finally, it is stressed that only a portion of the derived data has been illustrated. This has served to highlight the operation of the model and the behaviour and main features of the data. Emissivity coefficients, line power coefficients and cross coupling coefficients have been derived for all ions of beryllium, carbon and oxygen.

# 4.3: THE PROJECTION/EXPANSION CALCULATION


4.3.1: Introduction
4.3.2: Calculation Methodology and Expansion of Indirect Couplings
4.3.3: Illustration of Results
(a) Effective Contributions and Emission Coefficients
(b) Ionisation Coefficients
(c) Recombination Coefficients
(d) Radiated Line Power Coefficients
(e) Metastable Cross Coupling Coefficients
(f) Parent Cross Coupling Coefficients
4.3.4: Concluding Remarks


## 4.3.1: Introduction

This calculation develops a refinement to both the bundle-n S and low level resolved calculations. It involves the projection of bundle-n S matrices for the high level populations onto the low level set of LS couplings. The level set for this calculation is then LS resolved terms up to a maximum quantum shell of typically $n_{max}$=3,4 or 5 and bundle-n S quantum shells from $n_{max}$+1 to n=500. The necessity for this calculation stems from the deficiencies of the two previous models, namely the over simplification of low levels in the bundle-n S model and the limited level set of the low level model, lacking connection through higher levels for low level studies. These are highlighted in Fig. 4.3.1 for $Be^{+1}$.

The bundle-n S model bundles level and terms into principal quantum shells and extends to a maximum of $n_{max}$ = 500 for recombination coefficients and $n_{max}$ = 40 for ionisation coefficients. The bundling approximation is good for for hydrogen- and helium-like ions and for highly excited states of more complex ions but is poor at describing the low level structure of ions with more than 3 electrons. Fig. 4.3.1 illustrates this for a lithium-like ion, which is the simplest such system. The main deficiency of the bundle-n S model is its inability to include the $\Delta n=0$ excitation from 2s-2p. As a result, the excitation from complex ions in their ground state is not properly modelled. For example, compare the large energy difference between n=2 and n=3 and the smaller energy differences between 2s-2p and 2p-3s, 2p-3p, 2p-3d etc. For other isoelectronic sequences with more complex low level structures (i.e. Be-,

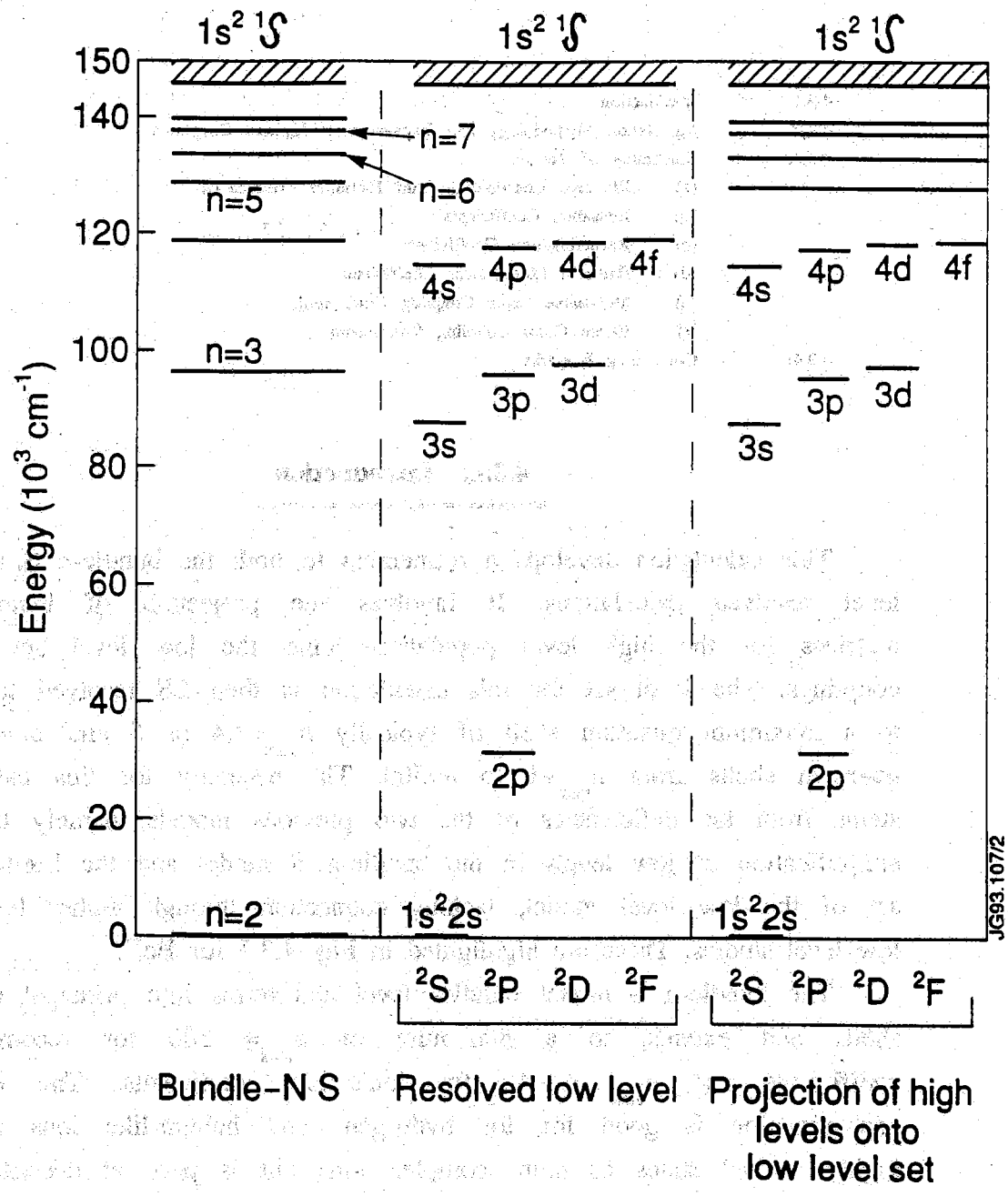


**Figure 4.3.1:** Schematic of levels considered by the various population models for the structure of $Be^{+1}$. The principal quantum shells in the bundle-n S and projection models extend to n=40 or n=500.

B-, C-, N- and O-like) the limitations of the bundle-n S model in this respect are even more pronounced.

The low level set for $Be^{+1}$ for which high quality atomic data exists comprises the 9 LS resolved terms with $2 \le n \le 4$. The low level calculation neglects levels with $n>4$. As can clearly be seen in Fig. 4.3.1, the n=5 levels are very close to n=4, yet in the low level model there will be no correction for stepwise excitation to levels with $n>4$.

In this section of the thesis, the projection/expansion calculation is described in detail. Then a comparison is made between the populations and collisional-radiative coefficients calculated by this model and those calculated by the separate bundle-n S and low level models.

### 4.3.2 Calculation Methodology and Expansion of Indirect Couplings

The projection model is based upon the algebra for projection described in Appendix A2.3. It entails preparation of condensations of the bundle-n S collisional- radiative matrices onto a low set of n-shells but with direct coupling between the low levels excluded. The indirect matrices for each bundle-n S pathway are then statistically expanded over the LS terms associated with the particular parent and spin system

#### (a) Calculation Steps

The calculation proceeds in several steps:

(a.1) The projected indirect bundle-n S matrices are derived in the main bundle-n S calculation. At this stage it is assumed that the targeted low level set extends to a maximum quantum shell of $n_{max}=5$. The indirect matrices are stored in a formatted data set for subsequent use. They are denoted by $C^{ind}_{IJ}(\gamma,S)$, $r^{ind}_{J}(\gamma,S)$, $L^{ind}_{\sigma J}(\gamma,S)$ and $\beta^{ind}_{\sigma\gamma}(\gamma,S)$ where $\gamma$ and S index the parent and spin system of the recombined state, $\sigma$ indexes alternative parents populated by autoionisation, and I,J index the bundle-n S quantum shells of the low level group and are respectively the collisional- radiative coupling part, the recombination part, the loss vector part and the indirect parent cross coupling part.

(a.2) Then a resolved low level population calculation is executed and in the course of this it is possible to expand the projected indirect matrices over the low level couplings and add them onto the low level

matrices. To facilitate this, an expansion data file is defined which specifies the statistical weight factors required to expand the bundle-n S matrices and identifies the LS resolved terms with which they are associated. At this stage, it may be necessary to condense the indirect projected bundle-n S matrices further to match the actual maximum n-shell of a particular low level data set. The condensation routine was tested by condensing the projected matrices onto the lowest quantum shell. The collisional radiative coefficients of the original bundle-n S calculation are correctly recovered in all cases. If the low level data set does not contain recombination or ionisation data then it is also possible to statistically expand such more approximate data from the bundle-n S model.

The bundle-n S indirect projected matrices are expanded over the low level LS resolved collisional radiative matrix using statistical weight factors only. The implicit assumption in this is that the populations of the separate l subshells within each bundle-n S shell are statistically populated. This is reasonable at moderate and high densities because collisional mixing of the high n-shell group is large. However, this assumption does introduce an error at low electron densities. This is examined in Section 4.3.3.

If the LS resolved levels are indexed by i,j,k... , and it is assumed that level i forms part of the level group for the n-shell indexed by I, the data can be expanded using the relationships

$$C_{ij} = C_{ij}^{dir} + \Sigma_{\gamma,S}\ \omega_{ij}^{c}(\gamma,S)\ C_{IJ}^{ind}(\gamma,S) \qquad \text{E(4.3.1)}$$

$$r_{j\gamma} = r_{j}^{dir} + \Sigma_{S}\ \omega_{j}^{r}(\gamma,S)\ r_{J}^{ind}(\gamma,S) \qquad \text{E(4.3.2)}$$

$$L_{\sigma j} = L_{\sigma j}^{dir} + \Sigma_{\gamma,S}\ \omega_{j}^{L}(\gamma,S)\ A_{\sigma J}^{ind}(\gamma,S) \qquad \text{E(4.3.3)}$$

The derivation of the expansion factors is discussed in section (b).

(a.3) The low level calculation is completed in the resolved coupling scheme. This involves high quality data for all direct couplings and optionally, high quality ionisation and recombination data. Collisional-radiative ionisation, recombination and metastable cross coupling coefficients and effective emission coefficients are calculated

as before. The effective parent cross coupling coefficients are calculated following Appendix A2.3. These parameters now include the influence of the high n shells.

**(b) Expansion Factors**

The expansion factors are determined by assigning statistical weights to describe the parentage, spin system, and normalised n-shell weight of each LS resolved level. The key to the expansion is to associate LS terms with particular parent/spin system pathways. For example, consider a hydrogen-like ion. In this case the low level group spans n=1-5 and all the levels are associated with one parent/spin system calculation (i.e. $X^{+z0}$ $^1S$ parent recombining into $X^{+(z0-1)}$ $^2L$). The relative weight of each term within a particular quantum shell is determined by statistical weight factors. These are denoted by $\omega_i(I,\gamma,S)$ and are calculated by summing the statistical weights, (2S+1)(2L+1), of all the resolved levels within the n-shell group and then normalising the individual weights with the sum. For example, 3s $^2S$, 3p $^2P$ and 3d $^2D$ contribute to the statistical weight of the n=3 doublet shell with $\omega_i(I,\gamma,S)$ = 0.111, 0.333 and 0.555 respectively.

For complex ions, the situation is more complicated. Table 4.3.1 illustrates the expansion details for a boron-like recombined ion in which the low level set spans n = 2,3. Firstly, the levels within the LS resolved group are distinguished by recombined spin system and then associated with a particular parent/spin system group. Some levels may be associated with more than one parent. For example, doublet states in boron like ions can be associated with either the $2s^2$ $^1S$ or 2s2p $^3P$ parents. A 'fractional parentage', $\omega_s(\gamma)$ is assigned to each recombined spin system which is based entirely on the spin system weight of the parents. That is, the doublet states are associated with $2s^2$ $^1S$ and 2s2p $^3P$ with $\omega_s(\gamma)$ = 0.25 and 0.75 respectively. For quartet states there is no ambiguity and all are associated with the triplet parent with $\omega_s(\gamma)$ = 1.00. States of the form $2s2p^2$ $^2L$ were associated with the both the $2s^2$ $^1S$ and 2s2p $^3P$ parents even though their structure suggests that they should properly be associated only with the population structures of 2s2p $^1P$ and 2s2p $^3P$ parents. This decision was made because excitations of the form $2s^22p$ $^2P$ - $2s2p^2$ $^2L$ - $2s^23l$ $^2L$ are strong and form a major part of the excitation pathways for the ($2s^2$ $^1S$) nl $^2L$ population structure. Similarly, radiative transitions from $2s^23l$ $^2L$ - $2s2p^2$ $^2L$ - $2s^22p$ $^2P$ are strong and so these levels will be populated by cascade. Next, the relative weight of each

Boron Sequence

| | |
|---|---|
| Number of parents: | 2 |
| Number of resolved n-shells: | 2 |
| Total number of resolved levels: | 16 |

| Information on Parent No.: | 1 | 2 |
|---|---|---|
| Term: | (1S) | (3P) |
| Spin: | 1 | 3 |
| No. of recombined spin systems: | 1 | 2 |

Information on Recombined Spin Systems for Parent No. 1:

| | |
|---|---|
| Spin system: | 2 |
| Lowest n-shell | 2 |
| No. of resolved n-shells: | 2 |
| Fractional Parentage | 0.25 |

Information on Recombined Spin Systems for Parent No. 2:

| | | |
|---|---|---|
| Spin system: | 2 | 4 |
| Lowest n-shell | 2 | 2 |
| No. of resolved n-shells: | 2 | 2 |
| Fractional Parentage | 0.75 | 1.00 |

**Table 4.3.1(a):** Expansion parameters for Boron-like ions.

Boron Sequence (continued)

Information on LS Resolved Terms:

| | | | | | n-shell normalised weights | |
|---|---|---|---|---|---|---|
| Index | Term | Spin | Parent | Shell | n=2 | n=3 |
| 1 | $2s^2 2p\ ^2P$ | 2 | 1 | 2 | 0.25 | - |
| 1 | $2s^2 2p\ ^2P$ | 2 | 2 | 2 | 0.25 | - |
| 2 | $2s2p^2\ ^4P$ | 4 | 2 | 2 | 0.786 | - |
| 3 | $2s2p^2\ ^2D$ | 2 | 1 | 2 | 0.45 | - |
| 3 | $2s2p^2\ ^2D$ | 2 | 2 | 2 | 0.45 | - |
| 4 | $2s2p^2\ ^2S$ | 2 | 1 | 2 | 0.05 | - |
| 4 | $2s2p^2\ ^2S$ | 2 | 2 | 2 | 0.05 | - |
| 5 | $2s2p^2\ ^2P$ | 2 | 2 | 2 | 0.25 | - |
| 5 | $2s2p^2\ ^2P$ | 2 | 2 | 2 | 0.25 | - |
| 6 | $2s^2 3s\ ^2S$ | 2 | 1 | 3 | - | 0.0667 |
| 6 | $2s^2 3s\ ^2S$ | 2 | 2 | 3 | - | 0.0667 |
| 7 | $2s^2 3p\ ^2P$ | 2 | 1 | 3 | - | 0.333 |
| 7 | $2s^2 3p\ ^2P$ | 2 | 2 | 3 | - | 0.333 |
| 8 | $2p^3\ ^4P$ | 4 | 2 | 2 | 0.214 | - |
| 9 | $2s^2 3d\ ^2D$ | 2 | 1 | 3 | - | 0.600 |
| 9 | $2s^2 3d\ ^2D$ | 2 | 2 | 3 | - | 0.600 |
| 10 | $2s2p3s\ ^4P$ | 4 | 2 | 3 | - | 0.1089 |
| 11 | $2s2p3p\ ^4D$ | 4 | 2 | 3 | - | 0.1881 |
| 12 | $2s2p3p\ ^4S$ | 4 | 2 | 3 | - | 0.0297 |
| 13 | $2s2p3p\ ^4P$ | 4 | 2 | 3 | - | 0.1089 |
| 14 | $2s2p3d\ ^4F$ | 4 | 2 | 3 | - | 0.2673 |
| 15 | $2s2p3d\ ^4D$ | 4 | 2 | 3 | - | 0.1881 |
| 16 | $2s2p3d\ ^4P$ | 4 | 2 | 3 | - | 0.1089 |

**Table 4.3.1(b):** Expansion parameters for Boron-like ions.

level within a parent/spin system shell is determined as before. For example, within the n=2 shell of the doublet system, the terms $2s^2 2p\ ^2P$, $2s2p^2\ ^2D$, $2s2p^2\ ^2P$ and $2s2p^2\ ^2S$ contribute to the statistical weight.

The expansion factors are then defined by

$$\omega^c_{ij}(\gamma,S) = \omega_s(\gamma) \cdot \omega_i(I,\gamma,S) \quad \text{for } I \neq J \qquad \text{E(4.3.4)}$$

$$\omega^c_{ij}(\gamma,S) = \omega_s(\gamma) \quad \text{for } I = J \qquad \text{E(4.3.5)}$$

$$\omega^r_i(\gamma,S) = \omega_i(I,\gamma,S) \qquad \text{E(4.3.6)}$$

$$\omega^L_i(\gamma,S) = \omega_s(\gamma) \qquad \text{E(4.3.7)}$$

which can be derived from the parameters in Table 4.3.1.

### 4.3.3: Illustration of Results

A selection of results are presented to demonstrate the operation and main features of the projection calculation. Since the bundle-n S model is a reasonable representation of H-like ions, extensive testing of the procedures were undertaken on $C^{+5}$. No significant differences were found between the bundle-n S and projection calculations. The application of the model to non-hydrogenic systems was extensively tested on $Be^{+1}$, a lithium like ion. This ion was chosen for several reasons. Firstly, the low level atomic structure is simple enough for the influences of the projection calculation to be examined in detail. This is the simplest example of two or more terms being present in the ground principal quantum shell. Also, the influence of the $\Delta n=0$ 2s-2p excitation on the collisional-radiative ionisation coefficient can be explored. Secondly, it was possible to extend the low level set to a maximum of n=8. The atomic data for the extended low level set was calculated in the Born approximation using Cowan's code. An illustration of the accuracy of these collision strengths was given in Chapter 3. This extension enabled a more in-depth check of the influence of stepwise excitation. Finally, $Be^{+1}$ is of special interest to JET where spectral lines from n=4-3 transitions are routinely observed. Illustrations are given from these test cases and from other more complex

ions.

Unless otherwise stated, all illustrations referring to 'low level calculations' have used the standard low level set for each ion. These are as detailed in Appendix A3.

**(a) Effective Contributions and Emission Coefficients**

The standard low level set for $Be^{+1}$ comprises the lowest 9 LS terms with $n_{max}=4$ (see Figure 4.3.1). The populations of these levels were calculated using the low level model and the projection model. Additionally, the low level set was extended to $n_{max}$ = 6, 7 and 8 with 14, 20 and 26 and 32 LS terms respectively. The orbitals 7i, 8i and 8j were not included. With the extended level sets the populations were evaluated in the pure low level model only. The effective excitation contributions for the $1s^2 4p\ ^2P$ and $1s^2 3d\ ^2D$ populations are illustrated in Figures 4.3.2 and 4.3.3. It can be seen that the inclusion of the high levels significantly alters the populations of these levels. For $4p\ ^2P$, there is a significant cascade contribution (~50%) at low electron densities. This is due to $2s\ ^2P \rightarrow ns\ ^2S$ excitations which cascade entirely to np levels. At high electron densities, stepwise excitation is effective at depopulating both $3d\ ^2D$ and $4p\ ^2P$ so that the low level model significantly overestimates the populations. In both cases, the projection calculation is a reasonable but not exact match with the 32 term low level calculation with $n_{max}$ = 8. The assumption in the projection calculation that the bundle-n S shells are statistically populated results in a slight underestimate of the cascade contributions for $4p\ ^2P$ and an overestimate for $3d\ ^2D$. At high electron densities, the projection model appears to underestimate the depopulation due to stepwise excitation.

Figures 4.3.4 and 4.3.5 illustrate the behaviour of the $1s^2 np\ ^2P$ populations of $Be^{+1}$ as a function of density and temperature. The $2p\ ^2P$ level is only slightly influenced by the projection calculation whereas 3p and 4p have significant cascade and stepwise excitation corrections at low and high density respectively. The projection calculation describes well the cascade contributions to 3p and 4p over the entire temperature range.

The effective excitation contributions for the $1s^2 2s3p\ ^1P$ population of $Be^{+0}$ and $C^{+2}$ and the $1s^2 3p\ ^2P$ population of $Be^{+1}$ are illustrated in Figure 4.3.6. It can be seen that the projection calculation introduces low density cascade corrections for all these ions. At an electron density of $10^8$ $cm^{-3}$, the corrections are 6% for $Be^{+0}$, 10% for $Be^{+1}$ and 25% for $C^{+2}$. It should be noted that the low level data sets for these ions extend

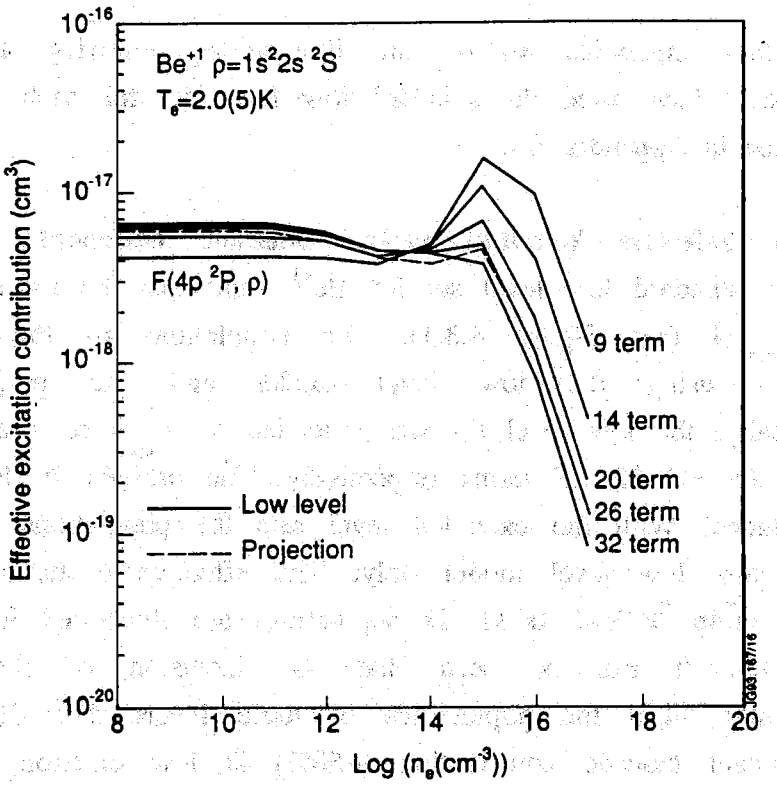


**Figure 4.3.2:** Effective excitation contributions for $Be^{+1}$ $1s^2 4p$ $^2P$ as a function of electron density. Derived by the low level model, the low level model with the extended level set and the projection model.

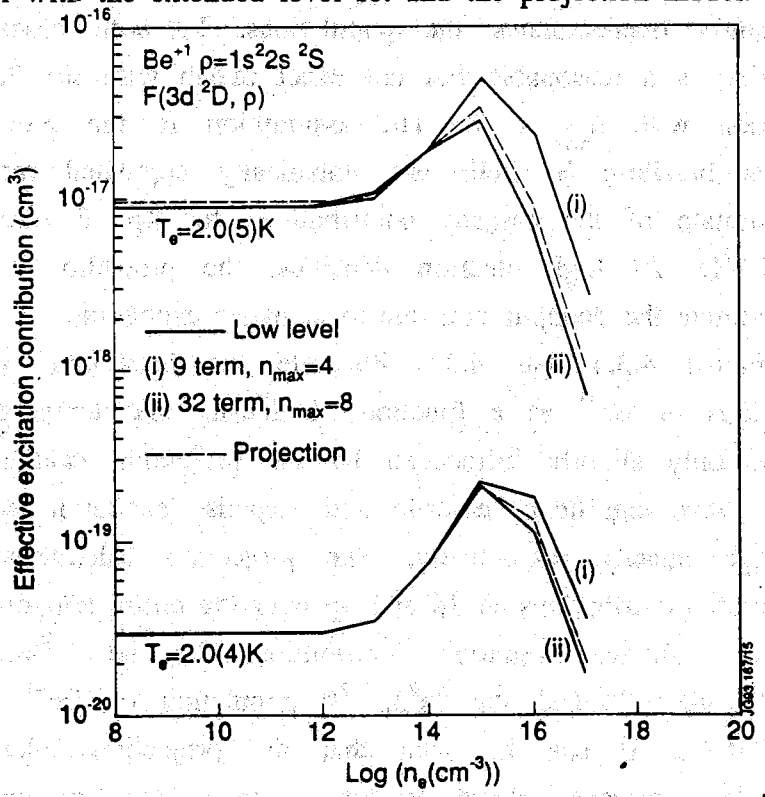


**Figure 4.3.3:** Effective excitation contributions for $Be^{+1}$ $1s^2 3d$ $^2D$ as a function of electron density. Derived by the low level model, the low level model with the extended level set and the projection model.

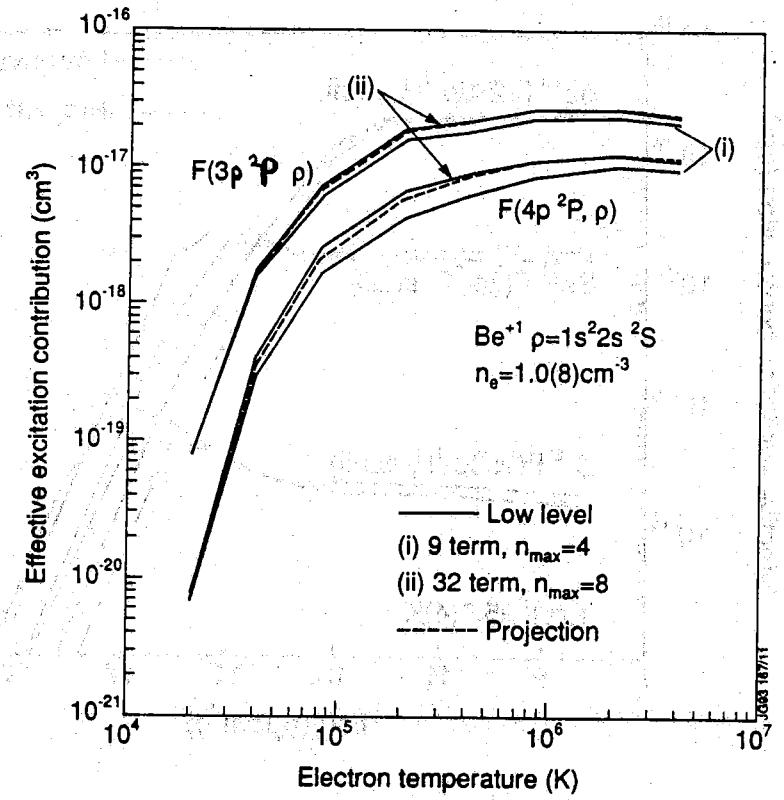


**Figure 4.3.4:** Effective excitation contributions for $Be^{+1}$ $1s^2np$ $^2P$ as a function of electron temperature. Derived by the low level model, the low level model with the extended level set and the projection model.

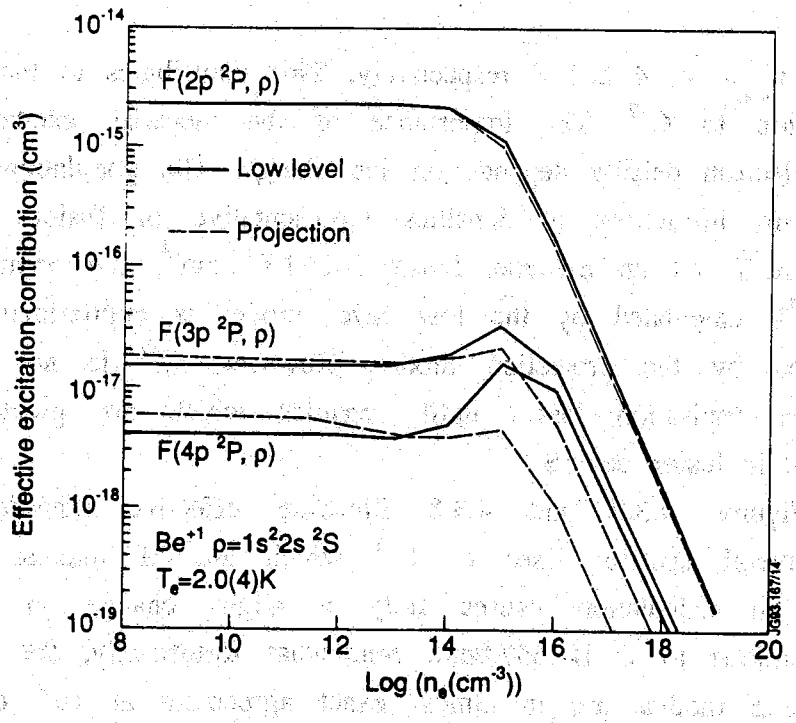


**Figure 4.3.5:** Effective excitation contributions for $Be^{+1}$ $1s^2np$ $^2P$ as a function of electron density. Derived by the low level model and the projection model.

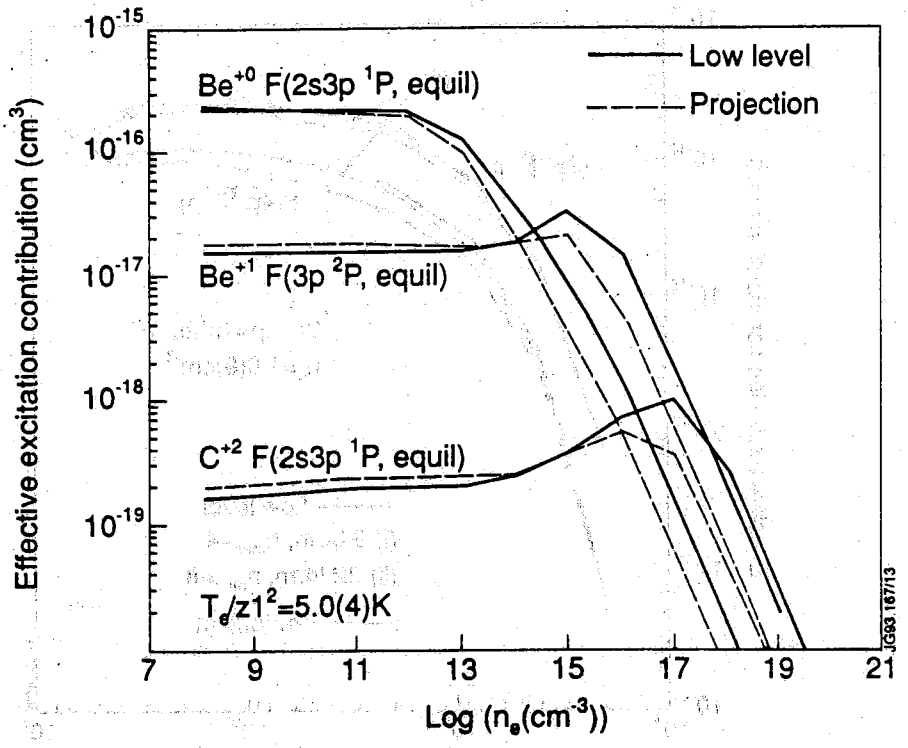


**Fig. 4.3.6:** Effective excitation contributions for several 3p terms in Li- and Be-like ions as a function of ion charge and electron density. Derived by the low level model and the projection model.

up to $n_{max}$ = 4, 4 and 3 respectively. This contributes to the large cascade correction to $C^{+2}$. The importance of the stepwise excitation losses at high electron density depends on ion charge. The populations of $Be^{+0}$ and $Be^{+1}$ are influenced at densities representative of fusion plasmas ($10^{12}$-$10^{14}$ $cm^{-3}$). At an electron density of $10^{14}$ $cm^{-3}$, the population of $Be^{+0}$ 2s2p $^1P$ calculated by the low level model is approximately twice that obtained by the projection model. However, $C^{+2}$ is not influenced by stepwise ionisation losses until densities which are greater than those attained in fusion devices.

Figures 4.3.7 and 4.3.8 illustrate effective emission coefficients for several spectral lines of $C^{+1}$ which are of interest at JET. The projection calculation causes only a slight change in the excitation contributions to C II 657.9nm. Somewhat fortuitously, the low level and projection models are in almost exact agreement at $10^{14}$ $cm^{-1}$ (c.f. $Be^{+1}$ $1s^23p$ $^2P$ in Figure 4.3.6). There is a ~ 15% correction for cascade for densities less than $10^{13}$ $cm^{-3}$, and a correction for stepwise ionisation at electron densities greater than $10^{14}$ $cm^{-3}$. The upper level of this

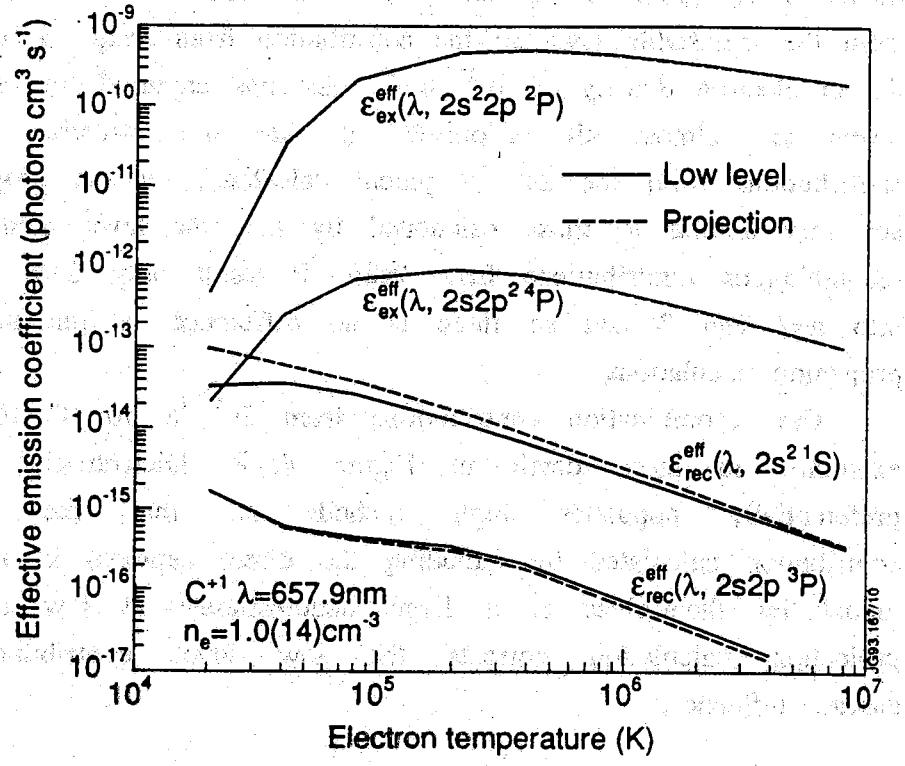


**Fig. 4.3.7:** Effective emission coefficients for $C^{+1}$ 657.9nm ($2s^2 3p\ ^2P$ - $2s^2 3s\ ^2S$) as a function of electron temperature.

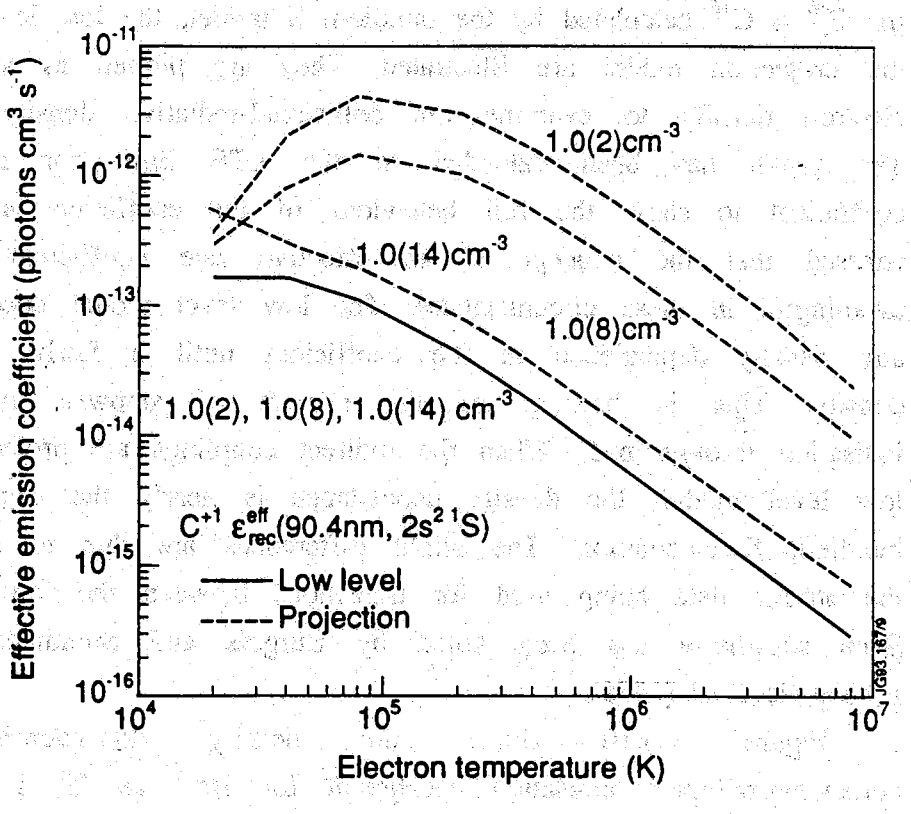


**Fig. 4.3.8:** Effective emission coefficients for $C^{+1}$ 90.4nm ($2s2p^2\ ^2P$ - $2s^2 2p\ ^2P$) as a function of electron temperature and electron density.

transition is $2s^2 3p\ ^2P$ in the n=3 shell. There is no direct excitation from the metastable level so the contribution from $2s2p^2\ ^4P$ is very small. At an electron density of $10^{14}$ $cm^{-3}$, electrons captured into high bundle-n levels are almost all re-ionised so that the effective recombination contributions from the $2s^2\ ^1S$ parent calculated by the projection model are very similar to those calculated by the low level model only. The recombination contributions from $2s2p\ ^3P$ result only from recombination into n=2 and 3 and so there is no difference in the low level and projection calculations.

The recombination contributions from $2s^2\ ^1S$ for C II 90.4nm are examined in more detail in Figure 4.3.8. Dielectronic recombination preferentially populates high n-shells so that the recombination contribution calculated by including the direct captures in the low level model by themselves is a large underestimate at low densities. The projection calculation corrects the low level contribution for this cascade influence.

**(b) Ionisation Coefficients**

In Figure 4.3.9 the collisional- radiative ionisation coefficients for $C^{+5} \rightarrow C^{+6}$ calculated by the bundle-n S model, the low level model and the projection model are illustrated. They are plotted as a function of electron density to examine the collisional-radiative density dependence. The graph has been extended to the LTE limit for the ionisation coefficient to show the full behaviour of the coefficient although it is stressed that the concept of an effective rate coefficient is not too meaningful in these circumstances. The low level model does not exhibit any density dependence in the coefficient until a fairly high electron density. This is because of the neglect of stepwise excitation and ionisation through n>5. When the indirect couplings are projected onto the low level model, the density dependence is nearly the same as in the bundle-n S calculation. The slight differences are due to differences in the atomic data being used for transitions between the low level group. Such sensitivity has been noted by Burgess and Summers (1976) and Ljepojevic et al (1985).

Figure 4.3.10 shows the density dependence of the collisional-radiative ionisation coefficient for $Be^{+1}\ 2s\ ^2P \rightarrow Be^{+2}\ 1s^2\ ^1S$ as calculated by the bundle-n S, the low level and the projection models. To test the sensitivity of the bundle-n S model to the energy of the ground state shell, for this case the coefficient was calculated using

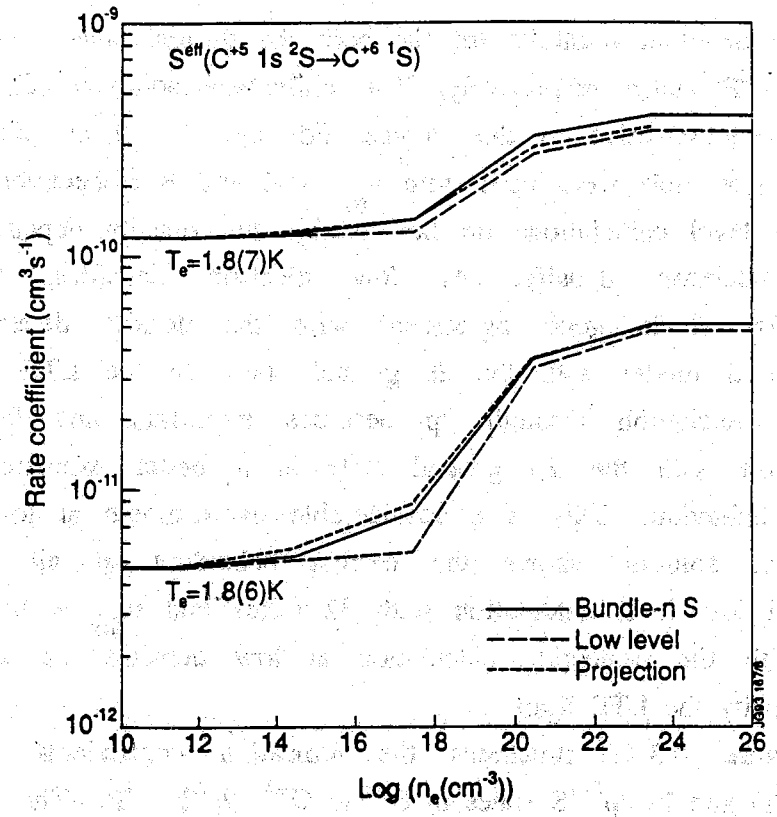


**Figure 4.3.9:** Electron density dependence of the collisional-radiative ionisation coefficient for the hydrogen- like ion $C^{+5}$.

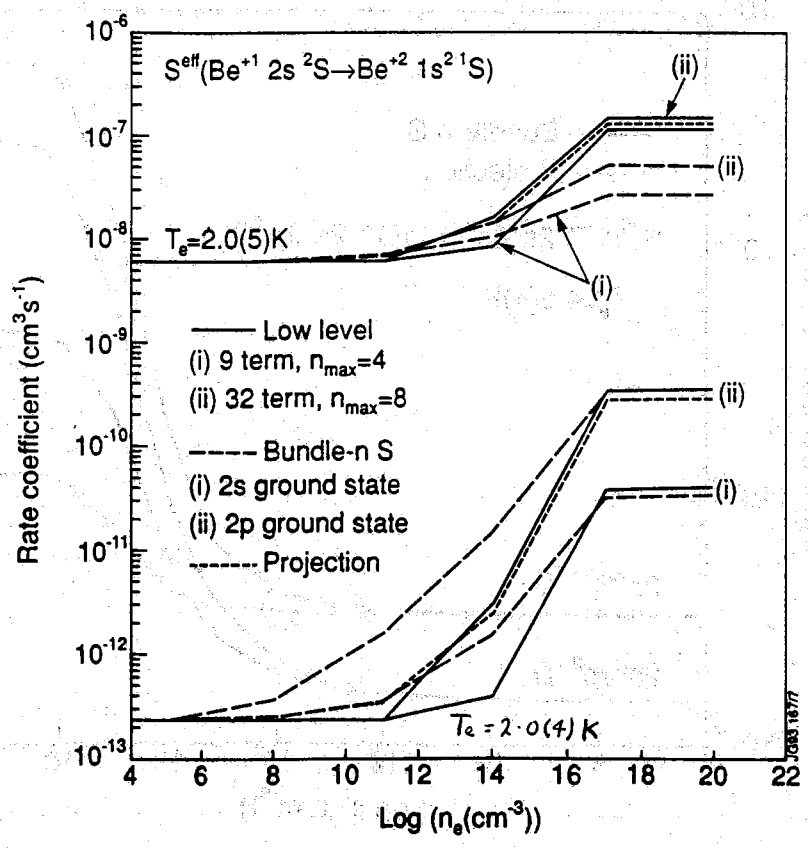


**Figure 4.3.10:** Electron density dependence of the collisional-radiative ionisation coefficient for the lithium- like ion $Be^{+1}$.

effective quantum numbers for the both the ground state, which is 2s $^2$S, and 2p $^2$P states respectively. The collisional-radiative behaviour is seen to be very sensitive to this choice. For the low level calculation, the 9 and 32 term sets were used with $n_{max}$ = 4 and 8 respectively. As for $C^{+5}$, the low level calculations do not exhibit any density dependence until a higher electron density. At low electron densities, the projection calculation is in good agreement with the density dependence of the bundle-n S model with the 2s ground state. In the LTE limit however, stepwise excitation through 2p becomes important and the bundle-n S calculation with the 2p ground state is a better estimate of the high density behaviour. This is a considerable overestimate at low density. The projection solution shows the correct behaviour at all densities. The extended low level calculation with 32 terms and $n_{max}$ = 8 compares very well with the projection calculation at low densities as well as in the high density the LTE limit.

Figure 4.3.11 illustrates the ionisation coefficients from the the $2s^22p^2$ $^1$D and $2s^22p^2$ $^1$S states in $O^{+2}$ to $O^{+3}$ $2s^22p$ $^2$P. The bundle-n S

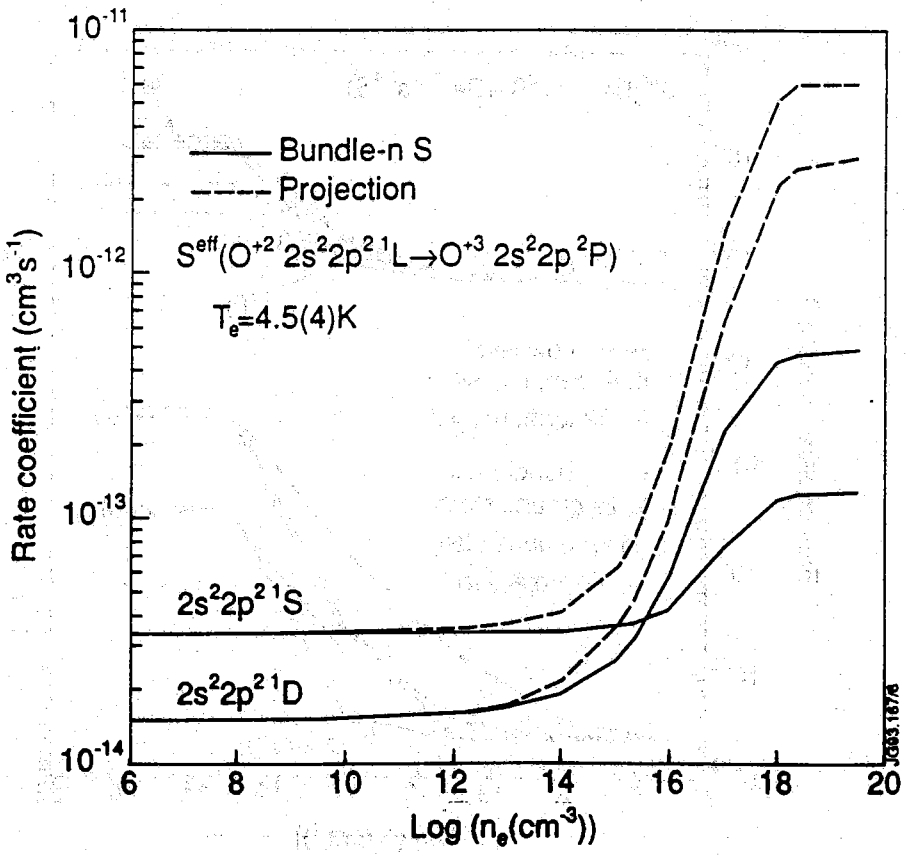


**Figure 4.3.11:** Electron density dependence of the collisional-radiative ionisation coefficient for the carbon- like ion $O^{+2}$.

model could not resolve between these coefficients because the recombined metastables are both within the same spin system. The collisional-radiative contribution to the effective ionisation coefficients was split up using statistical weight factors. It was assumed that 0.17 of the stepwise excitation losses was due to excitation from $2s^2 2p^2\ ^1S$ and 0.83 was due to $2s^2 2p^2\ ^1D$. The low level model explicitly includes the excitation pathways within n=2 and 3 and so allows a more precise estimate of the excitation contributions and the ionisation coefficients. It can be seen that the bundle-n S model again underestimates the density dependence of the coefficients. Further, the stepwise excitation losses from $2s^2 2p^2\ ^1S$ and $2s^2 2p^2\ ^1D$ as calculated by the projection model are of comparable magnitude. At an electron density of $10^{14}$ $cm^{-3}$, the zero density ionisation rate coefficients are enhanced by 45% and 25% respectively.

**(c) Recombination Coefficients**

The collisional-radiative recombination coefficient for $C^{+6} \rightarrow C^{+5}$ is plotted in Fig. 4.3.12. As for the ionisation coefficients, this graph is extended to the LTE limit to display the full behaviour of the coefficients. The low level model underestimates both the total recombination coefficient at low density and also the density dependence of the coefficient. However the projection model and the bundle-n S model are in almost exact agreement. Again, the differences are attributed to differences in the low level atomic data.

Figure 4.3.13 shows the collisional- radiative recombination rate coefficient for $Be^{+2}\ 1s^2\ ^1S \rightarrow Be^{+1}\ 2s\ ^2S$ as calculated by each of the models. As for $C^{+6} \rightarrow C^{+5}$, the low level model underestimates the rate coefficient and does not match the correct behaviour of the coefficient with density. The projection calculation recovers the density dependence of the bundle-n S model almost exactly.

The recombination coefficients from $O^{+3}\ 2s^2 2p\ ^2P$ to the $2s^2 2p^2\ ^1D$ and $2s^2 2p^2\ ^1S$ states in $O^{+2}$ are illustrated in Figures 4.3.14(a) and 4.3.14(b). The differences at low temperatures are due to improved calculations of radiative recombination rate coefficients for the resolved low levels. Again the bundle-n S model could not distinguish between these metastables because they are in the same spin system. It was assumed that 0.83 of the recombined electrons cascaded to $2s^2 2p^2\ ^1D$ and 0.17 to $2s^2 2p^2\ ^1S$. From the illustrations it can be seen that this approximation is not quite exact. It is worth describing in detail the resolution of the

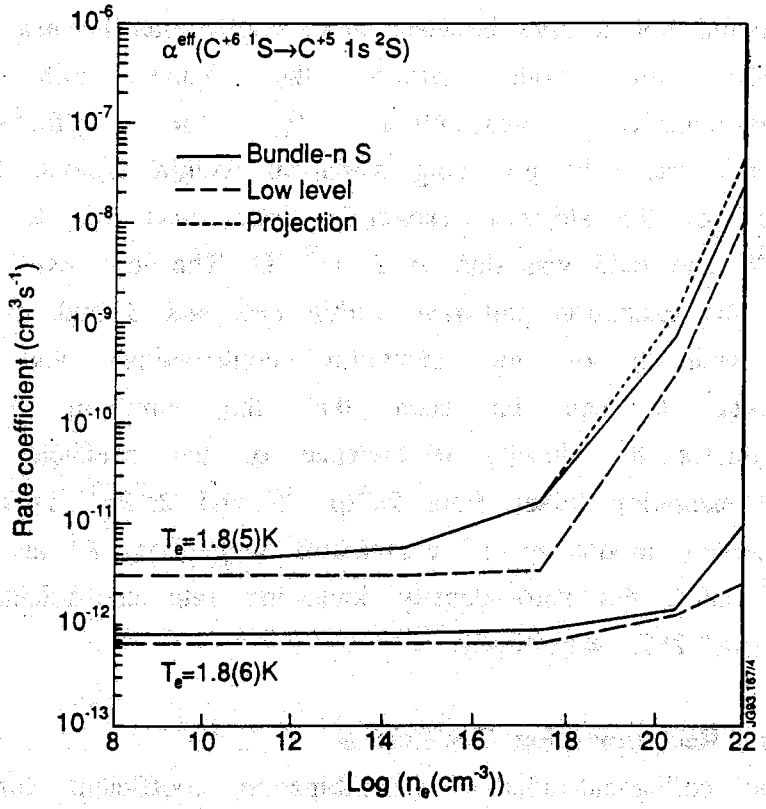


**Figure 4.3.12:** Electron density dependence of the collisional-radiative recombination coefficient for the hydrogen- like ion $C^{+5}$.

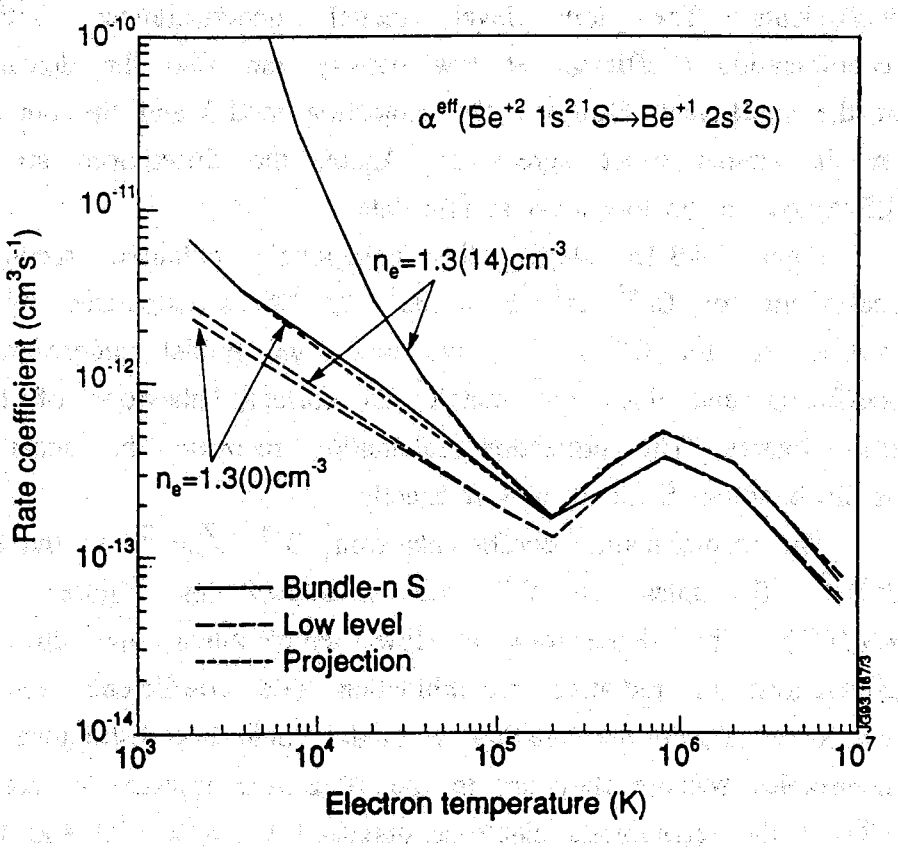


**Figure 4.3.13:** Electron density dependence of the collisional-radiative recombination coefficient for the lithium- like ion $Be^{+1}$.

(a)

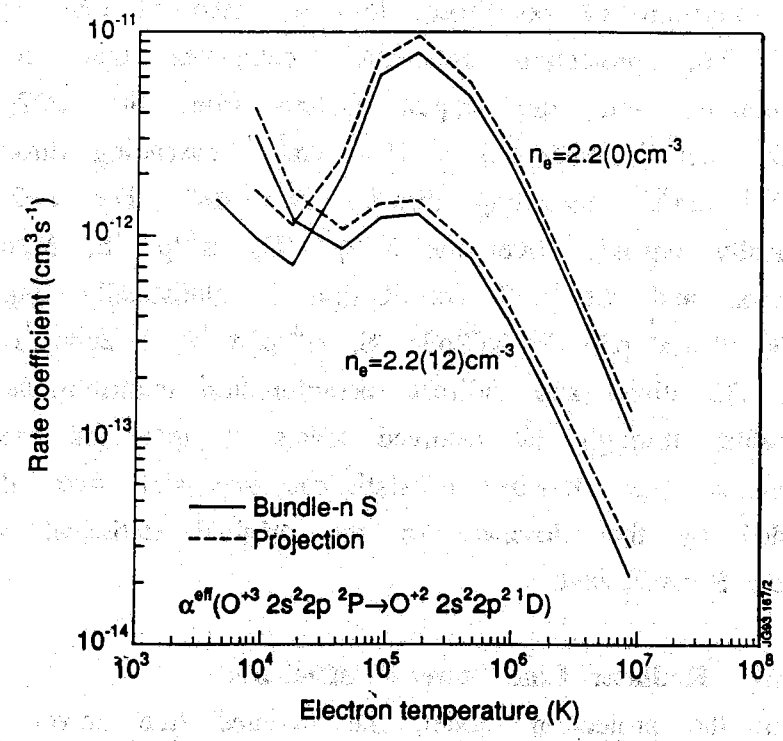


(b)

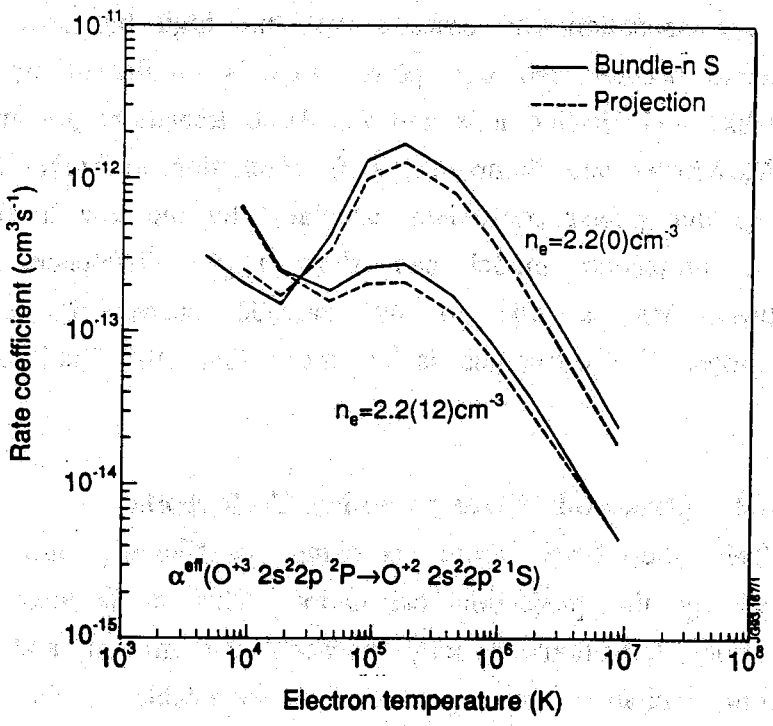


**Figure 4.3.14:** Collisional-radiative recombination coefficients for the carbon- like ion $O^{+2}$.

(a) $\alpha^{eff}(O^{+3}\ 2s^22p\ ^2P \rightarrow O^{+2}\ 2s^22p^2\ ^1D)$

(b) $\alpha^{eff}(O^{+3}\ 2s^22p\ ^2P \rightarrow O^{+2}\ 2s^22p^2\ ^1S)$

recombination coefficient by the projection calculation. At an electron temperature of 9.0x $10^4$ K and electron density of 2.2x$10^0$ $cm^{-3}$, the summed direct recombination coefficient into the resolved low levels is 3.2x$10^{-13}$ $cm^3s^{-1}$. The projection calculation calculates that the total indirect recombination into the singlet system from the $2s^22p$ $^2P$ parent is 7.2x$10^{-12}$ $cm^3s^{-1}$, with 4.3 x $10^{-12}$ $cm^3s^{-1}$ cascading directly to n=2 and 2.9x$10^{-12}$ $cm^3s^{-1}$ cascading directly into n=3. The n=2 contribution is statistically expanded over the $2s^22p^2$ $^1D$, $2s^22p^2$ $^1S$, $2s2p^3$ $^1D$ and $2s2p^3$ $^1P$ terms and the n=3 contribution is statistically expanded over the $2s^22p3s$ $^1P$, $2s^22p3p$ $^1P$, $2s^22p3p$ $^1S$, $2s^22p3d$ $^1P$, $2s^22p3d$ $^1D$ and $2s^22p3d$ $^1F$ terms. The direct and indirect recombination contributions cascade to the metastables through the resolved levels to give the metastable resolved coefficients. The strategy of statistical expansion over the LS terms is defended by the closeness of the original statistical split up of the bundle-n S coefficient.

**(d) Radiated Line Power Coefficients**

In the projection model, the radiated line power is calculated by considering the populations of the low level group only. No allowance is made for excitation and cascade with the high bundle-n S shells. This is reasonable because the line power loss is dominated by $\Delta n=1$ excitations for H-like and He-like ions and for $\Delta n=0$ transitions for more complex ions (see McWhirter and Summers 1979). Excitation to higher shells falls off as $n^{-3}$. The line power coefficient calculated by the low level model only and by the projection model can show slight differences at low electron densities. This is due to the cascade corrections to the low level populations. The difference is no more than 10% and generally less than 5%.

**(e) Metastable Cross Coupling Coefficients**

The metastable cross coupling coefficients are not significantly affected by the projection calculation. This is because these coefficients arise from transitions directly between the ground and metastable levels or from excitation from ground and metastable levels to normal excited states followed by cascade. At low electron density, no change was found in any of the calculated cross coupling coefficients. At high density, the projection calculation depopulates the normal excited states due to stepwise excitation and this tends to decrease the cross coupling coefficients slightly (<10%).

**(f) Parent Cross Coupling Coefficients**

The low level model does not consider autoionising levels and so the parent cross coupling coefficients derived by the projection model consist entirely of the projected influence of the high n-shells. These coefficients differ from those calculated by the bundle-n S model by at most a few percent.

### 4.3.4: Concluding Remarks

The results illustrated in this section show that merging the high level bundle-n S and low level LS resolved population structures via the projection/expansion calculation leads to a more complete and accurate calculation of atomic populations and collisional-radiative coefficients.

At low electron densities, the projection calculation introduces a cascade correction to the low level populations, especially to terms within the n=3 and 4 principal quantum shells. At high electron densities, the projection model corrects the low level populations for stepwise excitation losses. The n=3 and 4 populations are again most sensitive. The necessity of using the full projection/expansion calculation to derive low level populations is dependent on ion charge and electron density. From the work presented in this section, it can be concluded that the full calculation is necessary for neutral atoms and for resolved terms within the n=3 and 4 shell of singly charged ions. For higher charged ions, the projection model does not significantly change the populations until densities higher than those attained in fusion plasmas, so that the low level model by itself is an adequate representation of the excited state populations.

The projection calculation appears to be essential in deriving accurate collisional-radiative ionisation and recombination coefficients. The ionisation coefficients are particularly sensitive to the precise structure and energy levels in the ground quantum shell. The bundle-n-S recombination coefficients are corrected by using more refined radiative recombination data for the LS resolved terms. The projection calculation is able to distinguish between metastables within a spin system to give full parent and metastable resolved coefficients.

# CHAPTER 5

# INTEGRATION OF MODELS

# 5.1: INTRODUCTION

5.1.1: Discussion on Population Models and Derived Data
5.1.2: Reconstruction of Ionisation Balance and Spectral Emission
(a) Equilibrium and Transient Ionisation Balance Models
(b) Spectral Emission and Radiated Power

## 5.1.1: Discussion on Population Models and Derived Data

In the preceding chapter, detailed population models have been developed which enable collisional-radiative coefficients and effective emission coefficients to be derived. From the illustrated results, two points are clear. Firstly, metastable populations have a considerable influence on the behaviour and radiation from light ions. At electron densities appropriate to fusion plasmas, metastable populations can be comparable with ground state populations. Spectral intensities and radiated power line coefficients are dependent on excitation from more than one populated metastable (including spin changing excitation) in general. The relaxation timescales of metastable states indicate that in relatively high temperature plasmas, ground and metastable states will evolve on comparable timescales. Secondly, the best estimates of the collisional radiative coefficients and emission coefficients are obtained by using the projection calculation to merge calculations involving resolved low levels with bundled high levels. The results from this composite model will thus be used exclusively in all future work.

The low level and projection models can describe both metastable populations in quasi-static equilibrium with the ground state or uncoupled ground and metastable populations. It is thus possible to examine two integrated usages in this section. The metastable resolved data usage will be referred to as the 'resolved model'. In it, ground and metastable populations are fully distinguished by resolved coefficients. The other usage in which quasi-static equilibrium metastable fractions are forced is referred to as the 'unresolved model'. This data corresponds to a stage to stage ionisation balance picture with no resolution of initial or final state. Table 5.1.1 summarises the various classes of data which are derived by the three population models of Chapter 4 and then associated in

the two usages.

In this section of the thesis, integrated ionisation state and radiation models are constructed. The present work will be assessed by comparing the results of the unresolved model with the current astrophysical benchmark ionisation balance calculations of Arnaud and Rothenflug (1985) and radiated power calculations of Bonnin et al (1992). The influence of metastable populations on equilibrium ionisation balance,

| Class of Data | Levels of Resolution | Types of Calculation |
|---|---|---|
| Effective Recombination Coefficient | U,R | BNS, LL, PJ |
| Effective Ionisation Coefficient | U,R | BNS, LL, PJ |
| Effective Metastable Cross Coupling Coeff. | R | LL, PJ |
| Effective Parent Cross Coupling Coeff. | R | BNS, PJ |
| Effective Recom/Brems. Power Coefficient | U,R | BNS |
| Effective Line Power Coefficient | U,R | LL, PJ |
| Photon Emissivity Coefficients | U,R | LL, PJ |

**Table 5.1.1:** Classes of data derived from the three population models. The 'resolution' column denotes whether the data is relevant to an (u)nresolved ground state only model or to a metastable/parent (r)esolved model. BNS - bundle-n S calculation, LL - low level resolved calculation, PJ - projection of bundle-n S indirect couplings onto low level group.

time dependent ionisation and overall spectral emission will be investigated by comparing the results of the unresolved and resolved models. To summarise, the precise features of these two models are as follows

*unresolved*: metastables and normal excited states in quasi-static equilibrium with ground states. Low level populations and radiated powers calculated from low level collisional radiative matrix which includes excitations from metastable states, excited state ionisation, collisional redistribution between excited states and projection of high level couplings. Effective ionisation and recombination rate coefficients are evaluated in terms of ground state populations. These are summed over final states. Recombination from ground state parents only.

*resolved*: metastable populations fully distinguished by resolved collisional radiative coefficients, emission coefficients and radiated power coefficients. Recombination from ground and metastable parents.

It can be seen that even the unresolved model in fact considers metastables with quite a high degree of sophistication. Examples of emissivity coefficients and radiated power coefficients calculated by assuming equilibrium metastable populations have already been illustrated in Section 4.2. Figure 5.1.1 illustrates the resolved and unresolved ionisation rate coefficients from $C^{+2}$ as a function of electron temperature and density. The unresolved ionisation rate coefficient is a weighted sum of the metastable resolved ionisation rate coefficients

$$S^{eff}(C^{+2}) = \Sigma_{\rho} \left( S^{eff}(\rho) \cdot (N^{+z}_{\rho\text{-}eq} / N^{+z}_{\rho=1}) \right) \qquad E(5.1.1)$$

where $N^{+z}_{\rho=1}$ is the ground state population, $(N^{+z}_{\rho\text{-}eq} / N^{+z}_{\rho=1})$ are the equilibrium fractional populations of the metastables relative to the ground state population and $S^{eff}(\rho)$ are the effective ionisation rate coefficients for each metastable $\rho$. At temperatures appropriate to the temperature of maximum abundance of $C^{+2}$ ($T_{max}$ = $4.5 \times 10^4$K), the metastable population is large and causes a significant increase in the total loss rate from $C^{+2}$. For comparison, the calculations of Arnaud and Rothenflug only consider ionisation and recombination from ground state ions with no corrections for metastable or excited state ionisation.

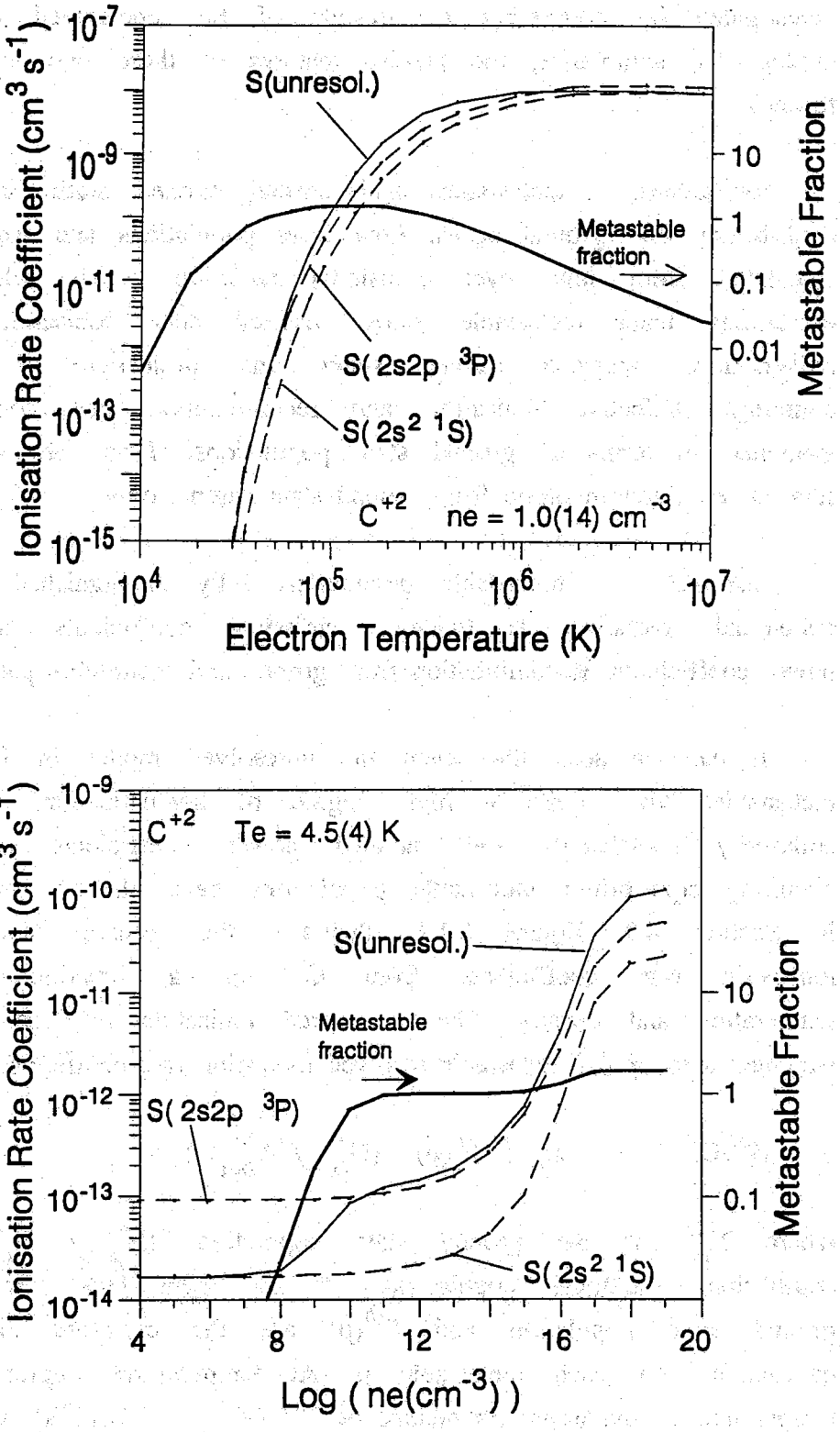


**Figure 5.1.1:** Resolved and unresolved effective ionisation rate coefficients for $C^{+2} \rightarrow C^{+3}$ as a function of electron density. Also plotted is the metastable/ground population fraction of $C^{+2}$ in quasi- static equilibrium.

In equilibrium ionisation balance, there should not be too much difference between the resolved and unresolved models. The metastable populations derived from the resolved model should be similar to those derived by the equilibrium low level population calculation. The main difference between the models will be in transient ionisation environments when metastables are not in equilibrium ratios with ground state populations.

It is convenient in this section to investigate the influence of field enhanced dielectronic recombination on the effective recombination coefficient. This is a reappraisal of the recent work of Reisenfeld (1992) and Reisenfeld et al (1992) which used recombination rate coefficients which were serious overestimates.

## 5.1.2: Reconstruction of Ionisation Balance and Spectral Emission

### (a) Ionisation Balance Models

To establish the state of ionisation of a plasma (that is, the distribution of dynamic population densities) far from LTE it is necessary to consider all the individual processes between the dynamic populations, and all processes influencing ionisation and recombination. The complete solution should include ion transport mechanisms such as diffusion and convection as is given by the solution of

$$d/dt\ N_{\rho}^{+z} + d/dx\ \Gamma(N_{\rho}^{+z}) = S(N_{\rho}^{+z}) \quad ,$$

$$\text{for } \rho = 1,m(z) \text{ and } z = 1,z_0 \qquad \text{E(5.1.2)}$$

the one dimensional continuity equation. m(z) is the number of metastables in stage $X^{+z}$. In the unresolved model, m(z) = 1 for all z. $\Gamma$ represents the flux of particles due to transport and S represents the source terms due to atomic processes. In tokamak plasmas transport can have a dominant influence (see Peacock 1984 and references therein), but as the details depend strongly on particular geometries and initial conditions it is difficult to incorporate transport in a general overview. Thus attention in this section is confined to the cases of equilibrium ionisation balance and the time dependent ionisation of ions in a homogeneous plasma, representing extremes of the dynamic plasma.

Equilibrium ionisation balance is applicable to plasmas of long steady duration in which there is time for the state of ionisation to settle to a constant value. Such conditions are seldom found in laboratory plasmas but are widely assumed for astrophysical plasmas. Calculations of equilibrium ionisation balance have been performed for most cosmologically abundant elements. The current benchmark is the work of Arnaud and Rothenflug (1985).

For laboratory plasmas, atomic processes are insufficiently rapid for the plasma to establish equilibrium in its own lifetime. McWhirter (1981) estimates that the time required for a plasma to reach its steady state of ionisation is

$$\tau_{ion} = 10^{12}/n_e(cm^{-3})\ sec \qquad \text{E(5.1.3)}$$

For JET, with typical electron densities of the order $10^{12}$- $10^{14}$ $cm^{-3}$, $\tau_{ion} \approx$ 0.01 - 1 sec which is comparable with global confinement times. Peacock (1985) states that in order for there to be ionisation equilibrium, the effective confinement time in the local temperature region must exceed the ionisation time. In tokamak edge plasmas, strong transport mechanisms and steep temperature and density gradients imply that equilibrium ionisation balance cannot be taken for granted and indeed is seldom attained. In central regions of the plasma, where the temperature and density gradients are flatter and transport mechanisms are less influential, steady state conditions can nearly be attained following the initial transient diffusion of ions from the wall. In such regions, temperatures are high (several KeV) so that only heavy impurities remain partially ionised (e.g. Ni, Cl). The light impurities are ionised easily in the edge plasma and their partially stripped species are never dominant in achieving equilibrium ionisation balance.

To illustrate the nature of the edge plasma environment and to indicate the magnitude of the atomic timescales, the time dependent ionisation model is adopted. This treats a homogeneous plasma of constant temperature and density into which a small sample of impurity is introduced. The temporal evolution of ionisation stages is followed until the system reaches equilibrium.

Exploration of these two models will thus enable a comparison to be made between the present work and previous calculations of ionisation balance and will also enable the influence of metastable populations to be explored in ionisation equilibrium and in an ionising environment which is similar to that experienced in tokamak edge plasmas. The composition of the source term in equation E(5.1.2) is dependent on whether an unresolved or metastable resolved model is adopted. For the unresolved model, only ground state populations are considered. The populations of adjacent charge states are coupled by effective ionisation and recombination processes only. With no transport contributions, E(5.1.2) reduces to a set of equations of the form

$$d/dt\ N_\rho^{+z} = - S_{\rho\rho}^{eff} N_\rho^{+z} - \alpha_{\rho\rho}^{eff} N_\rho^{+z} + S_{\tau\tau}^{eff} N_\tau^{+(z-1)} + \alpha_{\gamma\gamma}^{eff} N_\gamma^{+z1}$$

$$\text{for } \rho = 1,\ \gamma = 1 \text{ and } z = 1, z_0 \qquad \text{E(5.1.3)}$$

where $S_{\rho\rho}$ is the total ionisation rate coefficient from $X_\rho^{+z}$ and $\alpha_{\gamma\gamma}$ is the total recombination rate coefficient from $X_\gamma^{+z1}$. In equilibrium ionisation balance with $d/dt\ N_\rho^{+z} = 0$ for all z, this gives

$$\frac{N_\gamma^{+z1}}{N_\rho^{+z}} = \frac{S_{\rho\rho}^{eff}}{\alpha_{\gamma\gamma}^{eff}} \qquad \text{for } z = 0, \ldots z_0 - 1 \qquad \text{E(5.1.4)}$$

where S and $\alpha$ are ionisation and recombination coefficients for ions of initial charge +z and +z1 respectively. In the models it is assumed that the number density of element X, N(X), remains constant. The fractional abundances

$$FA(X_\rho^{+z}) = N(X_\rho^{+z}) \ / \ N(X) \qquad \text{E(5.1.5)}$$

of each ionisation stage can thus be derived.

In the metastable resolved model, it is necessary to consider the metastable and parent cross coupling coefficients so that the time dependent equations are

$$\begin{aligned} d/dt\ N_\rho^{+z} = & - \Sigma_\gamma S_{\gamma\rho} N_\rho^{+z} - \Sigma_\tau \alpha_{\tau\rho} N_\rho^{+z} \\ & + \Sigma_\tau S_{\rho\tau} N_\tau^{+(z-1)} + \Sigma_\gamma \alpha_{\rho\gamma} N_\gamma^{+z1} \\ & + \Sigma_{\varepsilon \neq \rho} q_{\rho\varepsilon} N_\varepsilon^{+z} - \Sigma_{\varepsilon \neq \rho} q_{\varepsilon\rho} N_\rho^{+z} \\ & + \Sigma_{\varepsilon > \rho} \beta_{\rho\varepsilon} N_\varepsilon^{+z} - \Sigma_{\varepsilon < \rho} \beta_{\varepsilon\rho} N_\rho^{+z} \end{aligned}$$

$$\begin{aligned} &\text{for} \quad \rho, \varepsilon = 1, m(z) \text{ and } z = 0, \ldots z_0 \\ &\qquad \gamma = 1, m(z1) \\ &\qquad \tau = 1, m(z-1) \end{aligned} \qquad \text{E(5.1.6)}$$

where $\gamma$ and $\tau$ represent the metastable states of stages $N^{+z1}$ and $N^{+(z-1)}$ respectively, and $\rho$ and $\varepsilon$ represent the metastable states of $N^{+z}$. $S_{\gamma\rho}$ and $\alpha_{\rho\gamma}$ are metastable resolved ionisation and recombination coefficients, and $q_{\varepsilon\rho}$ and $\beta_{\varepsilon\rho}$ are the metastable and parent cross coupling coefficients.

Both sets of equations, E(5.1.3) and E(5.1.6) can be written in matrix form as

$$d/dt\ \underset{\sim}{N} = \mathbb{S}.\underset{\sim}{N} \qquad \text{(E5.1.7)}$$

or in terms of fractional abundances as

$$d/dt\ FA = \mathbb{S}.FA \qquad \text{(E5.1.8)}$$

which for constant $\mathbb{S}$ is an eigenvalue equation. If the total number of dynamic populations is equal to NP then there are NP eigenvalues, $\lambda$, and eigenvectors, $\underset{\sim}{U}$. The temporal evolution of the fractional abundances is expressed as

$$FA(t) = \Sigma_{i=0}^{i=NP} C_i \exp(\lambda_i t)\ \underset{\sim}{U}_i \qquad \text{E(5.1.9)}$$

where the constants $C_i$ are derived from boundary conditions at t=0. That is,

$$FA(t=0) = \Sigma_{i=0}^{i=NP} C_i\ \underset{\sim}{U}_i \qquad \text{E(5.1.10)}$$

where FA(t=0) has been chosen to represent the initial state of ionisation at time, t=0. The equilibrium solution of the system corresponds to the solution with the eigenvalue, $\lambda_{eq} = 0$ so that

$$FA_{eq}(t) = C_{eq}\ \underset{\sim}{U}_{eq} \qquad \text{E(5.1.11)}$$

A computational solution to the above set of equations was obtained using eigenvalue subroutines from the Numerical Algorithm Group (NAG) Libraries. Equilibrium and transient ionisation balance can be calculated for arbitrary species at arbitrary values of temperature and density. For the unresolved model, the equilibrium fractional abundances obtained by E(5.1.4) and by the eigenvalue/eigenvector solution agree exactly.

**(b) Spectral Intensities and Radiated Power**

Spectral intensities are reconstructed from the fractional abundances as

$$I(\lambda,i\rightarrow j) = \left( \Sigma_{\rho} n_e \varepsilon_{ex}^{eff}(\lambda,\rho)\, FA(X_{\rho}^{+z}) + \Sigma_{\gamma} n_e \varepsilon_{rec}^{eff}(\lambda,\gamma)\, FA(X_{\gamma}^{+z1}) \right) N(X)$$

photons $s^{-1}$ $cm^{-3}$ E(5.1.12)

The theoretical combination of effective emissivity coefficient with ionisation balance fractional abundance and elemental abundance is a quantity often used in solar coronal studies (Lang et al 1990). It is the so called '$G(T_e)$' function which is used to connect line of sight integrated spectral intensities to differential emission measure through an integral relation. A modified function is more useful in the present work where the assumption of solar elemental abundances is not made and electron density is incorporated in the definition. Then, spectral intensities are expressible in terms of ion densities as

$$I(\lambda,i\rightarrow j)/N(X) = \Sigma_{\rho} G_{ex}^{eff}(\lambda,\rho) + \Sigma_{\gamma} G_{rec}^{eff}(\lambda,\gamma) \qquad \text{photons } s^{-1} \text{ ion}^{-1}$$

E(5.1.13)

The total radiated power is given by summing over line and recombination/ bremsstrahlung contributions as

$$n_e P_{rad}/N(X) = \Sigma_z \Sigma_{\rho} FA(X_{\rho}^{+z})\, n_e \left( P_L(\rho,z) + \Sigma_{\tau} P_{RB}(\rho\rightarrow\tau,z) \right)$$

W $s^{-1}$ $ion^{-1}$ E(5.1.14)

where $\tau$ indexes the metastables of stage $X^{+(z-1)}$.

# 5.2: EQUILIBRIUM IONISATION BALANCE AND RADIATED POWER


5.2.1: Comparison Of Unresolved Model With Previous Work
5.2.2: Resolved Model
5.2.3: Influence of Field Enhanced Dielectronic Recombination


## 5.2.1: Comparison of unresolved model with previous work

We consider first the ionisation balance calculations of Arnaud and Rothenflug (1985). These authors presented a critical review of unresolved ionisation and recombination coefficients and computed equilibrium ionisation balance for the elements of H, He, C, N, O, Ne, Na, Mg, Al, Si, S, Ar, Ca and Fe in the limit of zero electron density. The main difference between these calculations and the unresolved calculations of the present work are (i) the inclusion of density effects in the present work, (ii) the choice of fundamental atomic data. Point (i) presents no difficulty since a comparison can be made at low electron density where collisional radiative effects are negligible, matching their assumption. Point (ii) is a matter of debate. The ionisation cross sections used in the present work are based on the same data as Arnaud and Rothenflug. The present high temperature dielectronic recombination data however is different, and indeed should be a significant improvement. Also, Arnaud and Rothenflug include low temperature dielectronic recombination rate coefficient adjustments in their calculation. This will influence ionisation balance below ~ 5eV.

Figure 5.2.1 shows a comparison between the present work and Arnaud and Rothenflug (1985) for the equilibrium ionisation balance of carbon. The present work was calculated at an electron density of $10^4$ $cm^{-3}$ so that collisional radiative effects are small. In general there is good agreement between the two calculations. The largest differences are in the abundances of the $C^{+1}$ and $C^{+2}$ stages. The ionisation and recombination rate coefficients between these stages were examined to determine the reason for this difference. This is illustrated in Fig. 5.2.2. For comparison, the low temperature dielectronic rate coefficients of Nussbaumer and Storey (1983) were added onto the present work. It can be

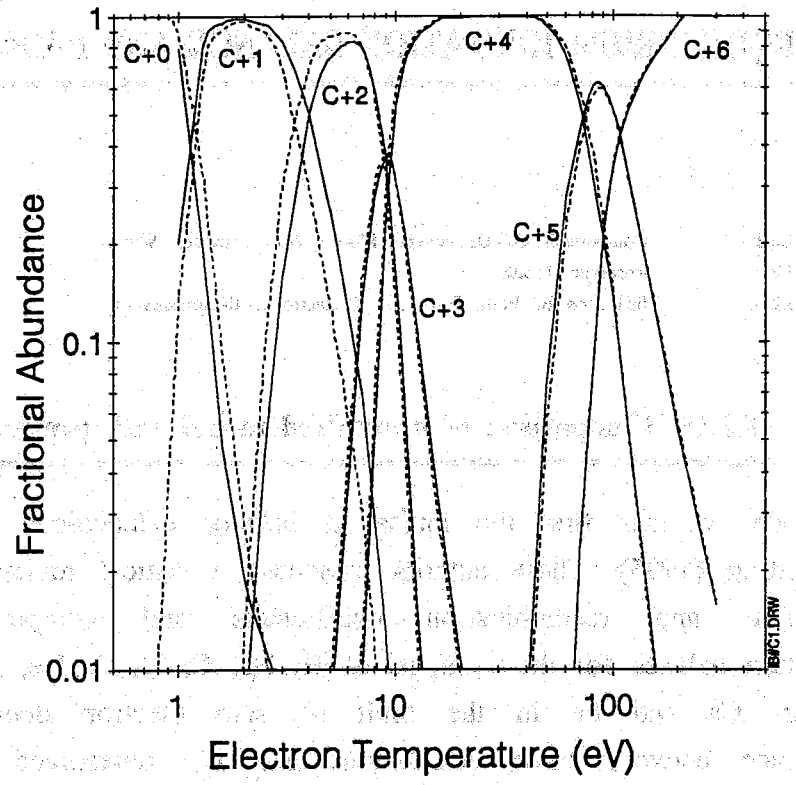


**Figure 5.2.1:** Comparison between the equilibrium ionisation balance for carbon of Arnaud and Rothenflug (1985) and that of the present work.

- - - - Present work, $n_e = 1.0 \times 10^4$ cm$^{-3}$

——— Arnaud and Rothenflug (1985)

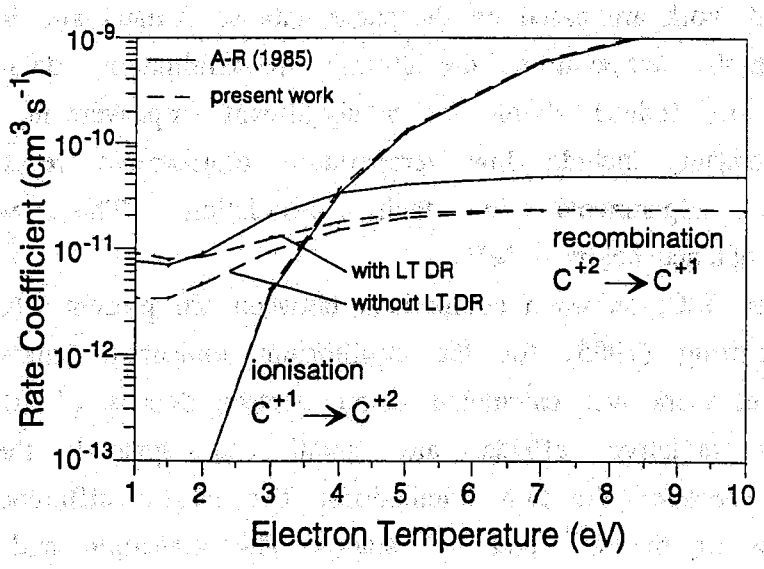


**Figure 5.2.2:** Comparison between ionisation and recombination rate coefficients for $C^{+1} \rightarrow C^{+2}$. $n_e = 1.0 \times 10^4$ cm$^{-3}$. The present work is shown with and without the addition of low temperature dielectronic recombination (LT DR) rate coefficients.

seen that the ionisation rate coefficients are in exact agreement and that there is a difference in the recombination rate coefficients which it not entirely due to the low temperature dielectronic recombination. The high temperature dielectronic recombination data of Arnaud and Rothenflug is from the calculations of Jacobs (1977). The more recent work of Badnell (1990) used in the present work should be a better estimate. The crossing point of ionisation and recombination rate coefficients determines the point at which the $C^{+1}$ and $C^{+2}$ fractional abundances are equal. The difference in the recombination rate coefficients thus causes this temperature to shift from 3.6eV to 4.0eV which explains the differences in ionisation balance. For oxygen equilibrium ionisation balance at $n_e$ = $1.0x10^4$ $cm^{-3}$ the comparison between Arnaud and Rothenflug and the present work is also very good. Small differences were again traced to differences in the recombination rate coefficients.

To illustrate the influence of electron density on ionisation balance (a situation not addressed by Arnaud and Rothenflug), Figures 5.2.3 and 5.2.4 plot equilibrium ionisation balance for carbon and oxygen as a function of electron temperature and density. The carbon data is plotted at $10^4$ and $10^{13}$ $cm^{-3}$, which corresponds to effectively zero electron density and a density relevant to fusion plasmas. The oxygen data is plotted at $10^4$ and $10^8$ $cm^{-3}$ to compare results at densities relevant to the solar corona. It can be seen that there are considerable changes in the fractional abundances of the low ionisation stages, especially for the lithium like ions $C^{+3}$ and $O^{+5}$. These changes are due to the density dependence of the ionisation and recombination coefficients. The ionisation rate coefficients tend to increase with electron density whereas the recombination rate coefficients decrease. Both these effects shift fractional abundances to lower temperatures. Test calculations were performed in which either the zero density ionisation or recombination rate coefficients were used in place of the density dependent coefficients. The density sensitivity of both the ionisation and recombination rate coefficients contribute to the changes in Figures 5.2.3 and 5.2.4.

Figure 5.2.5 plots radiated power in equilibrium ionisation balance for beryllium, carbon and oxygen. The results of the present work are compared with the recent calculations of Bonnin et al (1992). It can be seen that there are slight differences in the two calculations. Bonnin et al published details of the calculated line power coefficients for each

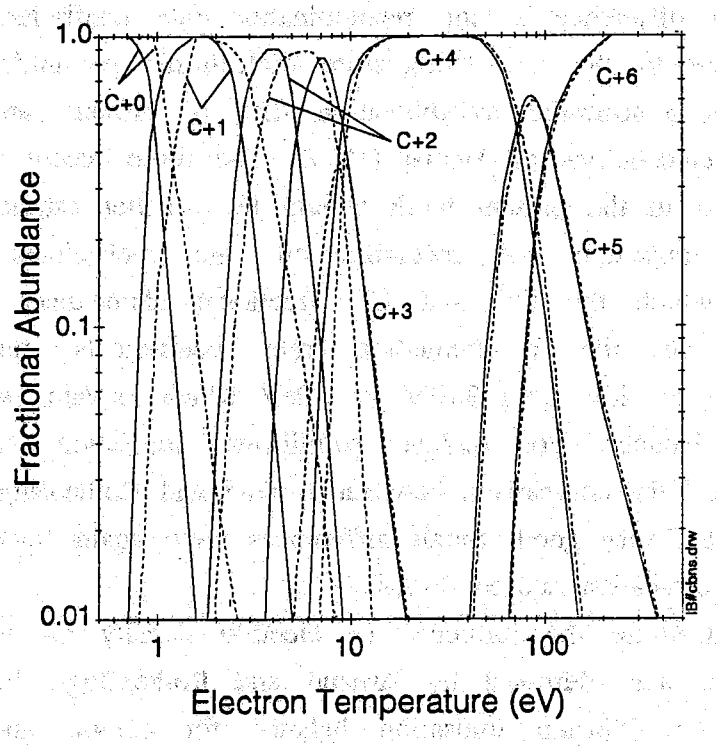


**Figure 5.2.3:** Equilibrium ionisation balance for carbon as a function of electron density.

- - - - $n_e = 1.0x10^4$ cm$^{-3}$ ——— $n_e = 1.0x10^{13}$ cm$^{-3}$

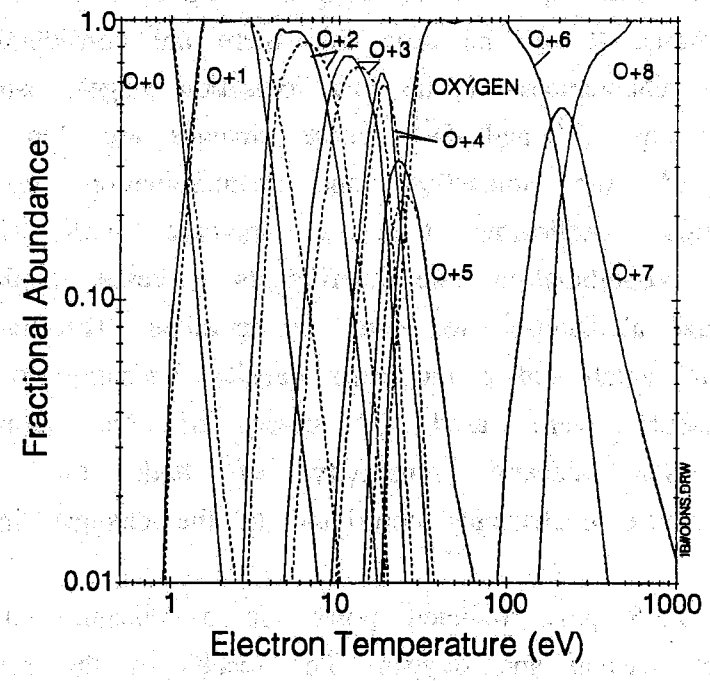


**Figure 5.2.4:** Equilibrium ionisation balance for oxygen as a function of electron density.

- - - - $n_e = 1.0x10^4$ cm$^{-3}$ ——— $n_e = 1.0x10^8$ cm$^{-3}$

ion, and the total power in equilibrium ionisation balance. The line power coefficients for each ion were compared and found to be in good agreement, with the exception of $C^{+2}$, for which the coefficient derived in the present work is ~ twice that of Bonnin et al. This large coefficient is due to excitation from the 2s2p $^3P$ metastable which is highly populated at $n_e = 10^{14}$ cm$^{-3}$. It is not possible to compare directly with Bonnin et al because they do not publish details of the calculated metastable fractions. Similarly, these authors do not publish any numerical details of ionisation balance, although a description of the method used is given in the text. Their density dependent recombination rate coefficients for ionisation balance calculations were obtained by scaling the zero density dielectronic rate coefficients of Badnell (1989) with the hydrogenic scaling factor of Roszman (1989). They do not use a density dependant

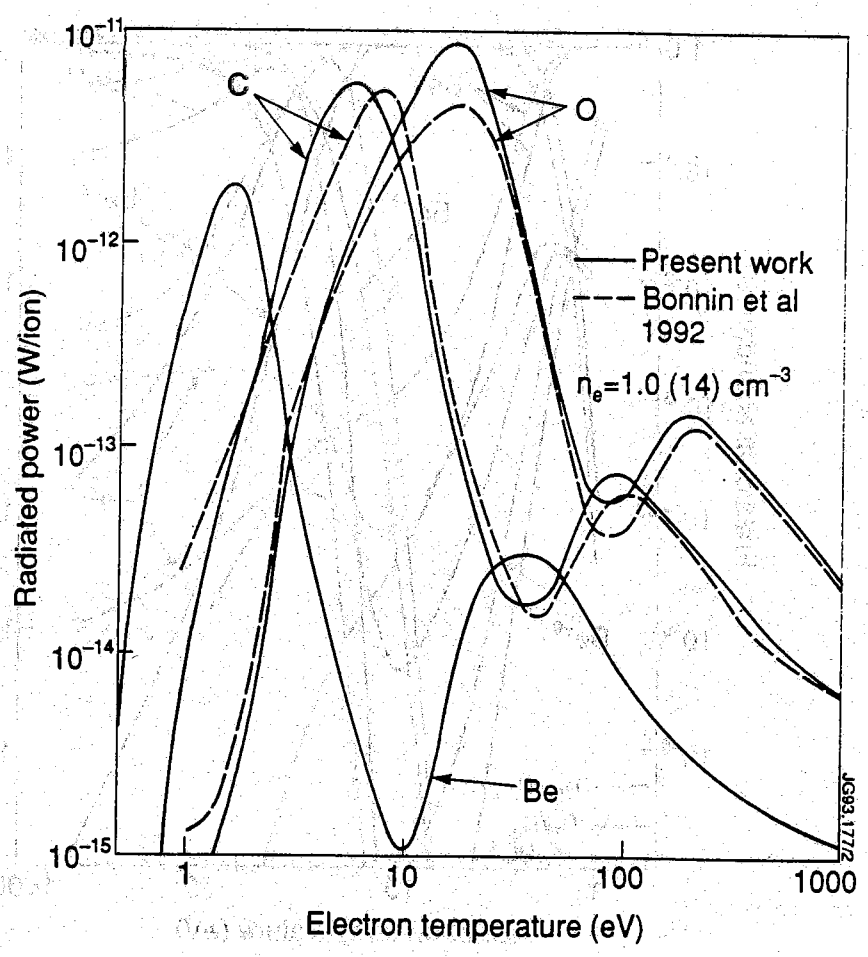


**Figure 5.2.5:** Total radiated power in equilibrium ionisation balance for Be, C, and O. $n_e = 1.0 \times 10^{14}$ cm$^{-3}$.
——— Present work - - - - Bonnin et al (1992)

adjustment for the collisional- radiative ionisation rate coefficients. This results in inaccurate density dependent ionisation balance calculations. The differences in Fig. 5.3.5 can thus be attributed to changes in ionisation balance. The full density dependent ionisation balance in the present work shifts the peak of radiated power to lower temperature (for C) and enhances the radiation from the lithium like stage (for O).

Figure 5.2.6 plots equilibrium ionisation balance and radiated power for Beryllium with and without the presence of neutral hydrogen. It can be seen that even a modest amount of hydrogen ($n_H/n_e$ = 0.001 with $n_e$ = $1.0x10^{14}$ $cm^{-3}$) has a considerable effect on ionisation balance. Charge transfer reactions enhance the fractional abundances of the low ionisation stages leading to an increase in the total radiated power.

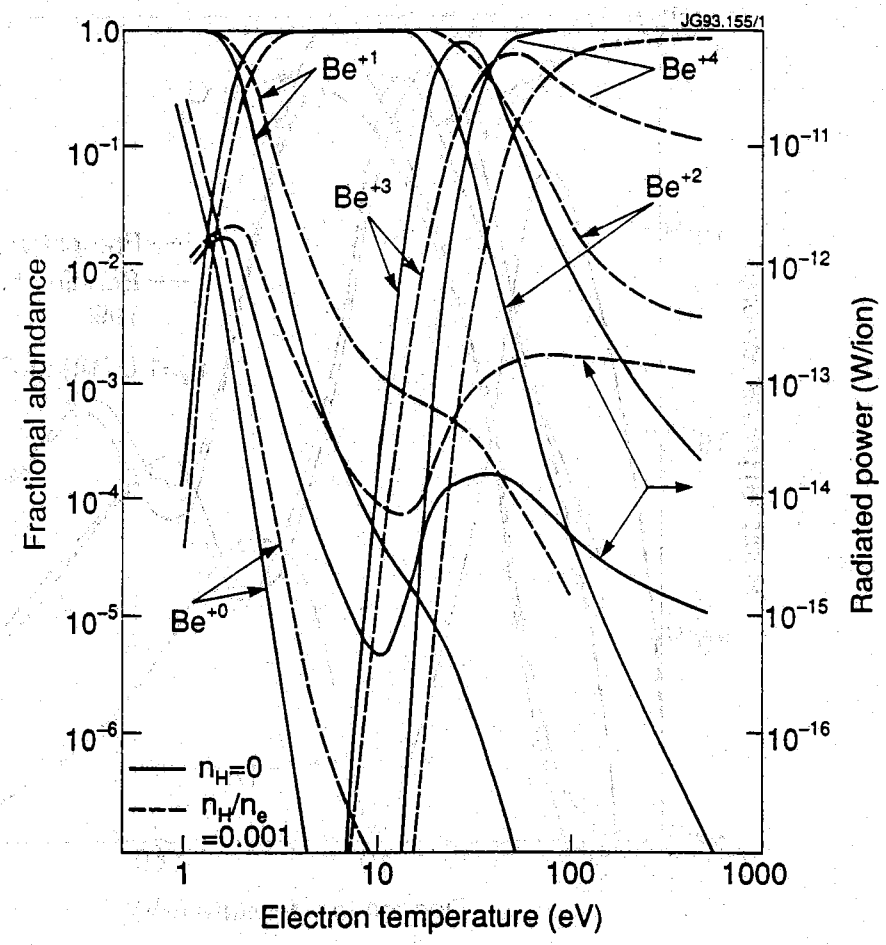


**Figure 5.2.6:** Equilibrium ionisation balance and radiated power for beryllium. $n_e$ = $1.0x10^{14}$ $cm^{-3}$.

——— $n_H/n_e$ = 0.0 – – – – $n_H/n_e$ = 0.001

### 5.2.2: Resolved Model

Metastable resolved equilibrium ionisation balance and radiated power calculations for beryllium, carbon and oxygen are illustrated in Figures 5.2.7, 5.2.8 and 5.2.9.

Beryllium ionisation balance is plotted at electron densities of $10^4$ and $10^{14}$ $cm^{-3}$. It can be seen that the electron density sensitivity of the ionisation and recombination coefficients has a considerable influence on the fractional abundances. The $Be^{+0}$ $2s2p\ ^3P$ metastable population is significant even at electron densities as low as $10^4$ $cm^{-3}$. Indeed, excitations from the metastable dominate radiated power from $Be^{+0}$ at high electron densities. Even though the $Be^{+2}$ $1s2s\ ^3S$ metastable is not as highly populated (the metastable fraction is ~ $2.0x10^{-4}$ at 200eV), excitations from this metastable still contribute substantially to the radiated power from $Be^{+2}$. This reflects the greater efficiency of the $\Delta n=0$ $1s2s\ ^3S \rightarrow 1s2s\ ^3P$ excitation compared to the $\Delta n=1$ $1s^2\ ^1S \rightarrow 1s2p\ ^1P$ excitation from the ground state.

For carbon, the $2s2p\ ^3P$ metastable is again highly populated. The other metastables have fraction populations of <10% of that of the corresponding ground state. Considering the radiated power contributions, $C^{+2}$ $2s2p\ ^3P$ and $C^{+4}$ $1s2s\ ^3S$ both contribute as much to the radiated power as the $C^{+2}$ and $C^{+4}$ ground states. $C^{+1}$ $2s2p^2\ ^4P$ contributes ~50% of that of the $C^{+1}$ ground state.

Oxygen is plotted at an electron density of $10^8$ $cm^{-3}$ which is appropriate to the solar corona. At this low density, the metastable populations of $O^{+3}$, $O^{+4}$ and $O^{+6}$ have not yet reached their collisionally depopulated values and have fractional populations of ~0.001% of that of the corresponding ground state populations. The contributions to radiated power from the B-like and Be-like metastables are not as important in low density plasmas. The radiated power from the $O^{+6}$ $1s2s\ ^3S$ metastable is the dominant contribution from the He-like and H-like stages. This is more important than in high density plasmas because the $1s2s\ ^3S$ population is depleted by ionisation at high density (c.f. Figure 5.2.7 with carbon at $n_e = 1.0x10^{13}$ $cm^{-3}$). Considering the $O^{+2}$ and $O^{+1}$ stages, the $2s^22p^2\ ^1D$ and $2s^22p^3\ ^2D$ metastable populations are the largest with fractional populations of ~30-50% of that of their respective ground states. The radiated power contributions from these stages is dominantly from the ground state ions, even at high electron density.

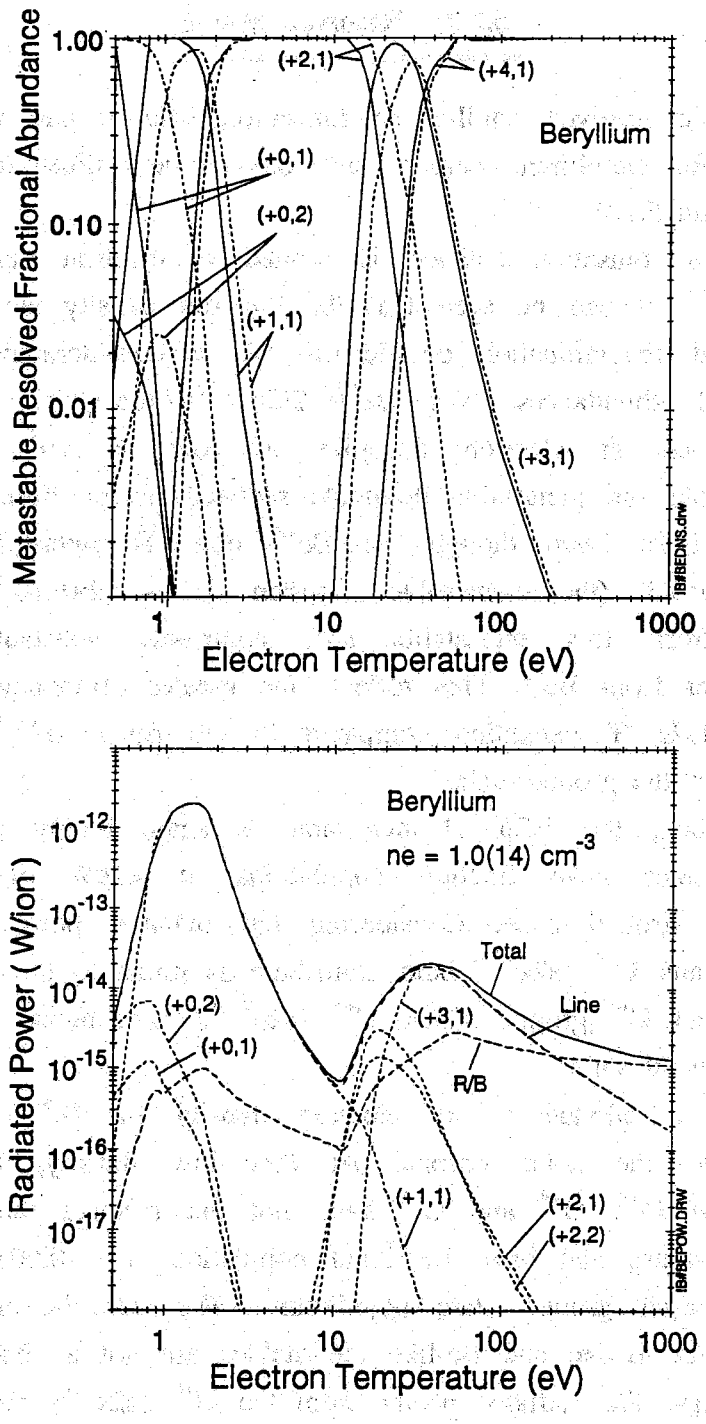


**Figure 5.2.7:** Metastable resolved equilibrium ionisation balance and radiated power for beryllium. Ionisation balance is plotted at electron densities $10^4$(——) and $10^{14}$ $cm^{-3}$ (- - -) whereas radiated power is only plotted at $n_e = 10^{14} cm^{-3}$. Curves are labelled by (+z,ρ) where z is the ion charge and ρ is the metastable index. The radiated power graph shows the total radiation, the total line power (line), the total recombination/ bremsstrahlung contribution (R/B) and the line power contributions from each metastable.

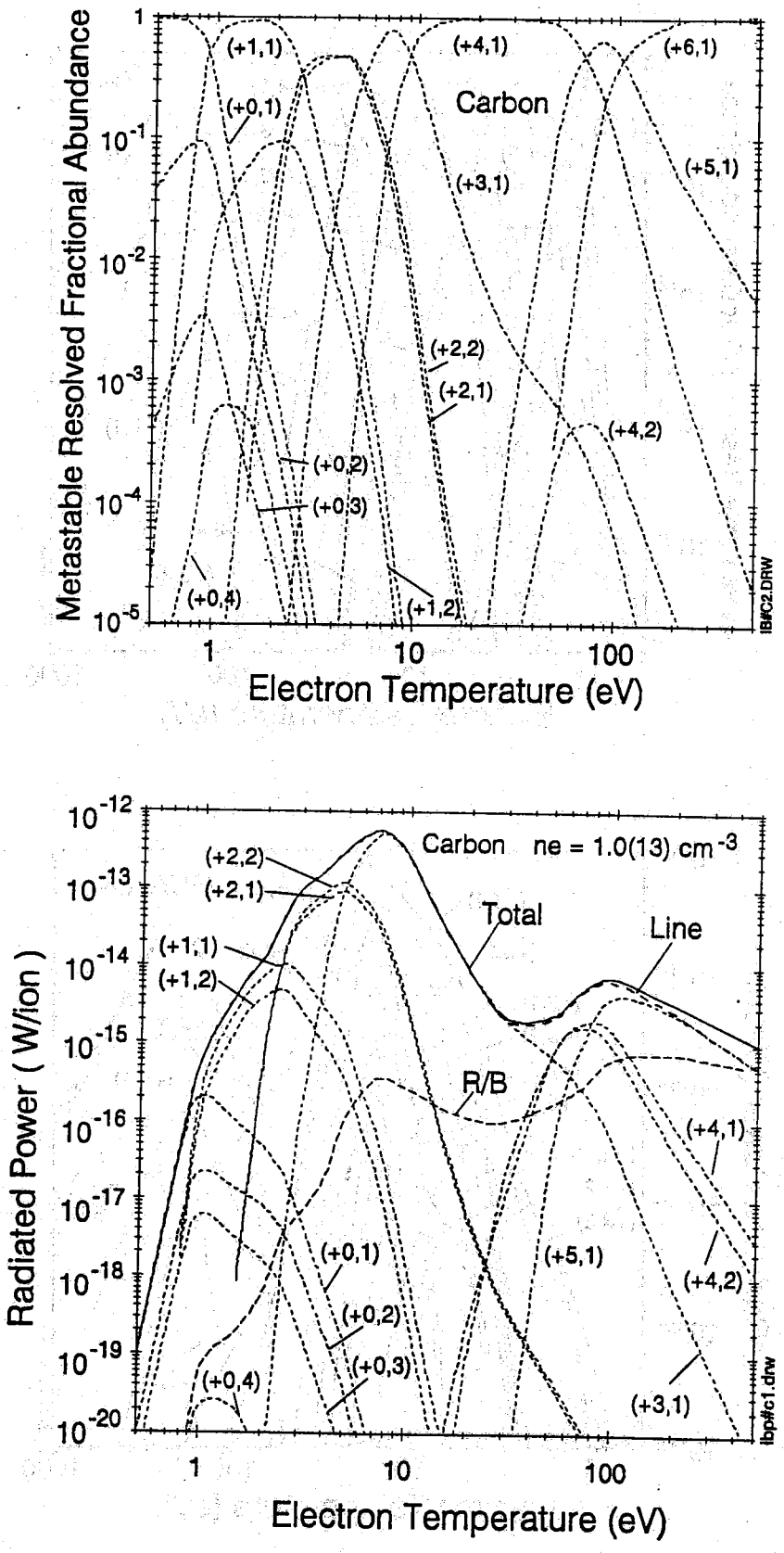


**Figure 5.2.8:** Metastable resolved equilibrium ionisation balance and radiated power for carbon. $n_e$ = 1.0x10$^{13}$ cm$^{-3}$. Annotation as Figure 5.2.7.

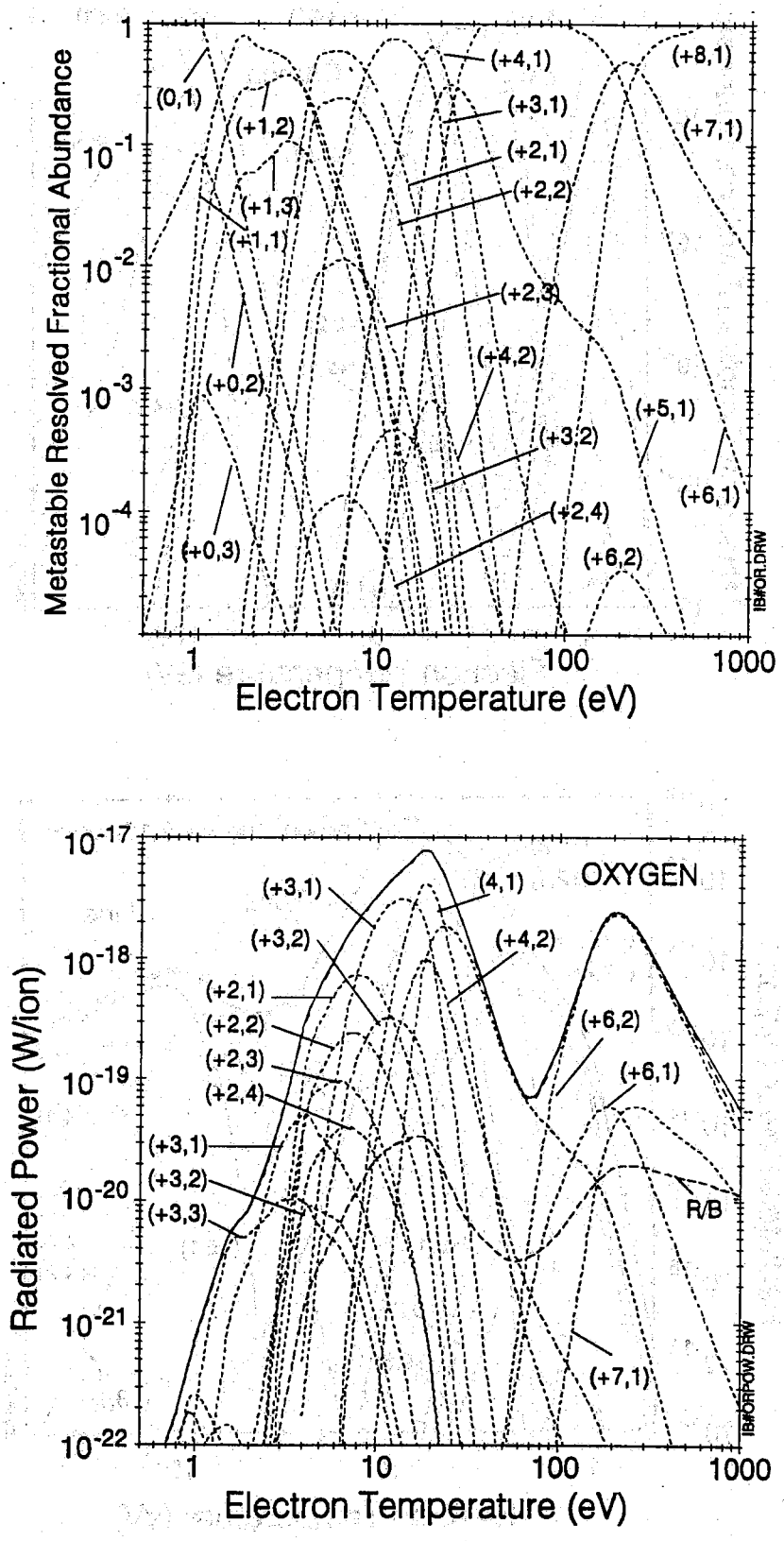


**Figure 5.2.9:** Metastable resolved equilibrium ionisation balance and radiated power for oxygen. $n_e$ = 1.0x10$^8$ cm$^{-3}$.Annotation as Figure 5.2.7.

Figures 5.2.10 and 5.2.11 examine in detail the metastable populations of $Be^{+0}$, $O^{+0}$, $O^{+1}$, $O^{+2}$, $O^{+3}$, $O^{+4}$ and $O^{+6}$. The populations are plotted relative to the ground state populations. From Figure 5.2.10 it can be seen that ionisation and recombination process contribute to the metastable population of $Be^{+0}$ as well as collisional processes within the low level group. At low electron temperatures, the metastable fraction in equilibrium ionisation balance is almost identical to that obtained in low level quasi-static equilibrium. At high electron temperatures, ionisation from the metastable becomes important and significantly depletes the population given by the low level model. Without ionisation, purely collisional processes are establishing the metastable population. In equilibrium ionisation balance, recombination processes counteract the depopulation due to ionisation and maintain a relatively high metastable

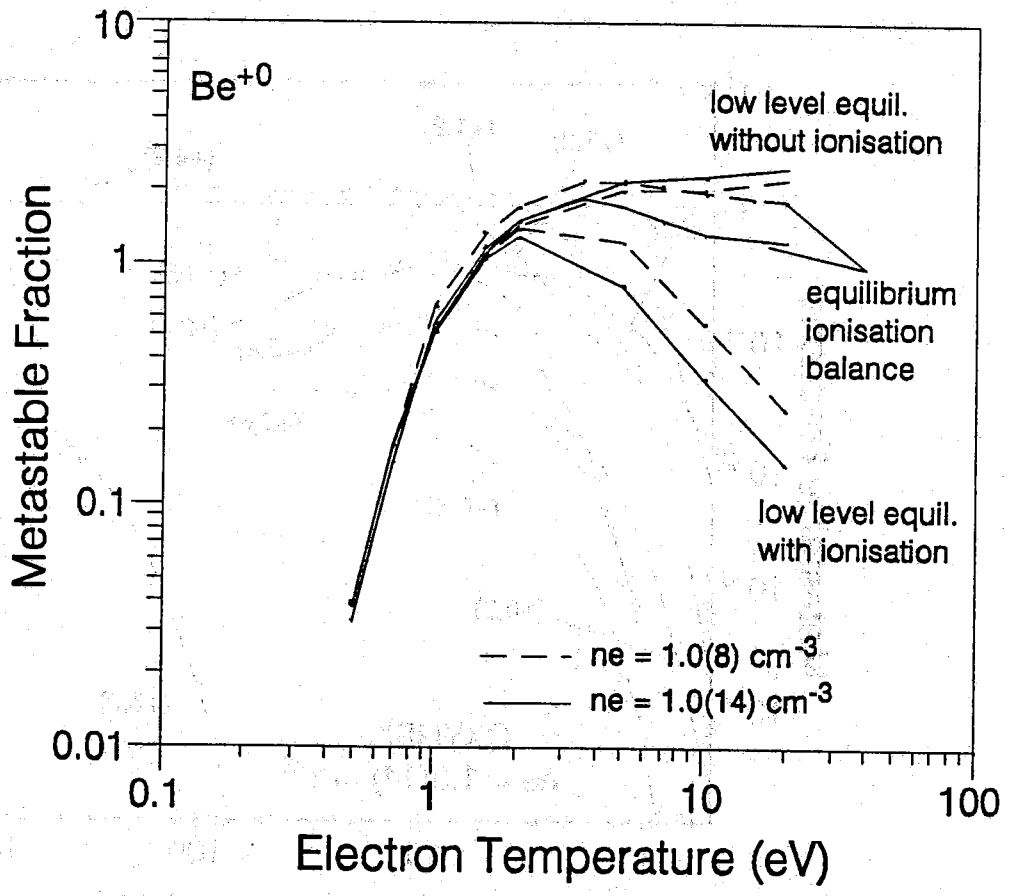


**Figure 5.2.10:** Metastable/ ground population fractions of $Be^{+0}$ calculated in quasi- static low level equilibrium (with and without ionisation) and in equilibrium ionisation balance.

fraction. It should be stressed that this is not a LTE balance of processes. The active recombination processes at $10^{14}$ $cm^{-3}$ are dielectronic and radiative recombination. True Saha-Boltzmann populations will only be achieved in high density plasmas when three body recombination balances the direct ionisation losses. The metastable fractions of oxygen in Figure 5.2.11 are plotted in equilibrium ionisation balance. At $10^{14}$ $cm^{-3}$, the most important metastables are $O^{+1}$ $2s^22p^3$ $^1D$, $O^{+2}$ $2s^22p^2$ $^1D$, $O^{+3}$ $2s2p^2$ $^4P$ and $O^{+4}$ $2s2p$ $^3P$.

In Figure 5.2.12, spectral intensities of two spectral lines of carbon are synthesised in equilibrium ionisation balance. For C II 133.5nm, ~ 70% of the intensity is due to excitation from the $2s^22p$ $^2P$ ground state and 30% is due to excitation from the $2s2p^2$ $^4P$ metastable. For C IV 31.2nm, the recombination contribution to the spectral intensity is plotted. This is small and can be ignored for practical purposes.

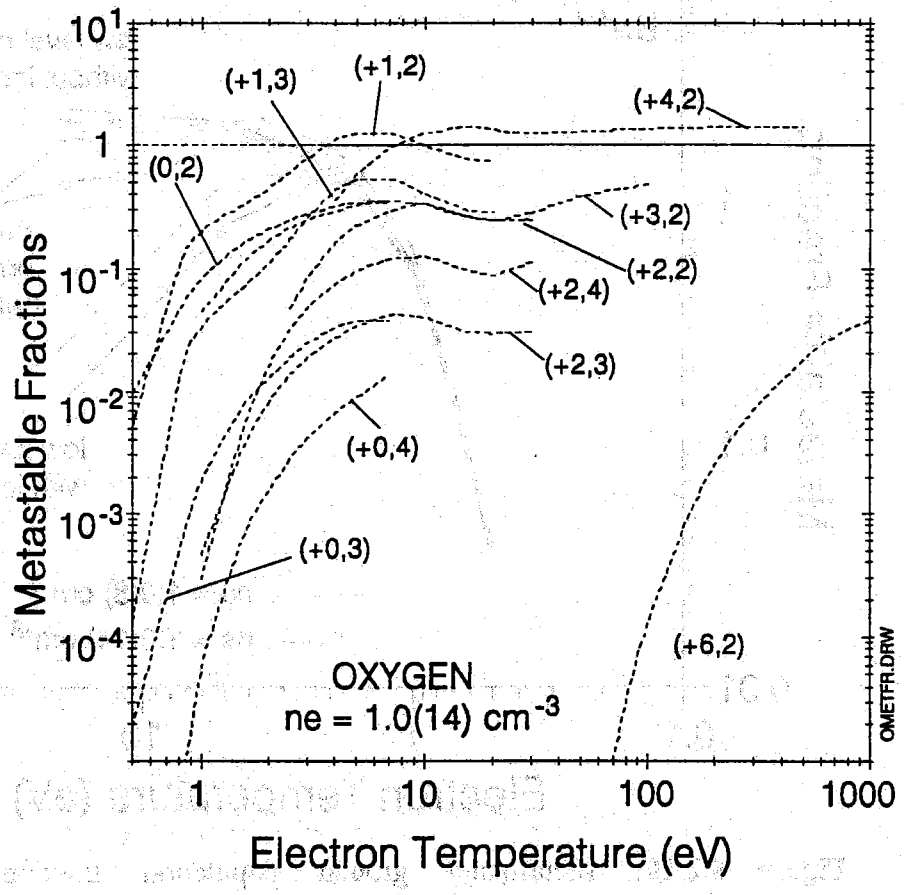


**Figure 5.2.11:** Metastable/ground population fractions of $O^{+1}$, $O^{+2}$, $O^{+3}$ and $O^{+4}$ in equilibrium ionisation balance.

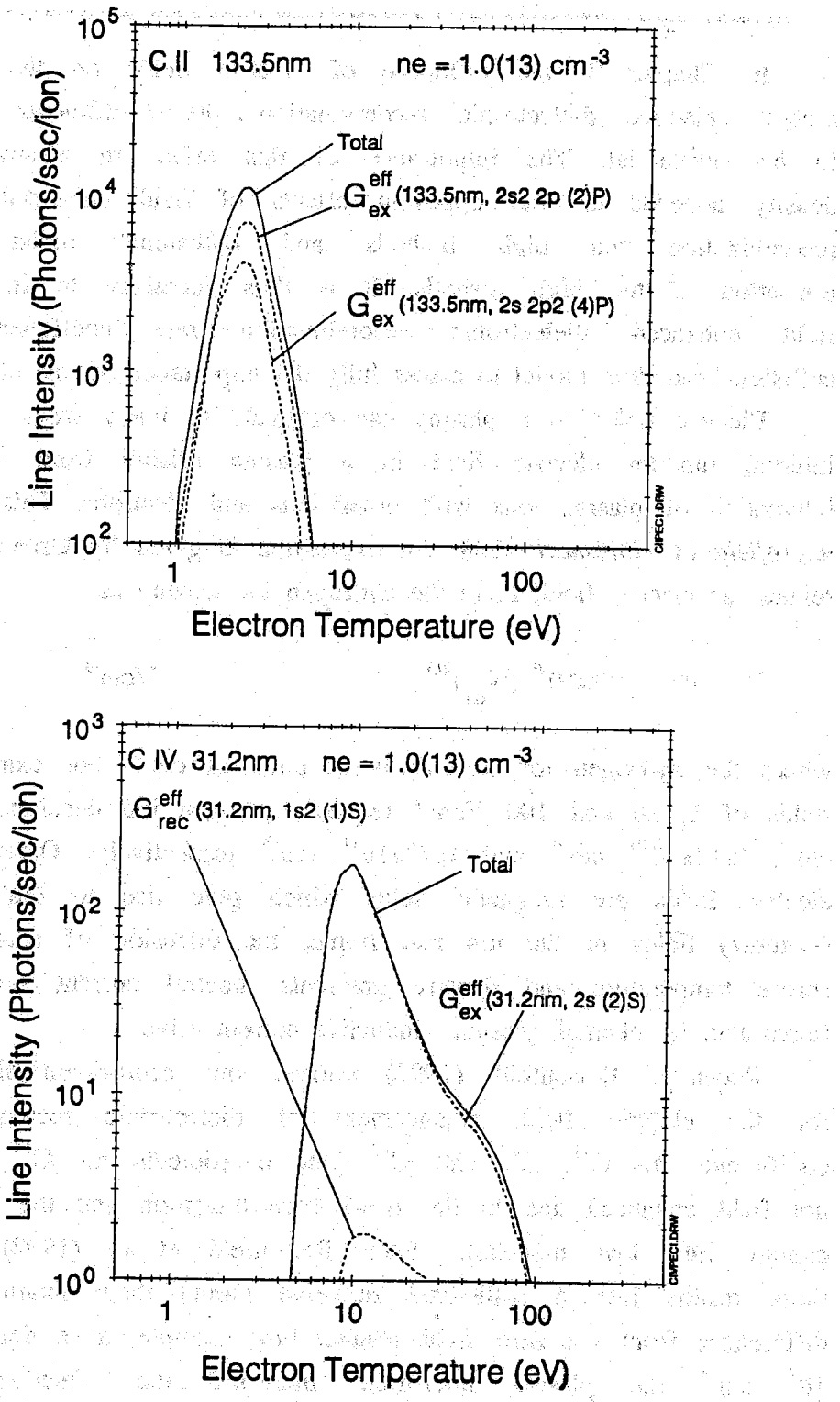


**Figure 5.2.12:** Intensities of spectral lines of C in equilibrium ionisation balance showing the excitation and recombination contributions.

(a) $C^{+1}$ ($2s2p^2\ ^2D$ - $2s^22p\ ^2P$) at 133.5nm.

(b) $C^{+3}$ ($1s^23p\ ^2P$ - $1s^22s\ ^2S$) at 31.2nm.

### 5.2.3: Influence of Field Enhanced Dielectronic Recombination

In Chapter 3, the influence of electric fields on the fundamental n-shell selective dielectronic recombination rate coefficients was shown to be substantial. The importance of this effect in plasmas of finite density depends on the opposing effects of field enhanced dielectronic recombination via high n-shells and collisional redistribution and ionisation of the high n-shells. It is thus necessary to incorporate the field enhanced dielectronic recombination rate coefficients into a collisional-radiative model to assess fully the importance of this effect.

Electric fields in a plasma can originate in many ways. There is the internal random electric field in a plasma arising from the screening interaction of plasma ions with other ions and electrons. This the the *ion microfield* or *Holtzmark* field. An expression is given by Griem (1974) who relates the electric field, F, to the hydrogen ion density as

$$F = 1.3\times10^{-6} (N_{H+})^{2/3} \quad Vcm^{-1} \qquad E(5.2.3)$$

where the hydrogen ion density is in units of $cm^{-3}$. For example, electric fields of 1, 10 and 100 $Vcm^{-1}$ require hydrogen ion densities of $6.75\times10^{8}$ $cm^{-3}$, $2.13\times10^{10}$ $cm^{-3}$ and $6.75\times10^{11}$ $cm^{-3}$ respectively. Other sources of electric fields are magnetic fields which give rise to motional electric (Lorentz) fields in the ion rest frame, the diffusion of charged particles across temperature and density gradients, neutral current sheets in solar flares and, in tokamak plasmas, inductive current drive.

Recently, Reisenfeld (1992) carried out semi-empirical calculations for the electric field enhancement of dielectronic recombination rate coefficients for $C^{+1}$, $C^{+2}$ and $C^{+3}$ (rate coefficients for $C^{+4}$ and $C^{+5}$ are not field enhanced due to the $\Delta n=1$ core transition and the dominance of capture into low n-shells). When Reisenfeld et al (1992) incorporated these results into a collisional radiative model they obtained substantial differences from the zero field results. For example, at a density of $n_H = 10^9$ $cm^{-3}$ the plasma microfield increased the effective dielectronic recombination rate coefficient for $C^{+3}$ by nearly a factor of three. $C^{+1}$ and $C^{+2}$ were not influenced, collisions dominating over any field enhancement.

The size of this effect questions the validity of using zero field dielectronic recombination rate coefficients in ionisation balance models.

However, Badnell et al (1993) have performed fully quantal calculations of field enhanced dielectronic recombination rate coefficients. These show that the semi-empirical approach used by Reisenfeld (1992) grossly overestimates the field enhancement. This is illustrated in Figure 5.2.13 for an electric field of 1 $Vcm^{-1}$.

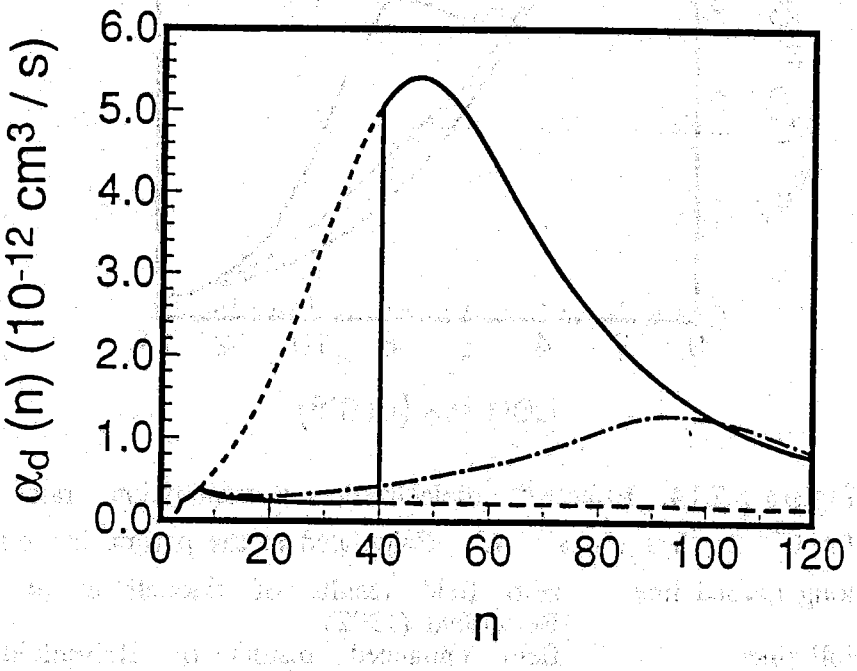


**Figure 5.2.13:** Dielectronic recombination rate coefficients for

$C^{+3}$ 2s $^2S$ + $e^-$ → $C^{+2}$

as a function of principal quantum shell. V = 1 $Vcm^{-1}$.

| | |
|---|---|
| long dashed line | zero field results of Badnell et al (1993) and Reisenfeld (1992) |
| short dashed line | field enhanced results of Reisenfeld (1992) asuming full Stark mixing |
| full line | field enhanced results of Reisenfeld (1992) asuming partial Stark mixing |
| dot-dash line | field enhanced results of Badnell et al (1993) |

The more accurate field enhanced dielectronic rate coefficients for $C^{+3}$→ $C^{+2}$ of Badnell et al were incorporated in to the collisional-radiative population models of the present work. Effective recombination recombination rate coefficients were then computed as a function of plasma microfield. In Figure 5.2.14, the results of Reisenfeld and the results of the present work are compared. To facilitate the

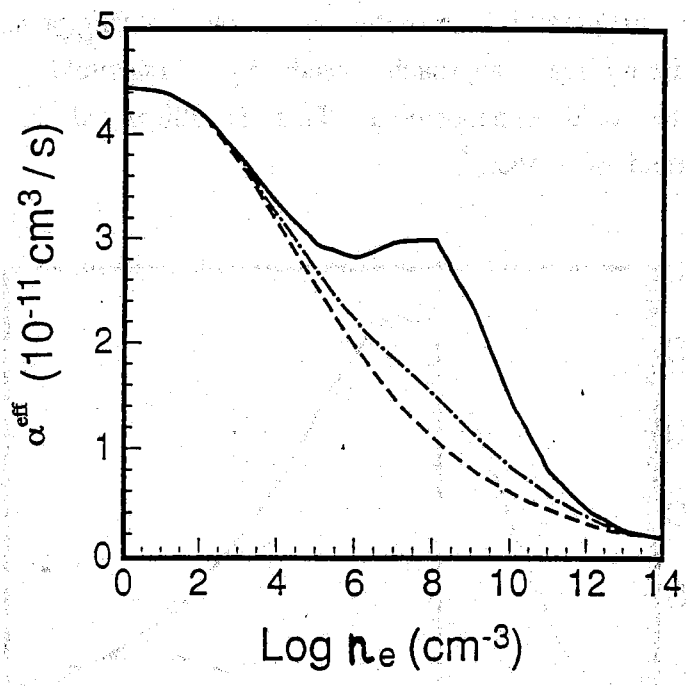


**Figure 5.2.14:** Effective dielectronic recombination rate coefficients for $C^{+3}$ 2s $^2S$ + $e^-$ → $C^{+2}$. Calculated at the plasma ion microfield.

| | |
|---|---|
| long dashed line | zero field results of Badnell et al (1993) and Reisenfeld (1992) |
| full line | field enhanced results of Reisenfeld (1992) asuming partial Stark mixing |
| dot-dash line | field enhanced results of Badnell et al (1993) |

comparison, the rate coefficients are matched at zero electron density. The overestimate of the fundamental field enhanced dielectronic rate coefficients by Reisenfeld leads in turn to an overestimate of the effective recombination rate coefficient. It is found that the effective dielectronic recombination rate coefficient is only field enhanced by ~40% at $n_H = 10^9$ $cm^{-3}$, compared to the factor of three enhancement obtained by Reisenfeld. At $n_H = 10^{13}$ $cm^{-3}$ there is no increase in the effective dielectronic recombination rate coefficient.

In the absence of applied external fields in excess of the ion microfield, there are not enormous changes in the ionisation balance of $C^{+3}$. In the presence of large external fields however, then it will be necessary to reconsider the influence of field enhanced dielectronic recombination. Reisenfeld et al have discussed the interpretation of spectroscopic intensities from solar flare regions.

In tokamak plasmas, field enhanced dielectronic recombination due to the ion microfield is unlikely to be of importance because of the high electron densities involved. At an electron density of $2x10^{13}$ $cm^{-3}$, the ion microfield in ~ 1000 $Vcm^{-1}$ and field enhancement is entirely offset by collisional ionisation. For completeness, it is necessary to consider other sources of electric fields. The magnetic field strength in JET is ~ 3T. A $C^{+3}$ ion with a temperature of 50eV will experience a Lorentz field of ~ 600 $Vcm^{-1}$ if it is travelling perpendicular to the magnetic field. In practice, most of the kinetic energy of the ion will be directed along the magnetic field lines so that the Lorentz field will be less. This is comparable with or less than the ion microfield and unlikely to be important. Electric fields also arise in the edge plasma due to pressure gradients. These are estimated to be ~ 200 - 300 $Vcm^{-1}$ (Hawkes et al 1993). This value is less than the ion microfield and again of no importance for the recombination.

# 5.3: TIME DEPENDENT IONISATION STUDIES

5.3.1: Influx ions Be+1 and Be+2
5.3.2: Time Dependent Ionisation of $C^{+1}$ and $C^{+2}$

## 5.3.1: Influx ions $Be^{+0}$ and $Be^{+1}$

Spectral emission from $Be^{+0}$ and $Be^{+1}$ is routinely observed at JET. These ions only occur near the plasma boundaries and are inflowing in an ionising environment. $Be^{+0}$ is initially released from the surface with physical sputtering being the dominant release mechanism. In the edge plasma, electron temperatures are in the range 10-50eV. This is evidently not the natural temperature region where $Be^{+0}$ and $Be^{+1}$ radiate in equilibrium ionisation balance ($T_e$~ 2eV being more typical). Ionisation times are very short (~ 10μs and 100μs for $Be^{+0}$ and $Be^{+1}$ in a plasma of $T_e$ = 30eV, $n_e$ = $5x10^{12}$ $cm^{-3}$). Figure 5.3.1 illustrates the ionisation length for $Be^{+0}$ in a plasma of $n_e$ = $5.0x10^{12}$ $cm^{-3}$. This was calculated by assuming that the Beryllium is sputtered with an energy of 10eV, which is suggested from doppler measurements of $Be^{+0}$ temperatures. It can be seen that using the zero-density ground state ionisation rate coefficient leads to an overestimate of the ionisation length. The ionisation length varies directly with $1/n_e$ and so $Be^{+0}$ will be localised to within a few cm of the source. Once ionised the motion of the charged beryllium ions is controlled by magnetic fields. Diffusion along field lines is much greater than cross field diffusion. Because the ionisation time of $Be^{+1}$ is short, the ion is effectively confined and moves along the field line at which its neutral predecessor was ionised. The temperature and density may be assumed the same for neutrals and ions. This approximation does not hold for ions with longer ionisation times as they penetrate to higher temperature zones.

One of the principal aims of spectroscopic interpretation is measuring the influx of beryllium atoms entering the plasma. Techniques for this purpose have been described in detail by Behringer et al (1989).

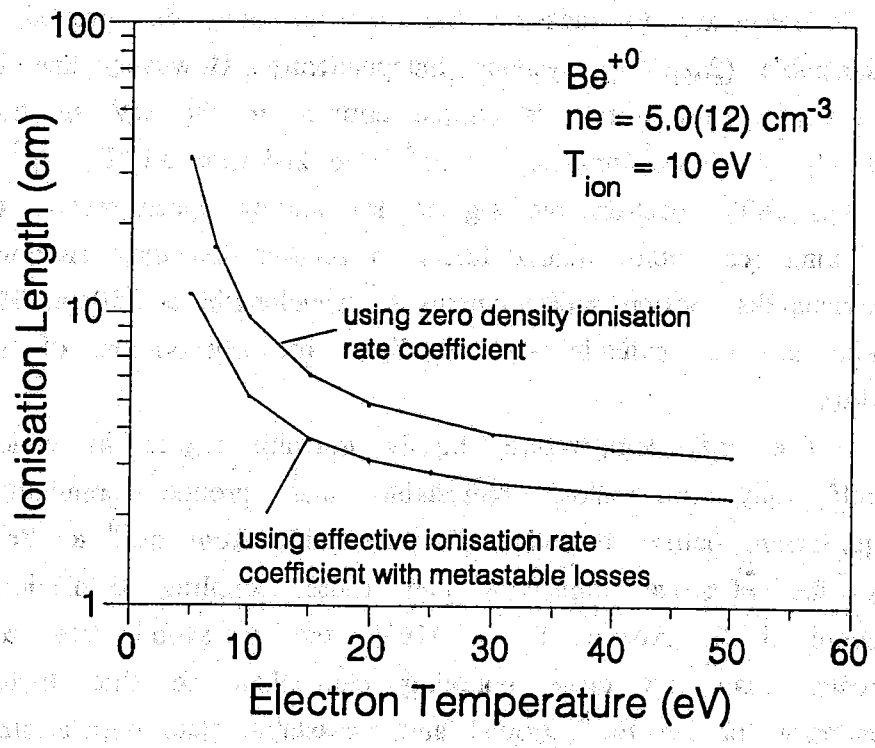


**Fig. 5.3.1:** Ionisation length of $Be^{+0}$. Assumes neutral sputtered with an energy of 10eV.

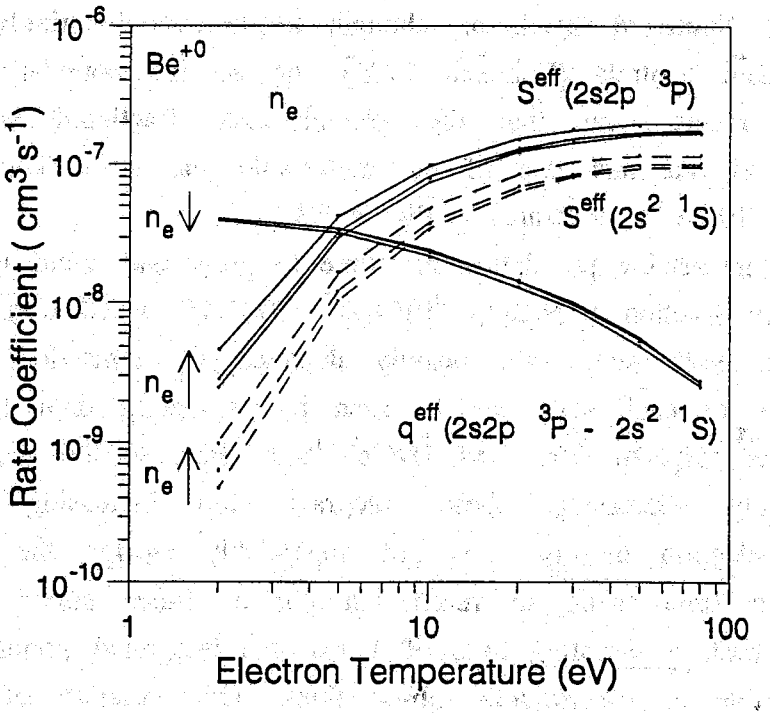


**Fig. 5.3.2:** Collisional-radiative ionisation and de-excitation cross coupling coefficients for $Be^{+0}$. Plotted at electron densities of $1.0x10^{11}$, $1.0x10^{12}$ and $1.0x10^{13}$ $cm^{-3}$.

It is necessary to measure the flux in both the ground ($2s^2\ ^1S$) and metastable ($2s2p\ ^3P$) systems independently. However, line radiation from the triplet spin system is almost entirely in the UV spectral range ( $3s\ ^3S - 2p^2\ ^3P$ @ 332.1nm, $3p\ ^3P - 2p^2\ ^3P$ @ 265.1nm, $3d\ ^3D - 2p^2\ ^3P$ @ 249.4nm ). On JET, spectroscopic signals for survey spectrometers are transferred by long (ca 150m) quartz fibers to remote detectors. Attenuation of short wavelengths restricts measurements to wavelengths > 350nm. This means that there are no suitable spectral lines for observation of the metastable influx.

The high temperature, highly ionising region in which $Be^{+0}$ finds itself may not allow metastable and ground populations to reach equilibrium before ionisation. The evolution from $Be^{+0}$ to $Be^{+1}$ is mediated by the effective ionisation and cross coupling coefficients shown in Figure 5.3.2. Above $T_e$ = 10eV, the ionisation rate coefficients are greater than the cross coupling coefficient so that there will be a tendency for the $Be^{+0}$ ground and metastable state populations to freeze as if at birth from the surface.

The transient ionisation model was used to study the evolution of the $Be^{+0}$ ground and metastable states for a range of typical plasma conditions. Sputtered metals are thought to be overwhelmingly produced as ground state neutrals (Behrisch 1982) and so the boundary condition at time of release was that the ground state fractional abundance was specified as one and that of the metastable was zero. The result for a plasma of 10 eV is illustrated in Figure 5.3.3.

The metastable population has time to grow and eventually reaches an equilibrium fraction ( $N(2s2p\ ^3P)/N(2s^2\ ^1S)$=1.45 at 10 eV). However by this time, both states are heavily depleted by ionisation. The relative importance of each state can be seen by evaluating their time integrated populations $\int N(2s2p\ ^3P)dt$ and $\int N(2s^2\ ^1S)dt$. Because the stage populations are rapidly decreasing, these integrals stop increasing after ~10μs. Varying electron density does not appreciably change the result but it scales the time taken to reach equilibrium. Since survey spectrometers have, at best, a sampling time of 1 ms, the integrated populations will be representative of spectrometer observations. The variation of the ratio of metastable/ground integrated populations, $\int N(2s2p\ ^3P)dt / \int N(2s^2\ ^1S)dt$ with electron temperature is shown in Figure 5.3.4. For comparison, the equilibrium metastable fraction is also plotted.

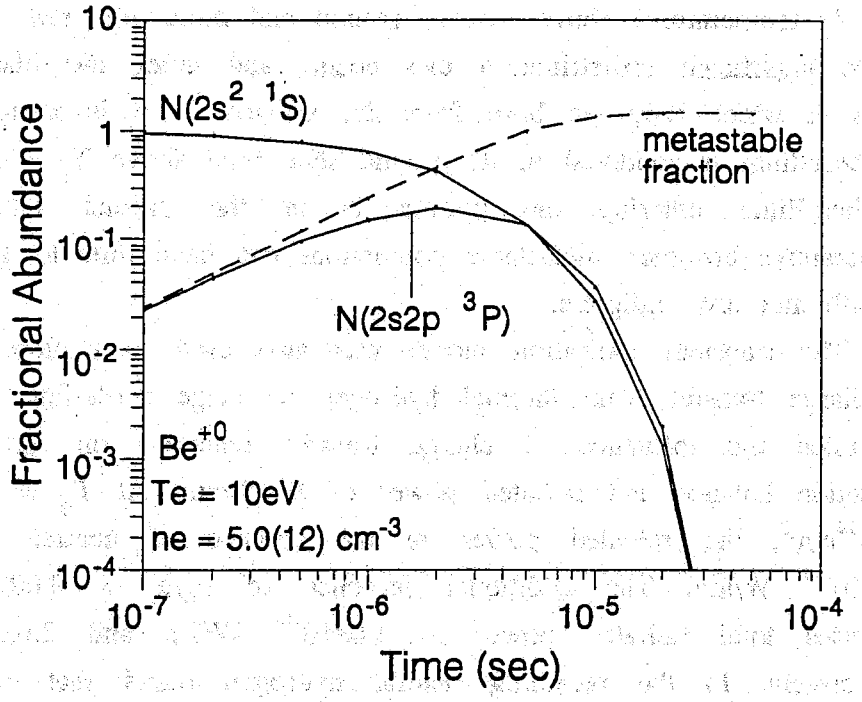


**Figure 5.3.3:** Evolution of $Be^{+0}$ ground and metastable populations and metastable/ground fraction in a plasma of $T_e$=10eV and $n_e$=5x10$^{12}$cm$^{-3}$. Assumes that only ground state is initially populated.

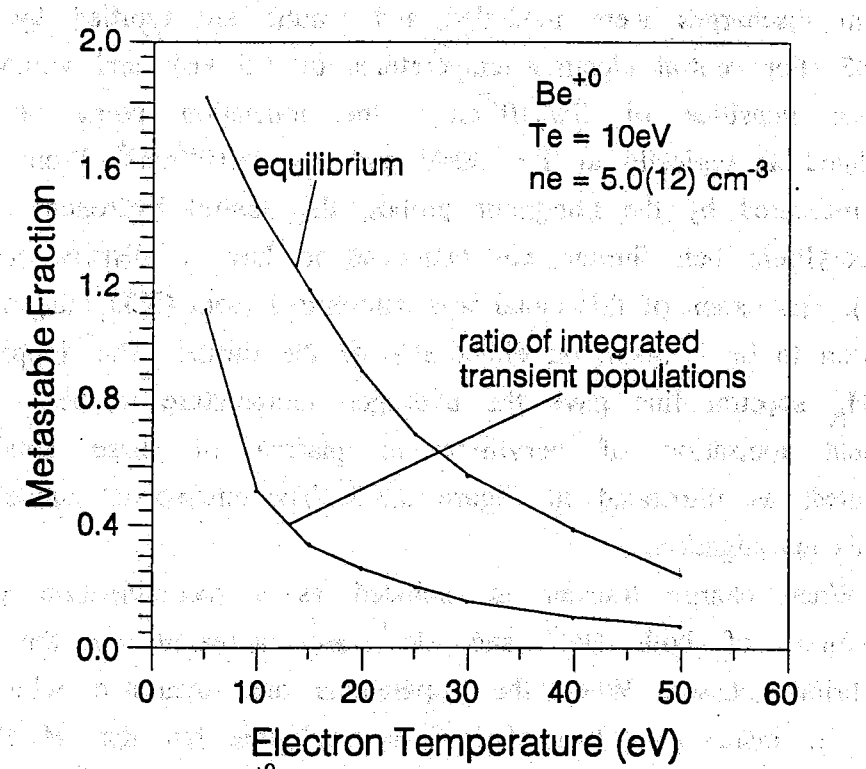


**Figure 5.3.4:** $Be^{+0}$ metastable/ground fraction for quasi-static equilibrium and transient integrated populations.

At temperatures above ~10eV, ground and metastable states are ionised before significant redistribution can occur, and enter the plasma in the ratios at which they are born from the surface. If it is assumed that all the beryllium is sputtered in its ground state then above $T_e$ = 10eV, >70% of beryllium entering the plasma is in the ground state. At low temperatures however, metastable populations can have time to grow even if at birth they are negligible.

The transient ionisation model was also used to explore the effects of charge transfer from thermal hydrogen on stage evolution. Figure 5.2.6 illustrated the influence of charge transfer reactions on the equilibrium ionisation balance and radiated power of beryllium. At $T_e$ = 10eV, $n_e$ = $1x10^{14}cm^{-3}$, the radiated power in the absence of neutral hydrogen is $4.8x10^{-16}$ W/ion. The additional presence of $n_H/n_e$ = 0.001 and 0.01 increases total radiated power to $1.0x10^{-14}$ W/ion and $2.0x10^{-13}$ W/ion respectively. In the recycling neutral hydrogen cloud that exists around material belt limiters at JET, $n_H/n_e$ can be as much as a few percent. In a detailed study of recycling power losses in JET ohmic limiter discharges (Loarte et al 1991), this effect was investigated for a plasma out of ionisation balance. Only brief details of our study are presented here. Several discharges were modelled and results are typified by JET pulse #20943. For central electron temperatures of 1.5 keV and volume averaged electron densities of $3.5x10^{13}cm^{-3}$, the ionisation point of $Be^{+0}$ was calculated as typically at $T_e$ = 30eV and $n_e$ = $5x10^{12}cm^{-3}$. From the particle flux measured by the Langmuir probes, the neutral hydrogen cloud around the beryllium belt limiter was estimated to have a density of $5x10^{10}cm^{-3}$ (~1%). The extent of this cloud was determined from CCD images of $H_\beta$ line radiation to be ~ 30cm on either side of the limiter. The doppler width of the $H_\beta$ spectral line gave the hydrogen temperature to be ~ 40eV. The transient ionisation of beryllium in plasma of these conditions was simulated, as illustrated in Figure 5.3.5. The unresolved model was used for this investigation.

When charge transfer is included as a recombination process, the populations of both $Be^{+0}$ and $Be^{+1}$ are increased on the decay and equilibrium phases. When the populations are integrated with respect to time, the increase in that of $Be^{+0}$ is negligible but that of $Be^{+1}$ can be significant. From Figure 5.3.6, the important parameters are the neutral concentration and the time spent by the ion in the neutral cloud. For limiter plasma conditions under discussion here, particle diffusion along

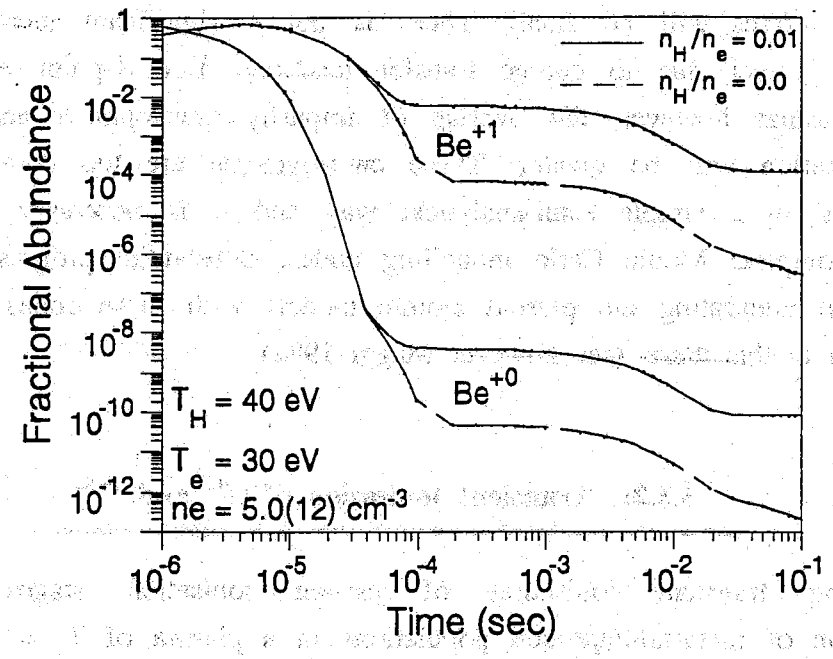


**Figure 5.3.5:** Evolution of $Be^{+0}$and $Be^{+1}$ ionisation stages with $n_H/n_e$=0.0 (- - -)and $n_H/n_e$=0.01 (—). $T_e$=30eV, $n_e$=5x$10^{12}$$cm^{-3}$.

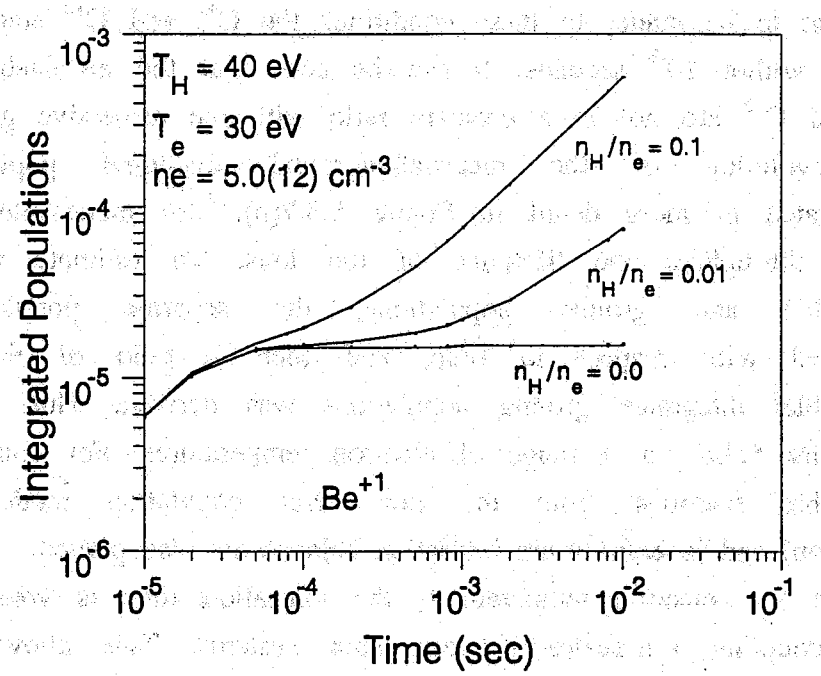


**Fig. 5.3.6:** Time integrated populations of $Be^{+1}$ in a plasma with varying amounts of neutral hydrogen. $T_e$=30eV, $n_e$=5x$10^{12}$$cm^{-3}$.

field lines takes the $Be^{+1}$ ion out of the hydrogen cloud in ~ 100 μs and so this effect will be small. There is not a significant increase in Be radiated power due to charge transfer reactions. For X-point and divertor type plasmas however, the overlap of impurity development and hydrogen concentration will be greater. These environments are too complex to be modelled in a simple semi-analytical way and it is necessary to use the more complete Monte Carlo modelling codes. Substantial progress has been made in integrating the present atomic models with these codes but is not reported in this thesis (see however Maggi 1992)

### 5.3.2: Transient Ionisation of $C^{+1}$ and $C^{+2}$

The transient ionisation of carbon ionisation stages and the evolution of metastable/ground populations in a plasma of $T_e$ = 20eV, $n_e$ = $10^{13}$ $cm^{-3}$ is illustrated in Figures 5.3.7(a) and (b). It was assumed that all of the population was initially in the $C^{+0}$ ground state. The metastable populations of $C^{+0}$ have been omitted from the diagram for clarity and because they will not be calculated with sufficient accuracy (because of $C^{+0}$ fundamental atomic data incompleteness) to enable precise comment to be made. In these conditions the $C^{+1}$ and $C^{+2}$ stages are fully ionised within $10^{-3}$ seconds. It can be seen that the metastable stages of $C^{+1}$ and $C^{+2}$ are not in a constant ratio with the respective ground states. The evolution of the metastable/ground fractional populations are investigated in more detail in Figure 5.3.7(b). The metastable populations evolve throughout the lifetimes of the ions. To estimate the effective metastable and ground populations, the separate populations were integrated with respect to time, and then a ratio of the integrated metastable/ integrated ground populations was derived. This is illustrated in Figure 5.3.8 for a range of electron temperatures. For comparison, the metastable fractions from the low level population model (including ionisation) and in equilibrium ionisation balance are also plotted.

At low electron temperatures, the ionisation time is greater than the cross coupling timescales between spin systems. This allows metastable populations to reach equilibrium well within the ionisation time of the ion so the ratio of the transient integrated metastable and ground populations is almost equal to the ratio in equilibrium ionisation balance. At high temperatures, the ionisation time is comparable to or

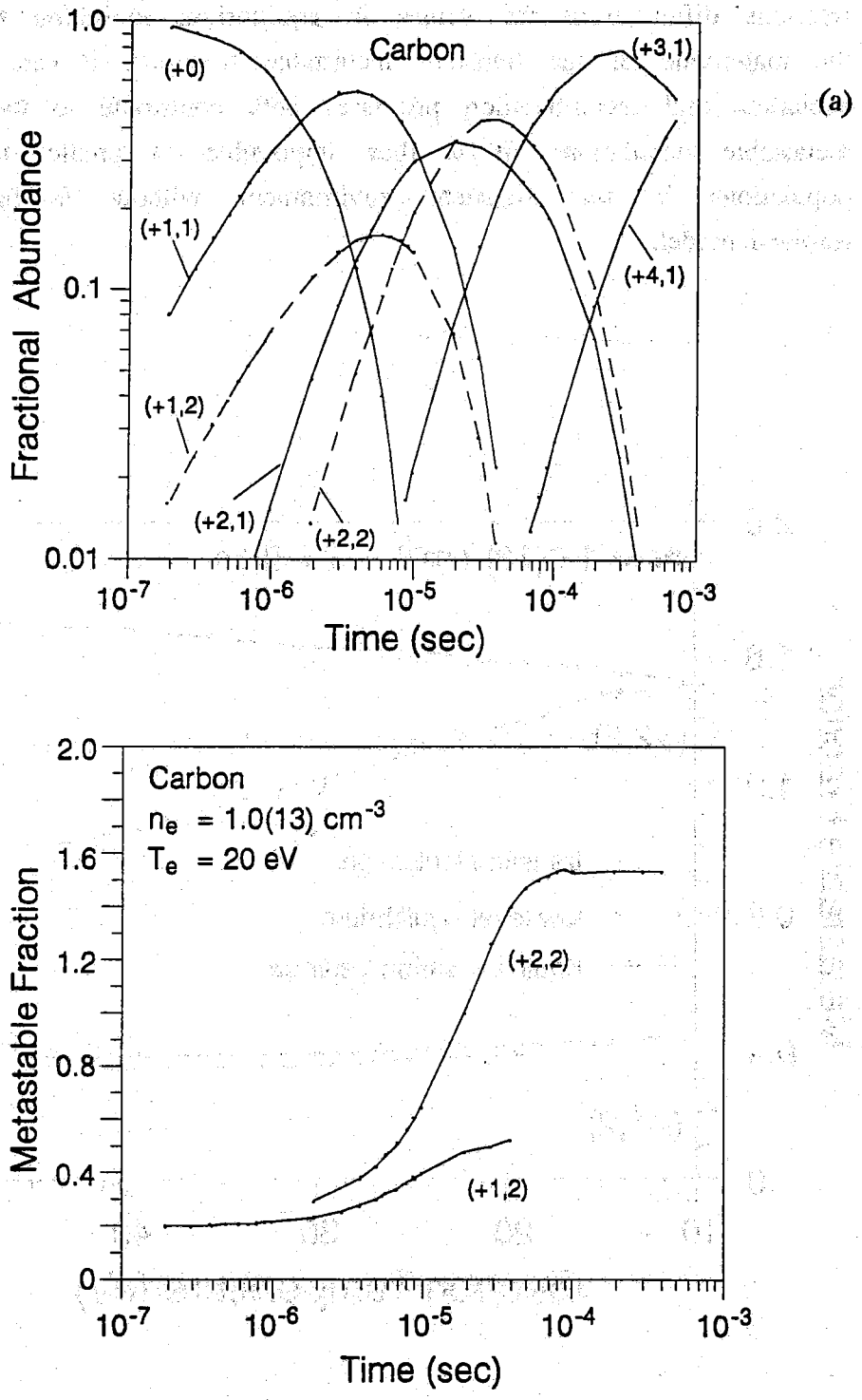


**Figure 5.3.7:** Time dependent ionisation of C. $T_e$ = 20eV, $n_e$ = $1.0 \times 10^{13}$ $cm^{-3}$.

(a) Populations

(b) $C^{+1}$ and $C^{+2}$ metastable fractions

greater than cross coupling timescales and the transient metastable fractions differ from the values in equilibrium ionisation balance. From the magnitude of the transient metastable fractions, it can be seen that excitation and recombination processes both contribute to the ground and metastable populations. It is thus impossible to predict the metastable populations in this transient environment without a full metastable resolved model.

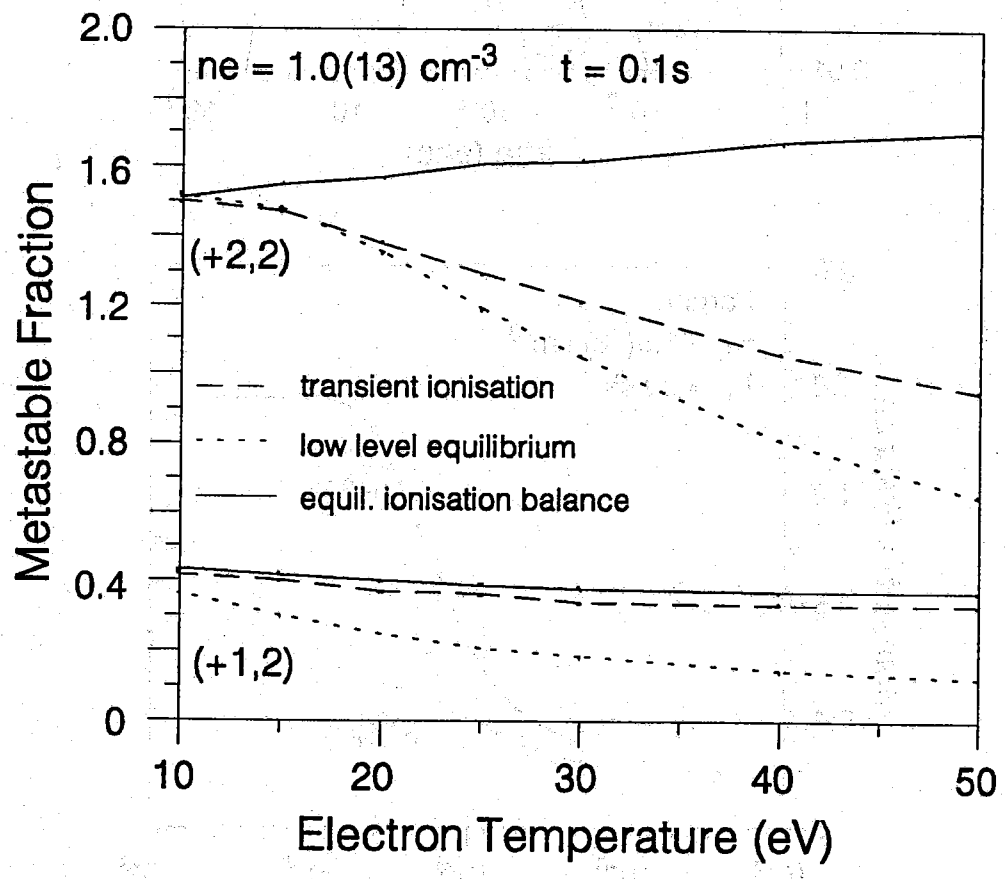


**Figure 5.3.8:** Metastable fractions of $C^{+1}$ and $C^{+2}$ in equilibrium ionisation balance, low level equilibrium (with ionisation) and transient ionisation. The transient populations are integrated to 0.1s. $n_e$ = $1.0x10^{13}$ $cm^{-3}$.

## 5.4: CONCLUDING REMARKS

The unresolved equilibrium ionisation balance derived from the present work compares well with the previous work of Arnaud and Rothenflug (1985) at low electron density. However even at plasma densities appropriate to the solar corona, there are substantial changes in equilibrium ionisation balance due to the finite electron density modification of the ionisation and recombination rate coefficients.

It is clear from the illustrations in this Chapter that metastable populations have high fraction abundances and radiated power contributions and influence ionisation balance through enhancing ionisation rate coefficients. A direct comparison between the results of the present resolved and unresolved models can potentially be misleading. This is because a metastable population can be a large fraction of the total population of the ion yet radiated power and spectral intensities are normally expressed in terms of the ground state population. For example, consider the equilibrium ionisation balance of oxygen at $n_e = 10^{14}$ $cm^{-3}$. The unresolved model gives the peak radiated power to be $9x10^{-5}$ W/ion at $T_e$ = 14eV with $O^{+4}$ contributing $6.5x10^{-5}$ W. The unresolved model gives the peak radiated power to be $5.5x10^{-5}$ W/ion with $O^{+4}(2s^2\ ^1S)$ contributing $1.38x10^{-5}$ W and $O^{+4}(2s2p\ ^3P)$ contributing $1.36x10^{-5}$ W. The radiated power in the resolved case is apparently ~ 60% of that in the unresolved model and this is due to radiation from the $O^{+4}$ stage being reduced by ~ 50%. However, the fractional abundance of $2s^2\ ^1S$ in the unresolved model is 0.581, and the fractional abundances of $2s^2\ ^1S$ and $2s2p\ ^3P$ in the resolved models are 0.283 and 0.399 respectively. If the total radiated power from $O^{+4}$ is normalised onto the $2s^2\ ^1S$ fractional abundance we obtain $1.07x10^{-11}$ W/FA$(2s^2\ ^1S)$ in the unresolved model and $9.68x10^{-12}$ W/FA$(2s^2\ ^1S)$ in the resolved model which agree within 10%. This smaller difference is due to differences in the $(2s2p\ ^3P)/(2s^2\ ^1S)$ relative populations as calculated by the low level model and in equilibrium ionisation balance.

The temperatures of maximum abundance of each ion do not differ significantly between the resolved and unresolved models. This is because the unresolved model already includes ionisation from metastable states. Test calculations were performed with the resolved model in which ionisation and recombination from metastable states were excluded. This

reduced the density dependent shifts of ionisation balance to lower temperature which occur at high density. The inclusion of metastable populations in quasi- static equilibrium in the unresolved model appears to be a reasonable representation of the metastable effects in equilibrium ionisation balance.

In transiently ionising environments similar to tokamak edge plasmas, ionisation timescales are comparable with times taken for metastables to reach equilibrium populations. The effective metastable/ground population ratios are not equal to the ratios in equilibrium ionisation balance or in a quasi-static low level equilibrium. To accurately model radiated power and spectral intensities it is necessary to use a fully metastable resolved time dependent model.

# CHAPTER 6

# CONCLUDING REMARKS

## 6.1: Review of Present Work

A solution to the statistical balance population structure equations for excited level populations of impurity ions in optically thin, thermal plasmas has been developed which maintains full distinction between ground, metastable and parent populations. This has been based upon and extended the generalised collisional-radiative theory of Summers and Hooper (1983). Detailed calculations have been performed for all ions of the isonuclear sequences of beryllium, carbon and oxygen. Derived data includes collisional-radiative ionisation, recombination, metastable cross coupling and parent cross coupling coefficients, line and recombination bremsstrahlung radiated power coefficients and emissivity coefficients for arbitrary spectral lines.

The main thrust of the new theoretical population modelling was in the development of LS resolved low level and bundle-n S quantum shell population models and then their merging via the projection and expansion of the high level calculation for bundled populations over the LS resolved low level populations. These techniques allow the calculation of both collisional-radiative coefficients and populations with a new level of completeness and precision. The projection calculation introduces corrections to the effective excitation contributions and emission coefficients obtained by the low level model alone. At low electron density there is a cascade correction and at high electron density there is a correction for stepwise excitation losses. The necessity of using the full projection/expansion calculation to derive excited state populations is dependent on electron density and ion charge. From the work presented in this thesis, it can be concluded that the full calculation is necessary for neutral atoms and for resolved terms within the n=3 and n=4 shell of singly charged ions. For higher charged ions, the projection model does not significantly alter the populations until densities higher than those attained in fusion plasmas, so that the low level model is an adequate representation of the excited state populations.

The projection calculation leads to a more refined calculation of collisional radiative ionisation and recombination rate coefficients. The ionisation coefficients are particularly sensitive to the precise structure and energies of the ground quantum shell. The bundle-n S recombination coefficients are corrected by using new more refined

radiative and dielectronic data than has hitherto been possible and by explicitly resolving cascade pathways within the lowest few quantum shells.

The results from the population models were integrated so as to allow the first fully resolved metastable and parent model for equilibrium ionisation balance as well as improving the older unresolved 'stage to stage' model. The unresolved model considers the metastable populations to be in quasi-static equilibrium with the ground state ion. Composite ionisation, emission and radiated power coefficients are derived for the unresolved model in which metastable resolved coefficients are weighted by the fractional populations of the metastables. It was demonstrated that in such composite coefficients, excitation from both ground and metastable states accounts for comparable proportions of excited state populations and radiated power. Due to changes in threshold, ionisation rates from metastable states can be considerably greater than those from ground state and this leads to ground and metastable composite ionisation rate coefficients which are substantially greater than the ground state coefficients alone.

New equilibrium ionisation balance and radiated power calculations were performed with both the unresolved and improved resolved models. The density sensitivity of both the ionisation and recombination rate coefficients leads to significant changes of the ionisation balance of low charged ions at typical coronal and tokamak electron densities. The metastable resolved calculations illustrate that metastable fractional abundances are comparable with ground state abundances and excitation from metastable states substantially contributes to radiated power density. A comparison between the results of the unresolved and resolved models indicate that the inclusion of metastable populations (albeit in quasi -static equilibrium) in the unresolved model is a reasonable representation of metastable effects in equilibrium ionisation balance.

Metastable relaxation times were illustrated using $O^{+2}$ as an example, although this is typical of all other ions considered. Metastable populations are populated on similar timescales to normal excited states but relaxation timescales are much slower. In high temperature plasmas, metastable to metastable times are comparable with those for ionisation. Metastable states in the same spin system (e.g. $2s^2 2p^2\ ^1D$ and $2s^2 2p^2\ ^1S$) relax on similar timescales to each other. Metastable and parent cross coupling coefficients have been defined which allow the evolution of

metastable populations to be followed in dynamic plasmas. At low electron temperatures and high electron densities the parent cross coupling coefficients can be comparable with the metastable cross coupling coefficients and both must be considered together to give the total rate coefficient for the metastable. In conditions appropriate to edge plasma conditions in JET, metastable populations do not have time to relax to their quasi-static equilibrium populations within the ionisation time of the particular ion. To properly model spectral emission and radiated power in such dynamic plasmas it is necessary to use the full metastable resolved model.

The figures and diagrams presented in this thesis are representative and show only a fraction of the derived data. The fundamental data, processing codes and derived data sets developed in this thesis form a core component of the primary 'Atomic Data and Analysis Structure' now used for spectroscopic and radiation modelling at JET. No extensive tabulations of data are given in this thesis, these being reserved for a JET Joint Undertaking Report.

## 6.2: Applications

The data derived in this thesis has many applications in spectral interpretation and diagnostic modelling of fusion and astrophysical plasmas. This ranges from routine uses such as influx and concentration measurements to more specific and specialised applications. The most active application at this time at JET is in the understanding and interpretation of the operation of the pumped divertor. This has involved the integration of the present atomic models with plasma models which predict and simulate divertor performance and experimental observations.

Divertor design is optimised by simulations using the 1-D and 2-D fluid models EDGE1D and EDGE2D (Simonini et al 1992). In particular these codes are used to model impurity control and screening. In both models, fluid equations for the conservation of particles, momentum and energy are solved for hydrogen and impurity ions to predict plasma conditions in the divertor. The distribution of light impurity charge states and radiated power is an important factor in determining the performance of the divertor. The ionisation, recombination and radiated power coefficients, based on the improved unresolved model, derived in the present work are

used in these codes.

For more direct spectroscopic diagnostic applications, a DIVertor IMPurity Monte-Carlo model (DIVIMP) has been developed (Stangeby 1990). This does not predict the plasma conditions self consistently but uses either experimental measurements or the results from EDGE2D to provide a background plasma. Trace sputtered neutrals are generated at surfaces and then followed through the plasma until they are lost. The densities of the ionisation stages at representative points are derived (the code uses an orthogonal cell mesh). This is then used to calculate two dimensional profiles of specific line emission and total radiated powers for comparison with experimental measurements from spatially scanning spectrometers and bolometers. These investigations give important insight into the location of impurity sources and the nature of impurity transport and screening in the divertor region. The ionisation, recombination and radiated power coefficients derived in the present work are used in this model. Also for simulation of spectral features, the present photon emissivity coefficients are adopted. At present this code operates with the unresolved ionisation stage picture but the extension to the resolved metastable picture is in progress. This is necessary for realistic simulation at this planning phase and will later be used for interpretation in the operational phase.

A specific application for astrophysical plasmas is in support of analysis of spectra from the CDS (Coronal Diagnostic Spectrometer) and SUMER (Solar Ultraviolet Measurement of Emitted Radiation) spectrometers on the SOHO satellite (Domingo and Poland 1989). CDS is an EUV instrument with a wavelength range from 15.5 - 79 nm, viewing ~ 7 - 12 nm ranges simultaneously. SUMER is an UV instrument with a 50 - 160 nm range, viewing ~ 3nm simultaneously. These spectrometers are intending to use line ratio and emission measure diagnostics to investigate temperature and density structures in the solar atmosphere. This will support the aims of SOHO, namely to understand the acceleration of the solar wind and the nature and heating mechanisms of the solar corona. The scientific analysis is based on theoretical prediction of spectral features and requires the coupling of ionisation, recombination and emission data with plasma models of the solar environment. Amongst the spectral lines to be used for this purpose are several lines from carbon and oxygen ions including temperature sensitive line ratios from O V, O IV and O III. The data derived in this thesis will be central to this work and a large fraction

of the data and modelling structure described in this thesis are at this time being translated for operation on the CDS analysis workstations.

## 6.3: Development and Future Work

There are three principal areas in which the present modelling could be extended, namely, in the choice and range of fundamental atomic data, in a refinement of the population models, and to ions of greater nuclear charge.

The principal requirements for improved atomic data are electron impact excitation rate coefficients for the neutral atoms of carbon and oxygen and some adjustment of the low temperature dielectronic recombination rate coefficients for all ions. The incorporation of intermediate coupling calculations for dielectronic recombination of lithium -like ions is also planned. A major extension of this work would involve the inclusion of charge transfer. Throughout the work of this thesis, charge exchange contributions have been retained in the population structure equations without an attempt to derive complete effective coefficients due to this process. This is due to a lack of fundamental state selective low energy charge transfer collision data. Some data is available, but the review and compilation of this was beyond the scope of this thesis. Charge exchange can be incorporated in a manner similar to the treatment of electron recombination. The coefficients required to complete the theoretical model are effective emission coefficients, effective charge exchange recombination coefficients and effective charge exchange recombination power coefficients. The methodology for calculation of these coefficients has been established within the present work.

The treatment of direct and excitation-autoionisation from metastable states in the B-, C-, N- and O-like isoelectronic sequences can be improved by both an improvement of the fundamental atomic data and by a development of the low level population model to treat autoionising levels in the low level population model. Fundamental calculations of metastable and parent resolved direct ionisation cross sections are necessary, as well as cross sections for excitation from ground and metastable configurations to autoionising levels. The inclusion of parent resolved Auger transition probabilities in the equations of statistical balance is in principle straightforward and presents no difficulty. The difficulties

arise from the number of autoionising states which are required to be modelled. For the sequences where this process is important (B-, C-, N- and O-like) many discrete levels contribute to the excitation-autoionisation process. The inclusion of these levels in the population codes would considerably increase the size of the calculation. Further, the excitation autoionisation contribution is most important below the direct ionisation threshold and dipole excitation is not always dominant. High quality excitation data is thus required to accurately model this process. Born calculations are not accurate at low temperature and for non-dipole excitations. This is thus a considerable problem for which there is no immediate solution.

The other main limitation in the population modelling is the merging of the bundle-n populations with low level resolved data at a relatively low quantum shell e.g. n=4 or 5. Collisional redistribution of the bundle-n shell is not always ensured at these densities and this leads to errors in the cascade contributions to low level populations. A more accurate and complete solution would be to use an intermediate level of resolution which maintains resolution between separate $l$ levels. This would be the so-called bundle-n $l$ S model which averages over the angular quantum number. e.g. in $O^{+2}$, $2s^2 2p3p$ $^1S$, $^1P$ and $^1D$ would all be treated as one level - $2s^2 2p3p$ $^1L$. The low levels would still be treated in LS or LSJ resolution up the a maximum quantum shell for which high quality data is available. The bundle-n $l$ S resolution could then be used for the next few quantum shells. Up to a maximum of n=10 would probably be sufficient. After that, levels would again be treated in the bundle-n S model. This approach would enable a more accurate treatment of recombination and cascade contributions.

To extend modelling to ions of greater nuclear charge, it would be necessary to adopt an intermediate coupling scheme and to take account of fine structure resolved metastability. An LSJ resolved low level population structure presents no particular difficulties and can be treated in a manner similar to the LS resolved term populations in this present work.

However for the next two years the primary development will be in the exploitation of the new calculations and derived data presented in this thesis in analysing the data stream from the new instrumentation in the divertor phase at JET. This is due to commence in January 1994.

**Acknowledgements**

A Ph. D. is not completed without the help and assistance of many people, whom it is now my pleasure to thank.

It has been a pleasure working with my supervisor, Hugh Summers, who has been a constant source of encouragement and inspiration. I am deeply grateful for all the support and advice I have received in the last three years. I have also had the pleasure of working with Nigel Badnell of Strathclyde University. I would like to thank Nigel for the extensive dielectronic recombination data that he made available, for assistance in using the *Autostructure* code and for many constructive discussions. I am grateful to Martin o' Mullane of Cork University/Culham Laboratory, who installed the Cowan Atomic Structure code on the JET IBM computer and thereafter, assisted me in many calculations with this code. Nigel and Martin also deserve a great deal of thanks for providing suggestions on improving this manuscript. I would like to thank Jim Lang of Rutherford Appleton Laboratory for assistance in many points and for maintaining a keen scientific interest in this work. I am grateful for the computational support given by Paul Briden and Jim Spence.

This thesis was completed at the JET Joint Undertaking. I would like to express my thanks to members of Experimental Division II for their hospitality and assistance. In particular, I wish to thank Paul Thomas for continuous support and encouragement of this work. I am grateful to Stuart Morris and Charlie Weaver of the JET graphics department for help in preparing the diagrams for this thesis.

Finally, on a more personal note, I wish to express sincere thanks to members of my family and friends who have expressed an interest and provided continued support throughout this work. I am especially grateful to Nicola Hall who was a continual source of encouragement and who understood being sadly neglected during the final few months in which this thesis was completed.

# REFERENCES


Aggarwal, K.M., 1983, *Astrophysics J. Supp. Ser.*, **52**, p387.

Aggarwal, K.M., 1985, *Astron. and Astrophys.*, **146**, p149.

Aggarwal, K.M., 1986, *Mon. Not. R. Astron. Soc.*, **218**, p123.

Arnaud, M. and Rothenflug, R., 1985, *Astrophys. J. Supp. Ser.*, **60**, pp425-457.

Attaourti, Y., Defrance, P., Makhoute, A. and Joachain, C.J., 1991, *Physica Scripta*, **43**, pp578-586.

Badnell, N.R., 1986, *J. Phys. B*, **19**, pp3827-3835.

Badnell, N.R., 1988, *J. Phys. B*, **21**, pp749-767.

Badnell, N.R., 1989a, *Physica Scripta*, **T28**, pp33-35.

Badnell, N.R. and Pindzola, M.S., 1989b, *Phys. Rev. A*, **39**, No. 4, pp1690-1695

Badnell, N.R., Pindzola, M.S. and Griffin, D.C., 1990, *Phys. Rev. A*, **41**, p2422.

Badnell, N.R., 1992, private communication.

Badnell, N.R., Pindzola, M.S., Dickson, W.J., Summers, H.P., Griffin, D.C. and Lang, J., 1993, *Astrophys. J. Letters*, **407**, L91.

Bashkin, S. and Stoner, J.O., 1978, *Atomic Energy Levels and Grotian Diagrams*, North Holland, Amsterdam.

Bates, D.R., Kingston, A.E. and McWhirter, R.W.P., 1962, *Proc. Royal Soc. of London*, **267 A**, pp297-312.

Behringer, K., Summers, H.P., Denne, B., Forrest, M., and Stamp, M.F., 1989, *Plasma Physics and Controlled Fusion*, **31**, p2059.

Bell, K.L., Gilbody, H.B., Hughes, J.G., Kingston, A.E. and Smith, F.J., 1983, *J. Phys. Chem. Ref. Data*, **12**, No. 4, pp891-916.

Behrisch, R. (ed.), 1981 and 1982, *'Sputtering by Particle Bombardment'* I and II, Topics in Applied Physics, Springer-Verlag.

Berrington, K.A., 1985, *J. Phys. B*, **18**, L397.

Berrington, K.A. et al, 1979, *J. Phys. B*, **12**, L275.

Berrington, K.A. et al, 1985, *Atomic and Nuclear Data Tables*, **33**, p195.

Berrington, K.A. et al, 1989, *J. Phys. B*, **22**, p665.

Bhatia, A.K, et al, 1979, *Astron. and Astrophys.*, **76**, p359.

Bonnin, X., Marchand, R. and Janev, R.K., 1992, *Nuclear Fusion Supp. Ser.*

Bottcher, C., Griffin, D.C. and Pindzola, M.S., 1986, Phys. Rev. A, **34**, 860

Burgess, A., 1964, *Proc. Symp. Atomic Collision Processes in Plasmas*, Culham, UKAEA Report **AERE-R4818**, p63.

Burgess, A., 1964, *Astrophys. J.*, **139**, pp776-780.

Burgess, A., 1965, *Astrophys. J.*, **141**, pp1588-1590.

Burgess, A. and Summers, H.P., 1976, *Mon. Not. R. Astr. Soc.*, **174**, p345.

Burgess, A., Summers, H.P., Cochrane, D.M. and McWhirter, R.W.P., 1977, *Mon. Not. R. Ast. Soc.*, **179**, p275.

Burgess, A. and Chidichimo, M.C., 1983, *Mon. Not. R. astr. Soc*, **203**, pp1269-1280.

Burgess, A. and Summers, H.P., 1987, *Mon. Not. R. Astr. Soc.*, **226**, p257.

Burke, P.G., 1973, *Comput. Phys. Commum.*, **6**, p288.

Chidichimo, M.C., 1982, *J. Phys. B.*, **15**, pp3333-3345.

Clark, R.E.H., Sampson, D.H. and Goett, S.J., 1982, *Astrophys. J. Supp.*, **49**, pp545-554.

Cochrane, D.H. and McWhirter, R.W.P., 1986, *Daresbury Laboratory Report*, **DL/SC1/R24**, p53

Cohen, M. and McEachran, R.P., 1979, *J. Quant. Spectros. Rad. Transfer*, **21**, p1.

Cowan, R.D., 1981, *The Theory of Atomic Structure and Spectra*, University of California Press, Berkeley.

Domingo, V. and Poland, A.I., 1989, *European Space Agency Publication* **SP-1104**, p7.

Danielsson, M., von Hellerman. M.G., Kallne, E., Mandl, W., Morsi, H.W., Summers, H.P. and Zastrow, K-D, 1992, *Rev. Sci. Instrum.*, **63**, p2241. Also available as JET laboratory preprint **JET-P(91)19**.

Dufton, P.L., 1977, *Comput. Phys. Commun.*, **13**, p25.

Edlen, B., 1983, *Physica Scripta*, **28**, p483.

Edlen, B., 1985, *Physica Scripta*, **31**, p345.

Eissner, W. and Seaton, M.J., 1972, *J. Phys. B*, **5**, pp2187-2198.

Eissner, W., Jones, M. and Nussbaumer, H., 1974, *Computer Physics Comm.*, **8**, pp270-306.

Engelhardt, W.W. in *Diagnostics for Contemporary Fusion Experiments*, proc. of workshop organised by International School of Plasma Physics, Varenna, Italy, 1986.

Fawcett, B.C., 1984, *Atomic and Nuclear Data Tables*, **30**, p423.

Fischer, C.F. and Saha, H.P., 1985, *Physica Scripta*, **32**, pp181-194.

Fon, W.C., Berrington, K.A., Burke, P.G. and Hibbert, A., 1991, *J. Phys. B*, **25**, p507.

Gabriel, A.H. and Jordan C., 1972, In *Case Studies in Atomic Collision Physics,* **2**, p209. Eds. McDaniel and McDowell, M.R.C., North Holland, Amsterdam.

Greenland, P.T., 1982, *Phys. Rep.*, **81**, p131.

Greenland, P.T., 1988, *Harwell Laboratory Report*, **AERE R 13136.**

Griem, H.R., 1963, *Physical Review*, **131**, pp1170-1176.

Griem, H.R., 1964, *Plasma Spectroscopy*, Magraw-Hill, New York.

Griem, H.R., 1974, *Spectral Line Broadening by Plasmas*, Academic Press, New York.

Griffin, D.C., Pindzola, M.S. and Bottcher, C., 1985, ORNL Report TM-9478.

Griffin, D.C., Pindzola, M.S. and Bottcher, C., 1986, *Phys. Rev. A*, **33**, p3124.

Gordon, H., Summers, H.P., Tully, J.A., 1982, *Culham Laboratory Report* **CLM-R229.**

Hahn, Y., 1985, *Adv. Atomic Mol. Physics*, **21**, p123.

Hawkes, N. et al, 1993, Proceedings of 20th EPS Conference on Controlled Fusion and Plasma Physics, Lisbon.

Hayes, M.A., 1983, *J. Phys. B*, **16**, p285.

Hayes, M.A. and Nussbaumer, H., 1984, *Astron. and Astrophys.*, **134**, p193.

Henry, R.J.W., 1981, *Physics Reports*, **68**, p1.

Hibbert, A., 1980, *J. Phys. B*, **13**, p1721.

Ho, Y.K. and Henry, R.J.W., 1983, *Astrophys. J.*, **264**, p733.

Hoekstra, R.A., 1990, *Photons Shedding Light on Electron Capture By Highly Charged Ions*, Ph. D. Thesis, State University of Groningen, The Netherlands.

Hulse, R.A., Post, D.E., and Mikkelson, D.R., 1980, *J. Phys. B.*, **13**, pp3895-3907.

Hutchinson, I.H., 1987, *Principles of Plasma Diagnostics*, Cambridge University Press.

Itikawa, Y. and Ichimura, A., 1990, *J. Phys. Chem. Ref. Data*, **19**, No. 3, pp637-651.

Jacobs, V.L., Davis, J., Kepple, P.C., Blaha, M., 1976, *Astrophys. J.*, **211**, pp605-616.

Jacobs, V.L. and Davis, J., 1978, *Phys. Rev. A*, **18**, No. 2, pp697-710.

Janev, R.K. and Presnyakov, L.P., 1981, *Phys. Rep.*, **70**, pp1-107.

Jordan, C., 1969, *Mon. Not. R. Astr. Soc.*, **142**, p501.

Jordan, C., 1970, *Mon. Not. R. Astr. Soc.*, **148**, p17.

Kastner, S.O., 1981, *J. Quant. Spectrosc. Rad. Transfer*, **26**, No. 4. pp371-375.

Kato, T, Lang, J. and Berrington, K., 1990, *Atomic and Nuclear Data Tables*, **44**, pp133-187.

Kato, T., Masai, K. and Arnaud, M., 1991, *Japanese Institute for Fusion Science Research Report*, **NIFS-DATA-14**.

Keane, C. and Skinner, C.H., 1986, *Phys. Rev. A*, **33**, p4179.

Keen, B.E., Watkins, M.L. and the JET Team, 1992, *Europhysics News*, **23**, p123.

Kelly, R.L., 1987, *J. Phys. Chem. Ref. Data*, **16**, Supplement No. 1 - Atomic and Ionic Spectrum Lines below 2000Å: Hydrogen through Krypton.

Kingston, A.E. and Tayal, S.S., 1983, *J. Phys. B*, **16**, p3465.

Laher, R.R. and Gilmore, F.R., 1990, *J. Phys. Chem. Ref. Data*, **19**, p277.

Lang, J., Mason, H.E. and McWhirter, R.W.P., 1990, *Solar Physics*, **129**, pp31-81.

Lawson, J.D., 1957, *Proceeedings of the Physical Society B*, **70**, 6.

Lennon, D.J., Dufton, P.L., Hibbert, A. and Kingston, A.E., 1985, *Astrophysical J.*, **294**, p200.

Ljepojevic, N.N., Hutcheon, R.J., McWhirter, R.W.P., 1984, *J. Phys. B*, **17**, pp3057-3073.

Loarte, A., Harbour, P.J., Summers, H.P., Tagle, J.A. and Dickson, W.J., 1991, Proceedings IOP Conf. Plasma Physics, Colchester. Also available as JET preprint **JET-P(91)22.**

Lotz, W., 1967, *Astrophys. J. Supp. Ser.*, **14**, pp207-238.

Luken and Sinanoglu, 1976, *J. Phys. Chem. Ref. Data*, **64**, p1495.

Lee, Y.T., 1987, *J. Quant. Spectrosc. Radiat. Transfer*, **38**, p131.

Ljepojevic, N.N., Hutcheon, R.J. and McWhirter, R.W.P., 1984, *J. Phys. B*, **17**, pp3057-3073.

Magee, N.H., Mann, J.B., Merts, A.L. and Robb, W.D., 1977, *Los Alamos Laboratory Report*, **LA 6691 MS**.

Maggi, C.F., 1992, Masters Thesis, University of Milan. Also available as JET Report **JET-IR(93)05.**

Mandl, W., Wolf, R.C., von Hellerman, M.G. and Summers, H.P., 1993, *Plasma Physics and Controlled Fusion* - in press. Also available as JET preprint **JET-R(92)93.**

Martinson, I., 1989, *Rep. Prog. Phys.*, **52**, pp157-225.

Matthews, G.F., Stangeby, P.C., Elder, J.D., Gottardi. N.A.C., Harbour. P.J. et al, 1992, *J. Nuc. Mat.*, **196-198**, p374. Proceedings of 10th PSI Conference, Monterey.

McWhirter, R.W.P., 1981, in *Plasma Physics and Nuclear Fusion Research*, Ed. R.D. Gill, Academic Press.

McWhirter, R.W.P. and Summers, H.P., 1984, in *Applied Atomic Collision Physics*, **2**, Eds. Massey, H.S.W., McDaniel, E.W. and Bederson, B., Academic Press.

Menzel, D.H. and Peckeris, C.L., 1935, *Mon. Not. R. Astr. Soc.*, pp96-97.

Merts, A.L., Mann, J.B., Robb, W.D. and Magee, N.H., 1980, *Los Alamos Laboratory Report*, **LA 8267 MS.**

Moore, C.E., 1970, NSRDS-NBS 34 (Washington, DC: US Govt Printing Office).

Moores, D.L. and Reid, K.J., 1989, *Phys. Rev. A*, **39**, No. 4, pp1747-1755.

Morgan, P.D., Behringer, K.H., Carolan, P.G., et al, 1984, *Rev. Sci. Instrum.*, **56**, p862.

Nussbaumer, H. and Storey, P.J., 1975, *Astron. and Astrophys.*, **44**, p321.

Nussbaumer, H. and Storey, P.J., 1978, *Astron. and Astrophys.*, **64**, p139.

Nussbaumer, H. and Storey, P.J., 1979, *Astron. and Astrophys.*, **74**, p244.

Nussbaumer, H. and Storey, P.J., 1981, *Astron. and Astrophys.*, **76**, p91.

Nussbaumer, H. and Storey, P.J., 1983, *Astron. Astrophys.*, **126**, pp75-79

Orlinskij, D.V. and Magyar, G, 1988, *Nuclear Fusion*, **28**, No.4, p611.

Pasini, D., Giannella, Lauro-Taroni, L., Mattioli, M., Denne-Hinnov, B., Hawkes, N., Magyar, G. and Weisen, H., 1992, *Plasma Physics and Controlled Fusion*, **34**, pp667-685. Also available as JET Laboratory preprint **JET-P(91)36.**

Peacock, N.J., 1984 in *Applied Atomic Collision Physics*, **2**, Eds. Massey, H.S.W., McDaniel, E.W. and Bederson, B., Academic Press.

Percival, I.C., 1973, *J. Phys. B*, **6**, pp2236-2253.

Percival, I.C. and Richards, D., 1975, *Adv. Atom. Molec. Phys.*, **11**, pp1-82.

Percival, I.C. and Richards, D., 1978, *Mon. Not. R. Astr. Soc.*, **183**, pp329-334.

Post, D.E., Jensen, R.V., Tarter, C.B., Grasberger, W.H., and Lokke, W.A., 1977, *At. Nucl. Data Tables*, **20**, p397.

Pradhan, A.H., 1976, *Mon. Not. R. astr. Soc.*, **177**, p31.

Pradhan, A.H., Norcross, D. and Hummer, D., 1981, *Astrophysics J.*, **246**, p1013.

Reid, K.J., Chen, M.H. and Moores, D.L., 1991, *Phys. Rev. A*, **44**, No. 7, p4336.

Reisenfeld, D.B., 1992, *Astrophy. J.*, **398**, pp386-393.

Reisenfeld, D.B., Raymond, J.C., Young, A.R. and Kohl, J.L., 1992, *Astrophys. J.*, **389**, L37-40.

Roszman, L.J., 1989, *Phys. Rev. A*, **39 No. 4**, pp2073-2077.

Ryufuku, H. and Watanabe, T., 1978, *Phys. Rev. A*, **18**, pp2005-2015.

Sampson, D.H. and Parks, 1974, *Astrophysics J. Supp. Series*, **28**, p323.

Sampson, D.H. and Golden, L.B., 1981, *J. Phys. B*, **14**, pp903-913.

Sampson, D.H., Goett, S.H. and Clark, R.E.H., 1983, *Atomic and Nuclear Data Tables*, **29**, p467.

Saraph, H., 1980, *J. Phys. B*, **13**, p3129.

Simonini, R., Taroni, A., Keilhacker, M., Radford, G., Spence, J., Vlases, G., Watkins, M.L. and Weber, S., 1992, *Proceedings of 10th International Conference on Plasma Surface Interctions*, Monterey, CA, USA. Also available as JET laboratory preprint **JET-P(92)32.**

Seaton, M.J., 1964, Planet, Sp. Sci., **12**, p55.

Shull, J.M. and Van Steenberg, M., 1982, *Astrophys. J. Supp. Ser.*, **48**, pp95-107.

Smith, E.R. and Henry, R.J.W., 1973, *Phys. Rev. A.*, **7**, 1585.

Spitzer, L, 1956, *Physics of Fully Ionised Gases*, Interscience, New York.

Spence, J. and Summers, H.P., 1986, *J. Phys. B*, **19**, p3749.

Stamp, M.F. and Summers, H.P., 1990, *Proc. 17th EPS Conf. on Controlled Fusion and Plasma Heating*, **14B**, p1377.

Stangeby, P.C., 1991, Proceedings of 9th PSI Conference, *J. Nuc. Mat.*, **176** and **177**, pp51-64.

Stangeby, P.C. and McCracken, G.M., 1990, Nucl. Fusion, **30**, p1225.

Storey, P.J., 1981, *Mon. Not. R. Astr. Soc.*, **195**, *Short Communication*, pp27-31.

Stott, P.E., 1992, *Reports on Progress in Physics*, **55**, p1715.

Stott, P.E., Akulina, D.K., Gorini, G. and Sindoni, E., 1991, (editors) *Diagnostics for Contemporary Fusion Experiments*, proc. of workshop organised by International School of Plasma Physics, Varenna, Italy, Aug. - Sept. 1991.

Summers, H.P., 1974a, *Appleton Laboratory Report*, **Al-R-5.**

Summers, H.P., 1974b, *Mon. Not. R. Astr. Soc.*, **169**, p663.

Summers, H.P., 1977, *Mon. Not. R. Astr. Soc.*, **178**, pp101-122.

Summers, H.P. and McWhirter, R.W.P., 1979, *J. Phys. B.*, **12**, p2387.

Summers, H.P., and Hooper, M.B., 1983, *Plasma Physics and Controlled Fusion*, **25**, pp1311-1344.

Summers, H.P., Behringer, K. and Wood, L., 1987, *Physica Scripta*, **35**, pp303-308.

Summers, H.P. and von Hellermann, M., 1993, in *Atomic and Plasma-Material Interaction Processes in Controlled Thermonuclear Fusion*, Ed. Janev, R.K., Elsevier, Amsterdam.

Tayal, S.S. et al, 1982, *Proc. of ICPEAC, Berlin*, p192.

Tayal, S.S., 1986, *Phys Rev. A*, **34**, p1847

Tayal, S.S., 1992, *J. Phys. B*, **25**, pp2639-2647.

Tayal, S.S. and Kingston, A.E., 1984, *J. Phys. B*, **17**, p1383

Thomas, P.R., 1991, Proceedings of 9th PSI Conference, *J. Nuc. Mat.*, **176** and **177**, pp3-13.

Vernazza, I.E., and Raymond, J.C., 1979, *Astrophys. J.*, **228**, L89.

von Hellermann, M.G., Mandl, W., Summers, H.P., Weisen, H., Boileau, A., Morgan, P.D., Morsi, H., Koenig, R., Stamp, M.F. and Wolf, R., 1991, *Rev. Sci. Instrum.*, **61**, pp3479-3486.

Weiss, A.W., 1972, *Phys. Rev. A*, **6**, p1261.

Welton, R.F., Moran, T.F. and Thomas, E.W., 1991, *J. Phys. B*, **24**, pp3815-3823.

Wesson, J., 1985, *Tokamaks*, Oxford University Press.

Westhaus, P. and Sinanoglu, O., 1969, *Phys. Rev.*, **183**, pp56-68.

Widing, K.G., Doyle, J.G., Dufton, P.L and Kingston, A.E., 1982, *Astrophysics J.*, **257**, p913.

Wiese, W.L., Smith, M.W. and Glenon, B.M., 1966, *Atomic Transition Probabilities*, **1**, NSRDS-NBS 4 (Washington, DC: US Govt Printing Office).

Winter, J., 1991, Proceedings of 9th PSI Conference, *J. Nuc. Mat.*, **176** and **177**, pp14-31.

Younger, S.M., 1981a, *J. Quant. Spectrosc. Radiat. Transfer*, **26**, No. 4, pp329-337.

Younger, S.M., 1981b, *Phys. Rev. A*, **24**, No. 3, pp1278-1285.

Younger, S.M., 1982, *J. Quant. Spectrosc. Radiat. Transfer*, **27**, No. 5, pp541-544.

Zhang, H.L., Sampson, D.H. and Fontes, C.J., 1990, *Atomic and Nuclear Data Tables*, **44**, pp31-77.

# APPENDIX 1: UNITS AND SYMBOLS

SI units have been used whenever possible but on occasion these have been replaced by units which are generally used in the field of atomic physics. In particular, number densities are expressed in units of $cm^{-3}$. Two body rate coefficients are thus expressed in units of $cm^3s^{-1}$ and radiated power coefficients are expressed in units of J $s^{-1}cm^3$ or W $cm^3$. Note that 1 W $cm^3$ ≡ $10^7$ erg $s^{-1}cm^3$.

Plasma physicists frequently express plasma temperatures in electron volts, which is a measure of equivalent energy. Additionally, the Rydberg ($R_H$) and reciprocal cm ($cm^{-1}$) are frequently used as units of energy in atomic physics. These units are related by the following:

| | | | | | | |
|---|---|---|---|---|---|---|
| 1 eV | = | $1.602\times10^{-19}$ J | ≡ | $1.1604\times10^{4}$ K | ≡ | 8065.5 $cm^{-1}$ |
| 1 $R_H$ | = | 13.6058 eV | ≡ | 109737.3 $cm^{-1}$ | | |

It is also worth noting that wavelengths are expressed in units of nm:

| | | | | |
|---|---|---|---|---|
| 1 nm | = | $10^{-9}$ m | = | 10 Å |

The z times ionised state of element X is denoted by $X^{+z}$. No distinction is made between the *m* ground and metastable configurations. These are denoted by the subscripts ρ and ε. The parent ion $X^{+z1}$, with charge z1 = z + 1, has *m1* parent metastable levels denoted by the subscripts γ and σ.

To avoid continual definition of frequently used symbols, a list of such symbols is given in the following:

| | |
|---|---|
| z | ion charge |
| z1 | z+1 |
| $z_0$ | nuclear charge |
| n | principal quantum shell |
| *l* | orbital quantum number |
| L | total orbital angular momentum quantum number |

| | | |
|---|---|---|
| S | total spin quantum number | |
| J | total angular momentum quantum number | |
| $T_e$ | electron temperature | (K or eV) |
| $T_i$ | ion temperature | (K or eV) |
| $n_e$ | electron density ($cm^{-3}$) | |
| $n_H$ | neutral hydrogen density ($cm^{-3}$) | |
| $\tau_E$ | energy confinement time | |
| $\tau$(e-e) | electron self collision time | |
| $\tau$(p-p) | proton self collision time | |
| $\tau$(e-p) | electron-proton equipartion time | |
| $\tau_{ion}$ | ionisation time | |
| v | particle velocity | |
| f(v) | distribution function (normalised to 1.0) | |
| $\Lambda$ | Coulomb logarithm | |
| $m_e$ | rest mass of electron | ($9.10953 \times 10^{-31}$ kg) |
| $m_p$ | rest mass of proton | ($1.67265 \times 10^{-27}$ kg) |
| h | Planck's constant | ($6.62618 \times 10^{-34}$ $Js^{-1}$) |
| k | Boltzmann constant | ($1.3807 \times 10^{-23}$ $JK^{-1}$) |
| c | speed of light | ($2.997925 \times 10^{8}$ $ms^{-1}$) |
| $a_0$ | Bohr radius | ($5.29177 \times 10^{-11}$ m) |
| $\alpha$ | fine structure constant | ($7.29177 \times 10^{-3}$ or $1/\alpha = 137.0360$) |
| $\delta$ | quantum defect | |
| $\nu$(n) | effective quantum number of principal quantum shell n | |
| $n_{th}$ | threshold principal quantum shell for autoionisation. $n_{th}$ is the lowest shell which will autoionise. | |
| $I_H$ | ionisation energy of hydrogen (13.6058eV or $1R_H$) | |
| I(n,*l*) | ionisation energy of state with quantum numbers n and *l* | |
| $\zeta$ | number of electrons | |
| $E_{LS}$ | LS term averaged energy | |
| $E_{LSJ}$ | J resolved level energy | |
| $\Gamma$ | particle flux | |
| D | Diffusion coefficient | |
| $v_c$ | convective velocity | |
| $\lambda$ | wavelength (nm) | |
| $\lambda_{sat}$ | satellite line wavelength (nm) | |
| $E_{sat}$ | satellite line energy | |
| I($\lambda$) | Intensity of spectral line of wavelength $\lambda$ (photons $s^{-1}$ $cm^{-3}$) | |

| | |
|---|---|
| $\omega(i)$ | statistical weight of level i |
| $\Omega(i,j)$ | collision strength for transition between i and j |
| $k_i^2$ | electron energy |
| $\sigma(i \rightarrow j)$ | cross section for transition between states i and j |
| $\Delta E$ | transition energy |
| U | threshold parameter (= $k_i^2/U$) |
| S | ionisation rate coefficient ($cm^3s^{-1}$) |
| q | collisional excitation/de-excitation rate coefficient ($cm^3s^{-1}$) |
| $A^r$ | radiative transition probability ($s^{-1}$) |
| $A^a$ | autoionisation transition probability ($s^{-1}$) |
| $A^{cap}$ | transition probability for dielectronic capture ($s^{-1}$) |
| $\alpha$ | recombination rate coefficient. Superscripts r,d,t or cx denote radiative, dielectronic, three body and charge exchange recombination respectively ($cm^3s^{-1}$) |
| $C_{ij}$ | collisional-radiative matrix element ($s^{-1}$) |
| $L_{\sigma j}$ | loss vector from level j to parent $\sigma$ ($s^{-1}$) |
| $r_{i\gamma}$ | composite recombination rate coefficient from parent $\gamma$ to level i ($cm^3s^{-1}$) |
| $F_{i\rho}$ | effective population of level i due to excitation from metastable $\rho$ (dimensionless) |
| $R_{i\gamma}$ | effective population of level i due to recombination from parent $\gamma$ (dimensionless) |
| $\varepsilon_{ex}^{eff}(\lambda,\rho)$ | effective emission coefficient for transition with wavelength $\lambda$ arising from excitation from metatsable $\rho$ (photons $s^{-1}$) |
| $\varepsilon_{rec}^{eff}(\lambda,\gamma)$ | effective emission coefficient for transition with wavelength $\lambda$ arising from recombination from parent $\gamma$ (photons $s^{-1}$) |
| $S_{\gamma\rho}^{eff}$ | efffective ionisation rate coefficient from metastable $\rho$ to parent $\gamma$ ($cm^3s^{-1}$) |
| $\alpha_{\rho\gamma}^{eff}$ | efffective recombination rate coefficient from parent $\gamma$ to metastable $\rho$ ($cm^3s^{-1}$) |
| $q_{\varepsilon\rho}^{eff}$ | efffective cross coupling rate coefficient from metastable $\rho$ to metastable $\varepsilon$ ($cm^3s^{-1}$) |
| $\beta_{\sigma\gamma}^{eff}$ | effective parent cross coupling coefficient from parent $\gamma$ to parent $\sigma$ ($cm^3s^{-1}$) |
| $g^I$ | bound-bound Gaunt factor |
| $g^{II}$ | bound-free Gaunt factor |

| | |
|---|---|
| $g^{III}$ | free-free Gaunt factor |
| $<g^{II}>$ | energy averaged bound-free Gaunt factor |
| N(X) | number density of element X $(cm^3s^{-1})$ |
| $FA(X^{+z})$ | fraction abundance of the $X^{+z}$ ionisation stage |
| F | electric field $(Vcm^{-1})$ |
| $P_{RB}(\gamma,z1)$ | composite recombination/ bremsstrahlung radiated power coefficient for $X_{\gamma}^{+z1}$ $Wcm^3$ |
| $P_B(\gamma,z1)$ | bremsstrahlung radiated power coefficient for $X_{\gamma}^{+z1}$ $Wcm^3$ |
| $P_{RR}(\gamma\rightarrow\rho,z1)$ | recombination radiated power coefficient arising from radiative recombination from $X_{\gamma}^{+z1}$ towards $X_{\rho}^{+z}$ |
| $P_{RS}(\gamma\rightarrow\rho,z1)$ | satellite radiated power coefficient arising from dielectronic recombination from $X_{\gamma}^{+z1}$ towards $X_{\rho}^{+z}$ |
| $P_{RC}(\gamma\rightarrow\rho,z1)$ | cascade radiated power coefficient arising from recombination from $X_{\gamma}^{+z1}$ towards $X_{\rho}^{+z}$ |
| $P_L(\gamma,z1)$ | line power coefficient arising from excitation of $X_{\gamma}^{+z1}$ |

# APPENDIX 2: EXTENDED COLLISIONAL-RADIATIVE THEORY


A2.1: Equivalence of Expressions
A2.2: Generalisation of Projection and Indirect Couplings
A2.3: Matrix Condensation


## A2.1: Equivalence of Expressions

It is necessary to prove formally the equivalence between the collisional-radiative coefficients first defined by Bates et al (1962) which are based upon the rate of change of the ground and metastable states of $X^{+z}$ and those derived in the present work which are based upon the rates of change of the parent states of $X^{+z1}$. The work of Summers and co-workers uses the formulation of Bates et al.

Firstly, consider the expressions for ionisation rate coefficients. The ionisation rate coefficient used by Summers and co-workers is the total loss rate for the ground state of interest with no resolution of final state. This should be equivalent to the sum of the parent resolved coefficients derived in the present work.

$$\Sigma_\sigma \, S^{eff}_{\sigma\rho} \, |_{PW} \quad \equiv \quad S^{eff}_{\rho\rho} \, |_{S} \qquad \text{E(A2.1.1)}$$

where $\sigma$ indexes an arbitrary parent, $|_{PW}$ denotes the expression derived in the present work and $|_S$ denotes the expression used by Summers. Expanding the expressions of both sides of the equivalence we require

$$\Sigma_\sigma \left( L_{\sigma\rho} - \Sigma_j \, L_{\sigma j} \, n_e \, F_{j\rho} \right) \equiv \quad C_{\rho\rho} - \Sigma_j \, C_{1j} \, n_e \, F_{j\rho} \qquad \text{E(A2.1.2)}$$

$$\text{where} \qquad n_e \, F_{j\rho} \quad = \quad \Sigma_k \, C^{-1}_{jk} \, C_{k\rho} \qquad \text{E(A2.1.3)}$$

with $C_{jk}$ the collisional- radiative matrix. This requires

$$\Sigma_\sigma \, L_{\sigma\rho} - C_{\rho\rho} \quad \equiv \quad \Sigma_j \left( \left(\Sigma_\sigma \, L_{\sigma j}\right) - C_{\rho j} \right) n_e \, F_{j\rho} \qquad \text{E(A2.1.4)}$$

but, from the definitions of the matrix elements

$$C_{\rho\rho} = (\Sigma_\sigma L_{\sigma\rho}) - \Sigma_j C_{j\rho} \qquad \text{E(A2.1.5)}$$

$$C_{jj} = (\Sigma_\sigma L_{\sigma j}) - C_{\rho j} - \Sigma_{i \neq j} C_{ij} \qquad \text{E(A2.1.6)}$$

which after substitution and rearrangement gives

$$\Sigma_j C_{j\rho} \equiv \Sigma_j (\Sigma_i C_{ij}) n_e F_{j\rho} \qquad \text{E(A2.1.7a)}$$

$$\equiv \Sigma_j (\Sigma_i C_{ij}) \Sigma_k C^{-1}_{jk} C_{k\rho} \qquad \text{E(A2.1.7b)}$$

$$\equiv \Sigma_k C_{k\rho} \left( \Sigma_j (\Sigma_i C_{ij}) C^{-1}_{jk} \right) \qquad \text{E(A2.1.7c)}$$

$$\equiv \Sigma_k C_{k\rho} \left( \Sigma_i \delta_{ik} \right) \qquad \text{E(A2.1.7d)}$$

$$\equiv \Sigma_i C_{i\rho} \qquad \text{E(A2.1.7e)}$$

and so the equivalence is established. A similar argument also proves the equivalence between the recombination coefficient of Summers and co-workers and that defined in the present work. That is

$$\alpha^{eff}_{\sigma\sigma}\big|_{PW} \equiv \Sigma_\rho \alpha^{eff}_{\rho\sigma}\big|_S \qquad \text{E(A2.1.8)}$$

or

$$\Sigma_\rho r_{\rho\sigma} + \Sigma_j r_{j\sigma} - \Sigma_j L_{\sigma j} R_{j\sigma} \equiv \Sigma_\rho (r_{\rho\sigma} - \Sigma_j C_{\rho j} R_{j\sigma}) \qquad \text{E(A2.1.9)}$$

In the work of Summers and co-workers, there is no analogy to the parent cross coupling coefficient, $\beta^{eff}_{\varepsilon\gamma}$. Note that the total loss rate from the recombining parent is given by the sum of recombination rates and cross coupling coefficients.

## A2.2: Generalisation of Projection and Indirect Couplings

Consider a level set with one recombining parent, $X^{+z1}_\gamma$, and several alternative parents, $X^{+z1}_\sigma$, which can be populated by ionisation or autoionisation. The extension of the theory to accommodate several recombining parents is straightforward but not necessary. The total level

set is partitioned into the set of low levels, indexed by I, J, ...., and a set of high levels, indexed by i, j, ... . The rate of change of the high levels can be written as

$$d/dt\ N_i^{+z} = -\Sigma_j C_{ij} N_j^{+z} - \Sigma_J C_{iJ} N_J^{+z} + n_e r_{i\gamma} N_\gamma^{+z1} \qquad \text{E(A2.2.1)}$$

with the usual convention for the signs of the elements of the collisional radiative matrix. In quasi- static equilibrium this gives the populations in terms of effective contributions from the low levels and from recombination as

$$N_j^{+z} = \Sigma_J n_e F_{jJ} N_J^{+z} + n_e R_{j\gamma} N_\gamma^{+z1} \qquad \text{E(A2.2.2)}$$

where as before

$$F_{jJ} = -\Sigma_i C_{ji}^{-1} C_{iJ} / n_e \qquad \text{E(A2.2.2)}$$

$$R_{j\gamma} = \Sigma_i C_{ji}^{-1} r_{i\gamma} \qquad \text{E(A2.2.3)}$$

Now consider the rate of change of the low level set

$$d/dt\ N_J^{+z} = -\Sigma_K C_{JK} N_K^{+z} - \Sigma_j C_{Jj} N_j^{+z} + n_e r_{J\gamma} N_\gamma^{+z1} \qquad \text{E(A2.2.4)}$$

which upon substitution of E(A2.3.2) for $N_j$ becomes

$$d/dt\ N_J = -\Sigma_K C_{JK} N_K^{+z} - \Sigma_j C_{Jj} (\Sigma_K n_e F_{jK} N_K^{+z} + n_e R_{j\gamma} N_\gamma^{+z}) + n_e r_{J\gamma} N_\gamma^{+z1} \qquad \text{E(A2.2.5)}$$

$$= -\Sigma_K ( C_{JK} + \Sigma_j C_{Jj} n_e F_{jK} ) N_K^{+z} + ( r_{J\gamma} - \Sigma_j C_{Jj} R_{j\gamma} ) n_e N_\gamma^{+z1}$$

↑ direct coupling; ↑ indirect coupling; ↑ direct recom; ↑ cascade contribution

E(A2.2.6)

$$= \Sigma_K \left( C_{JK}^{dir} + C_{JK}^{ind} \right) N_K^{+z} + \left( r_J^{dir} + r_J^{ind} \right) n_e N_\gamma^{+z1}$$

E(A2.2.7)

This expresses the population equations between the low level set in terms of direct and indirect couplings and direct and indirect (cascade) recombination.

In a similar way, indirect contributions to the loss vector can be derived by considering the equation

$$d/dt\ N_\sigma^{+z1} = \Sigma_K L_{\sigma K} N_K^{+z} + \Sigma_j L_{\sigma j} N_j^{+z} \qquad \text{E(A2.2.8)}$$

$$= \Sigma_K L_{\sigma K} N_K^{+z} + \Sigma_j L_{\sigma j} \left( \Sigma_K n_e F_{jK} N_K^{+z} + n_e R_{j\gamma} N_\gamma^{+z1} \right)$$

E(A2.2.9)

$$= \Sigma_K \left( L_{\sigma K} + \Sigma_j L_{\sigma j} n_e F_{jK} \right) N_K^{+z} + \Sigma_j L_{\sigma j} R_{j\gamma} n_e N_\gamma^{+z1}$$

E(A2.2.10)

$$= \Sigma_K \left( L_{\sigma K}^{dir} + L_{\sigma K}^{ind} \right) N_K^{+z} + \beta_{\sigma\gamma}^{ind} N_\gamma^{+z1} \qquad \text{E(A2.2.11)}$$

↑ direct ionis. ↑ indirect ionis. ↑ indirect cross coupling

where the quantity $\beta_{\varepsilon\gamma}^{ind}$ arises from recombination/autoionisation to levels in the high level set. The parent cross coupling coefficient is then derived from

$$\beta_{\sigma\gamma}^{eff} = \Sigma_K \left( L_{\sigma K}^{dir} + L_{\sigma K}^{ind} \right) n_e R_{K\gamma} + \beta_{\sigma\gamma}^{ind} \qquad \text{E(A2.2.12)}$$

which adds the indirect parent cross coupling coefficient to that due to the low level populations.

## A2.3: Matrix Condensation

It is also necessary to show that the use of matrix condensation techniques and a representative set of n-shells does not change the form of the equations. The populations of the complete set of levels are related to those of the representative set by 3 point Lagrangian interpolation as

$$N_i = \Sigma_{(k)} \omega_{i(k)} N_{(k)} \qquad \text{E(A2.3.1)}$$

where level indices in brackets are those of the representative set, $\omega_{i(k)}$ are the interpolation coefficients and $N_{(k)}$ are the populations of the representative set. When the above expression is substituted into the equations of statistical balance, the equations are identical in form to the original equations:

$$d/dt\ N_{(i)} = \Sigma_j C_{(i)j} N_j \qquad \text{E(A2.3.2)}$$

$$= \Sigma_j C_{(i)j} \Sigma_{(k)} \omega_{i(k)} N_{(k)} \qquad \text{E(A2.3.3)}$$

$$= \Sigma_{(k)} C_{(i)(j)} N_{(k)} \qquad \text{E(A2.3.4)}$$

where

$$C_{(i)(j)} = \Sigma_j C_{(i)j} \omega_{i(k)} \qquad \text{E(A2.3.5)}$$

is the condensed collisional-radiative matrix. The solution to the population equations can now be obtained by inverting matrices of order 24x24 instead of 500x500. To derive collisional-radiative coefficients it is also necessary to condense the loss vector. That is

$$d/dt\ N_\gamma^{+z1} = L_{\gamma\rho} N_\rho + \Sigma_j L_{\gamma j} N_j \qquad \text{E(2.3.6)}$$

$$= L_{\gamma\rho} N_\rho + \Sigma_j L_{\gamma j} \Sigma_{(j)} \omega_{j(j)} N_{(j)} \qquad \text{E(2.3.7)}$$

$$= L_{\gamma\rho} N_\rho + \Sigma_{(j)} L_{\gamma(j)} N_{(j)} \qquad \text{E(2.3.8)}$$

which is the same form as before. In conclusion, the use of a representative level set and matrix condensation does not alter the form of the equations. The accuracy of this technique was investigated by

Summers (1969) and Burgess and Summers (1976). Except for the populations of the lowest few principal quantum shell, the populations vary smoothly with n. The representative set given in Section 2.3 was considered suitable. This includes the lowest 10 shells explicitly.

# APPENDIX 3: INCLUDED LOW LEVELS

**(A3.1) Sequence: H-like**

| | | Term index | | |
|---|---|---|---|---|
| | Term | Beryllium | Carbon | Oxygen |
| * | 1s $^2$S | 1 | 1 | 1 |
| | 2s $^2$S | 2 | 2 | 3 |
| | 2p $^2$P | 3 | 3 | 3 |
| | 3s $^2$S | 4 | 4 | 4 |
| | 3p $^2$P | 5 | 5 | 5 |
| | 3d $^2$D | 6 | 6 | 6 |
| | 4s $^2$S | 7 | 7 | 7 |
| | 4p $^2$P | 8 | 8 | 8 |
| | 4d $^2$D | 9 | 9 | 9 |
| | 4f $^2$F | 10 | 10 | 10 |
| | 5s $^2$S | 11 | 11 | 11 |
| | 5p $^2$P | 12 | 12 | 12 |
| | 5d $^2$D | 13 | 13 | 13 |
| | 5f $^2$F | 14 | 14 | 14 |
| | 5g $^2$G | 15 | 15 | 15 |
| | $n_0$ | 1 | 1 | 1 |
| | $n_{max}$ | 5 | 5 | 5 |
| | No. of terms | 15 | 15 | 15 |
| | Member Name | WJD92#BE | WJD92#C | WJD92#O |

* indicates populated metastable (or ground) states

member name is the file name in the fundamental computer database indicating compilers initials, year and element.

JL Dr. J. Lang, Rutherford Appleton Laboratory

HPS Prof. H.P. Summers

WJD self

**(A3.2) Sequence: He-like**

| | | Term index | | |
|---|---|---|---|---|
| | Term | Beryllium | Carbon | Oxygen |
| * | $1s^2\ ^1S$ | 1 | 1 | 1 |
| * | $1s2s\ ^3S$ | 2 | 2 | 2 |
| | $1s2s\ ^1S$ | 3 | 3 | 4 |
| | $1s2p\ ^3P$ | 4 | 4 | 3 |
| | $1s2p\ ^1P$ | 5 | 5 | 5 |
| | $1s3s\ ^3S$ | 6 | 6 | 6 |
| | $1s3s\ ^1S$ | 7 | 7 | 8 |
| | $1s3p\ ^3P$ | 8 | 8 | 7 |
| | $1s3d\ ^3D$ | 9 | 9 | 9 |
| | $1s3d\ ^1D$ | 10 | 10 | 10 |
| | $1s3p\ ^1P$ | 11 | 11 | 11 |
| | $1s4s\ ^3S$ | 12 | - | - |
| | $1s4s\ ^1S$ | 13 | - | - |
| | $1s4p\ ^3P$ | 14 | - | - |
| | $1s4d\ ^3D$ | 15 | - | - |
| | $1s4d\ ^1D$ | 16 | - | - |
| | $1s4f\ ^1F$ | 17 | - | - |
| | $1s4f\ ^3F$ | 18 | - | - |
| | $1s4p\ ^1P$ | 19 | - | - |
| | $1s5s\ ^3S$ | 20 | - | - |
| | $1s5s\ ^1S$ | 21 | - | - |
| | $1s5p\ ^3P$ | 22 | - | - |
| | $1s5d\ ^3D$ | 23 | - | - |
| | $1s5d\ ^1D$ | 24 | - | - |
| | $1s5f\ ^1F$ | 25 | - | - |
| | $1s5g\ ^1G$ | 26 | - | - |
| | $1s5f\ ^3F$ | 27 | - | - |
| | $1s5g\ ^3G$ | 28 | - | - |
| | $1s5p\ ^1P$ | 29 | - | - |
| | $n_0$ | 1 | 1 | 1 |
| | $n_{max}$ | 5 | 3 | 3 |
| | No. of terms | 29 | 11 | 11 |
| | Member Name | HPS89BE | JL1989C | JL1989O |

## (A3.3) Sequence: Li-like

| | | Term index | | |
|---|---|---|---|---|
| | Term | Beryllium | Carbon | Oxygen |
| * | $1s^2 2s\ ^2S$ | 1 | 1 | 1 |
| | $1s^2 2p\ ^2P$ | 2 | 2 | 2 |
| | $1s^2 3s\ ^2S$ | 3 | 3 | 3 |
| | $1s^2 3p\ ^2P$ | 4 | 4 | 4 |
| | $1s^2 3d\ ^2D$ | 5 | 5 | 5 |
| | $1s^2 4s\ ^2S$ | 6 | 6 | 6 |
| | $1s^2 4p\ ^2P$ | 7 | 7 | 7 |
| | $1s^2 4d\ ^2D$ | 8 | 8 | 8 |
| | $1s^2 4f\ ^2F$ | 9 | 9 | 9 |
| | $1s^2 5s\ ^2S$ | - | - | 10 |
| | $1s^2 5p\ ^2P$ | - | - | 11 |
| | $1s^2 5d\ ^2D$ | - | - | 12 |
| | $1s^2 5f\ ^2F$ | - | - | 13 |
| | $1s^2 5g\ ^2G$ | - | - | 14 |
| | $n_0$ | 2 | 2 | 2 |
| | $n_{max}$ | 4 | 4 | 5 |
| | No. of terms | 9 | 9 | 14 |
| | Member Name | WJD91#BE | WJD92#C | WJD92#O |

**(A3.4) Sequence: Be-like**

| | Term index | | |
|---|---|---|---|
| Term | Beryllium | Carbon | Oxygen |
| * $1s^2 2s^2\ ^1S$ | 1 | 1 | 1 |
| * $1s^2 2s2p\ ^3P$ | 2 | 2 | 2 |
| $1s^2 2s2p\ ^1P$ | 3 | 3 | 3 |
| $1s^2 2s3s\ ^3S$ | 4 | 10 | 7 |
| $1s^2 2s3s\ ^1S$ | 5 | 7 | 8 |
| $1s^2 2p^2\ ^1D$ | 6 | 5 | 5 |
| $1s^2 2s3p\ ^3P$ | 7 | 11 | 8 |
| $1s^2 2p^2\ ^3P$ | 8 | 4 | 10 |
| $1s^2 2s3p\ ^1P$ | 9 | 8 | 9 |
| $1s^2 2s3d\ ^3D$ | 10 | 12 | 11 |
| $1s^2 2s3d\ ^1D$ | 11 | 9 | 12 |
| $1s^2 2s4s\ ^3S$ | 12 | - | - |
| $1s^2 2s4s\ ^1S$ | 13 | - | - |
| $1s^2 2s4p\ ^3P$ | 14 | - | - |
| $1s^2 2s4p\ ^1P$ | 15 | - | - |
| $1s^2 2s4d\ ^3D$ | 16 | - | - |
| $1s^2 2s4f\ ^1F$ | 17 | - | - |
| $1s^2 2s4f\ ^3F$ | 18 | - | - |
| $1s^2 2s4d\ ^1D$ | 19 | - | - |
| $1s^2 2p^2\ ^1S$ | 20 | 6 | 6 |
| $n_0$ | 2 | 2 | 2 |
| $n_{max}$ | 4 | 3 | 3 |
| No. of terms | 20 | 12 | 12 |
| Member Name | WJD91#BE | JL1990C | WJD92#O |

**(A3.5) Sequence: B-like**

| | | Term index | |
|---|---|---|---|
| | Term | Carbon | Oxygen |
| * | $1s^2 2s^2 2p\ ^2P$ | 1 | 1 |
| * | $1s^2 2s 2p^2\ ^4P$ | 2 | 2 |
| | $1s^2 2s 2p^2\ ^2D$ | 3 | 3 |
| | $1s^2 2s 2p^2\ ^2P$ | 4 | 5 |
| | $1s^2 2s 2p^2\ ^2S$ | 5 | 4 |
| | $1s^2 2s^2 3s\ ^2S$ | 6 | 9 |
| | $1s^2 2s^2 3p\ ^2P$ | 7 | 10 |
| | $1s^2 2p^3\ ^4S$ | 8 | 6 |
| | $1s^2 2s^2 3d\ ^2D$ | 9 | 11 |
| | $1s^2 2s 2p 3s\ ^4P$ | 10 | 12 |
| | $1s^2 2s 2p 3p\ ^4D$ | 11 | 13 |
| | $1s^2 2s 2p 3p\ ^4S$ | 12 | 14 |
| | $1s^2 2s 2p 3p\ ^4P$ | 13 | 15 |
| | $1s^2 2s 2p 3d\ ^4F$ | 14 | 16 |
| | $1s^2 2s 2p 3d\ ^4D$ | 15 | 17 |
| | $1s^2 2s 2p 3d\ ^4P$ | 16 | 18 |
| | $1s^2 2p^3\ ^2D$ | - | 7 |
| | $1s^2 2p^3\ ^2P$ | - | 8 |
| | $n_0$ | 2 | 2 |
| | $n_{max}$ | 3 | 3 |
| | No. of terms | 16 | 18 |
| | Member Name | JL1990C | WJD92#O |

**(A3.6) Sequence: C-like**

| | Term index | |
|---|---|---|
| Term | Carbon | Oxygen |
| * $1s^2 2s^2 2p^2\ ^3P$ | 1 | 1 |
| * $1s^2 2s^2 2p^2\ ^1D$ | 2 | 2 |
| * $1s^2 2s^2 2p^2\ ^1S$ | 3 | 3 |
| * $1s^2 2s 2p^3\ ^5S$ | 4 | 4 |
| $1s^2 2s^2 2p 3s\ ^3P$ | 5 | 10 |
| $1s^2 2s^2 2p 3s\ ^1P$ | 6 | 11 |
| $1s^2 2s 2p^3\ ^3D$ | 7 | 5 |
| $1s^2 2s^2 2p 3p\ ^1P$ | 8 | 13 |
| $1s^2 2s^2 2p 3p\ ^3D$ | 9 | 14 |
| $1s^2 2s^2 2p 3p\ ^3S$ | 10 | 15 |
| $1s^2 2s^2 2p 3p\ ^3P$ | 11 | 16 |
| $1s^2 2s^2 2p 3p\ ^1D$ | 12 | 18 |
| $1s^2 2s 2p^3\ ^3P$ | 13 | 6 |
| $1s^2 2s^2 2p 3p\ ^1S$ | 14 | 19 |
| $1s^2 2s^2 2p 3d\ ^1D$ | 15 | 20 |
| $1s^2 2s^2 2p 3d\ ^3D$ | 16 | 22 |
| $1s^2 2s^2 2p 3d\ ^3F$ | 17 | 21 |
| $1s^2 2s^2 2p 3d\ ^1F$ | 18 | 24 |
| $1s^2 2s^2 2p 3d\ ^1P$ | 19 | 25 |
| $1s^2 2s^2 2p 3d\ ^3P$ | 20 | 23 |
| $1s^2 2s 2p^3\ ^1D$ | 21 | 7 |
| $1s^2 2s 2p^3\ ^3S$ | 22 | 8 |
| $1s^2 2s 2p^3\ ^1P$ | 23 | 9 |
| $1s^2 2p^4\ ^3P$ | - | 12 |
| $1s^2 2p^4\ ^1D$ | - | 17 |
| $1s^2 2p^4\ ^1S$ | - | 26 |
| $n_0$ | 2 | 2 |
| $n_{max}$ | 3 | 3 |
| No. of terms | 23 | 26 |
| Member Name | WJD92#C | WJD92#O |

**(A3.7) Sequence: N-like**

| Term | Term index Oxygen |
|---|---|
| * $2s^2 2p^3\ ^4S$ | 1 |
| * $2s^2 2p^3\ ^2D$ | 2 |
| * $2s^2 2p^3\ ^2P$ | 3 |
| $2s2p^4\ ^4P$ | 4 |
| $2s2p^4\ ^2D$ | 5 |
| $2s2p^4\ ^2S$ | 6 |
| $2s2p^4\ ^2P$ | 7 |
| $(2s^2 2p^2\ ^3P)3s\ ^4P$ | 8 |
| $(2s^2 2p^2\ ^3P)3p\ ^4D$ | 9 |
| $(2s^2 2p^2\ ^3P)3p\ ^4P$ | 10 |
| $(2s^2 2p^2\ ^3P)3p\ ^4S$ | 11 |
| $(2s^2 2p^2\ ^3P)3d\ ^4F$ | 12 |
| $(2s^2 2p^2\ ^3P)3d\ ^4D$ | 13 |
| $(2s^2 2p^2\ ^3P)3d\ ^4P$ | 14 |
| $(2s^2 2p^2\ ^3P)3s\ ^2P$ | 15 |
| $(2s^2 2p^2\ ^3P)3p\ ^2S$ | 16 |
| $(2s^2 2p^2\ ^3P)3p\ ^2P$ | 17 |
| $(2s^2 2p^2\ ^3P)3p\ ^2D$ | 18 |
| $(2s^2 2p^2\ ^3P)3d\ ^2P$ | 19 |
| $(2s^2 2p^2\ ^3P)3d\ ^2D$ | 20 |
| $(2s^2 2p^2\ ^3P)3d\ ^2F$ | 21 |

**(A3.8) Sequence: O-like**

| Term | Term index Oxygen |
|---|---|
| * $2s^2 2p^4\ ^3P$ | 1 |
| * $2s^2 2p^4\ ^1D$ | 2 |
| * $2s^2 2p^4\ ^1S$ | 3 |
| * $(2s^2 2p^3\ ^4S)3s\ ^5S$ | 4 |
| $(2s^2 2p^3\ ^4S)3s\ ^3S$ | 5 |
| $(2s^2 2p^3\ ^4S)3p\ ^5P$ | 6 |
| $(2s^2 2p^3\ ^4S)3p\ ^3P$ | 7 |
| $(2s^2 2p^3\ ^4S)3d\ ^5D$ | 8 |
| $(2s^2 2p^3\ ^4S)3d\ ^3D$ | 9 |

| | | |
|---|---|---|
| $n_0$ | 2 | 2 |
| $n_{max}$ | 3 | 3 |
| No. of terms | 21 | 9 |
| Member Name | JL1990O | WJD92#O |

# APPENDIX A4:
# CALCULATION OF RADIATED POWER COEFFICIENTS

Metastable and parent resolved radiated power coefficients are defined so that the total radiated power density arising from $X_{\gamma}^{+z1}$ is

$$n_e \, N_{\gamma}^{+z1} \, P_{rad}(\gamma,z1) \quad = \quad n_e \, N_{\gamma}^{+z1} \, ( \, P_L(\gamma,z1) \quad + \quad P_{RB}(\gamma,z1) \, ) \qquad \text{E(A4.1)}$$

$\text{Ws}^{-1}$

where $P_L$ is the radiated line power from excitation within the low level group and $P_{RB}$ is a composite coefficient which sums cascade, recombination radiation , dielectronic stabilisation and bremsstrahlung contributions (consult Section 2.2.4, *Radiative Power Loss Coefficients*). $P_L$ is derived from the low level populations in either the low level or the projection model. $P_{RB}$ is derived from the bundle-n S model.

## A4.1: Radiated Line Power Coefficients

The line power coefficient is derived by summing over all radiative transitions within the low level group.

$$P_L(\gamma,z1) \quad = \quad \Sigma_{(i \to j)} \, \frac{hc}{\lambda} \, . \, \varepsilon_{ex}^{eff}(\lambda,\gamma) \qquad \text{E(A4.2)}$$

where h is Plancks constant, c is the speed of light, $\lambda$ is the wavelength of radiation for transition i→j and $\varepsilon_{ex}^{eff}(\lambda,\gamma)$ is its effective emission coefficient following excitation to level i from metastable $\gamma$.

In the projection model, no line radiation from outwith the low level group included. The accuracy of this approximation is discussed in Section 4.3, *The Projection/Expansion Calculation.*

## A4.2: Recombination/Bremsstrahlung Power Coefficients

The composite recombination/bremsstrahlung coefficient is defined as

$$P_{RB}(\gamma,z1) = P_B(\gamma,z1) + \Sigma_\rho \left( P_{RR}(\gamma\rightarrow\rho,z1) + P_{RS}(\gamma\rightarrow\rho,z1) + P_{RC}(\gamma\rightarrow\rho,z1) \right) \qquad \text{E(A4.3)}$$

where $P_B$, $P_{RR}$, $P_{RS}$ and $P_{RC}$ are the bremsstrahlung, radiative recombination, dielectronic satellite and recombination cascade radiated power loss coefficients respectively. The calculation of these coefficients is almost identical to the procedures described by Summers and McWhirter (1979), with a few adjustments for metastable resolution. For completeness the procedures are summarised below.

The treatment presented here is accurate for hydrogen-like ions, and fairly good for helium-like ions, but is less reliable for more complex ions. However it should be noted that recombination and bremsstrahlung radiation are most important at high temperature when line radiation is least effective i.e. i.e. for hydrogen and helium like ions.

### (a) Bremsstrahlung Power Loss

The bremsstrahlung contribution due to free-free electron transitions in the field of the ion $X^{+z1}(\gamma)$ is given as

$$P_B = \left( \frac{33\sqrt{\pi}}{3\sqrt{3}} \alpha^4 a_0^2 I_H \right) z^2 \left( kT_e/I_H \right) < \bar{g}^{III} > \qquad \text{E(A4.4)}$$

where $< \bar{g}^{III} >$ is the photon integrated and Maxwell averaged free-free Gaunt factor. The constant in round brackets is equal to $5.663^{-32}$ W cm$^3$. The Gaunt factor is evaluated following Summers and McWhirter (1979).

### (b) Recombination Radiation Power Loss

The process of free electron recombination leads to the emission of a photon of energy

$$hc/\lambda = E + z1^2/\nu^2 \qquad \text{E(A4.5)}$$

where E is the energy of the free electron and $\nu$ is the effective quantum

number of the bound state. For a fixed bound state the expression for the Maxwell averaged energy emission coefficient is given by Burgess and Summers (1987) as

$$P_{RR} = 8\left(\frac{\pi a_0^2 I_H}{kT_e}\right)^{\frac{3}{2}} \frac{4\,\alpha^4 c}{3\sqrt{3}\,\pi a_0}\; z1^4 \left(\frac{2}{\nu^3}\right) \zeta^{eff}\; (kT_e) \int_0^{\infty} g^{II} \exp(-X)\, dX \qquad E(A4.6)$$

where
$a_0$ = Bohr radius
$\alpha$ = fine structure constant
$X$ = $E/kT_e$
$\nu$ = effective quantum number of final bound state
$\zeta^{eff}$ = statistical weight factor
$g^{II}$ = bound free Gaunt factor

which is similar to the radiative recombination rate coefficient given in E(3.4.3). The radiative recombination contribution is evaluated for each individual n-shell in the bundle-n S model. Electrons captured into autoionising levels may not contribute to the effective recombination coefficient but they still contribute to the radiated power coefficient.

**(c) Dielectronic Stabilisation (or Satellite) Radiation**

The number of stabilising photons emitted is given by the zero density dielectronic recombination coefficient. This contribution to the power loss coefficient is thus given by summing over all core transitions and all captured levels

$$P_{RS} = \Sigma_{(i\rightarrow j)} \Sigma_n \Delta E_{sat}(i\rightarrow j,n)\ .\ \alpha^d(i\rightarrow j;n) \qquad E(A4.7)$$

where

$$\Delta E_{sat}(i\rightarrow j,n) = hc/\lambda_{sat} \qquad E(A4.8)$$

is the satellite line energy and $\lambda_{sat}$ is the satellite line wavelength.

The stabilising photons are assumed to have the same energy as the core transition. The largest deviation from this is for capture into low n-shells, but the error is small.

**(d) Recombination Cascade Contributions**

Dielectronic and radiative recombination also contribute to power loss through cascade of the recombined electrons. The bundle-n S model is used to calculated this contribution. This is appropriate because the dominant contribution is from dielectronic recombination which primarily populates high n-shells. In low density plasmas, the electron in its cascade will liberate close to the ionisation potential energy. At high electron densities however the energy loss decreases as electrons are ionised before they cascade. The contribution of each parent/spin system resolved pathway is given by

$$P_{RC} = \Sigma_i \Sigma_{j<i} z1^2.(1/\nu(j)^2 - 1/\nu(i)^2 ) A^r(i\rightarrow j) n_e R_{i\gamma} \qquad E(A4.9)$$

where $R_{i\gamma}$ is the effective recombination contribution to the population of principal quantum shell i. Cascade power coefficients calculated in this manner have the full density dependence included explicitly.